Characterisation of a novel interaction between the cardiac myosin binding protein-C and the ryanodine receptor/calcium release channel

PAULINA JULIANNA STANCZYK

A thesis submitted for the degree of
Doctor of Philosophy

September 2016

Word count: 62853

DECLARATION

This work has not been submitted in substance for any other degree or award at this or any other university or place of learning, nor is being submitted concurrently in candidature for any degree or other award.

Signed .... Date ....

STATEMENT 1

This thesis is being submitted in partial fulfilment of the requirements for the degree of PhD.

Signed .... Date ....

STATEMENT 2

This thesis is the result of my own independent work/investigation, except where otherwise stated. Other sources are acknowledged by explicit references. The views expressed are my own.

Signed .... Date ....

STATEMENT 3

I hereby give consent for my thesis, if accepted, to be available for photocopying and for inter-library loan, and for the title and summary to be made available to outside organisations.

Signed .... Date ....

Acknowledgements

First of all, I would like to thank Professor F. Anthony Lai, who gave me the opportunity to perform my PhD research in the Institute of Molecular and Experimental Medicine, Cardiff University.

Further, I am forever grateful to my co-supervisor Dr Spyros Zissimopoulos, for his scientific input, continuous guidance and inspiring motivation throughout duration of this project. I want to thank him especially for always being approachable and patiently listening to all my questions, no matter how big or small.

I would like to acknowledge Karen Shihao Chen, for her contribution in minimal RyR2 binding region co-IP analysis, and Dr Monika Seidel, for helping me with the single cell Ca^{2+} imaging, and also for her advice regarding the statistical analysis. I also would like to thank Dr Christopher George for his assistance with confocal microscopy and co-localisation study, and for providing me with mCherry plasmid. Additionally, I would like to thank Dr Pierre Rizkallah, for his assistance with PyMOL, and Mike Robinson from Medical Physics, for letting me use the Scintillation Counter. Thanks to the whole Wales Heart Research Institute for the wonderful working atmosphere and it's always helpful cooperative colleagues. I thank particularly to all the past and present members of the Lai group for all their support and company.

Of course, I would like to also acknowledge my parents and all my friends, for their unwavering support, understanding and love. Thank you for putting up with me, for believing and cheering me up when I doubted myself and felt overwhelmed.

Summary

Muscle excitation-contraction coupling (ECC) is a fundamental physiological process by which electrically-evoked sarcoplasmic reticulum (SR) Ca^{2+} release triggers cardiomyocyte contraction. Human ryanodine receptor 2 (RyR2) is an ion channel present in the SR membrane of cardiac myocytes, responsible for mediating calcium efflux. Cardiac myosin binding protein-C (cMyBP-C) is a modular protein anchored to the thick filament through its C-terminal region, whereas the N-terminal region of cMyBP-C is thought to regulate myocardial contractility by modifying actin-myosin association. Here, we present several lines of evidence indicating potential RyR2:cMyBP-C interaction, which could provide a novel retrograde regulation of SR Ca^{2+} release by the sarcomere.

Firstly, co-immunoprecipitation (co-IP) experiments indicated that the detected putative association between RyR2 and cMyBP-C can be applicable to large mammalian species as well as to recombinant human proteins heterologously expressed in a mammalian cell line, with RyR2 N-terminus and cMyBP-C C-terminus being responsible for the binding. A 3D co-localisation immunocytochemistry study supported the possibility for the proteins to be readily available for protein-protein interaction, with recombinant human RyR2 and cMyBP-C shown to co-localise in HEK293 cells.

Secondly, with the aid of two complementary techniques, namely co-IP and yeast 2-hybrid (Y2H), we showed that RyR2 residues 1-906 comprise the main cMyBP-C site, with residues 1-346 (corresponding to subdomain A and B of RyR2 NTD) and 654-906 (domain SPRY1 and P1) being important determinants for the binding with cMyBP-C C-terminus. Further mapping studies implied that cMyBP-C residues 820-972 and 1061-1274 are involved in the interaction with RyR2 N-terminus, with cMyBP-C Fn domain/s proposed to be directly responsible for the binding. Additionally, parallel experiments with the skeletal muscle RyR1 demonstrated that the corresponding N-terminus region (RyR2 1-906 amino acids) of mammalian isoform RyR1 can also interact with MyBP-C, which could indicate that the detected association can also be relevant in the regulation of ECC in skeletal muscle.

Thirdly, we pursued the possible functional significance of RyR2:cMyBP-C interaction. The results from single cell Ca^{2+} imaging indicated that cMyBP-C interaction with RyR2 may have an inhibitory effect on Ca^{2+} release channel function, with cMyBP-C binding diminishing RyR2 channel activity. In particular, HEK293 cells co-expressing RyR2 and cMyBP-C had a reduced frequency of spontaneous intracellular calcium oscillations compared to cells expressing only RyR2.

Lastly, further co-IP data demonstrated that cMyBP-C:RyR2 binding is not affected by four different RyR2 single point mutation variants (S166C, R176Q, R420Q and L433P) associated with different pathological phenotypes. Thus, while a physical and functional association between RyR2 and cMyBP-C was shown to possibly regulate normal cardiac physiology, it is unlikely to be involved in RyR2-related cardiac disease. In order to unravel the pathological significance of the detected cMyBP-C:RyR2 association, more studies are needed to understand what role cMyBP-C plays in RyR2 channel dysfunction that could potentially affect muscle contraction/relaxation.

Publications

Poster communications:

Stanczyk P. J., Lai F. A., Zissimopoulos S. 2015. Characterisation of a novel interaction between the cardiac myosin binding protein-C and the ryanodine receptor/calcium release channel. In Proceedings of The Physiological Society 2015. The Physiological Society.

Seidel, M., Stanczyk, P. J., Lai, F. A., Zissimopoulos, S. 2014. Mapping the interacting sites mediating tetramerisation of Ryanodine Receptor amino-terminus. Biophysical Journal 106(2), 106a-107a.

Peer reviewed publications:

Stanczyk, P. J., Lai F. A., and Zissimopoulos, S. 2016. Genetic and biochemical approaches for in vivo and in vitro assessment of protein oligomerization: the Ryanodine Receptor case study. JoVE 113, e54271-e54271.

Evans, A. G., Davey, H. M., Cookson, A., Currinn, H., Cooke-Fox, G., Stanczyk, P. J., & Whitworth, D. E. 2012. Predatory activity of Myxococcus xanthus outer-membrane vesicles and properties of their hydrolase cargo. Microbiology, 158(11), 2742-2752.

In-progress publication related to this work:

Stanczyk, P. J, Seidel, M., White, J., Viero, C., George, C. H., Zissimopoulos, S., Lai, F. A., 2017, Cardiac myosin binding protein-C association with the ryanodine receptor Ca^{2+} release channel.

Table of Contents

Abbreviations List

Ab	Antibody
AM	Acetoxymethyl
AP	Action potential
ARVD	Arrhythmogenic right ventricular dysplasia
β-AR	β-adrenergic response
β-gal	β-galactosidase
BLAST	Basic Local Alignment Search Tool
BSA	Bovine serum albumin
Ca^{2+}	Ionised calcium
$[Ca^{2+}]_i$	Intracellular Ca^{2+}
CaM	Calmodulin
CaMKII	Ca^{2+}/calmodulin-dependent kinase II
CCD	Central core disease
CICR	Ca^{2+}-induced Ca^{2+} release
cMyBP-C	Cardiac myosin binding protein C
Co-IP	Co-immunoprecipitation
CPVT	Catecholaminergic polymorphic ventricular tachycardia
DA-1	Distal arthrogryposis type-1
DCM	Dilated cardiomyopathy
DMEM	Dulbecco’s modified eagle medium
DMSO	Dimethyl sulfoxide

dNTP	Deoxynucleotide
dH_2O	Deionised water
DTSSP	3,3'-Dithiobis(sulfosuccinimidylpropionate)
ECC	Excitation-contraction coupling
ECL	Enhanced chemiluminescence
EDTA	Ethylenediaminetetraacetic acid
ER	Endoplasmic reticulum
FBS	Foetal bovine serum
FKBP	FK506 binding protein
Fn	Fibronectin-like domain
GSK3β	Glycogen synthase kinase 3 β
HCM	Hypertrophic cardiomyopathy
HEK293	Human embryonic kidney 293 cells
HET	Heterozygous
HRP	Horseradish peroxidase
ICC	Immunocytochemistry
Ig	Immunoglobulin-like domain
IP3	Inositol 1, 4, 5-trisphosphate
IP3R	Inositol 1, 4, 5-trisphosphate receptors
KI	Knock-in
KO	Knock-out
KRH	Krebs-Ringer-Hepes
LB	Luria-Bertani medium
LiAc	Lithium acetate

LMM	Light meromyosin portion
LTCC	L-type Ca^{2+} channel (or dihydropyridine receptor)
LVNC	Left ventricular non-compaction
M-domain	MyBP-C-specific domain
MH	Malignant hyperthermia
MI	Myocardial infraction
MmD	Multiminicore disease
MyBP-C	Myosin binding protein C
MYH	Myosin heavy chain
NCX	Sodium-calcium exchanger
NEB	New England Biolabs
NTD	N-terminal domain
P/A	Proline- and alanine-rich region
PBS	Phosphate buffered saline
PCC	Pearson’s correlation coefficient
PCR	Polymerase chain reaction
PKA	Protein kinase A
PKC	Protein kinase C
PKD	Protein kinase D
PLB	Phospholamban
PMCA	Plasma membrane Ca^{2+}-ATPase
PVDF	Polyvinylidene difluoride
PEG 3350	Polyethylene glycol 3350
RLC	Regulatory light chain

ROI	Region of interest
RyR	Ryanodine receptor
RyR1	RyR skeletal muscle isoform (or RyR type 1)
RyR2	RyR cardiac muscle isoform (or RyR type 2)
RyR3	RyR type 3 isoform
SCR	Spontaneous Ca^{2+} release
SD	Standard deviation
SDY	Yeast minimal medium, synthetic defined
SDS	Sodium dodecyl sulphate
SDS-PAGE	SDS polyacrylamide gel electrophoresis
SEM	Standard error of the mean
SERCA	Sarco/endoplasmic reticulum Ca^{2+} ATPase
SCR	Spontaneous Ca^{2+} release
SOC	Super optimal broth supplemented with glucose
SOICR	Store overload-induced Ca^{2+} release
SR	Sarcoplasmic reticulum
TAE	Tris-acetate-EDTA
TATS	Transverse-axial tubule system
TBS	Tris-buffered saline
TBS-T	TBS with added 0.1% (v/v) Tween-20
TE	Tris/EDTA
TEMED	N,N,N',N'-tetramethylethylenediamine
TnC	Troponin C
TnI	Troponin I

TnT	Troponin T
TPC	Two-pore channels
Tris	2-amino-2-hydroxymethyl-proapne-1,3-diol
T-tubule	Transverse tubule
WB	Western blotting
WT	Wild type
VGCC	Voltage-gated calcium channel
X-gal	5-bromo-4-chloro-3-indolyl-β-D-galactopyranoside
YPD	Yeast complete medium, yeast extract peptone dextrose
Y2H	Yeast-2-hybrid

Chapter 1

General introduction

1 General introduction

1.1 Cardiac calcium signalling and contraction

Ionised calcium (Ca^{2+}) is a highly versatile intracellular signalling molecule, responsible for regulating a wide range of different cellular processes, including muscle contraction, neurotransmission, fertilisation, proliferation and apoptosis (Clapham 2007). To control so many diverse functions, the Ca^{2+}-signalling systems exhibit high degree of versatility in terms of Ca^{2+} signals' frequency, amplitude and spatio-temporal patterning, thus operating in a wide dynamic range from localised rapid brief bursts of Ca^{2+} to longer-lasting, global Ca^{2+} transients in the form of repetitive waves. Despite its importance in the cell function, sustained or high concentrations of Ca^{2+} are known to be cytotoxic, and for this reason Ca^{2+} fluxes must be tightly regulated. To assure that, the complexity of Ca^{2+} signals is aided by a subset of molecules and protein complexes that acts in a coordinated manner, allowing to regulate intracellular Ca^{2+} release and sequestration (Berridge et al. 2003; Berridge 2006).

1.1.1 Excitation-Contraction Coupling (ECC)

In the cardiac muscle, Ca^{2+} is an essential messenger directly transducing the electrical depolarisation stimulus into mechanical contraction of the heart, in a process termed Excitation-Contraction Coupling (ECC**,** see **Figure 1.1**)(Bers 2002). Cardiac Ca^{2+} signalling has been most extensively studied in cardiomyocytes isolated from the ventricles. It is well established that Ca^{2+} transients in mammalian ventricular myocytes take the form of homogenous whole-cell increases (Bers 2008). When the heart is at rest (diastole), intracellular Ca^{2+} is sequestered into the sarcoplasmic reticulum (SR), which is the major internal Ca^{2+} store of the cardiomyocytes. During systole, the cardiac ECC is initiated by the electrical excitation (originating from the sinoatrial node) of the myocyte sarcolemma, and concomitant change in the cardiomyocyte plasma membrane potential causing depolarisation (from ~-80 mV to ~+40 mV) in form of an action potential (AP) (Bers

2002). The propagation of AP depolarizes plasma membrane of cardiomyocyte and subsequently causes coordinated opening of the voltage-gated calcium channels (VGCCs) present on the sarcolemma. Their opening allows Ca^{2+} to enter the cardiac myocyte cytoplasm, increasing the local intracellular Ca^{2+} ($[Ca^{2+}]_i$) from a resting level of ~100 nM to 10µM within tens of microseconds (Fearnley et al. 2011). Cardiomyocytes exhibit two classes of VGCCs, namely L-type (LTCC) and T-type calcium channels. The latter are activated by low voltage and expressed mainly in conducting and pacemaker cells and at negligible levels in ventricular myocytes, whereas LTCCs are characterized by higher voltage activation profile and are the main contributors in the regulation of both AP (by providing an inward Ca^{2+} current) and ECC (by triggering the release of calcium from SR) (Bers 2008).

The mammalian ventricular cardiomyocytes are characterized by the presence of an extensive network of the transverse-axial tubule system (TATS), which plays a crucial role in the process of ECC and Ca^{2+} release from SR (Ferrantini et al. 2013). TATS are deep physical invaginations of the surface membrane that branch within the cell to form a complex network with predominantly transverse elements (T-tubules) that occur at each Z-line, but also longitudinal (axial) components running from one Z-line

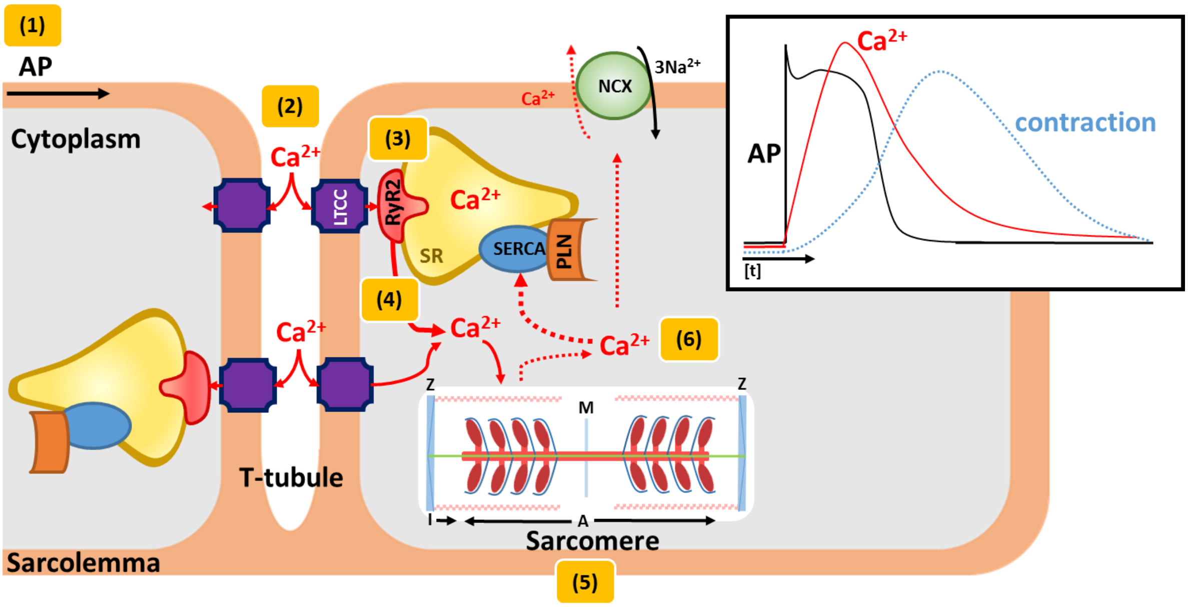

Figure 1.1 Schematic showing the major elements of ECC. Main panel: (1) AP travels along sarcolemma and (2) activates LTCC, which results in Ca^{2+} influx into the cytoplasm. This in turn (3) activates RyR2 and Ca^{2+} release from SR (4); the increase in cytoplasmic Ca^{2+} enables (5) acto-myosin cross-bridge formation and muscle contraction. During diastole, (6) Ca^{2+} returns to resting levels by SERCA-mediated pumping of Ca^{2+} back into SR and Ca^{2+} extrusion via NCX; (Small panel) the temporal relationship of cardiac AP (black) and the Ca^{2+} transient (red) and muscle contraction (blue) during the single ECC event. Adapted from (Bers 2002).

to the next (Ferrantini et al. 2013). The regions of close apposition of the T-tubules and the junctional SR (termed dyads) bring the LTCCs in close proximity (~15 nm) to clusters of Ca^{2+} release channels (ryanodine receptors type 2, RyR2) on the junctional SR membrane (Asghari et al. 2009). In this way, the formed RyR2:LTCC structures, known as junctions or couplons, are found in close proximity to the Z-lines, usually <250 nm (Jayasinghe et al. 2009). The architecture of the dyadic microdomains (also referred to as dyadic clefts) allows for the local increases in Ca^{2+} by influx of extracellular Ca^{2+} through the LTCCs, leading to increase of Ca^{2+} concertation within the cleft. In adult mammalian cardiac muscle, this initial rise of $[Ca^{2+}]_i$ is not substantial enough to trigger contraction but is sufficient to open RyR2 channels, leading to efflux of Ca^{2+} from the SR (Asghari et al. 2009). The activation of RyR2 clusters increases the concentration of Ca^{2+} in the dyadic cleft (>100 μM), which diffuses a through the cytoplasm, causing a global rise in intracellular Ca^{2+} (up to ~1 μM), constituting a Ca^{2+} transient (Bers 2008; Ferrantini et al. 2013). The phenomenon of global Ca^{2+} release from the SR stores in response to the relatively small influx of extracellular Ca^{2+} through the LTCCs is known as Ca^{2+}-induced Ca^{2+}-release (CICR) (Berridge 2006).

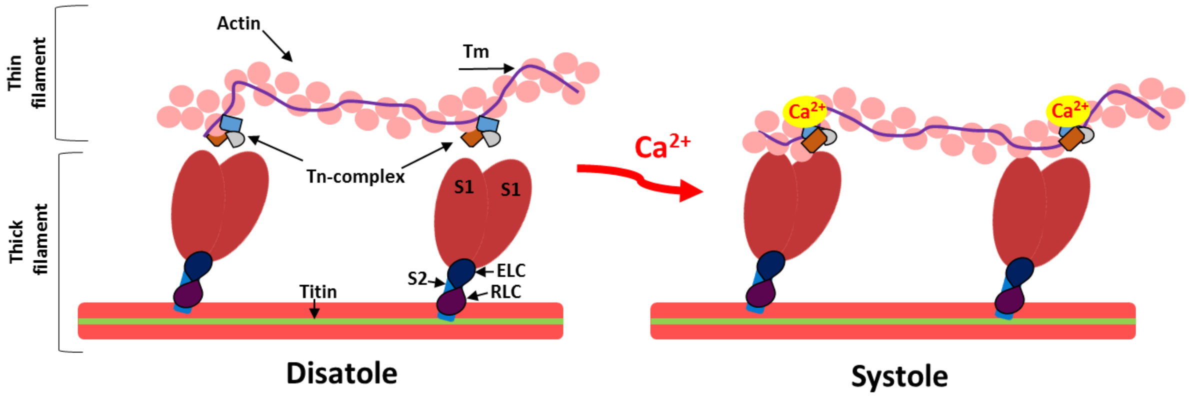

Figure 1.2 Schematic representation actin-myosin interaction triggered by Ca^{2+} binding. Depicted are the main components of the thick (lower bracket) filament and thin (upper bracket) filament of the sarcomere. The parallel arrays of myosin-containing thick filaments overlap with actin-containing thin filaments (actin polymers and troponin (Tn) complex/tropomyosin (Tm) units). The Tn complex is composed of three subunits: troponin C (TnC), troponin I (TnI) and troponin T (TnT). Muscle myosin contains two heavy chains (MYH) and four light chains, with two of the light chains belong to the essential light chain (ELC) family, and the other two are regulatory light chains (RLC). The N-terminal region of each MHC and two light chains make up the myosin head domain (the S1 fragment), and other portion of the rod is referred to as S2 and connects the myosin heads to the thick filament core. During the diastole, Tn-complex sterically obstructs binding sites for S1 myosin on the thin filament; Ca^{2+} binding to the TnC, causes an allosteric change in associated TnI, which allows Tn-complex to move, unblocking the binding sites on the actin. This allows myosin to interact with actin, enhancing Ca^{2+} binding and cross-bridge formation at neighbouring sites and thus resulting in systolic contraction. Adapted from (Bers 2008).

The RyR2-mediated global Ca^{2+} increase during systole engages the contractile machinery of the cardiomyocytes to drive ventricular contraction mediated by the sarcomere, the smallest contractile unit (Gautel and Djinovic-Carugo 2016). The sarcomere is defined as the region of myofilament structures between two Z-lines, with the distance between Z-lines (the sarcomere length) being ~2 μm in human hearts (Subramanian et al. 2001). SR released Ca^{2+} binds to troponin C (TnC) and causes a conformational change in an associated inhibitory subunit troponin I (TnI). This allows the S1 globular myosin heads to interact with actin. The contractile force is generated by repetitive acto-myosin cross-bridge cycling, which causes the relative sliding of thick and thin filaments past one another, leading to shortening of the sarcomere. During this process, ATP hydrolysis is required, which provides energy for the movement (Clark et al. 2002) (**Figure 1.2)**. The synchronized Ca^{2+} release during each membrane excitation allows co-ordinated contraction among the many sarcomere units within each working ventricular myocyte. Thus CICR reflects the spatial and temporal summation of signals from many Ca^{2+} release sites, thus allows for synchronized myofilament contraction within and among millions of working ventricular myocytes. Ultimately, the whole heart muscle will contract and generate the maximal contractile force with the least energy cost (Bers 2008).

The cardiomyocytes need to relax after a contraction phase so the ventricular chambers can be refilled and be prepared for the next contraction (Opie 2004). During diastole, the positive feedback cycle of CICR is broken due to depletion of SR Ca^{2+} content, which causes the closure of RyR2 channels and termination of Ca^{2+} release. Relaxation of the muscle is achieved by rapid removal of Ca^{2+} from the cytosol in preparation of the next wave of membrane depolarisation. This process of depletion of $[Ca^{2+}]_i$ to diastolic levels (~100 nM) is carried out by four types of transporters: (1) SR Ca^{2+}-ATPase pump (SERCA), (2) Na^+-Ca^{2+} exchanger (NCX), (3) Plasma membrane Ca^{2+}-ATPase (PMCA) and (4) mitochondrial Ca^{2+}-uptake (Bers 2002). The major contribution in Ca^{2+} removal in human cardiomyocytes is ~70% by SERCA and ~28% by NCX, while the other two transporters play a minor role (~1% each), a pattern also observed in other species such as dog, guinea pig and rabbit. In mouse and rat, the ratio is ~92% and ~7% for SERCA and NCX, respectively (Fearnley et al. 2011). The global decline of $[Ca^{2+}]_i$ leads to the dissociation of Ca^{2+} from TnC and cross-bridge detachment as the thick and thin filaments slide back to their original positions, causing myocyte to relax (Fearnley et al. 2011; Eisner et al. 2013). Thus, the three distinct events can limit the rate of cardiac muscle relaxation: (1) the rate of intracellular Ca^{2+} decline, the rate of thin-filament de-activation and the kinetics of cross-bridge cycling (reviewed by (Biesiadecki et al. 2014)).

1.1.2 ß-adrenergic regulation of ECC.

During times of emotional stress and/or exercise, increase of cardiac output is required to meet higher physiological demands of the body (Opie 2004). Rapid change in the heart rate (chronotropy), force of contraction (inotropy) and relaxation (lusitropy) is achieved by catecholamine activation of ß-adrenergic response (ß-AR), which leads to intracellular production of cyclic AMP and subsequent activation of protein kinase A (PKA) (Scoote and Williams 2004). Cyclic AMP-mediated PKA phosphorylation is central to the regulation of ECC as part of the fight-or-flight response, leading to increase both Ca^{2+} levels within the SR, and produce larger and faster Ca^{2+} transients (Bers 2002). The main functional targets of PKA include: (1) LTCC (causes an increase in Ca^{2+} influx from the extracellular space), (2) phospholamban (PLB, which relieves SERCA inhibition and accelerates Ca^{2+} re-uptake into the SR, increasing the Ca^{2+} load), (3) NCX (resulting in activation of the exchanger and enhanced extrusion of Ca^{2+}), and (4) TnI (enhances dissociation of Ca^{2+} from myofilaments, thus allows for faster relaxation), (5) RyR2 (see **Section 1.2.3.5**) and also (6) cardiac myosin binding protein C (cMyBP-C, see **Section 1.3.4.1)** (Bers 2002; Eisner et al. 2013). It is however important to note that whilst PKA-mediated phosphorylation can improve contractile function, during prolonged activation it may disturb the physiological relationship between heart rate and myocardial performance, leading to cardiovascular disease and ultimately heart failure (Fearnley et al. 2011).

1.2 Ryanodine Receptor (RyR)

RyRs are the largest known Ca^{2+} channels in the human body and were initially observed in skeletal muscle electron micrographs as large, electron-dense bridging structures, situated between T-tubules and the junctional SR (Franzini-Armstrong et al. 1999). The RyR name originates form the ability of the channel to bind the plant alkaloid ryanodine, which interacts with RyR at its open state with high affinity and specificity. Ryanodine is found naturally in the roots and stems of members of the genus *Ryania,* and has proven to be a vital tool for RyR channel identification and isolation (Inui et al. 1987). Ryanodine locks the channel in a permanently-open subconductance state at low nanomolar concentrations, and blocks it entirely at higher micromolar concentrations, thus allowing it to act as a marker of channel activation.

1.2.1 Molecular characterization

Ryanodine receptors are homotetrameric Ca^{2+} release channels that traverse the SR membrane, and consist of four identical ~565 kDa subunits (protomers), creating a centrally located pore (Lanner et al. 2010). There are three known mammalian isoforms of RyR: RyR1, RyR2 and RyR3, whereas an alternative terminology is based on the location of their primary identification. RyR1, also known as skeletal isoform, is the most thoroughly examined isoform due to its high expression levels. It was cloned from mammalian skeletal muscle (Takeshima et al. 1989), while RyR2 (cardiac isoform) was originally cloned from rabbit cardiac muscle (Otsu et al. 1990). Both of these isoforms are also expressed in a variety of other tissues: RyR1 is expressed at lower levels in vascular smooth muscle (Neylon et al. 1995), Purkinje cells, cerebellum, testis, ovaries, adrenal glands, spleen, stomach and kidney (Giannini and Sorrentino 1995), while RyR2 is the predominant isoform in cardiac muscle (Otsu et al. 1990), but can be found at high levels in brain, in cerebellum and cerebral cortex (Lai et al. 1992), but also at low levels in lungs, stomach, kidney, adrenal glands, ovaries and thymus (Giannini et al. 1995). A third isoform, RyR3, was initially identified in rabbit brain (Hakamata et al. 1992), but later was found to be expressed in various tissues including abdomen, slow twitch skeletal muscle and diaphragm (Giannini and Sorrentino 1995).

Genes of the three mammalian isoforms are located on different chromosomes, mapped to chromosomal locus 19q13.2, 1q43 and 15q13.3-4 for human RyR1, RyR2 and RyR3, respectively (Mattei et al. 1994). RyR isoforms share high peptide sequence homology (~65%), with the three major regions of diversity: D1 (residues 4210-4562 for cardiac sequence), D2 (RyR2 residues 1353-1397) and D3 (1852-1890 of RyR2 amino acids) (Lanner et al. 2010). Those regions have been proposed to be responsible for the functional differences between RyR isoforms. For example, region D2, completely absent in RyR3, in RyR1 is critical for the mechanical interaction with LTCC (Perez et al. 2003) and mutations in D1 alter Ca^{2+} and caffeine sensitivity (Du et al. 2000). It also has been shown that D3 may contain Ca^{2+} inactivation sites in RyR1 (Hayek et al. 1999). The highest degree of RyRs sequence identity is located in the extreme pore-forming C-terminus, which is essential for the channel oligomerisation into functional tetramers (Gao et al. 1997). RyR diversity is further extended by the presence of alternatively spliced variants of each isoform, which exhibit tissue- and developmental-stage specific distribution (Futatsugi et al. 1995; Marziali et al. 1996; Tunwell et al. 1996), also linked to pathological conditions (George et al. 2007; Kimura et al. 2007).

For a long time, the massive size of the receptor and its dynamic nature constituted a major challenge in determining its structure, with the computational analysis of the channel’s primary sequence revealing several functional motifs seen in other proteins (Lanner et al. 2010). Detailed crystal structures were available only for few short domains, including the N-terminal fragments (Amador et al. 2009; Lobo and Van Petegem 2009; Kimlicka et al. 2013; Borko et al. 2014), the phosphorylation domain of RyR (Sharma et al. 2012; Yuchi et al. 2012) and FKBP12 binding region (Yuchi et al. 2015) (see **Section 1.2.3.4**). However, recent advances in single-particle cryo-EM have led for the first time to detailed visualization of the structural organization of RyR1 at the closed state, solved independently by the three labs at near-atomic resolution, ranging from 3.8 Å (Yan et al. 2015), 4.8 Å (Zalk et al. 2015) to 6.1 Å (Efremov et al. 2015). The latter has also provided the putative 8.5 Å open-form structure at 10 mM Ca^{2+}, but since RyR1 displays a bell-shaped Ca^{2+}-response curve with partial channel activation at micromolar $[Ca^{2+}]_i$ and closed state in the presence of 10 mM Ca^{2+} concertation (Bezprozvanny et al. 1991), the relevance of obtained structure to the physiological open-form channel awaits further investigation. Together, these studies have offered insights into the global architecture and conformational variations in the closed state of RyR1 at unprecedented scale, as well as the details of binding sites for a multitude of intracellular molecules responsible for modulating RyR activity, which was impossible in previous cryo-EM reconstructions at ≥10Å resolution (Samso et al. 2005; Serysheva et al. 2008). RyR1 was used for most cryo-EM studies due to its great abundance on the SR in skeletal muscle and its relatively easy purification when compared to other RyR isoforms.

The overall RyR structure is often described as a mushroom-like, with ~280×280×120 Å cytoplasmic cap (~80% of the entire protein) formed by the large N-terminal portion protruding into the cytosol. It provides about 500,000 $Å^2$ exposed surface area, which serves as a scaffold for an interaction with accessory proteins, ions and other regulatory molecules (see **Section 1.2.3**). The C-terminal part of the protein comprises a ~120×120×60 Å transmembrane stem (~20% of the entire protein) forming the transmembrane region (Van Petegem 2015). The structural architecture of RyR1 subunit can be further divided into large N-terminal cytoplasmic moiety and a C-terminal transmembrane-forming domain. The specific domain labelling differs in the terminology between the three published papers, however the general structure of the channel is similar. The distinct domains established by (Yan et al. 2015) are highlighted in **Figure 1.3.** The N-terminal domain (NTD) is formed by three subdomains, A, B, and C, with the latter composed of 5 additional α-helices compared to that in the previously published crystal structure (Tung et al. 2010). The subdomains A and B are rich in β-strands (folded into 2 β-trefoil subdomains), whereas C consists exclusively of 12 α-helices conforming to the first armadillo repeats (handle and helical domain), thus for instance (Zalk et al. 2015) labelled it as a separate solenoid domain, whereas (Efremov et al. 2015) assigned it directly to the first solenoid domain. The NTD is followed by a number of peripheral domains including three SPRY domains (SPRY1, SPRY2, and SPRY3), the first repeat domains (P1 or R1/2) and handle domain. It is of particular note that the three SPRY domains and P1 domain (or R1/2) appear to be intertwined (**Figure 1.3, C**) (Yuchi et al. 2015). Further, the subsequent helical (where second P2, or R3/4, repeat domain is located) and central α-solenoid domain act as a scaffold and links the N-terminal domains to the transmembrane region. The direct interactions between the central and channel pore-forming domain are thought to primarily regulate the conformational changes necessary for RyR opening and closing (Yan et al., 2015). Importantly, the central domain was predicted to contain the interaction sites for the ligand binding of channel modulators such as calmodulin (CaM, **Section 1.2.3.2**) and FKBPs (**Section 1.2.3.4**), further highlighting its importance to the regulatory role in channel function. The transmembrane domain was found to include six transmembrane helices (S1-S6) reminiscent of the voltage-gated ion channel superfamily (Efremov et al. 2015; Yan et al. 2015; Zalk et al. 2015), which forms the channel selectivity filter of ~10 Å in length, allowing rapid Ca^{2+} transport across the SR membrane (Zalk et al. 2015). As proposed by (Yan et al. 2015), interactions between the central region and the S6 transmembrane helix appear to be stabilized via a zinc-finger motif, with allosteric regulation of the RyR activation gate predicted to be determined by structural transitions of these domains and the four protomers' S6 helices forming a channel pore that conducts Ca^{2+} flow.

1.2.2 Distribution of RyR2 in the cardiomyocyte

Section 1.1 outlined the generally accepted view of RyR2 clusters location in the ventricular myocyte's dyad and their role in ECC. Besides the junctional SR, RyR2s are also found in the corbular SR (extra-junctional SR), positioned along the Z-line (<500 nm), functioning as a secondary amplification system to Ca^{2+} diffusion from sarcolemmal dyads (Scriven et al. 2013). Based on this RyR2 distribution, early mathematical models of propagating Ca^{2+} waves spreading in directions both perpendicular to and parallel with Z-line channels suggested that the resultant spatiotemporal Ca^{2+} gradients should lead to non-uniform and inefficient activation of contraction. This phenomenon, dubbed 'the calcium paradox', was theoretically corrected by introduction of additional Ca^{2+} release units through the length of the sarcomere, at a 20% density to that of RyR2s found on the Z-lines (Subramanian et al. 2001). Based on findings from super-resolution imaging (Baddeley et al. 2009; Jayasinghe et al. 2012; Hou et al. 2015), EM tomography (Hayashi et al. 2009;

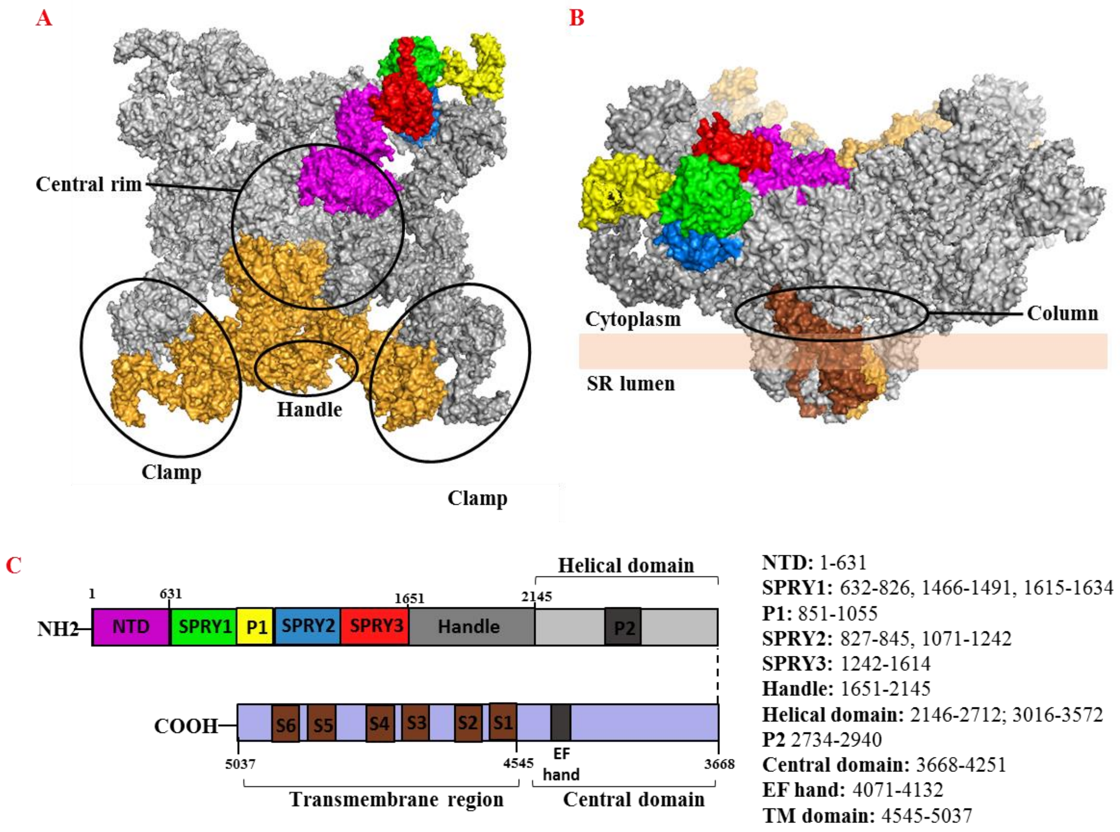

Figure 1.3 Overall structure and domain organization of the rabbit RyR1 at 3.8 Å. (A) The top view shows the large cytoplasmic domain and its previously assigned sub-regions (black circles). The corners, known as 'clamps' are connected through the 'handle' domain that surrounds the 'central rim' domain around the central cavity. Single RyR1 subunit is shown in orange, with the corresponding color-coded N-terminal domains from another subdomain as shown in (C). (B)The side view shows the transmembrane domain (brown) which is embedded in the SR membrane and is connected to the large cytoplasmic domain through the 'column'. (C) Left: a schematic illustration of domain organization in single RyR1 subunit; Right: the amino acids coordinates of each domain. Images created using The PyMOL Molecular Graphic Software (based on ((Yan et al. 2015), accession number 3J8H).

Asghari et al. 2014) and 3D reconstruction studies (Scriven et al. 2013; Rajagopal et al. 2015), it has been estimated that receptors form non-uniform arrays, with thechannels adopting multiple arrangements of 50-100 RyR2s within each cluster, as well as single, isolated tetramers. Importantly, these new data highlighted the existence of functional RyR2 outside of the dyads, with substantial populations of non-junctional RyR2s found to be either interspersed between the Z-disks (Salnikov et al. 2009) or present in the axial tubular system (Asghari et al. 2009) and/or on the periphery immediately under the sarcolemma but absent in the cell interior (Chen-Izu et al. 2006; Lukyanenko et al. 2007; Hiess et al. 2015). Notably, it has been suggested that up to fifth of the total RyR2 population can be localized outside the Z-line (Shacklock et al. 1995; Lukyanenko et al. 2007; Asghari et al. 2009; Jayasinghe et al. 2009), in line with the previous mathematical estimation (Subramanian et al. 2001).

In addition to these locations, RyR2 have also been reported at low levels in the SR around intermyofibrillar and perinuclear mitochondria (Lukyanenko et al. 2007) and in SR proximal to the nuclear envelope (Escobar et al. 2011; Ljubojevic et al. 2014). It has been proposed that these RyR2s could contribute to mitochondrial and nuclear signalling, as well as to Ca^{2+}-dependent gene regulation (Lukyanenko et al. 2007; Ljubojevic et al. 2014; Bround et al. 2016). It should be also noted that the RyR2 distribution is markedly different in adult atrial and neonatal cardiac myocytes, where due to lack of TATS, RyR2s are located at the cell periphery immediately under the sarcolemma, which makes these two cell types display different Ca^{2+} patterns in response to depolarisation compared to ventricular myocytes (Bootman et al. 2006).

1.2.3 Regulation of RyR2

The importance of RyR2 is shown by gene knock-out (KO) studies, where lack of protein causes early embryonic lethality, with visible degeneration of cardiac muscle and impaired Ca^{2+} homeostasis, including slowed rate of spontaneous diastolic depolarization and an absence of Ca^{2+} sparks. (Takeshima et al. 1998; Yang et al. 2002; Bround et al. 2013). RyR2 is known to act as a scaffold for a multitude of regulatory accessory proteins to form a macromolecular complex which enhance the versatility of the regulation of CICR. For example, RyR2 is directly regulated by Ca^{2+}, Mg^{2+} and ATP, which are its physiological ligands, as well as by other proteins (Lanner et al. 2010; Van Petegem 2015). To evaluate the functional effect of these regulators, a variety of model systems has been developed over the years, mostly *in vivo*. Despite the fact that the functions of the individual accessory proteins are known, the effect of their complex interplay in the massive array of RyR2s macromolecular complexes *in situ* is still not well understood, especially in pathophysiological conditions.

1.2.3.1 Calcium, magnesium and ATP

Ca^{2+} is by far the most potent and versatile effector of RyR function as it can bind to both cytosolic and luminal sides to activate or inactivate the channel, in an isoform-dependent manner (Lanner et al. 2010). RyR1 is known to display a bell-shaped dependence on cytosolic Ca^{2+} concentration with activatory micromolar and an inhibitory effect at milimolar (>1 mM $[Ca^{2+}]_i$) levels (Bezprozvanny et al. 1991), which is thought to be caused by cooperation between a high-affinity activating and an inhibitory low-affinity calcium binding sites. On the other hand, RyR2 and RyR3 were shown to have a decreased sensitivity to milimolar Ca^{2+} inhibition and also displayed a more potent response to Ca^{2+} activation, i.e. RyR1 can be activated by ATP even at very low nanomolar Ca^{2+} concentrations, but for the maximal activation it requires combination of both milimolar Ca^{2+} and ATP (Meissner 1984). Importantly, in skeletal muscle, RyR1 is physically coupled to LTCC, such that an AP-induced conformational change in the latter directly opens RyR1 channel even in the absence of Ca^{2+} influx (Beam et al. 1992). Nevertheless, for RyR2, the primary physiological trigger during the process of CICR is cytosolic Ca^{2+}. Under diastolic conditions (<100 nM $[Ca^{2+}]_i$), the rate of spontaneous activation of RyR2 clusters is negligible, with channel being activated at systole by low micromolar concentrations (1-10 µM $[Ca^{2+}]_i$) and inactivated at milimolar concentrations (>10 mM) of $[Ca^{2+}]_i$ (Meissner and Henderson 1987). Conversely, several mechanisms of luminal Ca^{2+} regulation of RyR activity have been proposed, with one attributing it to direct effect through luminal facing regulatory sites (Ching et al. 2000), whereas another envisages Ca^{2+} permeation to cytoplasmic sites (Laver et al. 2008) or through the 'luminal Ca^{2+} sensor' mediated by calsequestrin/junctin/triadin interaction with RyR luminal side (Gyorke et al. 2004) (see **Section 1.2.3.3**). How exactly cytoplasmic and luminal Ca^{2+} interplay regulates channel activity is still not well understood, but at least four Ca^{2+}-sensing sites (located in both the cytoplasmic and luminal regions, each displaying particular affinity towards different $[Ca^{2+}]_i$ levels) of single RyR2 protomer have been proposed (Laver 2010). The exact identities of these regulatory binding sites remain to be confirmed (Van Petegem 2015), but several reports have indicated the predicted EF hands motifs (residues 4071-4132) in the C-terminal area as possible Ca^{2+} sensors (Li and Chen 2001; Fessenden et al. 2004; Xiong et al. 2006). However, the recent work of (Guo et al. 2016) indicated that although the EF-hand domain (residues 4036–4082) is not required for RyR2 activation by cytosolic Ca^{2+}, it plays an important role in luminal Ca^{2+}activation and store-overload-induced Ca^{2+} release (SOICR).

Mg^{2+} is a physiological inhibitor of RyR and plays a role in shaping the cytoplasmic and luminal Ca^{2+} dependencies of channel activity by either competing with high-affinity Ca^{2+} activating sites or by binding to less selective inhibitory, low-affinity Ca^{2+} sites (Meissner and Henderson 1987; Laver et al. 1997). In cardiac muscle, the free Mg^{2+} concentration in the cytoplasm and SR are thought to be ∼1mM and not to change rapidly during EC coupling (Zahradnikova et al. 2003; Laver 2010). It has been proposed that when cytosolic $[Ca^{2+}]_i$ is at resting levels (during diastole) and the SR store is depleted of Ca^{2+}, Mg^{2+} may also occupy both luminal and cytoplasmic activation sites and thus rendering RyR2 inactive. This model further suggests that once the SERCA pump sequesters Ca^{2+} back into the SR and luminal Ca^{2+} is increased, Ca^{2+} displaces Mg^{2+} at the luminal site, relieving channel inhibition and allowing further RyR2 channel activation at the cytoplasmic site (Laver 2010). Notably, there is different Mg^{2+} effect between RyR isoforms, with RyR1 displaying stronger Mg^{2+} inhibition compared to the other two isoforms (Lanner et al. 2010). It has also been shown that RyR2 exhibits a species-specific profile of regulation by Ca^{2+} and Mg^{2+}, with human RyR2 having low sensitivity to cytoplasmic Mg^{2+} inhibition at 100 nM $[Ca^{2+}]_i$, and rat RyR2 being 10 times more sensitive to luminal Mg^{2+} than human (Walweel et al. 2014).

Several adenine nucleotides were found to activate RyR, among them ATP being the most efficacious (Meissner 1984). The cytoplasm of resting cardiac muscle contains approximately 3-5 mM ATP (Zahradnikova et al. 2003), which under physiological conditions predominantly exists as a complex with Mg^{2+}. Thus, it is possible that RyR is regulated by the Mg^{2+}/ATP complex, rather than free ATP. Nevertheless, ATP has been shown to have a potent effect on RyR1 function and a relatively modest impact on RyR2 (Laver 2010), with an ATP binding pocket proposed by (Popova et al. 2012) to be next to the C-terminal disease hotspot region in RyR1.

1.2.3.2 EF-hand proteins: Calmodulin, Sorcin and S100A1

In addition to direct Ca^{2+} sensing, several EF-hand-containing proteins can further fine-tune the response of RyRs to changing $[Ca^{2+}]_i$ levels. The most widely studied is CaM, a 17 kDa protein (containing four EF hands in two domains) expressed ubiquitously in all eukaryotic cells. It binds directly to RyRs, but the functional effect depends on both Ca^{2+} concertation and on the exact RyR isoform. It was shown that both forms (apo- and Ca^{2+} bound CaM) can associate with RyR1, with the primary binding site mapped to residues 3600-3637 (Moore et al. 1999) and an additional site located within residues 1975-1999 (Zhang et al. 2003). For RyR2, the corresponding sequence (residues 3583-3603) was found to be entirely responsible for binding with C-terminal lobe of both apo- and Ca^{2+} bound CaM, with the second RyR1 type-specific site proposed to being the cause for the differential functional CaM regulation of two isoforms (Yamaguchi et al. 2003). It was shown that CaM binding displays biphasic effect on RyR1 and RyR3: inhibitory at high micromolar calcium and activating at lower concentrations (Ikemoto et al. 1995; Chen et al. 1997). In rat cardiac myocytes the cellular concentration of CaM is around 2-6 μM, with CaM bound to more than 70% of RyR2 with a high affinity and shown to inhibit the channel at all Ca^{2+} concentrations (Fruen et al. 2003). The importance of this modulation is underscored by the fact that mutations in CaM can also give rise to ventricular tachycardia and sudden cardiac death, which was linked also to RyR channel’s dysfunction itself (Hwang et al. 2014; Sondergaard et al. 2015; Vassilakopoulou et al. 2015).

Another RyR modulator is sorcin, a 22 kDa Ca^{2+} binding protein with five EF hands, known to form dimers and tetramers in a Ca^{2+}-dependent manner. It has been shown that sorcin is abundantly expressed in the heart, where it co-localizes to T-tubules and has an isoform-specific impact on RyR channel function. Its exact binding site is unknown, but it has been reported to associate with RyR2 at high Ca^{2+} concentrations causing complete inhibition of channel activity (Farrell et al. 2003), while it has mild stimulatory effect on RyR1 (Lokuta et al. 1997). Because sorcin binds also to LTCC and is predicted to interact with other proteins involved in Ca^{2+} signalling, the exact understanding of its effects on RyR activity *in vivo* remains challenging.

S100A1 is also an EF-hand-containing protein, from the S100 protein family. It forms homodimers, with each subunit containing a high-affinity and a low-affinity EF hand. It promotes opening of both RyR1 (Treves et al. 1997) and RyR2 (Most et al. 2003). It has been proposed that the Ca^{2+} bound S100A1 engages the same binding site as Ca^{2+}/CaM, implying that there is competition between S100A1 and CaM (Wright et al. 2008), thus it is possible that the primary mechanism of RyR regulation by S100A1 is the removal of Ca^{2+}/CaM inhibition. In agreement with this model, a study by (Yamaguchi et al. 2011) has shown that mutation within CaM binding domain abolishes binding of both CaM and S100A1.

1.2.3.3 SR proteins: calsequestrin, triadin and junctin

The luminal accessory protein calsequestrin (CSQ) exists as a mixture of monomers and multimers in the SR where it acts as the principal Ca^{2+} buffer. It has a low affinity and high capacity for Ca^{2+} binding, with polymerisation of CSQ thought to confer its high Ca^{2+} binding capacity (Park et al. 2004). CSQ regulates SR Ca^{2+} release by acting as stores of releasable Ca^{2+} that can promote myocyte contraction. In addition to serving as a Ca^{2+} buffer, CSQ can directly regulate RyR2 activity via protein-protein interactions that involve the anchoring proteins triadin and junctin (Lanner et al. 2010). The current accepted model of RyR2 regulation by SR luminal proteins suggests that while junctin has the ability to bind directly to the luminal and/or transmembrane regions of RyR2, together with triadin they act as the anchoring proteins to position CSQ near the channel (Zhang et al. 1997; Gyorke et al. 2004). Further, the CSQ/junctin/triadin complex has been proposed to act as luminal Ca^{2+} sensor responsible for termination of Ca^{2+} release, where the CSQ-mediated inhibition of RyR2 function involves binding to triadin/junctin once SR Ca^{2+} concentration drops below a threshold level (Gyorke and Terentyev 2008). The importance of the regulatory role of this complex is further highlighted in pathological conditions, where perturbed luminal Ca^{2+} sensing due to mutations in the CSQ gene can lead to a life-threatening form of ventricular tachycardia (Song et al. 2007; Terentyev et al. 2008).

1.2.3.4 FK506-Binding Proteins

FK506-Binding Proteins (FKBPs, also known as calstabins) are immunophilins expressed in most tissues that bind the immunosuppressant drugs FK506 and rapamycin. They display peptidylpropyl-cis-trans-isomerase activity thought to be important in protein folding, however this enzymatic activity does not contribute to their role in RyR modulation (Marks 1996). Two isoforms of FKBP are known to interact with RyR with high affinity: FKBP12 and FKBP12.6 (12 and 12.6 kDa, respectively) and were shown to co-purify readily with RyRs in a 4:1 stoichiometry (one FKBP per RyR subunit) (Jayaraman et al. 1992). Notably, recent RyR cryo-EM and obtained crystal structure of SPRY1 domain imply that FKBP12/12.6 docks between subdomains SPRY1 and P1 in the clamp region of the channel (Yan et al. 2015; Yuchi et al. 2015).

RyR1 binds both FKBP12.6 and FKBP12, with the latter being the predominant isoform bound to RyR1 due to its abundance in the skeletal muscle (Timerman et al. 1996; Chelu et al. 2004). Interestingly, RyR2 exhibits much higher affinity for FKBP12.6 than FKBP12, but FKBP12 is the predominant isoform in complex with RyR2, whereas FKBP12.6 occupancy is sub-stoichiometric (Zissimopoulos et al. 2012), with only <20% of RyR2 shown to be bound to this protein in ventricular myocytes (Guo et al. 2010). It has been hypothesised that the binding of FKBP isoforms to RyR2 channels inhibit Ca^{2+} release activity by stabilising the channels closed state and also proposed to underlie receptor dysfunction observed in arrhythmia-associated mutations and heart failure (Marx et al. 2001; Chelu et al. 2004). (Marx et al. 2000) demonstrated at the single channel level that FKBP12.6-deficient RyR2 channels exhibited pronounced subconductance states and enhanced activity. Consistent with this study, FKBP12.6 KO mice displayed an enhanced predisposition to heart failure and sudden cardiac death, tested using a pre-designed exercise program (Wehrens et al. 2003). However, both occurrence and the role of FKBP12.6 dissociation due to increased phosphorylation has been contested by other studies (Stange et al. 2003; Jiang et al. 2005; Liu et al. 2006; Zissimopoulos et al. 2009). The role of FKBP in channel modulation was further examined by (Xiao et al. 2007) with the aid of three independent techniques, i.e. single channel recordings, ryanodine binding and Ca^{2+} imaging. The authors concluded that the loss of FKBP12.6 does not alter channel function. More importantly, the same group also showed that FKBP12.6-null mice do not exhibit enhanced susceptibility to stress-induced arrhythmia further questioning the hypothesis of FKBP-mediated channel dysfunction. Providing a possible explanation for these discrepancies, (Galfre et al. 2012) demonstrated in a more recent single channel investigation that FKBP12, which is largely overlooked in cardiac cells in terms of function, activated RyR2 channels at very low concentrations, whilst FKBP12.6 did not. The FKBP12.6 isoform did however antagonise the effects imparted by FKBP12 (lowering channel Po), which led to the idea that (1) dual regulation between both isoforms may be important for channel function and (2) that an alteration in the ratio of FKBP12/FKBP12.6 can contribute to the defective Ca^{2+} handling seen in heart failure (Galfré et al., 2012).

1.2.3.5 Post-translational modifications: phosphorylation and oxidation.

Phosphorylation is an important mechanism by which RyR mediated SR Ca^{2+} release is fine-tuned within myocytes, with PKA (Takasago et al. 1989) and Ca^{2+}/CaM dependent protein kinase II (CaMKII) (Hohenegger and Suko 1993) shown to mediate RyR2 phosphorylation. S2808 was the first human RyR2 residue identified as a phosphorylation site and proposed to be the target of PKA, causing destabilisation of the closed state of the channel following dissociation of FKBP12.6, resulting in a ‘leaky’ channel and pro-arrhythmic phenotype (Marx et al. 2000; Wehrens et al. 2003; Li et al. 2013). However, this has been disputed other groups (Stange et al. 2003; MacDonnell et al. 2008), which have shown that PKA phosphorylation at S2808 does not have a major role in β-AR regulation of cardiac function. In agreement with those studies, another site, S2030, but not S2808, has been identified as the primary PKA phosphorylation site (Xiao et al. 2005; Xiao et al. 2006), but this also failed to be detected by others (Li et al. 2013). Interestingly, S2808 has also been shown to be a substrate for CaMKII mediated phosphorylation (Witcher et al. 1991). Notably, decrease of phosphorylation at another CaMKII specific site, S2815, was proposed to underlie an impaired heart function (Wehrens et al. 2004). With regards to the role of phosphatases, protein phosphatase 1 (PP1) and protein phosphatase 2 (PP2) were shown to be responsible for RyR2 dephosphorylation, but confounding reports demonstrated that PP-mediated dephosphorylation either enhances RyR2 activity (Terentyev et al. 2003), whilst others reported the opposite (Li et al. 2013). In conclusion, although the target sites for phosphatases/kinases are controversial and their interactions complex, it is clear that the phosphorylation status of RyR2 has notable effects on Ca^{2+} release activity and offers a versatile control over ECC (Dobrev and Wehrens 2014).

In addition to phosphorylation, RyR2 also has been shown to be regulated at the post-translational level by protein oxidation. Alteration in redox state has been show to increase RyR activity (Stoyanovsky et al. 1997; Eager and Dulhunty 1998), with approximately 100 cysteine residues per subunit to be available for modifications (Xu et al. 1998). It has been proposed that whereas reversible S-nitrosylation seems to control the basal redox state of the channel and its adaptive process in the initial stages of heart failure, oxidation is a pathological condition found in advanced heart disease, responsible for defective inter-domain interaction of the RyR (Yano et al. 2005).

1.2.4 RyR pathophysiology in skeletal and cardiac muscle disorders

Given the important role of RyR in SR Ca^{2+} release, it's not surprising that functional alterations of RyR can seriously perturb the process of EC coupling leading to various life-threating human disorders. RyR1 mutations have been shown to have direct causative role in several skeletal muscle disorders, including malignant hyperthermia (MH) (MacLennan et al. 1990) and central core disease (CCD) (Zhang et al. 1993), while mutations in RyR2 gene are directly linked to catecholaminergic polymorphic ventricular tachycardia (CPVT) (Priori et al. 2001) and arrhythmogenic right ventricular dysplasia (ARVD). Further, recent studies have reported alterations of the expression and the function of RyR in human brains affected with Alzheimer disease (Del Prete et al. 2014) as well as cardiomyocytes in patients with Diabetes (Pereira et al. 2014) .

MH is a pharmacogenetic disorder of skeletal muscle, inherited in an autosomal dominant fashion, in which sustained muscle contractions with attendant hypermetabolic response and elevation in body temperature are triggered by commonly used inhalational anaesthetics (i.e. halothane) and skeletal muscle relaxants (i.e. succinylcholine) (Rosenberg et al. 2015). The first mutation associated with the disease was identified in the N-terminal part of RyR1 protein (Gillard et al. 1991), but until now over 400 RyR1 variants have been linked to the MH phenotype. Notably, some mutations in the skeletal muscle LTCC can also cause this disorder (Monnier et al. 1997).

CCD is a morphologically distinct, autosomal dominant myopathy characterized by progressive muscle weakness and the presence of metabolically inactive tissue (or cores) in the centre of muscle fibres. These cores lack mitochondria, and the myofibrillar organization is disrupted. The common phenotype of CCD includes muscle atrophy, floppy infant syndrome, and skeletal muscle deformities (Jungbluth 2007). It was established early on that there is a connection between CCD and MH susceptibility (Zhang et al. 1993), and some RyR1 mutations have been found to cause both (Robinson et al. 2002). The majority of CCD mutations tend to cluster in the pore-forming region (Monnier et al. 2001; Tilgen et al. 2001). Another sub-type of CCD myopathy is multiminicore disease (MmD), inherited in recessive manner, manifested by the presence of multiple minicores with highly variable phenotype (Zorzato et al. 2007). Although MmD is mainly associated with mutations in RyR1, mutations in selenoprotein N1 (Ferreiro et al. 2002) and variants of α-actin have also been found to underlie MmD (Kaindl et al. 2004).

CPVT is an autosomal dominant disease which usually manifests itself at a very young age, with either syncope or sudden cardiac death as the first symptom. The affected individuals develop cardiac arrhythmias that are triggered by either physical exercise and/or emotional stress, typically without any detectable morphological abnormalities of the myocardium (van der Werf and Wilde 2013). CPVT is caused mostly by mutations in RyR2 (Priori et al. 2001), but variants of its auxiliary proteins, CSQ (Lahat et al. 2001), triadin (Roux-Buisson et al. 2012) and CaM (Nyegaard et al. 2012) have also been linked to the disease. Notably, RyR2 mutations have also been associated with ARVD, a similar condition under which the right ventricular muscle is gradually replaced by fibro-fatty deposits as a result of progressive cardiomyocyte inflammation and apoptosis (Dokuparti et al. 2005). In general, both CPVT and ARVD mutations confer gain-of-function phenotypes, causing uncontrolled release of SR Ca^{2+} during cardiac diastole leading to delayed after-depolarisations and cardiac arrhythmia (Jiang et al. 2002), thus it has been suggested that they correspond to variable phenotypic expression of the same disease (d'Amati et al. 2005). In some cases, the same mutation can present different severity of symptoms or even remain completely asymptomatic, indicating involvement of several factors contributing towards the disease (Priori et al. 2002). As such, roles of PKA and CaMKII phosphorylation and FKBP12.6 dissociation have been suggested as the main cause (Marx et al. 2000; Wehrens et al. 2003), while others proposed a change in RyR2 subunit composition (Milting et al. 2006) and increased RyR2 sensitivity to SR Ca^{2+} overload (Jiang et al. 2005). Importantly, impaired inactivation by Ca^{2+} has also been reported for some mutated channels (Thomas et al. 2005), with the reduction in sensitivity to Ca^{2+} mediated inhibition suggested to be a common defect in RyR2 mutations linked to arrhythmias and dilated cardiomyopathy (DCM, for overview of cardiomyopathies see **Section 1.3.5**) (Tang et al. 2012). Indeed, a recent multiscale DCM genotyping study by (Haas et al. 2014) has shown for the first time RyR2 mutations can be readily found in patients with DCM, with arrhythmogenic phenotype present in up to one-third of DCM cases (Spezzacatene et al. 2015). Interestingly, RyR2 gene mutations have also been proposed a role in the molecular pathogenesis of hypertrophic cardiomyopathy (HCM) (Xu et al. 2015). For example, the T1107M RyR2 mutation has been linked to HCM (Noboru F et al. 2006; Chiu et al. 2010), as well as CPVT (Medeiros-Domingo et al. 2009). It is unclear how a single variant could result in two different phenotypes, but functional experiments have clearly shown it to confer a rare loss-of-function phenotype with early termination of Ca^{2+} release (Tang et al. 2012).

1.3 The myosin binding protein-C (MyBP-C)

Sarcomere shortening is mechanically driven by the Ca^{2+}-dependent sliding of parallel arrays of actin-containing thin filaments past thick myosin filaments. Regulation of myocyte shortening involves controlling the thin and thick filament cross-bridge formation which ultimately affects the force and frequency of contraction. Besides actin and myosin, a whole host of accessory proteins is present in the myofilament involved in assembly, maintenance of structural integrity and coordination of sarcomere shortening (Clark et al. 2002). One of these regulators is the thick filament-associated protein, the myosin binding protein-C (MyBP-C). After its first description in skeletal muscle (Offer et al. 1973), MyBP-C was thought to play a principally structural role in the assembly and the stabilization of the sarcomere. However, in recent years the picture that has emerged is one in which MyBP-C is a key effector of contraction in physiology and disease, that is mediated by phosphorylation, ablation or mutation of the protein (Moss et al. 2015).

1.3.1 Molecular characterization

There are three isoforms of MyBP-C encoded by different genes and classified as fast skeletal, slow skeletal, and cardiac (fMyBP-C, sMyBP-C and cMyBP-C, located on chromosome 12, 19 and 11, respectively), which all share a highly homologous modular architecture despite the overall peptide sequence identity of about 50-55% (Weber et al. 1993; Yasuda et al. 1995). Both skeletal muscle isoforms contain 10 globular domains ~10 kDa each, designated C1-C10, seven of which are immunoglobulin-like domains (Ig) I-set and the remaining three being fibronectin-like (Fn) type 3 domains (Yasuda et al. 1995; Otey et al. 2009) (**Figure 1.4**). Because of that, MyBP-C belongs to the Ig superfamily, which are cell-surface and soluble proteins involved in the recognition, binding and adhesion process of the cell membrane. The cardiac isoform is the largest isoform (1274 amino acids, ~140.8 kDa) due to additional number of insertions between and inside of the C domains: 28-amino acids insertion within the C5 domain and the additional cardiac specific Ig domain localized at the extreme N terminus, named C0 (Yasuda et al. 1995). Further, all isoforms have a proline- and alanine-rich (P/A) linker found at the extreme N-terminus or between C0 and C1, in the skeletal isoforms or in the cardiac isoform, respectively. Importantly, there is a conserved MyBP-C-specific domain (M-domain) between C1 and C2 in all isoforms, which in cMyBP-C contains specific phosphorylation sites (Gautel et al. 1995). It was shown that purified MyBP-C exists as a single, flexible polypeptide chain, with an extended length of 50 nm (Furst et al. 1992) although biochemical and small angle X-scattering studies indicated that the protein possesses an ability to dimerize reversibly (Offer et al. 1973; Jeffries et al. 2011). Further, in electron microscopy images, MyBP-C molecules display a range of different forms, from elongated rod-shaped, angled V-shaped and tightly curved U-shaped (Swan and Fischman 1986). To date, high resolution structure of neither full-length MyBP-C isoform is available. However, based on crystallographic structure of

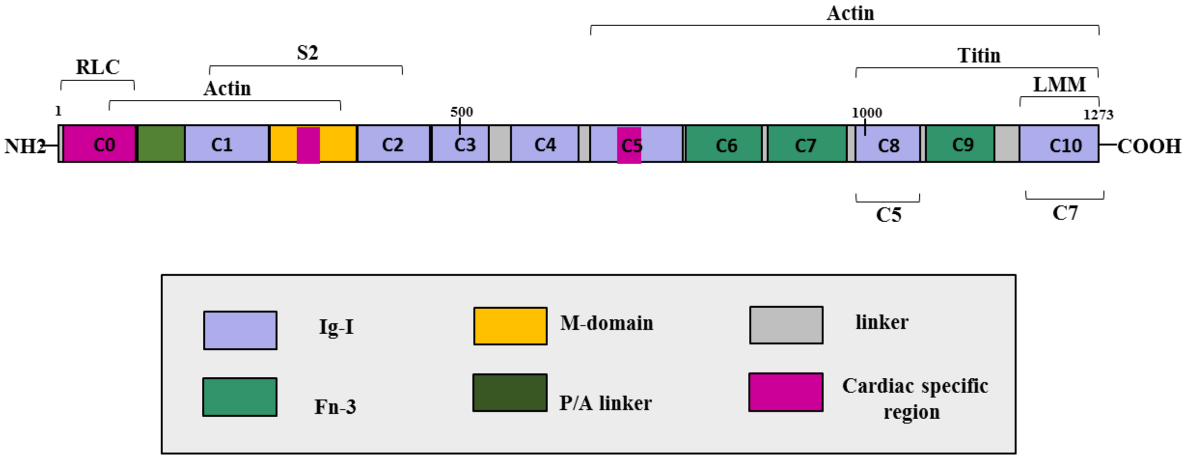

Figure 1.4 Schematic representation of the domain organization of cardiac MyBP-C. Brackets above indicate cMyBP-C regions reported to interact with the other sarcomeric components, labels below show domains responsible for dimerization of cMyBP-C. Adapted from (Sadayappan and de Tombe 2012).

Ig domain C1 (Govada et al. 2008) and NMR data for the C1 (Ababou et al. 2008), C2 (Ababou et al. 2007), and C5 (Idowu et al. 2003), MyBP-C Ig domains show a similar overall β sandwich organization, with each composed of a two β sheets containing three to four β strands held together by a disulphide bond (Otey et al. 2009), with the Fn domains predicted to be similar to the Ig domain fold (Oakley et al. 2004). On the other hand, there are discrepancies in the literature regarding the conformation of the M-domain. Recent M-motif NMR data obtained by (Howarth et al. 2012) implies that this domain has a unique structure, with a largely disordered N-terminal portion containing three known phosphorylation sites and a more ordered and folded C-terminal region, in line with AFM data (Karsai et al. 2011). This contrasts to previously proposed compact β-sheet composition of M-domain and general similarity to Ig fold (Jeffries et al. 2008).

1.3.2 MyBP-C binding partners

Cardiac MyBP-C interacts with several sarcomeric components via different domains (**Figure 1.4**). The major interactions important for anchoring cMyBP-C in the sarcomere are mediated by its binding with titin and/or light meromyosin portion (LMM) of the myosin rod. These occur within the C8-C10 and C10 modules of cMyBP-C, respectively, with inclusion of C7 to C9 increasing the binding affinity (Freiburg and Gautel 1996; Alyonycheva et al. 1997; Asghari et al. 2014).

Henceforth, complete association of cMyBP-C with thick filament requires the presence of domain C7 (Gilbert et al. 1996; Gilbert et al. 1999). At the other end of the molecule, cMyBP-C interacts also with the S2 head region of the myosin heavy chain. The binding site is located at the C1-C2 region (Gruen and Gautel 1999; Shannon et al. 2003). Further, another association between the cardiac C0 domain and the regulatory light chain (RLC) has also been reported (Salnikov et al. 2009), while a study by (Previs et al. 2015) demonstrated that domains C0-C3 are involved in Tm binding and activation of cross-bridge cycling (see **Section 1.3.4** for overview of cMyBP-C role in the contraction).

Apart from being the thick filament associated protein, cMyBP-C also interacts with actin. Initially it was shown that this interaction is mediated by cMyBP-C N-terminal portion including C0, C1 domains and the P/A region. In total, three regions of cMyBP-C bind with actin, however the relative binding affinity of C0 domain with actin was less comparing to C1-C2 (Kubalova et al. 2005). The interesting property of the M-domain is that it has the ability to reach both myosin and actin depending on its phosphorylation state (see **Section 1.3.4.1**) (Kubalova et al. 2005). Further, the research using laser trap assay demonstrated that the first 17 residues of M-domain are sufficient to interact with actin and affect actin-myosin motion generation (Baker et al. 2015). Sequence specific species differences in the P/A linker of cMyBP-C are also known to modulate acto-myosin interactions (Shaffer et al. 2010). Surprisingly, and in contrast to these findings, it was reported that cMyBP-C interacts with actin via a single site between C6-C10 domains, whereas C0, C1, M-domain, C0-C4 and C0-C5 domains are just weak binding sites (Zissimopoulos et al. 2006), but this observation was not supported by others. In conclusion, actin and cMyBP-C interaction does exist although it is not clear which binding region is critical for modulation *in vivo*. As studies using cMyBP-C fragments *in vitro* may be considered non-physiological, systematic mutation studies are required *in vivo* to determine precise actin-binding properties of cMyBP-C (Mead-Savery et al. 2009).

1.3.3 MyBP-C location in the sarcomere

MyBP-Cs are located to a specific sub-zone of the myosin filament A-band, the cross-bridge region C zone. They occupy a number of transverse stripes (1-7 or 1-9 in skeletal muscle and 1-9 in cardiac), in which MyBP-Cs are spaced in regular intervals of 43 nm, with each stripe composed of two to four MyBP-C molecules (Bennett et al. 1986). The fast and slow skeletal muscle isoforms are known to be abundant in both smooth and striated muscle (Dhoot et al. 1985), and can coexist in variable ratios leading to diverse arrangements of the sarcomere stripes (Reinach et al. 1983). On the other hand, cMyBP-C is exclusively expressed in the atrium and ventricle of heart of mammalian heart throughout development (Gautel et al. 1995), and it cannot be trans-complemented by skeletal MyBP-Cs (Gautel et al. 1998). The detailed cMyBP-C protein arrangement in the sarcomere is not fully elucidated, but to date, two models have been proposed. Results form i*n vitro* Y2H binding studies (Flashman et al. 2008) led to proposition of the trimeric collar model, in which C-terminal C5-C8 domains form the collar-like structure around the thick filament with the N-terminal domains extended perpendicular to the thin filament core (El-Armouche et al. 2007; van Dijk et al. 2009). On the other hand, 3D X-ray modelling (Yao et al. 1998) and recent EM microscopy results (Lee et al. 2015) support the rod model of the longitudinal arrangement of C8-C10 domains of cMyBP-C. Importantly, both models account for the apparent elasticity of N-terminal cMyBP-C suggested by NMR structural studies (Howarth et al. 2012) where individual C0-C3 domains are like elongated rod particles, sufficient to reach the thin filament. In conclusion, the most likely arrangement of cMyBP-C is one in which three C-terminal domains run along the thick filament surface, while the rest of the molecule flexibly extends out and may interact with the neighboring thin/thick filament (**Figure 1.5**).

1.3.4 Role and modulation of cMyBP-C

The functional implications of cMyBP-C were first reported by (Hofmann et al. 1991), where removal of the protein from the sarcomere resulted in enhanced shortening velocity and displayed increased Ca^{2+} sensitivity of force. It suggested that cMyBP-C acts as internal tether and inhibitor of acto-myosin cross-bridge kinetics, which ultimately depresses contraction in muscle. Importantly, extraction of the protein from the myofibril had no effect on the gross structure of the sarcomere, which was in line with apparent normal shape or size of single cardiac myocytes observed in cMyBP-C KO mice studies (Harris et al. 2002; Carrier et al. 2004). However, despite that the

KO mice were viable, ultrastructural examination revealed a loss of lateral alignment of adjacent myofibrils with their Z-lines misaligned, resulting in hypertrophy and reduced diastolic and systolic function.

1.3.4.1 cMyBP-C phosphorylation

Several studies have suggested that the interactions of cMyBP-C with its binding partners vary with its phosphorylation status of the M-domain. Up to four sites have been identified for both the human and murine cMyBP-C isoforms (S275, S284, S304, S311 and S273, S282, S302, S307, respectively), which are targeted by protein kinases in a hierarchical order of events starting with S282 enabling phosphorylation of the others (Gautel et al. 1995). It has been shown that cMyBP-C phosphorylation occurs (1) in response to ß-AR stimulation via PKA, (2) by increase in intracellular Ca^{2+} levels via CaMKII, (3) by protein kinase C (PKC) in a Ca^{2+}-independent manner (Gautel et al. 1995; Mohamed et al. 1998), (4) by protein kinase D (PKD) (Bardswell et al. 2010) and (5) by p90 ribosomal S6 kinase (Cuello et al. 2011). Furthermore, glycogen synthase kinase 3 β (GSK3β) was described as another protein kinase to phosphorylate cMyBP-C outside the M-domain in the P/A linker at S133 in human myocardium (mouse S131, (Kuster et al. 2013)). It is generally accepted that cMyBP-C is extensively phosphorylated at basal levels, with mono-, di- and tri-phosphorylated forms (Sadayappan et al. 2005), and that phosphorylated cMyBP-C improves force of contraction and is involved in the regulation of cross-bridge cycling by reversibly binding to the S2 region of myosin in the dephosphorylated state (Shannon et al. 2003). Importantly, phosphorylation of cMyBP-C by PKA removes its normal inhibition of the rate of force redevelopment and acto-myosin kinetics, which contributes towards improved diastolic function (Sadayappan et al. 2005). Further, the dephosphorylated cMyBP-C form can be released of protein from the sarcomere, with detectable levels of full-length cMyBP-C in the cytosol (Decker et al. 2012; Kuster et al. 2014; Baker et al. 2015). Notably, the increased rate of cMyBP-C dephosphorylation and subsequent degradation has been associated with pathological conditions, as observed in patients with heart failure, ischemia-reperfusion injury and pathological hypertrophy (El-Armouche et al. 2007; Decker et al. 2012; Govindan et al. 2012; Kuster et al. 2014; Baker et al. 2015). Transgenic expression of a phosphomimetic cMyBP-C mutant was shown to protect hearts from myocardial infraction (MI) injury (Sadayappan et al. 2005) and reduce the appearance of a 40-kDa proteolytic calpain degradation fragment of cMyBP-C (Govindan et al. 2012). Notably, a recent study by (Kooij et al. 2013) identified that up to 17 phosphorylation sites can be detected *in vivo*, 10 of which have not been

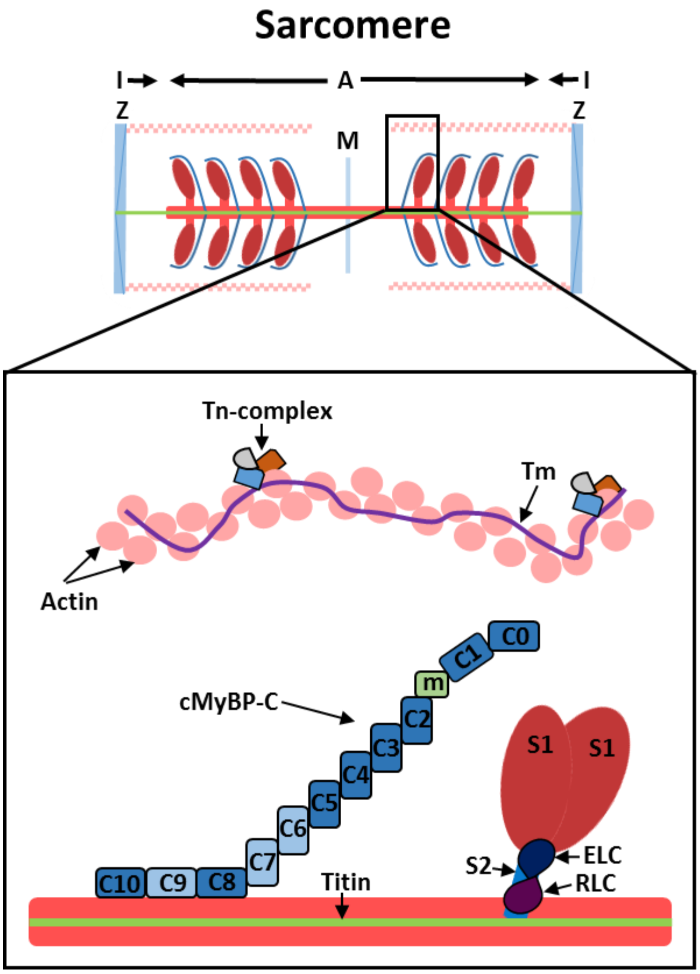

Figure 1.5 Proposed model of cMyBP-C organization in the sarcomere. cMyBP-C domain C8-C10 are responsible for anchoring the protein to the thick filament backbone, whereas remaining domains C0-C7 are extended to reach thin/thick filament. Adapted from (Lopes and Elliott 2014).

previously reported. Taken together, phosphorylation of cMyBP-C is considered as beneficial for cardiomyocyte function, and preservation of phosphorylation is cardioprotective.

1.3.4.2 Other post-translational modifications of cMyBP-C

In addition to phosphorylation, cMyBP-C function is also regulated by an ever-growing spectrum of posttranslational modifications. Several cMyBP-C acetylation sites were identified, and found to promote proteolysis and decrease stability of cMyBP-C in contrast to phosphorylation (Govindan et al. 2012), whereas S-glutathionylation was shown to abrogate protein phosphorylation and contribute towards increased myofilament Ca^{2+} sensitivity and human heart failure (Stathopoulou et al. 2016). Further, carbonylation of cMyBP-C was proposed as contributor to cardiac dysfunction observed during chemotherapy due to prolonged oxidative stress (Aryal et al. 2014). Notably, citrullination (Fert-Bober and Sokolove 2014) and S-nitrosylation (Kohr et al. 2011) of cMyBP-C were also reported, however they yet await further functional characterization.

1.3.5 Pathophysiology of MyBP-C in skeletal and cardiac muscle disorders

The importance of MyBP-Cs as essential sarcomere components and key regulators of muscle function is highlighted in pathological conditions, where they are involved in the development of skeletal and cardiac myopathies. Genomic linkage analysis has demonstrated that mutations in sMyBP-C are causally linked to the development of distal arthrogryposis type-1 (DA-1) (Gurnett et al. 2010), while cMyBP-C mutations can lead to various forms of cardiomyopathies, such as HCM, DCM and left ventricular non-compaction (LVNC) (Carrier et al. 2015).

DA-1 is an autosomal dominant disorder characterized by congenital contractures of the hands and feet. Two missense mutations have been identified to date, W236R and Y856H, which are present in the M-motif and C8 domain, respectively (Gurnett et al. 2010). Skeletal muscle biopsies obtained from affected individuals show that slow twitch fibres are significantly smaller than fast twitch fibres, with reduced phosphorylation of sMyBP-C detected in aged and diseased muscles (Ackermann et al. 2015).

HCM is defined by the presence of increased ventricular wall thickness and diastolic dysfunction in the absence of loading conditions (i.e. hypertension) sufficient to cause the observed abnormality (Cecchi et al. 2012). Familial HCM is an autosomal-dominant myocardial disease caused by mutations in genes that encode different proteins of the cardiac sarcomere, with myosin heavy chain (MYH) and cMyBP-C genes together contributing towards nearly 80% of all inherited HCM cases (McNally et al. 2015). In contrast to MYH, where majority of HCM mutations are amino acid substitutions, most (>60%) cMyBP-C pathogenic variants are premature stop codons or frame-shift mutations, expected to produce truncated forms of the protein that lack the C-terminus (van Dijk et al. 2012). Importantly, despite being transcribed to mRNA, these expected shortened cMyBP-C proteins have not been detected in myocardial tissue from affected HCM patients (Rottbauer et al. 1997; Marston et al. 2009; van Dijk et al. 2009) or mouse cMyBP-C HCM models (Yang et al. 1999; Palmer et al. 2004). On the other hand, a lower relative level of full-length protein content was reported for both truncation and missense mutations in affected heterozygous (HET) patients (Marston et al. 2009; van Dijk et al. 2009). HET phenotype is usually characterized as asymptomatic or mildly asymptomatic and displaying late disease onset (Dhandapany et al. 2009), suggesting haploinsufficiency as the major mechanism underlying the disease. In addition, HET mouse models of several MYBPC3 (gene encoding cMyBP-C) truncation mutations have shown various changes in cMyBP-C protein level, ranging from normal content to almost 50% reductions and variable phenotypes, including mild hypertrophy, diastolic dysfunction and altered Ca^{2+} sensitivity of force development (Harris et al. 2002; Carrier et al. 2004; Fraysse et al. 2012; Cheng et al. 2013). Furthermore, (Ingles et al. 2005) reported that about 5% of HCM patients carry more than one gene mutations encoding sarcomeric proteins, either in the same gene (compound mutations) or in two different genes, which result in a more severe clinical phenotype (i.e. greater left ventricular wall thickness) because of a ’double dose’ effect.

Interestingly, ablation of cMyBP-C has been shown to accelerate the kinetic of force development at submaximal Ca^{2+} activation and myocardial relaxation (Korte et al.

2003; Stelzer et al. 2006a; Stelzer et al. 2006b), whereas other studies showed slowed kinetics and phase of relaxation (Harris et al. 2002; Carrier et al. 2004; Palmer et al. 2004). These divergent findings are most likely related to alterations in Ca^{2+} handling as a result of functional remodelling of the heart as part of compensatory response to cMyBP-C ablation. Consistent with this idea, the intracellular Ca^{2+} transients have been reported to be altered in single cardiomyocytes from cMyBP-C null animals, which displayed slowed kinetics of Ca^{2+} transient decay (Song et al. 2003; Brickson et al. 2007; Pohlmann et al. 2007). Notably, faster Ca^{2+} transient decay was seen in myocytes isolated from a knock-in (KI) mouse model expressing an HCM missense mutation in MyBP-C that resulted in decreased MyBP-C expression (~20% in HET and ~90% in homozygous animals, when compared to wild-type, WT) (Fraysse et al. 2012), whereas (Cheng et al. 2013) has shown that HET mice presenting decreases in MyBP-C expression similar to those of HCM (~32% when compared to WT) displayed unchanged Ca^{2+} transient kinetics. These data indicate the presence of a compensatory mechanism(s) required to improve diastolic relaxation in the HCM cMyBP-C mutant hearts, with detected alternations directly linked to perturbed Ca^{2+} transients.

Furthermore, cMyBP-C mutations show substantial genotypic and phenotypic variability, implicated in multiple forms of cardiomyopathy. Interestingly, progression of HCM to DCM occurs in 10–15% of patients with HCM (Spirito and Bellone 1994). A cMyBP-C HCM model of transgenic mouse (corresponding to HET human HCM mutation in C8 domain) showed little or no truncated mutant with typical HCM phenotype, while homozygous mice carrying the same mutation developed DCM (McConnell et al. 1999). Another cMyBP-C missense variant, R820Q, has been found to be associated with variable clinical features, which are often delayed until middle age, with HCM progression to DCM in about 40% of the elderly patients (Konno et al. 2003). Further, another cMyBP-C variant initially associated with HCM (deletion in intron 32 leading to a frameshift) has also been also found in patients with DCM and restrictive cardiomyopathy (Waldmuller et al. 2003), with yet another HCM/DCM variant that causes truncation of cMyBP-C (R945fs/105) reported by other group (Hitomi et al. 2010). The observed DCM/HCM phenotypic variation, with single mutation capable of causing different effects of on fibre contractile velocity, force and Ca^{2+} sensitivity is still not well understood, although as a general rule, mutations that increases cardiac output are predicted to contribute towards HCM phenotype, while those that diminish motor function causative of DCM (Moore et al. 2012).

The clinical DCM is characterized by left ventricular dilatation and global systolic dysfunction in the absence of coronary artery disease or other identifiable causes (Cecchi et al. 2012). A recent multi-national study has shown that MYBPC3 mutations represent the second highest number of previously reported DCM-causing variants, found to contribute towards ~13% cases (Haas et al. 2014). Further, a follow-up study by (Lynch et al. 2015) (using the homozygous mouse cMyBP-C DCM model by (McConnell et al. 1999)), has reported elevated oxidative stress and proposed it to serve as additional factor which could add to DCM disease severity. Compared to HCM, DCM is thought to be far more genetically heterogeneous, with mutations found in genes encoding cytoskeletal, nucleoskeletal, mitochondrial, and calcium-handling proteins (McNally et al. 2015). Mutations in cMyBP-C have also been described in patients with LVNC, a cardiomyopathy characterized by deep trabecular invaginations in the left ventricle (Cecchi et al. 2012). A study by (Probst et al. 2011) identified 5 LVNC-linked mutations in cMyBP-C, however phenotypic variants in other sarcomeric proteins, i.e. MYH and Tm have also been reported, which shows genetic heterogeneity of LVNC. Together, these studies reveal MYBPC3 as one of the major mutated genes in cardiomyopathies and heart failure. Similar to HCM, both missense and truncating mutations were found in DCM and LVNC (Probst et al. 2011; Haas et al. 2014).

Although the role of the cMyBP-C in heart disease seems quite clear, little is known about an association between cMyBP-C and cardiac arrhythmia, though the mouse models have indicated that cMyBP-C mutations are likely to also induce ventricular arrhythmias (Berul et al. 2001), with single E334K mutation reported to cause HCM accompanied by arrhythmia (Bahrudin et al. 2008). This mutation was shown to induce ubiquitin–proteasome system impairment which led to accumulation of cardiac channel proteins, leading to electrophysiological dysfunction (Bahrudin et al. 2011). However, any direct relationship between cMyBP-C pathophysiology and altered Ca^{2+} transients remains a question requiring further scientific investigation.

1.4 Hypothesis and Aims

Impaired relaxation and altered Ca^{2+} transients have been reported in several cMyBP-C KO animal models (Song et al. 2003; Brickson et al. 2007; Pohlmann et al. 2007), pointing that cMyBP-C contributes not only to regulation of contraction, but also might be involved in modulation of Ca^{2+} homeostasis. The main hypothesis of this thesis is that cMyBP-C could constitute a novel retrograde link between contraction and its trigger, i.e SR- Ca^{2+} release, mediated by the direct cMyBP-C:RyR2 binding. Thus, the principal aim of this study was to characterise this novel interaction both biochemically and functionally. In particular, the following points will be addressed:

- Verify if the native cMyBP-C:RyR2 binding can be detected from the animal heart tissue preparations *in vitro*;
- Co-express full-length recombinant human RyR2 with cMyBP-C in a heterologous cell system and assess the interaction *in vitro*;
- Identify the minimal interacting regions/motifs involved in RyR2:cMyBP-C association in the chosen experimental system *in vitro* and *in vivo*;
- Assess the functional role of cMyBP-C in RyR2 channel regulation using recombinant expression system;
- Assess if single point RyR2 mutations can disrupt protein-protein association between the RyR2 and cMyBP-C.

Chapter 2

Materials and Methods

2 Materials and Methods

2.1. Materials

All chemicals and reagents were obtained from Sigma-Aldrich or Fisher Scientific, unless stated otherwise. All solutions were prepared using dH_2O, pH adjusted as required and stored at room temperature unless an alternative is noted. Solutions were filter sterilised where required using a 0.22 µM Millex syringe filter (Millipore).

2.1.1. Molecular biology

- **TAE buffer** 50x stock: 2 M Tris, 2 M acetic acid, 50 mM EDTA.
- **Ethidium Bromide**: 1% (w/v).
- **Agarose**: Hi-Res Standard Agarose (Geneflow).
- **DNA loading buffer, 5x stock**: 25% (v/v) glycerol, 0.25% (w/v) orange G.
- **Molecular weight DNA markers**: 1 kb plus DNA ladder (Life Technologies), stored at -20°C.
- **DNA polymerase**: *Pfu* DNA polymerase (Promega), together with optimised PCR buffer (with $MgSO_4$, 10x), all stored at -20°C.
- **dNTP mix**, 20 mM: dATP, dCTP, dGTP and dTTP, stored at -20°C.
- **Human cardiac muscle cDNA library** (BD Biosciences).
- **Plasmid purification kits**: Qiagen Plasmid Maxi Kit (Qiagen) and Wizard Plus SV Minipreps DNA Purification System (Promega).
- **PCR purification kit**: QIAquick PCR Purificatin Kit (Qiagen).
- **Gel extraction kit**: QIAquick Gel Extraction Kit (Qiagen).
- **Restriction endonucleases and ligase**: purchased from NEB, together with optimised reaction buffers (10x), all stored at -20°C.

2.1.2. Protein biochemistry

- **Homogenisation buffer:**
    - **organic-salt-based**: 150 mM NaCl, 20 mM Tris, pH adjusted to 7.4 with HCl, stored at 4^{o}C.
    - **iso-osmotic**: 5 mM HEPES, 0.3 M sucrose, pH adjusted to 7.4 with NaOH, stored at 4^{o}C, filtered prior each use.
- **Protease inhibitors**: Protease Inhibitor Cocktail Tablets (Roche), dissolved in 2 ml of dH_2O, resulting in 25x stock solution, stored at -20^{o}C.
- **Glass beads**: acid-washed, 425-600 µm, 30-40 U.S. sieve (Sigma-Aldrich).
- **Protein assay kit**: Pierce BCA Protein Assay Kit (Pierce), stored at 4^{o}C.
- **Co-IP buffer**: 150 mM NaCl, 20 mM Tris, 0.5% (w/v) CHAPS, pH adjusted to 7.4 with HCl, stored at 4^{o}C.
- **PBS buffer**: 1.37 M NaCl, 27 mM KCl, 100 mM Na_2HPO_4, 18 mM KH_2PO_4.
- **DTSSP**, 2 mM in PBS, freshly made prior to use.
- **Protein beads:** nProtein A and nProtein G Sepharose 4 Fast Flow beads (GE Healthcare Life Science), stored at 4^{o}C.
- **Tris-HCl, 0.5M (stacking buffer)**: pH adjusted to 6.8 with HCl.
- **Tris-HCl, 1.5M (separating buffer)**: pH adjusted to 8.8 with HCl.
- **SDS**, 10% (w/v).
- **Ammonium persulphate:** 10% (w/v), stored at 4^{o}C for up to 3 weeks.
- **Protein loading buffer, 5x**: 0.3 M Tris, 10% (w/v) SDS, 50% (v/v) glycerol, 0.025 mM EDTA**,** 0.25% (w/v) bromophenol blue.
- **Reducing protein loading buffer, 5x**: as above, supplemented with 10% β-mercaptoethanol.

- **SDS-PAGE running buffer, 10x**: 3% (w/v) Tris, 14.4 % (w/v) glycine, 1% (w/v) SDS.
- **Acrylamide**: 40% acrylamide/Bis mix solution, in 37:5:1 ratio (Bio-Rad), stored at 4°C.
- **TEMED.**
- **Protein molecular weight markers**: Precision Plus Protein Standards (Bio-Rad) and Kaleidoscope Prestained Standards (Bio-Rad), stored at -20°C.
- **Semi-dry transfer buffer**: 48 mM Tris, 39 mM glycine, 0.0375% (w/v) SDS, freshly made prior to use.
- **TBS buffer, 10x**: 200 mM Tris, 1.37 M NaCl, pH adjusted to 7.4 with HCl.
- **TBS-T**: 1x TBS, 0.1% (v/v) Tween-20, freshly made prior to use.
- **TBS-T/Marvel**: as above, supplemented with 5% (w/v) non-fat powdered milk (Marvel), pH adjusted to 7.4 with NaOH.
- **Sodium Azide**: 5% (w/v).
- **ECL system**: Pierce ECL Western Blotting Substrate (Thermo Scientific) used with Amersham Hyperfilm ECL (GE Healthcare).
- **BCA Protein Assay Kit:** (Pierce)

2.1.3. Bacterial culture

All glassware and sterile plastics were purchased from Fisher Scientific or Greiner Bio-One. Prior to use, all glassware was washed with dH_2O and autoclaved (135°C, 90 min). All bacterial growth media were autoclaved under the same conditions, before cooling to approximately 50°C prior to the addition of antibiotic.

- **LB medium**: purchased in form of pre-made powder and prepared at 2% (w/v) (Formedium), 1.5% (w/v) agar (for plates only), stored at 4°C for up to a month.
- **Ampicillin**: 100 mg/ml stock (Formedium), stored at -20°C.

- **LB/Ampicillin medium**: LB medium supplemented with 100 µg/ml Ampicillin, 1.5% (w/v) agar (for plates only), stored at 4ºC for up to a month.
- **Bacterial cell freezing medium:** 50% (v/v) LB/Ampicillin**,** 50% (v/v) glycerol (autoclaved).
- **SOC medium**: 2% (w/v) tryptone, 0.5% (w/v) yeast extract, 0.05% NaCl, 0.018% (w/v) KCl, 0.095% (w/v) $MgCl_2 \cdot 6H_2O$), 0.4% glucose (added after autoclaving), stored at -20°C.

2.1.4. Yeast culture

All glassware and sterile plastics were purchased from Fisher Scientific or Greiner Bio-One. All glassware was treated similar as in bacterial culture. All solutions were also autoclaved in the same manner, and stored at 4ºC.

- **YPD medium**: 2% (w/v) peptone, 1% (w/v) yeast extract, 2% w/v glucose (added after autoclaving), 2% (w/v) agar (for plates only).
- **SDY medium** (lacking leucine and tryptophan): 6.7 g/L of Yeast Nitrogen Base, 1.6 g/L Dropout supplement lacking leucine and tryptophan, 2% w/v glucose (added after autoclaving), 2% (w/v) agar (for plates only).
- **PEG 3350 stock solutio**n: 50% (w/v).
- **TE solution, 10x stock**: 100 mM Tris, 10 mM EDTA, pH adjusted to 7.5 with HCl.
- **LiAc solution, 10x stock**: 1 M lithium acetate, pH adjusted to 7.5 with CH_3COOH.
- **PEG/LiAC solution**: 40% (w/v) PEG 3350, 1x TE, 1x LiAc.
- **TE/LiAc solution**: 1x TE, 1x LiAc.
- **Z buffer**: 100 mM Na_2HPO_4, 40 mM NaH_2PO4, 10 mM KCl, 1 mM $MgSO_4$, pH adjusted to 7.4.

- **X-gal stock solution**: 2% (w/v) X-Gal in DMF, stored in dark at -20ºC.
- **Z buffer/X-gal solution**: 0.27% (v/v) β-mercaptoethanol, 0.033% (w/v) X-Gal in Z buffer, prepared fresh prior to use.
- **Z buffer/ β-mercaptoethanol**: 0.27% (v/v) β-mercaptoethanol in Z buffer, prepared fresh prior to use.
- **Herring testes carrier DNA** (Clontech).
- **Yeast Protein Extraction buffer**: 20 mM Tris, 150 mM NaCl, 1% Triton X-100, pH adjusted to 7.4

2.1.5. Mammalian culture

Sterile plastic ware was purchased from Greiner Bio-One and Corning. All cell culture reagents were from Gibco, unless otherwise stated. Saline and sterile water were obtained from Fresenius Kabi.

- **L-glutamine**: 100x, stored at -20ºC, filter sterilised before use.
- **FBS** (heat inactivated): stored at -20ºC, filter sterilised before use.
- **DMEM**: containing D-glucose, L-glutamine, sodium pyruvate, sodium bicarbonate, phenol red, stored at 4°C.
- **mDMEM**: DMEM supplemented with 1x L-glutamine (all filter sterilised), stored at 4°C.
- **cDMEM**: DMEM supplemented with 10% (v/v) FBS, 1x L-glutamine (all filter sterilised), stored at 4°C.
- **Trypsin-EDTA,** 0.05%, 1x, with phenol red, stored at -20°C, warmed to room temperature and filter sterilised before use.
- **$CaCl_2$, 2.5 M stock**: filter sterilised and stored at -20°C (1 ml aliquots).

- **HBS, 2x**: 280 mM NaCl, 10 mM KCl, 1.5 mM Na_2HPO_4, 12 mM glucose, 50 mM HEPES, pH adjusted to 7.05 with 1 M NaOH, stored at -20°C, filter sterilised before use.
- **Transfection reagents**: TurboFect Transfection Reagent (Thermo Scientific), Effectene (Qiagen)
- **Mammalian cell freezing medium**: 10% (v/v) DMSO in FBS, freshly made prior to use and filter sterilised.

2.1.6. Immunocytochemistry (ICC)

- **Poly-L-lysine (Sigma)**: used at 0.01% working dilution in saline, stored at 4°C.
- **Fixing solution**: 4% (w/v) paraformaldehyde in PBS.
- **Cell permeabilisation solution**: 0.1% (v/v) Triton X-100 in PBS.
- **Blocking solution**: 10% FBS in PBS
- **Mounting reagent:** ProLong Gold Antifade Mountant (Life Technologies)

2.1.7. Ca^{2+} imaging

- **Fluo-3 AM** (Life Technologies), prepared in a solution of 20% Pluronic acid in DMSO. Added to minimal mDMEM to generate a working concentration of 10 µM.
- **KRH buffer**: 120 mM NaCl, 5.5 mM Glucose, 25 mM Hepes, 4.8 mM KCl,1.2 mM KH_2PO_4, 1.2 mM $MgSO_4$, 1.3 mM $CaCl_2$, pH 7.4. Filter sterilised.
- **Caffeine**: 100 mM stock prepared in KRH buffer.

2.1.8. $[^3H]$ryanodine binding

- **Ryanodine binding buffer**: 1 M KCl, 25 mM PIPES, 1 mM EGTA, 1 mM HEDTA, 1 mM NTA, pH adjusted to 7.4 with KOH.
- **Caffeine**, 100 mM, prepared fresh prior to use.
- **$CaCl_2$**, 20 mM.
- **'Cold' Ryanodine stock**, 1 mM, stored in the dark at -20^{o}C.
- **Hot $[^3H]$ryanodine stock** (PerkinElmer), 1µM (9.25 MBq, 250 µCi), stored at -20^{o}C.
- **Ultima Gold Scintillation Fluid** (Perkin Elmer).

2.1.9. Oligonucleotides

Custom oligonucleotide primers were designed and ordered from Sigma Aldrich. Following the manufacturer's instructions, lyophilised pellets were re-suspended in an appropriate volume of sterile dH_2O to give 100 µM stock concentration, which was further confirmed by spectrophotometric quantification. Briefly, a 1:50 dilution aliquots were made and the absorbance at 260 nm (A_{260}) was measured (in triplicates) in a quartz cuvette using a spectrophotometer (MBA2000, Perkin-Elmer). Using the nucleotide sequence, the molecular weight and the melting temperature of the oligonucleotides (given that A260 = 1 corresponds to ~20-39 pg/ml of ssDNA depending on the base composition, with ~ 33 pg/ml taken on assumption of an equal mixture of the four bases), the concentration was calculated. Working stocks (20 µM for PCR amplification; 3.2 µM for DNA sequencing) were prepared and stored at -20°C. Full list of primers used in this study is provided in **Table 2.1**.

Table 2.1 Full list of primers.

Primer	Sequence	Restriction site	Length	Content	Tm (°C)	MW	Notes
HcMyBPC.FOR.27-56	CTC AGG ATC CCT GAG CCG GGG AAG AAG CCA	BamHI (M)	30b, 29b match HcMyBP-C	A 8, C 9, G 10, T 3	83.2	9255	F, includes 6b of the 5' UTR, 1b changed to produce a BamHI site, 4b clamp
HcMyBPC.REV.3849-3876	TCC CCT CGA GCC AGC CTG GTC ACT GAG G	XhoI (M)	28b, 26b match HcMyBP-C	A 4, C 11, G 8, T 5	82.8	8530	R, includes 19b of the 3' UTR, 2b changed to produce a XhoI site, 4b clamp
HcMyBPC.REV.2611-2630	TTA ACT CGA GGC ATG AAG GGC TGG GAG G	XhoI (A)	28b, 20b match HcMyBP-C	A 7, C 4, G 12, T 5	77.9	8762	R, 4b clamp
HcMyBPC.FOR.2481-2508	CGG TGA ATT CAG CTG AAC TTC GAC CTG A	EcoRI (M)	28b, 26b match HcMyBP-C	A 7, C 7, G 7, T 7	75.6	8592	F, 2b changed to produce a EcoRI site, 4b clamp
HcMyBPC.REV.3217-3237	A AGTC TCG AGG ACT TGG CTT GTC AAC AA	XhoI (A)	28b, 21b match HcMyBP-C	A 8, C 6, G 7, T 7	72.8	8616	R, 3b added to create XhoI site, 4b clamp
HcMyBPC.FOR.2925-2949	CAG GGG ATC CTG CAA CGG CCA CGG C	BamHI (M)	25b, 24 match HcMyBP-C	A 5, C 9, G 9, T 2	84.2	7681	F, 1b changed to produce BamHI site, 4b clamp

HcMyBPC-FOR.2331 - 2360	AGG GGG ATC CAC GTG CCA GAC GCA CTT GCG	BamHI (M)	30b, 27 match HcMyBP-C	A 7, C 10, G10, T 3	88.1	9247	F, 3b changed to produce BamHI site, 4b clamp
HcMyBPC.REV.2931-2958	GCA GCT CGA GCC GTG GCC GTT GCA GGA T	XhoI (M)	28b, 25 match HcMyBP-C	A 4, C 8, G 11, T 5	85.6	8650	R, 2b changed to create XhoI site, 4b clamp
HcMyBP-.FOR.2625-56	ATG CGG ATC CGT CCC CCC AGC GAA CCC ACC CA	BamHI (M)	32b, 29 match HcMyBP-C	A 7, C 16, G 6, T 3	90.5	9649	F, 3b changed to produce BamHI site, 4b clamp
HcMyBP-.REV.3519-3488	GG TCT CTA GAT AAA GAC GGG CTC CTT GTT GTT	XbaI(M)	32b, 29 match HcMyBP-C	A 6, C 6, G 11, T 9	75.5	9915	R, 3b changed to create XbaI site, 4b clamp
HcMyBP-.FOR.3204-35	CTG GGG ATC CAG GTT GTT GAC AGG CCA AGT CC	BamHI(M)	32b, 29 match HcMyBP-C	A 7, C 8, G 10, T 7	80.9	9869	F, 3b changed to produce BamHI site, 4b clamp
HcMyBP-.REV.2316-47	GG CAT CTA GAT GAC CTT GAC TGT GAG GTT GAC	XbaI(M)	32b, 29 match HcMyBP-C	A 7, C 6, G 10, T 9	74.5	9899	R, 3b changed to produce XbaI site, 4b clamp
HcMyBP-.REV.825-864	C TCC CTC GAG **C**TA GCG GCG GAA GGC TGA TAG GAG GTC CAG	XhoI (M)	40b, 30 match HcMyBP-C	A 8, C 11, G 15, T 6	87.2	10159	R, 4b clamp, stop codon added

HcMyBP-.FOR.792-824	CTC AGG ATC CAC GAG GCC ATG GGC ACC GGA GAC	BamHI (M)	33b, 30 match HcMyBP-C	A 8, C 11, G 11, T 3	87	12388	F, 3b changed to produce BamHI site, 4b clamp
mCherry.FOR.1-27	CGG CAA GCT TCC ACC ATG GTG AGC AAG GGC GAG GAG GAT AAC	HindIII (A)	42b, 31 match mCherry	A 12, C 10, G 15, T 5	88.6	13047	F, 4b clamp.
mCherry.REV.689-708	T GGC GCT AGC CTT GTA CAG CTC GTC CAT GC	NheI (M)	30b, 22 match mCherry	A 4, C10, G 8, T 8	81.2	9150	R, 3b changed to produce NheI site

Notes: restriction site underlined, (M) modified residue shaded in yellow, (A) added residues highlighted in blue, (F) forward, (R) reverse.

2.1.10. Plasmid vectors

All constructs used in the Y2H screen were previously made and kindly provided by Dr S. Zissimopoulos. The following plasmid vectors were used for co-transformation and recombinant protein expression in *Saccharomyces cerevisiae*:

- **pGBKT7, Figure 2.1 (A)**: cloning vector used to generate fusion of protein X/bait with GAL4 DNA-BD. It contains Kanamycin resistance gene for positive selection in *E.coli* and TRP1 prototrophic selection gene enabling identification of positive yeast clones.
- **pACT2, Figure 2.1 (B)**: cloning vector used to generate GAL4 AD fusion with protein Y/ prey. It contains Ampicillin resistance gene for positive selection in *E.coli* and LEU2 prototrophic selection gene for allowing selection of positive yeast clones.
- **pVA3-1**: positive control used with pTD1-1, encodes GAL4 DNA-BD fusion with murine p53 protein.
- **pTD1-1**: positive control used with pVA3-1, encodes GAL4 AD fusion with SV40 large T antigen.

All aforementioned plasmid vectors were provided with Matchmaker Gal4 Two-Hybrid System (Clontech).

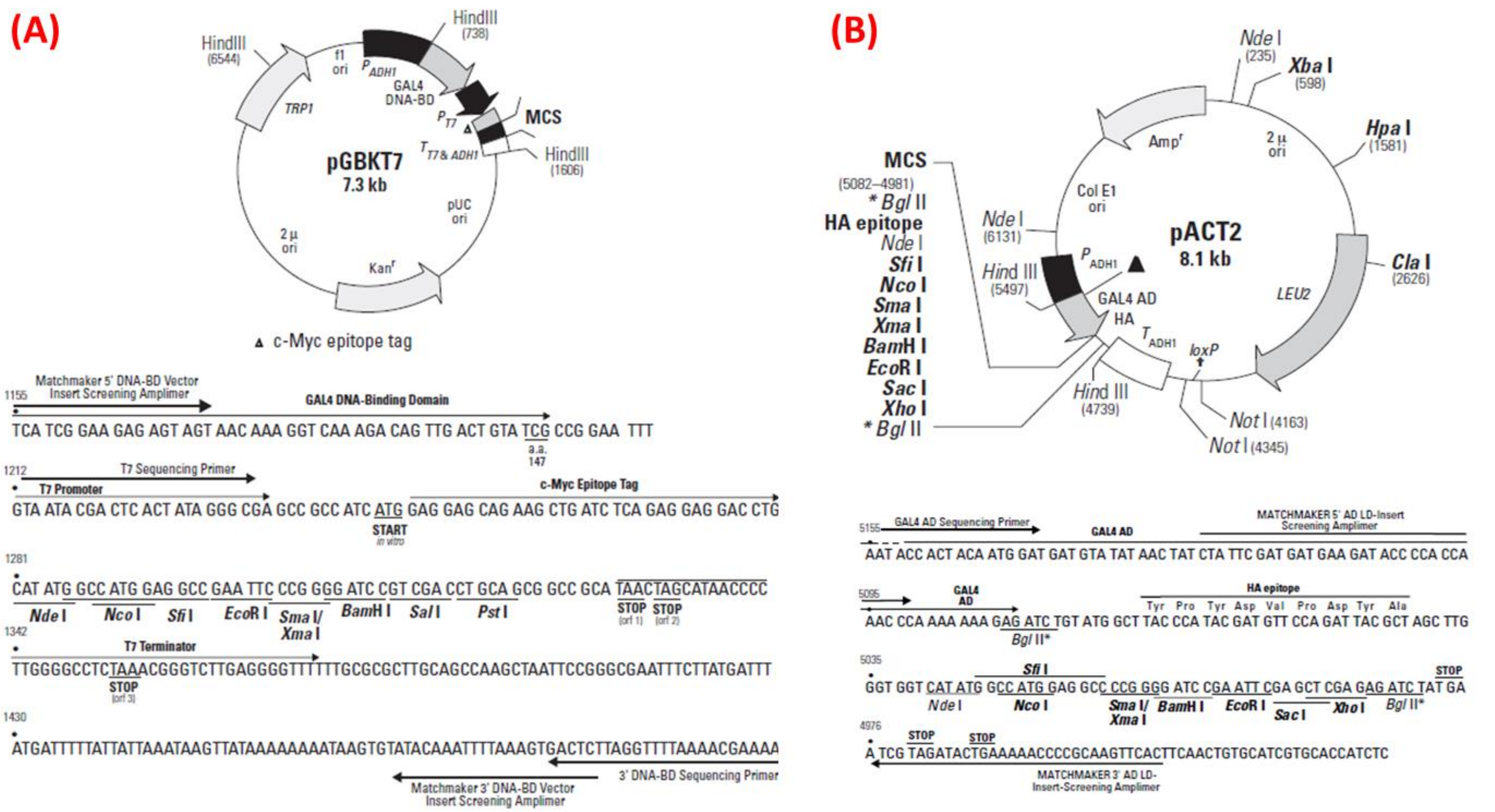

Figure 2.1 Illustration of plasmid vectors used in Y2H study. Restriction sites and a detailed map of multicloning site of (A) pGBKT7 vector and (B) pACT2 vector. All images shown were taken from the Clontech website (www. clontech.com) and modified.

Full length human WT (hRyR2 WT) and series of N-terminal (BT) RyR2 constructs were previously made and obtained from Dr C. George and Dr S. Zissimopoulos, respectively. The following mammalian expression vectors were used in this study:

- **pcDNA3** (Invitrogen), **Figure 2.2**: cloning vector used to generate full length human RyR2 WT. It contains Ampicilin resistance gene for positive selection in *E.coli* and Neomycin resistance gene for allowing selection of stably transformed mammalian cells.

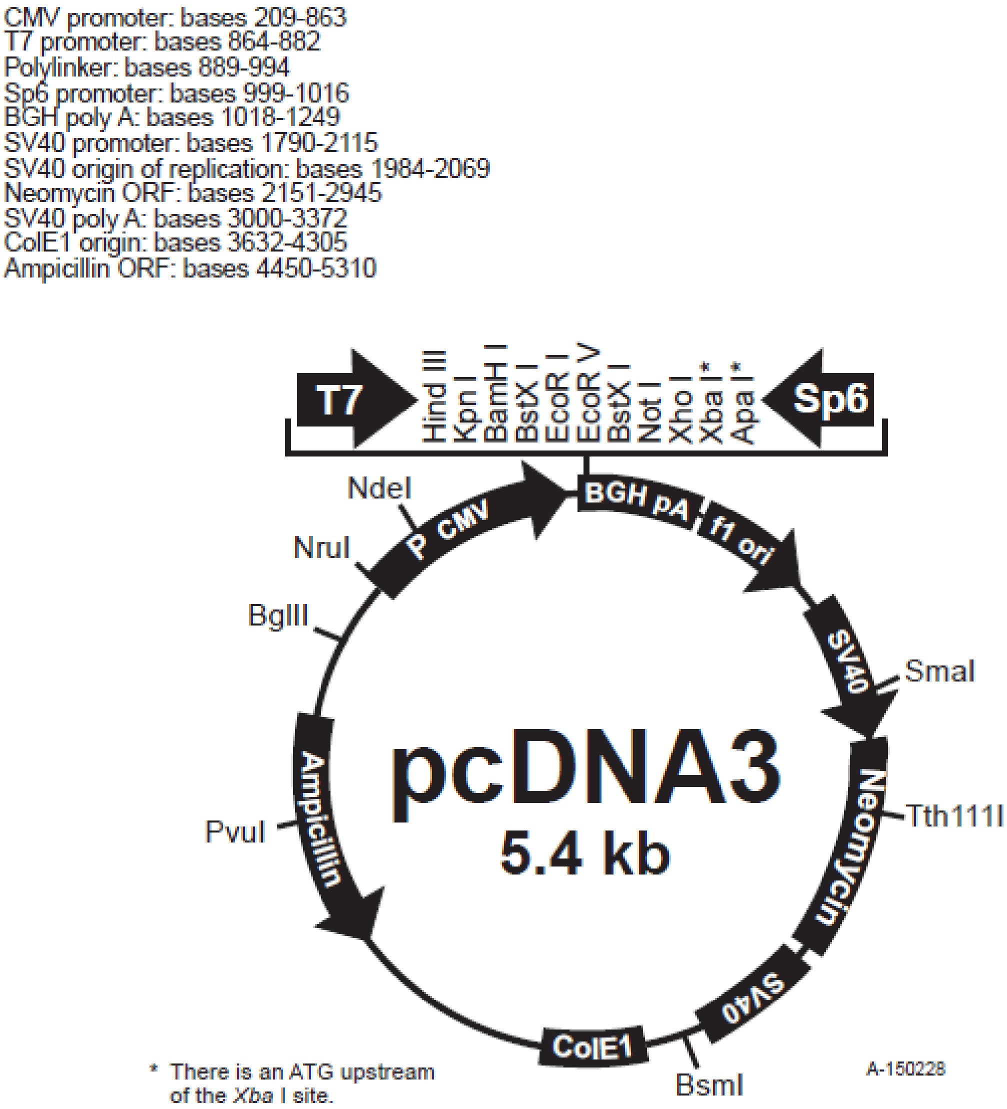
CMV promoter: bases 209-863
T7 promoter: bases 864-882
Polylinker: bases 889-994
Sp6 promoter: bases 999-1016
BGH poly A: bases 1018-1249
SV40 promoter: bases 1790-2115
SV40 origin of replication: bases 1984-2069
Neomycin ORF: bases 2151-2945
SV40 poly A: bases 3000-3372
ColE1 origin: bases 3632-4305
Ampicillin ORF: bases 4450-5310

* There is an ATG upstream of the *Xba* I site.

Figure 2.2 Illustration of restriction sites of mammalian expression pcDNA3 vector used in this study. Image shown was taken from the Life Technologies website (www.lifetechnologies.com) and modified.

- **pCR3** (Invitrogen), **Figure 2.3**: cloning vector that contains Ampicilin resistance gene for positive selection in *E.coli* and Kanamycin/Neomycin resistance genes for allowing selection of stably transformed mammalian cells.

CMV promotor: bases 1-596
Putative Transcriptional Start: bases 620-625
T7 promotor: bases 638-657
Multiple Cloning Site: bases 664-769
SP6 promotor: bases 774-791
BGH poly A: bases 796-1024
ColE1 origin: bases 1155-1738
TK poly A signal: bases 1923-2194
Kanamycin/Neomycin resistance: bases 2195-3191
SV40 promotor/origin: bases 3192-3549
Ampicillin Resistance: bases 3568-4599
F1 origin: bases 4600-5056

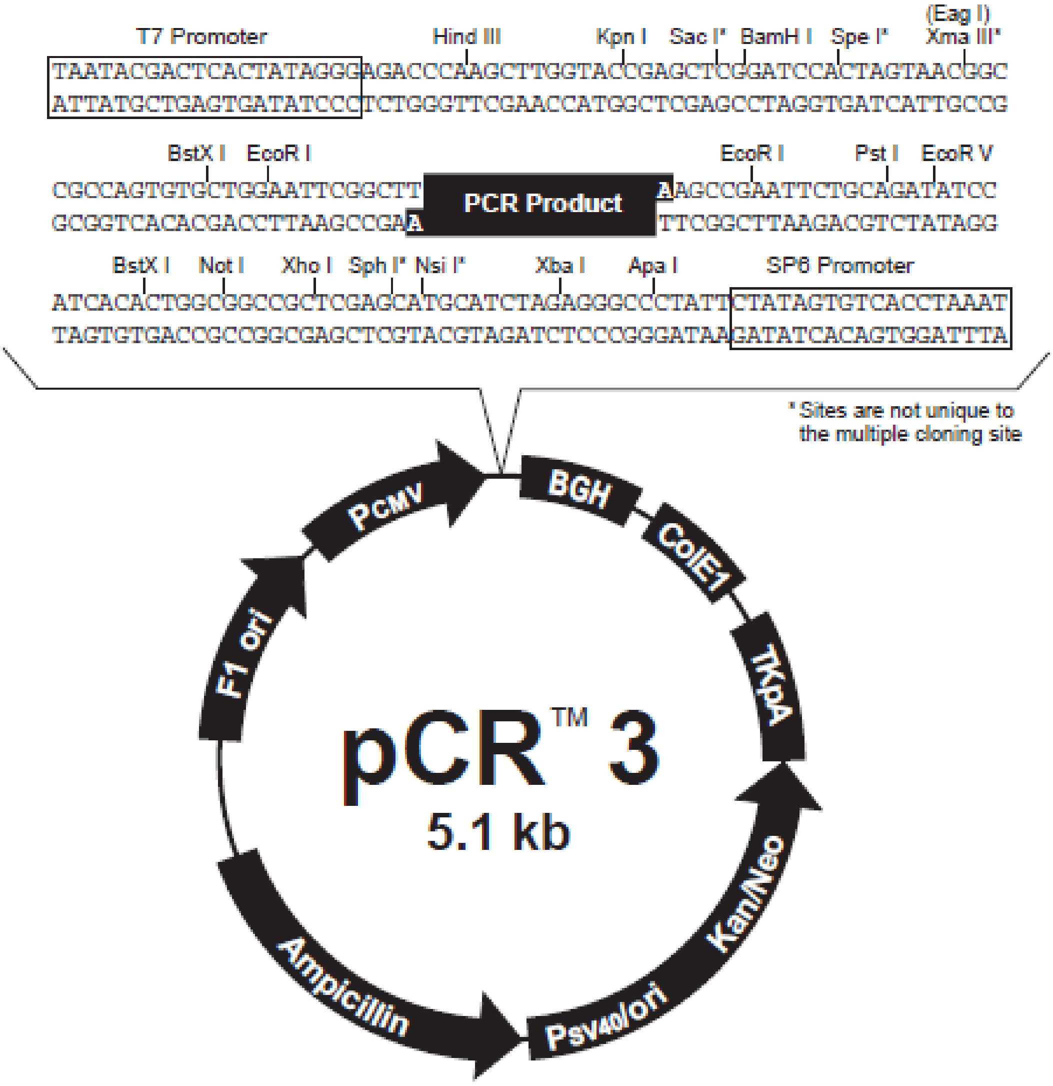

Figure 2.3 Illustration of restriction sites of the original mammalian expression pCR3 vector. Image shown was taken from the Life Technologies website (www.lifetechnologies.com) and modified.

- **mCherry-pCR3**, **Figure 2.4**: modified pCR3 vector, where original multiple cloning site has been altered to enable expression of mCherry tagged proteins. The coding sequence for synthetic peptide mCherry was obtained from Dr C. George and cloned into pCR3 vector as described in **Chapter 5**.

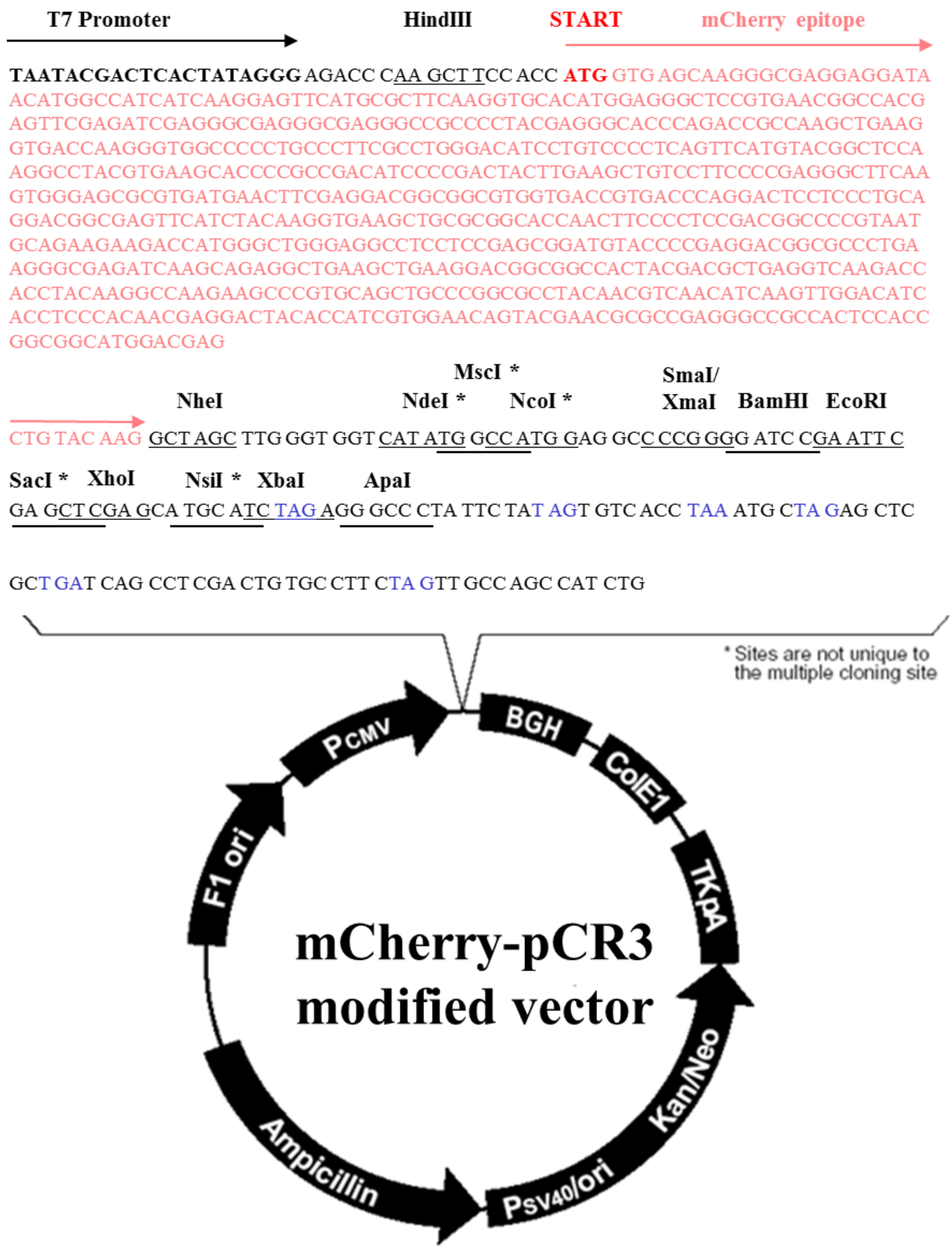

Figure 2.4 : Illustration of restriction sites and a detailed map of multicloning site of mCherry- pCR3 tagged vector. All images shown were taken from the Life Technologies website (www.lifetechnologies.com) and modified.

- **c-Myc-pCR3, Figure 2.5 (A):** modified pCR3 vector by Dr S. Zissimopoulos, where original multiple cloning site has been altered to enable expression of c-Myc (EQKLISEEDL) tagged proteins.
- **HA-pCR3, Figure 2.5 (B):** modified pCR3 vector by Dr S. Zissimopoulos, where original multiple cloning site has been altered to enable expression of influenza hemagglutinin HA (YPYDVPDYA) tagged proteins.

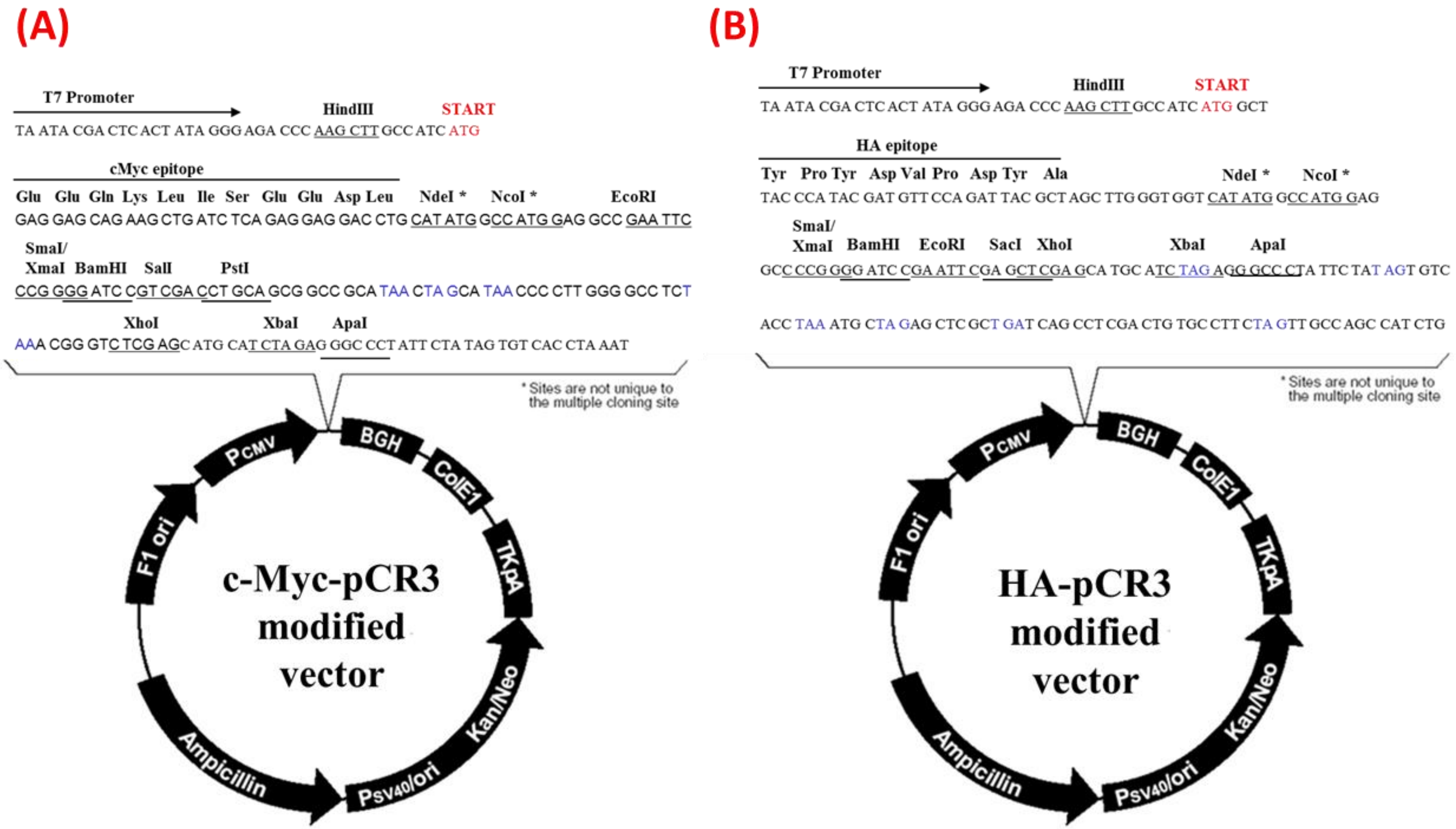

Figure 2.5 Illustration of restriction sites and a detailed map of multicloning site of (A) c-Myc-pCR3 tagged, (B) HA-pCR3 tagged vector. All images shown were taken from the Life Technologies website (www.lifetechnologies.com) and modified.

2.1.11. Antibodies

The following antibodies (**Ab**) were used in this study:

- **Ab 1093**, rabbit polyclonal antiserum, raised to residues 4454-4474 of human RyR2 (EDKGKQKLRQLHTHRYGEPEC) used in WB at 1:1000 dilution, in native co-IP at 1:10 dilution (2ug), and ICC at 1:100 dilution.
- **Ab C-t** (AF7199, R&D Systems), polyclonal anti-mouse sheep IgG, raised against *E. coli* derived recombinant mouse cMyBP-C residues 998-1100, used in WB at 1:200 dilution.
- **Ab N-t (**E7, Santa Cruz), mouse monoclonal IgG, raided against cMyBP-C amino acids 1-120 mapping at the N-terminus of human origin, used in WB at 1:500 dilution, co-IP at 1 µg, and ICC at 1:100 dilution.
- **Ab HA** (Y-11, Santa Cruz), rabbit polyclonal IgG, raised against internal region of the influenza hemagglutinin protein, used in co-IP at 1 µg.
- **Normal rabbit IgG** (Santa Cruz), used as negative control: 2 µg in native proteins co-IP, 1 µg recombinant proteins co-IP.
- **Ab HA** (16B12, Covance), mouse monoclonal $IgG_{2a,}$ raised against internal region of the influenza hemagglutinin protein, used in WB at 1:500 dilution.
- **Ab c-Myc** (9E10, Santa Cruz), mouse monoclonal IgG_1, raised against epitope corresponding to amino acids 408-439 within the carboxyl terminal domain of c-Myc of human origin, used in WB at 1:500 dilution.
- **Anti-mouse goat HRP conjugated Ab** (Santa Cruz), used in WB at 1:10.000 dilution.
- **Anti-sheep HRP conjugated Ab** (R&D Systems), polyclonal donkey IgG, used in WB at 1:5000 dilution.

- **Anti-rabbit polyclonal HRP conjugated Ab,** used in WB at 1:10.000
- **Alexa Fluor 488 conjugate** (A-11034, Life Technologies), goat anti-rabbit IgG secondary antibody, used in ICC at 1:500 dilution.
- **Alexa Fluor 594 conjugate** (A-11005, Life Technologies), goat anti-mouse IgG secondary antibody, used in ICC at 1:500 dilution.

2.2 Methods

General molecular biology and biochemistry techniques were performed according to protocols outlined in the Molecular Cloning laboratory manual (Sambrook et al. 1989) and procedures optimised by other members of Professor Lai's laboratory. When applicable, the manufacturer's instructions were followed. All equipment used for agarose and polyacrylamide gel electrophoresis, semi-dry transfer and image acquisition were purchased from Bio-Rad, unless stated otherwise. Centrifugation steps were undertaken using a range of Beckman Coulter and Eppendorf centrifuges. Where required, aseptic technique was employed and surfaces were swabbed with 70% (v/v) ethanol before and after use. All techniques conformed to local safety guidelines included in the WHRI Health and Safety Handbooks.

2.2.1 Molecular biology methods

2.2.1.1 Standard Polymerase Chain Reaction (PCR)

A series of PCR reactions were carried out using a GeneAmp PCR system 9700 thermal cycler (Applied Biosystems). To generate high-fidelity amplification products, *Pfu* (a *Pyrococus furiosus*) DNA polymerase was used, which possess 5'- 3' DNA polymerase activity and 3'- 5' exonuclease (proofreading) activity, allowing recognition and excision of any misincorporated bases during polymerisation. Annealing temperature of standard PCR reaction was usually set at approximately 5-

10°C below primers' melting temperature. The extension time was calculated based on the length of expected PCR product, assuming 2 min for every 1kb to be amplified. Typical PCR reaction set-up and cycling conditions are presented in **Table 2.2** and **2.3**, respectively.

Table 2.2 PCR reaction components.

Reagent	Final concentration	Volume
DNA template (20-300 ng of cDNA)	100 ng	0.5 µl of 200 ng/µl
Upstream primer (5-50 pmol)	20 pmol	1 µl of 20 µM
Downstream primer (5-50 pmol)	20 pmol	1 µl of 20 µM
PCR buffer	1x	5 µl of 10x stock
dNTP mix	0.2 mM	0.5 µl of 20 mM stock
***Pfu* DNA polymerase**	1 u	0.5 µl of 2 u/µl stock
Nuclease-free sterile dH_20	Up to 50 µl final volume	39 µl

Table 2.3 PCR amplification thermal cycling conditions.

Step	Temp (°C)	Time (min)	Number of cycles
Initial denaturation	95	2	1
Denaturation **Annealing** **Elongation**	95 42-65 72	1 1 ≥1	30
Final elongation	72	5-10	1
Incubation	4	Indefinite	1

2.2.1.2 Agarose gel electrophoresis

Agarose gel electrophoresis was used to verify DNA fragments following PCR amplification (**Section 2.2.1.1**) or restriction digest (**Section 2.2.1.3**). An agarose gel was prepared by dissolving the appropriate amount of agarose (see **Table 2.4)**; typically, 1% was used for fragments >1 kb) in 1x TAE buffer by boiling for ~1-2 min. Subsequently, the mixture was cooled to ~50°C and 0.01 % of ethidium bromide was added. The agarose solution was left to set in a gel cast, and then assembled into a minisub gel tank according to the manufacturer guidelines. DNA loading samples were prepared with 1x DNA loading buffer (containing Orange G for visualisation, which co-migrates with DNA fragments at ~100 bp), and for each gel a 1 kb DNA molecular weight marker was run alongside the samples as a reference of fragment molecular mass. Electrophoresis was carried out under constant voltage (typically 80 V) until sufficient DNA fragment separation was obtained. The Gel UV Imaging System (Alpha Innotech) was used to visualize the resolved DNA fragments by UV illumination.

Table 2.4 Agarose concentrations for DNA electrophoresis.

% (w/v) Agarose	Effective range of separation of linear DNA (kb)
0.7	0.8-10
1.0	0.5-8
1.2	0.4-6
1.5	0.2-3
2.0	0.1-2

2.2.1.3 DNA restriction endonuclease digest

DNA was digested with appropriate restriction endonucleases according to the manufacturer's recommendations. Briefly, each reaction was set in 10 µl, with 0.5-2 µg of DNA (depending on the subsequent downstream application). For double-enzyme-digest reaction, buffers compatibility was evaluated using the NEB online site (http://www.neb.uk.com). All reactions were incubated at 37°C for 2 h and analysed by agarose gel electrophoresis. For DNA cloning, the restriction digest set-up was preceded by DNA fragments visualisation using U.V transilluminator light box (Syngene) to evaluate the amount of DNA, excision of appropriate gel fragment and subsequent purification using the gel extraction kit. For two-step PCR reactions, the sample was first purified with the PCR purification kit. Both procedures were carried out according to the manufacturer's instructions.

2.2.1.4 DNA ligation

DNA ligation was conducted according to the manufacturer's guidelines. Briefly, a reaction was set-up in 30 µl and contained 20-200 ng of total DNA, with 3:1 molar ratio of insert:vector. Reaction was incubated for 2 h at room temperature before proceeding to bacterial transformation (**Section 2.2.3.1**).

2.2.1.5 Spectrophotometric DNA quantification

Nucleic acids have absorbance maxima at 260 nm, therefore DNA plasmid concentration was determined by spectrophotometric quantification of a 1:50 dilution sample at this wavelength. The concentration was calculated (in triplicate) taking into account that A_{260}= 1 corresponds to 50 pg/ml of double stranded DNA. Any contaminating proteins present will have a peak light absorbance at 280 nm, therefore plasmid purity can be quantified by using the ratio of A_{260}/A_{280}, with values of ~1.8 being generally accepted as pure. Additionally, the ratio A_{260}/A_{230} was also used as means of measure the presence of other contamination (i.e. ethanol carryover resulting from DNA purification), with the expected values in the range of 2.0-2.2 for pure DNA.

2.2.1.6 DNA sequencing

DNA sequencing was carried out by DNA Services & Sequencing facility, Dundee University (http://www.dnaseq.co.uk/). Each sequencing PCR reaction was prepared according to their guidelines, set up in 30 µl and contained ~500-600 ng of plasmid DNA and 3.2 pmol of given primer. Obtained electropherogram fluorescence intensities were visualised using Seq Scanner 2 software (Applied Biosystems). NCBI Basic Local Alignment Search Tool (BLAST, http://blast.ncbi.nlm.nih.gov/Blast.cgi) was used for pairwise sequence alignment, whereas multiple sequence alignment was produced using EMBL-EBI Clustal Omega (http://www.ebi.ac.uk/Tools/msa/clustalo/).

2.2.2 Protein biochemistry methods

2.2.2.1 Mammalian cell homogenization

Cell pellets of HEK293 cells expressing the proteins of interest (~2x 10^7 cells harvested from one 100 mm Petri dish) were re-suspended in appropriate volume of ice-cold homogenization buffer supplemented with protease inhibitors (typically 500 µl in total per one pellet, type of used buffer depending on the downstream application) and kept on ice.

For co-IP assay, cells were re-suspended in organic-salt-based buffer (see **Section 2.1.2**) with added protein inhibitors and homogenised by 20 passages through a 0.6 mm needle in the presence of 250 µl of glass beads (pre-washed in the homogenisation buffer). Nuclei and unbroken cells were removed by centrifugation at 1500 xg for 5 min at 4^{o}C and the post-nuclear supernatant was collected and subsequently solubilized with 0.5% CHAPS (500 µl total volume) and incubated overnight at 4^{o}C with continuous mixing. Further, sample was subjected to centrifugation at 20.000 xg for 10 min at 4^{o}C to pellet the insoluble material and the supernatant fraction was collected (referred to from this point on as ‘cell lysate’) and used in co-IP assay.

For [^{3}H]ryanodine binding assay, cells were first re-suspended in ice-cold iso-osmotic buffer (500 µl per cell pellet) with added protein inhibitors and passaged forcefully 20x through a sterile 23G needle aided by the use of an automated cell homogeniser (the “montygeniser”, designed and constructed by Richard Montgomery). The resultant homogenate was centrifuged at 2600 rpm (1000 xg) for 5 minutes, at 4°C and the resulting supernatant was collected and stored at 4^{o}C until further use.

2.2.2.2 Determination of protein concentration

Protein concentration was estimated with the use of BCA Protein Assay Kit according to the manufacturer’s guidelines. Briefly, the method is based on reduction of Cu^{2+} to Cu^{1+} by protein in an alkaline environment with the selective colorimetric detection of the Cu^{1+} by bicinchoninic acid (BCA). Duplicates of two dilutions (1/10 and 1/20) of the sample of interest were prepared together with serial dilutions of BSA protein (2000-62.5 µg/ml) and incubated with kit reagents for 30 min at 37^{o}C. Subsequently, absorbance at 560 nm of each prepared sample was measured using Multiscan EX

(Labsystems) spectrophotometer. Protein concentration was calculated using a standard curve produced by the linear regression of the absorbance against the known concentrations of BSA protein samples.

2.2.2.3 Co-immunoprecipitation (co-IP) assay

Co-IP was performed by adding the desired Ab to pre-washed 3x with IP buffer Protein A or G beads slurry (typically 25-30 µl of slurry with 2 µg of Ab in 200 µl of co-IP buffer) and incubated overnight at 4°C with continuous mixing.

Where appropriate, samples were subjected to DTSSP crosslinking, where protein A beads slurry was washed 3x with PBS buffer (instead of IP buffer) before adding the relevant antibody and incubated ~3 h at 4°C with continuous mixing. The beads were then washed once with PBS buffer and to each pre-captured Ab, 200 µl of freshly made 2 mM DTSSP in PBS was added and incubated for 30 min at room temperature. The reaction was stopped with addition of 200 µl IP buffer and followed by one subsequent 30 min wash with IP buffer and further incubated in 200 µl of IP buffer overnight at 4°C with continuous mixing.

To each pre-captured Ab (whether normal or crosslinked), 200 µl of cell lysate was added and incubated for 3 h at 4°C with continuous mixing. The beads were washed 2x with IP buffer and collected by centrifugation at 1500 xg for 2 min at 4°C. Immunoprecipitated proteins were eluted with 1x protein loading buffer (either reducing- to prevent formation of protein aggregates, or non-reducing- for DTSSP-treated samples to preserve crosslinked Ab complexes) and stored at -20°C prior to analysis by SDS-PAGE and WB.

2.2.2.4 Polyacrylamide gel electrophoresis (SDS-PAGE)

Depending on the size of the proteins to be separated, typically 6-12% polyacrylamide mini gels (8 cm x 10 cm, 0.75 cm thick) were prepared a day before electrophoresis. Detailed gel compositions are outlined in **Tables 2.5** and **2.6**.

Table 2.5 Separating gel composition Volumes given for 2 mini gels (μl).

	Separating gel %					
Reagents	**4%**	**6%**	**8%**	**10%**	**12%**	**15%**
Acrylamide/Bis (37.5:1) 40%	1000	1500	2000	2500	3000	3750
Water	6345	5845	5345	4845	4345	3595
Tris-HCl 1.5M, pH 8.8	2500	2500	2500	2500	2500	2500
SDS 10%	100	100	100	100	100	100
Ammonium Persulphate 10%	50	50	50	50	50	50
TEMED	5	5	5	5	5	5

Table 2.6 Stacking gel composition. Volumes given for 2 mini gels (μl).

Stacking Gel	
Acrylamide/Bis (37.5:1) 40%	500
Water	3170
Tris-HCl 0.5M, pH 6.8	1250
SDS 10%	50
Ammonium Persulphate 10%	25
TEMED	2.5

Briefly, the separating gel mixture was poured into assembled gel casting system up to 2/3rd of the glass plates' height. The solution was overlaid with dH_2O and allowed to polymerise for ~ 2 h. Subsequently, dH_2O was removed and the top of separating gel was dried with paper. Stacking mixture was poured to the top of glass plates and the comb was inserted to form loading wells. Gels were left to set for at least 2 h before transferring into mini-gel tank and immersing in the 1 x SDS-PAGE running buffer.

Native and recombinant RyR2 WT protein samples were separated using 4% polyacrylamide gel, strengthened with 0.5% agarose (4% acrylamide/0.5% agarose gel). To 5 ml of 8% polyacrylamide solution, 5 ml of 1% (w/v, freshly dissolved by boiling) agarose was added. The mixture was immediately poured into a pre-chilled, assembled gel casting system up to the top and the comb was inserted (no stacking gel). Gel stand was placed back into an ice-cold bath and left for 10 min for the agarose to solidify and allowed to polymerise overnight at room temperature. Following morning gels were transferred into mini gel tank as before.

Prior to loading, pre-made samples containing 1 x protein loading buffer were heated at either 85^{o}C (small protein fragments) or 50^{o}C (RyR2 WT samples) for 5 min followed by 3 min centrifugation at 14.000 xg. Samples were loaded alongside protein molecular weight markers and electrophoresis was run under constant current (typically 40 mA for gel tank containing 4 gels) until the appropriate separation of coloured markers were obtained. Following electrophoresis, gels were either processed for WB or stained with dye based protein stain.

2.2.2.5 Western blot (WB) analysis

SDS-PAGE separated proteins were transferred onto PVDF membranes using a semi-dry system, following the manufacturer's instructions. Briefly, following the electrophoresis, gels were washed in dH_2O and incubated ~5 min in transfer buffer together with blotting paper and methanol-activated PVDF membranes. The blotting sandwich was assembled and transfer was conducted at constant current, either 400 mA for 1 h at room temperature (small protein fragments blots), or 600 mA for 4 h at 4^{o}C (RyR2 WT blots). Following the transfer, blots were first blocked for 1 h in TBS-T/Marvel buffer, and then incubated overnight at 4^{o}C with the appropriate primary Ab (diluted in blocking buffer). The incubation with the corresponding secondary Ab (HRP-conjugated) was conducted for ~2-4 h at room temperature and was followed by 2x TBS-T washes, 5 min each. Proteins were visualised by chemiluminescence detection with ECL kit, following manufacturer's recommendation. X-ray films were developed using an automatic X-ray film processor (X-ograph Compact X4, Xograph Healthcare). Film exposure was adjusted to the signal strength, typically ≤15 min.

2.2.3 Bacterial culture

2.2.3.1 Chemical transformation of bacteria

Transformation of small plasmids (i.e., cMyBP-C constructs) was carried out using two chemically competent *E. coli* strains, either (1) OneShotTOP10 (Fisher Scientific) or (2) Sure2 (Stratagene). For (1), following the manufacturer's instructions, 15 µl of bacterial suspension was incubated on ice for 30 min in the presence of 10 ng of plasmid DNA. For (2), 50µl aliquot was first incubated with 2 µl of β-mercaptoethanol for 10 min on ice, with gentle agitation every 2 min. Subsequently 1ng of the ligation reaction was added, briefly mixed and incubated on ice for 30 minutes. Following steps were identical for (1) and (2). Bacteria were subjected to 45 sec heat shock treatment at 42°C in a water bath, followed by 2min incubation on ice. Further, 800 µl SOC medium was added and bacterial suspension was incubated at 37°C for 1 h with shaking at 225 rpm. Cultures were plated at two different densities (1/10th and 9/10th) onto pre-warmed LB/Ampicillin agar plates, and incubated overnight at 37°C (Heraeus Incubator, Thermo Scientific) before the colony selection.

Due to large size and the fragile nature of the hRyR2 WT plasmid construct, an optimised transformation method was employed with the following differences: 25 µl of XL-Gold Ultracompetent cells (Agilent Technologies) were incubated in the presence of 1 µl ß-mercaptoethanol, with 1 ng of hRyR2 WT, followed with 30 min incubation as described previously and heat pulsed for 30 sec at 42ºC. After transformation, all culture steps were as above, apart from incubation temperature (30°C).

2.2.3.2 Colony screen and plasmid isolation

Following bacteria transformation, a number of colonies were screened for the presence of the recombinant plasmid of interest (containing the correct orientation and size of the DNA insert) using small-scale plasmid DNA isolation (‘mini-prep’) with Wizard Plus SV Miniprep plasmid purification kit. Briefly, following O/N incubation, individual colonies were selected and used to inoculate ~3 ml of pre-warmed LB/Ampicillin growth medium and further incubated for 16-18 h at 37°C with continuous shaking at 225 rpm. 1.5 ml of each saturated culture was subsequently pelleted at 13,000 xg for 2 min and processed for plasmid isolation following the manufacturer protocol.

Briefly, it employs the alkaline bacterial lysis, salt-detergent precipitation of impurities and DNA binding to kit columns followed by two ethanol-based washing steps. After purification, plasmid DNA was eluted with 30 µl of sterile dH_2O and further verified (by DNA restriction endonuclease digests and agarose gel electrophoresis, **Sections 2.2.1.3** and **2.2.1.2**, respectively) before being prepared on a larger scale.

Small-scale cultures which produced plasmid DNA giving the correct endonuclease digest pattern were used to inoculate large volumes at a 1/400 dilution. Typically, 200 ml (small protein constructs) or 4x 400 ml (hRyR2 WT plasmid construct) flasks of LB/Amplicillin medium were processed for DNA purification. Each flask was incubated overnight at 37°C (for small protein constructs, for 16-18 h until saturated,) or 30°C (hRyR2 WT plasmid construct, unsaturated cultures were collected at OD_{600} ≤1-1.1), with shaking at 225 rpm, and processed with Qiagen Plasmid Maxi Kit (‘maxi-prep’). It employs modified alkaline lysis procedure, followed by binding of plasmid DNA to anion-exchange resin under low salt and appropriate pH conditions. Briefly, bacteria were harvested by centrifugation at 10.000 xg for 5 min and obtained cell pellet was subjected to cell lysis followed by lysate filtration, DNA column binding and medium-salt washing in order to remove impurities. Bound DNA plasmid was then eluted from the resin column with high-salt buffer, desalted with isopropanol and precipitated onto new filter module. Subsequently the filter was subjected to more washes, briefly air-dried and DNA plasmid was eluted with 500 µl of sterile dH_2O. Further, DNA was spectroscopically quantified (**Section 2.2.1.5**) and verified by DNA restriction endonuclease digests and agarose gel electrophoresis (**Sections 2.2.1.3** and **2.2.1.2**), before storing at -20°C. For confirmation of correct localisation and size of the DNA insert, all generated constructs were sent for DNA sequencing (**Section 2.2.1.6**).

2.2.3.3 Long term storage

For long-term storage of transformed bacteria, 1 ml of liquid culture grown in the presence of antibiotic for 16 h were subjected to centrifugation at 10.000 xg for 1 min at room temperature. Frozen glycerol stocks were made by resuspending the cell pellet in glycerol:LB/Ampicillin medium in a 1:1 ratio and frozen on dry ice and stored at -80^{o}C in cryo-tubes. Bacteria from this frozen stock were revived by streaking small portion (~10 µl) of the stock onto LB/Ampicillin plates and further cultured at 37^{o}C as required.

2.2.4 Yeast culture

All yeast two-hybrid techniques were carried out according to the Matchmaker GAL4 User Manual (Clontech) and Yeast Protocols Handbook (Clontech).

2.2.4.1 Yeast transformation

S. cerevisiae Y190 yeast strain (Clontech) was revived from glycerol stocks (stored in YPD medium with 50% glycerol at -80°C), plated on YPD agar plates and incubated at 30°C until yeast colonies reached ~2mm in diameter (4-5 days). Next, 50 ml of YPD growth medium was inoculated with single colony and incubated at 30°C O/N with shaking at 250 rpm for 16-18 h until saturated (i.e. $A_{600}\geq1.5$). The culture was then refreshed to early log phase (A_{600}= 0.2-0.3) by appropriate dilution in 400 ml of YPD and further cultured for 3-5 h until yeast reached mid-log phase (A_{600}=0.5-0.6). Cells were collected by centrifugation at 1000 xg for 5 min and washed once in sterile dH_2O. The final cell pellet was resuspended in 1.5 ml TE/LiAc solution. Competent cells were used immediately after preparation for highest transformation efficiency

For co-transformations using two different plasmids, 500 ng of each plasmid (an approximately equal molar ratio) was used, together with 100 µl of prepared competent cells and 100 µg of herring testes carrier DNA. 600 µl of PEG/LiAc was subsequently added before incubation at 30°C for 30 min with shaking at 200 rpm. DMSO (80 µl, 10% of final volume) was then added and mixed by gentle inversion. Cells were subjected to 15 min heat shock treatment at 42°C (mixed gently every 2-3 min), followed by immediate 2 min incubation on ice. Further, cells were collected by centrifugation at 14.000 xg for 10 sec, and the cell pellet was resuspended in 200 µl of TE buffer. Each 100 µl of cell suspension was plated onto SDY agar plate and incubated at 30°C until ~2 mm colonies appeared (4-5 days).

2.2.4.2 β-galactosidase colony-lift filter paper assay

A filter paper disc was pre-soaked in Z-buffer/X-gal solution, whereas a second dry filter paper was placed over the surface of the plate with the co-transformed yeast colonies to be assayed, and gently rubbed onto the plate with forceps and left for ~5 min for colonies to attach. The filter paper was then completely submerged into a pool of liquid nitrogen for ~30 sec in order to permeabilise the cells, let to thaw at room temperature for 2 min and placed on top of the pre-soaked filter paper inside the 100 mm plate (colony side up). The filters were incubated at 30°C and periodically (typically every 30 min) inspected for the appearance of blue colonies. Yeast co-transformed with the pVA3 and pTD1 were used as positive controls.

2.2.4.3 Cell homogenisation and protein extraction

For analysis of protein expression, yeast transformed with the construct of interest was grown in SDY minimal media. An overnight culture, which was inoculated with a single transformed colony, was used to obtain 100 ml of culture at A_{600} = 0.2-0.3 which was further incubated until mid-log phase (A_{600}=0.5-0.6) was reached. At this point, cells were collected by centrifugation (1500 xg for 5 min at 4 °C), washed in ice-cold dH_2O and again recovered by centrifugation. The cell pellet was re-suspended in 500 µl of ice-cold protein extraction buffer supplemented with protease inhibitors. Cells were homogenised by three rounds (1 min each) of vigorous vortexing in the presence of glass beads, which were earlier washed 3x with the protein extraction buffer. Cell debris was removed by centrifugation at 14 000 xg for 5 min. Protein concentration was evaluated as described in **Section 2.2.2.2.** Protein extracts were stored at -80°C and subsequently analysed for protein expression by WB.

2.2.5 Mammalian culture

2.2.5.1 HEK293 cell maintenance

All cell culture work was undertaken in a designated laboratory in HEPA filtered class II laminar flow containment hoods. In order to revive HEK293 cells, frozen aliquot was thawed to room temperature and re-suspended in cDMEM medium. Cells were recovered by centrifugation at 1000 xg for 3 min, the resulting pellet was re-suspended in 20 ml of medium and cells were seeded in a T75 flask and placed in the 37^{o}C humidifying incubator with 5% CO_2. To maintain a healthy adherent cell population, routine sub-culturing (passage) of the cell monolayer (at 80-90% confluency) was carried out. At this point, cells were washed with saline and were detached enzymatically with 1.5 ml of trypsin-EDTA, for ≤2min. Trypsin was inactivated by addition of 7.5 ml of cDMEM and cells were recovered by centrifugation (1000 xg, for 3 min). Resulting pellet was re-suspended in 10 ml of fresh medium and transferred into new T75 flask for further growth. The split ratio varied from 1:3 to 1:50, depending on the cell growth and the downstream application.

2.2.5.2 Long term storage

For long term storage, 90% confluent HEK293 cells were harvested from 100 mm Petri dish. Collected pellet was washed in saline, recovered by centrifugation and re-suspended in cell freezing medium. Cells, divided into 3x 1 ml aliquots, were slowly frozen down at -80^{o}C and stored until needed.

2.2.5.3 Calcium phosphate transfection

For large scale preparations, approximately 1.5x 10^6 cells were seeded in one 100 mm Petri dish a day before transfection in order to be 60-70% confluent the following day. Routinely, this was achieved by allowing cells to grow until 90% confluence and passaging 18h before transfection at a ratio of 1:5. To generate calcium phosphate-DNA precipitates, plasmid DNA (24 µg DNA in total per 100 mm dish) was mixed with 60 µl od 2.5 M $CaCl_2$ and dH_2O to a total volume of 600 µl. Subsequently, it was added dropwise to 600 µl of 2x HBS, with continuous, vigorous vortexing. To allow precipitate formation, the mixture was incubated for 20 minutes at room temperature, before adding dropwise (1200 µl per 100 mm Petri dish) to the cell monolayer. After ~6 h, the growth medium was changed and cells were further incubated in 37^{o}C humidifying incubator with 5% CO_2 for 24 h, before being harvested by trypsinisation and centrifugation at 1000 xg, 3 minutes. Pellets were re-suspended in saline, centrifuged and allowed to dry. Cell pellets were stored at -80°C.

2.2.5.4 TurboFect transfection

For small scale preparations and use in ICC, 0.25 x 10^6 cells were seeded onto poly-lysine coated glass coverslips (22 mm x 22 mm), and left to adhere overnight at 37°C with 5% CO_2. On the day of transfection, cells were washed 2x with saline and 2 ml of serum-free DMEM was added and cells were further incubated for 3-4 h at 37°C, 5% CO_2. Following manufacturer instructions, 4 µg of recombinant DNA (in total per well) was diluted in 400 µl of mDMEM. Subsequently 6 µl of TurbofFect transfection reagent was added and mixture was immediately vigorously vortexed. Following 20 min incubation at room temperature, mixture was added drop-wisely to the well and cells were incubated in 37^{o}C humidifying incubator with 5% CO_2 for 4 h. At this point medium was supplemented with 2.4 ml 20% FBS in DMEM and cells were further grown for 24 h until transgene expression analysis.

2.2.5.5 Effectene transfection

To prepare for Ca^{2+} imaging (**Section 2.2.6**), on the day of transfection, cells were seeded at a density of 0.7x10^5 cells into 35 mm glass bottom dishes (MatTek), pre-coated with poly-L-lysine the day before seeding. The cells were maintained in 200 µl menisci of cDMEM for 3-4 h (to encourage adhesion) before adding 2 ml fresh growth medium to each well. According to the manufacturers guidelines, 0.25 µg of recombinant DNA (per micro well) was mixed with 2 µl of enhancer and 30 µl DNA-condensing buffer, and incubated for 5 min (room temperature) before addition of 6.25 µl of Effectene reagent. Following incubation for 10 min at room temperature, the resultant Effectene-DNA complexes were mixed with 190 µl of cDMEM and added directly to the cells. Cells were incubated in 37^{o}C humidifying incubator with 5% CO_2 for 18 h and supplemented with 2 ml of fresh growth medium. Cells were further grown for 48 h prior to Ca^{2+} imaging.

2.2.6 Ca^{2+} imaging

Fluo-3 AM (50 µg) was dissolved in 15 µl DMSO containing 20% w/v Pluronic F-127, making a 3 mM stock. 5 µl of stock was added to 1500 µl mDMEM to make 10 µM solution and vortexed well to dissolve. Growth medium from transfected cells was removed and cells were loaded with 150 µl of prepared mixture per well. Further, cells were incubated at 30°C with 5% CO_2 for 45 min, and then de-esterified in 2 ml of mDMEM for 10 minutes. Image acquisition was completed on a Leica SP5 laser scanning confocal microscope (Leica, Heidelberg, Germany), with x63 objective lens and oil immersion. To visualise Ca^{2+} dependent Fluo-3 fluorescence, excitation was initiated at a wavelength of 488 nm with Argon laser and detected by a photomultiplier tube (PMT) set at 500-550 nm. MCherry fluorescence from co-transfected cells was excited using HeNe 594 laser at a wavelength of 594 nm and collected by a PMT set at 600-650 nm. Prior to view, the cells were immersed in a 200 µl meniscus of KRH buffer containing 1.3 mM $CaCl_2$ and spontaneous Ca^{2+} release events were imaged (100 msec time interval) for 3 min in total at 512 x 512 pixel resolution. To estimate cell ER load, 10 mM caffeine was added after 2 min 30 sec (20 µl of 100 mM caffeine stock dissolved in KRH) and recorded for further 30 sec. A caffeine response also allowed to verify the presence of functional RyR2 channels in non-oscillating cells since untransfected HEK cells loaded with Fluo3-AM did not display any SCR-like events (Jiang et al. 2002).

Obtained traces were further exported to Microsoft Excel for off-line examination and analysis: for RyR2 + mCherry-FL cMyBP-C n=70 cells were analysed, RyR2 alone n=73, and RyR2 + mCherry n=33, from ≥8 independent experiments (n=13, 21 and 4 outliers were determined, respectively and removed from the dataset based on numbers higher than 1.5x interquartile range). All subsequent statistical analysis was conducted using GraphPad prism using either one-way ANOVA (with Bonferroni's post-test) or the Kruskal-Wallis test (with Dunn's multiple comparisons test) (see **Section 2.2.11**). For summary of raw data see **Appendix, Figure 8.6.**

Figure 2.6 illustrates all examined parameters of the Ca^{2+} SCR events, as follows:

Basal Signal Intensity: The basal signal intensity (F_0) was calculated by taking an average of all inter-duration (i.e. baseline) fluorescence values of the single trace (measured in seconds). In example, F_0 of trace shown in **Figure 2.6** was calculated as $F_0 = [(S_2 - E_1) + (S_c - E_2)]/2$, where F_0 is the basal signal intensity; S_2 is the time at which SCR event 2 has started; E_2 is the time at which SCR event 1 has finished; S_c

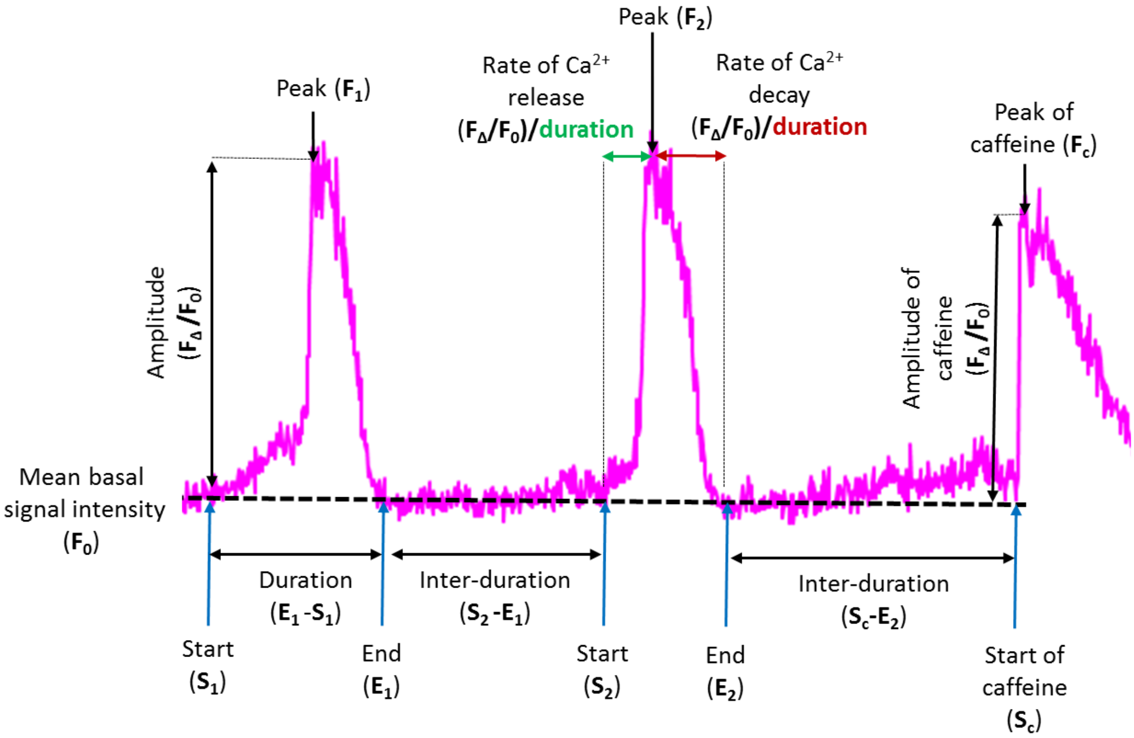

Figure 2.6 Illustration of the SCR kinetic parameters measured in RyR2 transfected HEK293 cells. A representative trace obtained from single Fluo-3 loaded HEK293 cell (in the presence of 1.3mM external Ca^{2+}) is shown in pink, where the parameters assessed are indicated with appropriate arrows. F_0 represents the basal Fluo-3 signal intensity (dashed line). The ER Ca^{2+} store load, was estimated by measuring the amplitude of caffeine-induced Ca^{2+} release.

is the time at which caffeine has been applied; E_2 is the time at which SCR event 2 has finished.

Amplitude: Subtraction (denoted as F_Δ) of the mean basal signal intensity (F_0) from peak signal intensity of each event (F), further normalized to mean basal signal intensity (F_Δ/F_0).

Duration: Measured in seconds, the duration of each event (single oscillation, i.e. corresponding to F_1 in **Figure 2.6**) was established by obtaining the difference between the time at which the event was initiated (S_1) and the time when the signal intensity returns to basal levels (E_1).

Rate of Ca^{2+} Release: Shown as a change in the signal intensity over time (amplitude/duration). Firstly, the time taken to reach peak Ca^{2+} levels (**Figure 2.6**, **green arrow**) was established by subtracting the time at which the SCR-event was initiated (S_2) from the time taken to reach peak signal intensity (F_2). To obtain the rate at which spontaneous Ca^{2+} release occurred, the amplitude (F_Δ/ F_0) was divided by the calculated duration (measured in seconds).

Rate of Ca^{2+} Decay: Also shown as a change in the signal intensity over time (amplitude/duration). The time taken for the Ca^{2+} peak to return to F0 (**Figure 2.6**, **red arrow**) was first established by subtracting the time at peak signal intensity (F_2) from the time taken for the SCR-event to return to baseline levels (E_2). To obtain the rate at which spontaneous Ca^{2+} release decayed, the amplitude of the event (F_Δ/ F_0) was divided by the calculated duration (measured in seconds).

Inter-SCR duration: Measured in seconds, the inter-SCR duration (representing the time period in between each event) was established by taking the time at which a new event occurred (i.e. S_2) and subtracting from it the time at which the previous event ended and returned to baseline (E_1).

Frequency of events: Measured as number of events per minute, the frequency was determined by first adding together each event duration and the following inter-duration (measured in seconds), and subsequently calculating the occurrence of these events per minute.

ER Ca^{2+} load: Estimated by calculating the Ca^{2+} release amplitude induced by caffeine application (10mM, supramaximal caffeine concentration that should fully activate all recombinant RyRs, and therefore result in complete Ca^{2+} release from ER to the cytosol (Jiang et al. 2002)). It was obtained by subtraction (denoted as F_Δ) of the average basal signal intensity (F_0) from peak caffeine-induced signal intensity (F_c) further normalized to mean basal signal intensity (F_Δ/F_0).

2.2.7 Immunocytochemistry (ICC)

Transfected HEK293 cells growing on poly-lysine coated glass coverslips were washed three times in PBS solution before fixing with 4% paraformaldehyde/PBS solution (pH 7.4) for 10 min at room temperature. The fixed cells were washed and re-hydrated with 2 ml of PBS solution for 1 h before permeabilisation at room temperature in 0.1% v/v Triton X-100 in PBS for 30 min. The cells were further washed twice in PBS before blocking in 10% FBS in PBS for 1 h at room temperature. Primary Abs (used at 1:100 dilution in PBS) were then added as a 150 µl meniscus, followed with 2 h incubation at room temperature. Coverslips were then washed three times with PBS, 5 min each with gentle rocking, and appropriate Alexa fluorescent secondary Abs were added (used at 1:500 dilution), again at room temperature for 2 h. Following three final wash steps in PBS and dH_2O, 5 min each, the coverslips were dried and mounted onto ethanol washed glass slides using mounting reagent. Control specimens were produced with the same protocol (1) without the use of any primary Abs or (2) without the use of any secondary Abs or (3) using only one primary Ab and probing with both secondary Abs. The slides were left to dry for 24 h at room temperature before storing at 4°C until required. To visualise the transfection efficiencies of recombinant RyR2 with cMyBP-C FL, the cells were imaged using an SP5 confocal microscope (Leica) with an oil immersion, x63 objective lens. The HEK293 cell expressing RyR2 and cMyBP-C were counted using LEICA software and obtained values were further normalized towards the total number of all cells present in selected field of view, represented as % transfection efficiency (see **Appendix, Figure 8.2**).

2.2.8 3D co-localisation analysis

Confocal images were acquired using a confocal Leica SP5 microscope (Leica, Heidelberg, Germany), with an oil immersion, x63 objective lens, and excitation lasers at 488 nm (PMT set at 500-550 nm) and 594 nm (PMT set at 600-700 nm). HEK293 with weakly fluorescent proteins were selected for analysis, to minimize any possible deleterious effect of RyR2 protein overexpression on the morphology and function of transfected cells. Based on 2D intensity histograms generated form single primary and both secondary Abs labelled control specimens, the range of settings for acquiring images were adjusted to fall within the response range of the system and to minimise the spectral cross-talk between channel 1 (Alexa 488) and channel 2 (Alexa 594). In selected settings, non-specific fluorescence from single-primary Ab controls generally accounted for <10% of mean fluorescent intensity, and autofluorescence levels in only-secondary Ab controls measured <5% of mean fluorescent intensity. All confocal images of the cells were acquired with 0.5 µm z-spacing and stored in 8-bit format for offline processing.

Next, using Leica Microsystems LAS-AF software, the threshold intensity values were defined for each cell, considering every singular layer of stack separately to discriminate between signal and background, with minimum of 40 grey levels signal threshold used for each channel (being equal to calculated non-specific signal, ~15% of mean fluorescent intensity). Except of adjustment of intensities to the full dynamic range, no further image processing was applied. Obtained thresholds were subsequently applied to imported z-stacks in IMARIS (Bitplane) for image analysis. The Coloc module of IMARIS was used to calculate and generate a new channel corresponding to the co-localised voxels (3D pixel volumes). Pearson's correlation coefficient of whole acquired field of view was calculated to describe the correlation of the intensity distribution between the two thresholded channel intensities being tested. To test for random voxel distribution, scrambled z-stack images were generated in IMARIS by (1) turning the channel 2 image by 90° versus channel 1 and (2) 3D shifting of 100 voxels the channel 2 in x-y plane and 5 voxels in z-plane, thus creating random voxel distribution with equal number of voxels and intensities. 40 new images were created in this way, 20% of the all images analysed (total of 224 z-stack images used in the co-localisation analysis). The images to be scrambled (10 z-stack images) were selected randomly form the original 184 z-stacks. The observed correlation between channel 1 and channel 2 were considered significant if they were greater than 95% of the correlation between channel 1 and scrambled channel 2 ($p \leq 0.05$). The statistical differences between the co-localisation results and scrambled images were calculated using unpaired, 2-tailed Student's t-test. In order to normalize the obtained % overlap to the cell volume, in Leica LAS-AF software, ROI was selected (representing the 2D area of cell at the maximum projection) and total number of 3D pixel intensities (0-255 grey levels) for each channel was calculated by multiplying by the number of z-stacks acquired for the given cell. These values were plotted versus number of total co-localised voxels from IMARIS to test for relationship between each channel pixel intensity values and number of co-localised voxels, Pearson's correlation coefficient was also calculated to assess the degree of correlation.

2.2.9 [^{3}H]ryanodine binding

[^{3}H]ryanodine binding assay was performed on cell homogenates obtained from HEK293 cells expressing recombinant RyR2 with or without full length (FL construct) cMyBP-C (prepared in triplicate). Prior to the assay, in order to have equal amounts of RyR2 protein in both samples expressing RyR2 alone versus RyR2 + cMyBP-C (n=3, prepared in pairs on three different days), RyR2 amounts were initially determined by WB and quantified by densitometry; they were subsequently evaluated by [^{3}H]ryanodine binding assay performed in the presence of 100 µM free Ca^{2+} and 10 mM caffeine (conditions promoting maximum channel activation and thus allowing to measure the total RyR2 content). The quantity of used homogenates was adjusted as required to have equal RyR2 content, and any discrepancies in total protein content were standardized to 600 µg of total protein with homogenate from untransfected HEK293 cells. For comparison of the general expression levels achieved using recombinant protein, 200 µg of pig cardiac SR was processed in parallel in the same assay as positive control, where it could be guaranteed that high RyR2 amounts are present.

Each reaction contained 600 µg of total protein and 8 nM [^{3}H]ryanodine and was prepared to a final volume of 500 µl using ryanodine binding buffer (containing the desired free Ca^{2+} concentration). Free Ca^{2+} content was calculated using MaxChelator software (http://maxchelator.stanford.edu./). For maximum channel activation, experiments were performed in the presence of 100 µM free Ca^{2+} and 10 mM caffeine. For estimation of channel activation at specific Ca^{2+} concentration, six Ca^{2+} concentration points were used: 100 nM, 250 nM, 500 nM, 1 µM, 5 µM and 100 µM. For estimation of non-specific binding, control samples were prepared (in duplicate) with 10 µM of ‘cold’ (non-radiolabelled) ryanodine. Following thorough mixing, all samples were incubated in a water bath at 37°C for 2h. Subsequently, 5 ml of ryanodine binding buffer was added to each sample and reactions were filtered through pre-soaked glass fibre filters and washed once with another 5 ml of ryanodine binding buffer, all under vacuum suction conditions. Each filter was placed into a scintillation vial and fully submerged in 5 ml of scintillation liquid. All samples were mixed and incubated overnight at room temperature, followed by the measurement of decays per minute (DCM) over a period of 2 min using Packard (Tri-Carb 2900TR) liquid scintillation analyzer. Analysis was performed in at least three separate biological samples each in technical replicates ($n \geq 3$) for each given Ca^{2+} concertation.

Subtraction of the non-specific counts obtained in control samples (in the presence of excess unlabelled ryanodine) from the total counts from the test samples was used to calculate specific [^{3}H] ryanodine binding (n=3 for specific and n=2 for non-specific for each tested point). The statistical difference between the cumulative RyR2 alone versus RyR2 + cMyBP-C activation results (n≥15 for each calcium point, after n=6 and n=7 outliers in total were removed, respectively, based on the values higher than 1.5x interquartile range) were calculated using unpaired, 2-tailed Student's t-test, with dose-response curves fitted with GraphPad Prism using a non-linear regression, four-parameter sigmoidal model with bottom constrained to 0. The two generated models (with or without cMyBP-C) were statistically assessed using the extra-sum of squares F test (GraphPad Prism). For summary of raw data analysis see **Appendix, Figure 8.7**.

2.2.10 Densitometry analysis

All image processing and densitometry analysis of Western blots were carried out using Quantity-one (Bio-Rad) software. First, background density of the X-ray film was subtracted from the density of the bands of interest. Subsequently, in order to correct for the potential differences in the expression level of input protein, optical density values obtained for co-immunoprecipitated proteins were normalised against the background and the amount of the input protein in the lysate (corresponding to 1/200th of the lysate volume processed in the co-IP sample). Statistical analysis was carried out using paired, 2-tailed Student's t-test (see **Section 2.2.11**) for specific co-precipitated protein and negative co-IP (non-specific) control. Comparison across the relative specific binding (calculated as the specific binding subtracted of the non-specific binding) of group of interest was assessed using either ANOVA or Kruskal-Wallis test (see **Section 2.2.11**).

2.2.11 Computer analysis and software

Microsoft Excel was used to store numerical data, while graph plotting (data expressed ±SD, standard deviation), fitting of sigmoidal curves and statistical analyses were carried out using GraphPad Prism (GraphPad Software Inc). Data were first subjected to Brown-Forsythe test for equality of group variances, and populations with equal variance (no significantly different standard deviations, *p*<0.05) were analysed using parametric tests: either Student's t-test (to determine if two sets of data are significantly different from each other) or ANOVA (with Bonferroni's post-test for multiple group comparison). For non-parametric data, Kruskal-Wallis test (with Dunn's post-test) was used instead of ANOVA. PyMOL (Molecular Graphic System) was used for protein structure visualisation and presentation, while remaining figures were prepared using Microsoft Power Point.

Chapter 3

Assessment of cMyBP-C as a potential binding partner for RyR2

3 Assessment of cMyBP-C as a potential binding partner for RyR2

3.1 Introduction

Up until recently, the possibility of direct link between cMyBP-C and Ca^{2+} regulation of cardiac contraction has not been investigated due to lack of biochemical evidence linking cMyBP-C with a Ca^{2+} signalling protein. The work of (Lu et al. 2012) combined fluorescence, NMR, and light and X-ray scattering to propose for the first time that cMyBP-C can participate in Ca^{2+} signalling pathways, evident via Ca^{2+} dependent interaction of the M-domain with calmodulin. This potentially could have consequences for synchronizing events between cMyBP-C and its binding partners during heart muscle contraction. Also, the recent data from two independent labs have suggested that phosphorylation of cMyBP-C may result in the formation of a calcium-binding motif within the M-domain (Colson et al. 2016; Previs et al. 2016), which previously has been proposed as a low affinity zinc binding site (Ababou et al. 2008), suggesting that phosphorylation and Ca^{2+} may antagonistically tune cMyBP-C function. Further, a new model of calcium activation of contraction has been proposed in which cMyBP-C, based on its the location in the C-zone, corrects the inhomogeneity in RyR2 released Ca^{2+} gradient across the sarcomere by sensitizing the contractile apparatus to calcium to ensure uniform force development across the sarcomere (Previs et al. 2015). In addition, in cMyBP-C KO models, impaired relaxation and altered Ca^{2+} transients have been reported (Song et al. 2003; Brickson et al. 2007; Pohlmann et al. 2007). Thus, cMyBP-C emerges as a multifaceted signaling node in cardiac myocytes that contributes to the maintenance of sarcomeric structure and regulation of systolic and diastolic function, with its precise role in relation to Ca^{2+} homeostasis yet to be determined.

Unpublished findings from our laboratory imply that cMyBP-C functionality might not be restricted exclusively to modulation of sarcomere cross-bridge kinetics, but is also relevant to the Ca^{2+} signalling toolkit, in particular to RyR2, the calcium release channel. This hypothesis is based on pilot data from Y2H and GST-pull down binding assays, where positive interaction was detected between truncated fragments of the human cMyBP-C C-terminus (817-1273 amino acids, CT) and the RyR2 N-terminus (1-906 amino acids, BT4L). Further analysis by co-IP assays indicated that the same synthetic cMyBP-C CT construct is capable of interaction with native RyR2 from solubilised cardiac SR vesicles (Zissimopoulos, unpublished data). Those preliminary results were the foundation of further investigation of putative cMyBP-C:RyR2 binding presented in this work. Since the originally detected interaction was observed between recombinant proteins/truncated fragments expressed in bacteria, yeast or cell-free systems (TNT, rabbit reticulocyte lysate), question remained whether the detected binding can be reproduced with the native and/or recombinant full-length proteins in a more physiological context.

The co-IP assay is a well-established method which involves the isolation of the native or recombinant protein of interest out of complex sample mixtures i.e. cell lysates, serum or tissue homogenates (Elion 2007; Kaboord and Perr 2008). An important consideration for co-IP assay is the choice and concentration of detergent to be included: higher concentrations and/or stronger detergents will substantially reduce non-specific binding but may also abolish protein-protein interaction, whereas lower concentrations and/or milder detergents may allow a weak interaction to be observed but could result in excessive non-specific binding. For this reason, in our experiments we used an intermediate strength detergent CHAPS at 0.5-1% concentration. Several optimizing approaches were employed to further reduce non-specific binding: (1) increase the number and/or duration of washes, and/or (2) use a neutral protein (e.g. bovine serum albumin, BSA) in the IP buffer to block non-specific binding sites, and/or (3) preclear the cellular lysate prior to incubation with protein-A resin alone, and/or (4) increase/reduce the salt content and/or detergent concentration in the IP buffer (Chi et al. 2003; Yang et al. 2008). In our experimental setting, the co-IP technique was used with the intention to determine the binding between the native proteins from animal heart tissue preparations, and once scored as positive, it was also used with recombinant human proteins, following co-expression in a heterologous mammalian system.

The benefits of using a mammalian cell line for protein expression are significant, since conformation, post-translational modifications and subcellular localization are likely to be similar to the native protein (Thomas and Smart 2005). Cloned RyRs have been heterologously expressed in various cell lines including CHO, COS-1 and

HEK293, with the latter being the most commonly used RyR2-deficient cell line (Takeshima et al. 1989; Chen et al. 1997; Du et al. 1998), for studies of recombinant, WT and mutant RyR2 function (Li and Chen 2001; Thomas et al. 2004; Jiang et al. 2005). HEK293 was generated by transfection of adenovirus DNA into normal human embryonic kidney cells (Graham et al. 1977) and despite epithelial in origin, the cells' biochemical machinery is able to reproducibly express large-scale, functional, recombinant proteins. The ability to efficiently express the protein of interest in a transient fashion in HEK293 cells by introduction of plasmid containing the cDNA for the protein of interest, depends on the selected transfection technique. One of the most widely used, and employed routinely in this study, is the calcium phosphate precipitation, based on spontaneous salt precipitation that occurs in supersaturated solutions (Jordan and Wurm 2004). The Co-IP assay using both native cardiac tissue and following transient expression in a HEK293 has been used extensively by the Lai laboratory i.e. to investigate oligomerization properties of RyR channel (Zissimopoulos et al. 2013; Zissimopoulos et al. 2014; Seidel et al. 2015) and to assess FKBP:RyR2 binding (Zissimopoulos and Lai 2005; Zissimopoulos et al. 2007; Zissimopoulos et al. 2012).

Since the DNA plasmids encoding cMyBP-C and RyR2 used in this study were both of human origin, the transfection efficiency of co-expressed proteins and their intracellular trafficking were assessed by immunocytochemistry experiments. However, observed severe changes in cell morphology induced by calcium phosphate transfection proved this approach to be unsuitable for co-localisation study. Instead, the commercial cationic polymer-based reagent TurboFect was used for small scale protein expression. The polymer forms positively-charged complexes with plasmid DNA that are both compact and stable. These complexes protect the DNA from degradation and facilitate efficient plasmid delivery into the cell, without any evident cytotoxic effect (Jordan and Wurm 2004; Thomas and Smart 2005).

Immunocytochemistry co-localisation analysis is often used to support the claim that two molecules are potential binding partners based on detection of their respective fluorescent signals in a very close physical location within the intact cell. The most common approach to co-localisation relies on 2D colour-coded pixel overlap, despite the fact that its scientific applicability is known to be frequently misleading (as it can be perceived differently by the eye). Therefore, the method applied in this study evaluates 3D co-localisation by objectively determining its quantitative characteristics (Pompey et al. 2013). Because it is conducted in three dimensions, observation of repeated coincidence of the two fluorescent probes in multiple regions throughout the cell volume increases the confidence that the two proteins occupy the same structure (Dunn et al. 2011). However, given that the optical resolution of confocal microscopy is <250 nm, these data should be only seen as support for our *in vitro* Co-IP results, rather than stand-alone evidence for protein-protein interactions occurring within atomic distance, as there may still be sufficient separation between molecules to prevent their binding. Another problem with confocal images analysis is the presence of considerable background fluorescence and/or auto-fluorescence levels (up to 30% maximum intensity), thus images of double-stained sections (with appropriate fluorescently-labelled Abs) must always be subjected to background correction prior to quantitative analysis to obtain reliable results. It includes the adjustment of all photomultiplier tubes to their respective channel intensities followed by the imaging of single-labelled control specimens. This allows to estimate a threshold value suitable for processing of double-labelled z-stack images, which corresponds to background and unspecific primary/secondary Abs binding captured by the confocal microscopy (Landmann and Marbet 2004).

The conducted mathematical investigation presented here utilizes microscopy image analysis software IMARIS, that calculates a percentage of fluorescent signal overlap together with Pearson's correlation coefficient (PCC) to quantify the degree of co-localisation occurring between two fluorophores. PCC is a standard statistical measure widely used in image correlation analysis and introduced to fluorescence microscopy by (Manders et al. 1993). It measures the intensity correlation based on voxel-by-voxel (voxel being the reconstructed 3D pixel volume) covariance in the signal levels of two images, which can give a PCC value between -1 and 1 (1 being perfect co-localisation, 0 random co-localisation, -1 anti-co-localisation). Because PCC subtracts the mean intensity from each individual voxel, it is independent of signal intensity levels and signal offset (background). Therefore, it can be measured in double-labelled images without any form of pre-processing, making it both simple and relatively safe from user bias. The square of PCC (denoted as r^2), also known as the 'coefficient of determination' was also used to aid the correlation analysis. It is a statistic that estimates the % fraction of variability in X that can be explained by its linear regression with Y (Adler and Parmryd 2010).

3.2 Chapter objectives

The current hypothesis tested in this study is that cMyBP-C C is capable of interaction with the SR-located RyR2 Ca^{2+} release channel. RyR2:cMyBP-C association could be physiologically relevant since cMyBP-C is known to dissociate form the sarcomere in its dephosphorylated form (**Section 1.3.4.1**), allowing cytosolic cMyBP-C to target RyR2. Therefore, cMyBP-C could provide a novel modulatory link between cardiac muscle contraction and SR Ca^{2+} release. The aim of this Chapter was to assess the sub-cellular cMyBP-C localisation and to biochemically test the putative cMyBP-C interaction with RyR2. Specifically, the following points will be discussed:

- the presence of cMyBP-C in sub-cellular fractions from animal cardiac tissue by Western blot analysis;
- detection of binding between the endogenous cMyBP-C and RyR2 proteins form animal cardiac tissue using the co-IP assay;
- verification of interaction between the full-length human recombinant proteins using the co-IP and ICC/3D co-localisation assays;
- assessment of initial findings that N-terminal region of RyR2 is responsible for cMyBP-C C-terminus binding using the co-IP assay.

3.3 Methods

3.3.1 cMyBP-C immunoblotting from different animal cardiac subcellular fractions

All animal cardiac tissue fraction samples were obtained from Dr S. Zissimopoulos (prepared as described previously by (Zissimopoulos et al. 2012)). Briefly, 200 g from one pig heart, 2 g from 16 mouse adult hearts (C57BL6/J), 2.5 g from three adult rat hearts (Wistar), 4 g from one adult rabbit heart (New Zealand white) were processed and ventricle muscle was homogenised in four volumes of homogenisation buffer (10 mM Na_2PIPES, 0.3 M sucrose, and protease inhibitors: 2 mM benzamidine, 0.2 mM AEBSF and 10 mM leupeptin, pH adjusted to 7.4) with the use of a blender. The obtained homogenate was centrifuged 100,000 xg for 1 h and collected supernatant represented the cytosolic fraction. Further, remaining pellet was re-homogenised in two volumes of homogenisation buffer and the SR fraction was prepared by sucrose density gradient centrifugation (collected at 30%–40% sucrose interface).

10% SDS-PAGE gels were made (**Section 2.2.2.4**) and 25 µl aliquots consisting of 50 µg of the homogenate/cytosol/SR from appropriate animal fractions were prepared with 5x reducing protein loading buffer and dH_2O. Subsequently, samples were loaded as follows: (1) pig, (2) guinea pig (G/P), (3) rat, (4) rabbit and (5) mouse. Following protein separation and transfer, immunoblotting analysis was carried out (**Section 2.2.2.5**) using cMyBP-C N-terminal and C-terminal specific antibodies (Ab N-t and C-t, respectively, see **Section 2.1.11**). Secondary anti-mouse and anti-goat HRP-conjugated Abs were used for protein visualisation using enhanced chemiluminescence detection.

3.3.2 Co-immunoprecipitation of endogenous cardiac proteins

Co-IP of native RyR2 and cMyBP-C from pig and rabbit cardiac muscle homogenates was performed using a diverse set of experimental conditions aiming to optimise the final result. For details of each experimental setting please refer to **Table 3.1**. The optimised version (**experiment 6**) was performed as follows: 8 mg pig cardiac homogenate was solubilised overnight with 0.5 % CHAPS and 100 µg/ml BSA in total volume of 1 ml. Concurrently, four 25 µl aliquots of pre-washed Protein A beads (supplemented with 100 µg/ml BSA) were incubated overnight with 10 µl of RyR2 specific Ab or 5 µl of non-immune Ab (2 µg each, Ab 1093 or normal rabbit IgG, respectively, see **Section 2.1.11**). The next day the insoluble material was removed by centrifugation at 20.000 xg for 10 min at 4ºC and the supernatant fraction was collected. 200 µl of pig lysate was incubated with beads-Ab complexes (~2 mg of lysate per IP sample) for 3 h and washed 2x for 10 min with BSA-supplemented IP buffer (**Section 2.2.2.3)**. Precipitated proteins were eluted with 5x reducing protein loading buffer and stored at -20ºC. The next day, samples were separated through 6% SDS-PAGE gels (**Section 2.2.2.4**) and subsequently the presence of co-precipitated native cMyBP-C (6 % gel) was tested by WB analysis (**Section 2.2.2.5**) using cMyBP-C Ab N-t or C-t (**Section 2.1.11**). In parallel experiments, successful precipitation of RyR2 was confirmed by immunoblotting with Ab 1093 (4%/0.5% agarose gel). Aliquots of lysate were also included in the gels to serve as molecular mass standard. The level of co-precipitated proteins was quantified by densitometry (**Section 2.2.10)** and statistical analysis was analysis conducted using GraphPad Prism (**Section 2.2.11**).

Table 3.1 A summary of experimental conditions undertaken in the immunoprecipitation of RyR2 and detection of cMyBP-C.

Exp.	Matrix	Protein precipitated	Amount of homogenate used per IP sample	IP buffer	Pre-clearing steps	Ab	Final washing steps
1	Protein A beads	RyR2	1 mg	150 mM NaCl, 20 mM Tris, 0.5% (w/v) CHAPS	n/a	1093 (2 µg)	2 x, 10 min
2	As above	As above	As above	20 mM NaCl, 20 mM Tris, 0.5% (w/v) CHAPS	n/a	As above	2 x, 15 min
3	As above	As above	As above	150 mM NaCl, 20 mM Tris, 1% (w/v) CHAPS	n/a	As above	2 x, 15 min

4	As above	As above	As above	150 mM NaCl, 20 mM Tris, 0.5% (w/v) CHAPS, 2 mM DTT	n/a	As above	3 x, 10 min
5	As above	As above	As above	150 mM NaCl, 20 mM Tris, 0.5% (w/v) CHAPS 100 µg/ml BSA	IP buffer	As above	2 x, 15 min
6	As above	As above	2 mg	150 mM NaCl, 20 mM Tris, 0.5% (w/v) CHAPS 100 µg/ml BSA	IP buffer	As above	3 x,10 min

Reciprocal co-IP experiments (direct precipitation of cMyBP-C and co-precipitation of RyR2) with use of Protein G beads and Ab C-t were unsuccessful as the Ab C-t proved to be not suitable for co-IP experiments, i.e. it did not precipitate cMyBP-C. Further, cMyBP-C precipitation with Ab N-t were also carried out, but despite significant amounts of cMyBP-C being precipitated, robust co-precipitated RyR2 band could not be detected (see **Section 3.4.2**). The same range of different experimental conditions (**Table 3.1**) were used in attempts to co-immunoprecipitate cMyBP-C from rabbit cardiac homogenate (2 mg per IP sample), and also from pig SR fraction (200µg per IP sample), however these proved also to be unsuccessful (see **Section 3.4.2**). It should be noted that while Ab N-t has been previously used by other labs in ICC (Barefield et al. 2014) and WB analysis of native cMyBP-C (Govindan et al. 2012; Barefield et al. 2014), Ab C-t has not been validated and was recommended only for cMyBP-C WB analysis (according to manufacturer’s guidelines), thus might explain the unsuccessful outcome of aforementioned native co-IP experiments with Ab C-t.

3.3.3 Generation of HA-tagged full length (FL) cMyBP-C construct

PCR amplification (**Section 2.2.1.1**) was used to generate the full length cMyBP-C coding sequence (33-3857 (b)) from a human cardiac muscle cDNA library using forward and reverse primers (HcMyBPC.FOR.27-56 and HcMyBPC.REV.3849-76, respectively, **Table 2.1**) designed to the human cMyBP-C cDNA (accession number:

X84075). Obtained product was cloned into HA-modified pCR3 vector and used for large scale plasmid isolation (for details, see **Sections 2.2.1.2-2.2.1.4,** and **2.2.3.1-2**).

3.3.4 Generation of the truncated HA-tagged N-terminal (NT) cMyBP-C construct

The NT cMyBP-C DNA fragment was obtained by PCR using previously made FL cMyBP-C construct as a template using appropriate forward and reverse primer (HcMyBPC.FOR.27-56 and HcMyBPC.REV.2611-30, respectively, **Table 2.1**). Obtained product was cloned into HA-modified pCR3 vector and used for large scale plasmid isolation (for details, see **Sections 2.2.1.2-2.2.1.4,** and **2.2.3.1-2**).

3.3.5 ICC and 3D co-localisation analysis

HEK293 cells were co-transfected using TurboFect transfection reagent with RyR2 and cMyBP-C FL plasmids (**Section 2.2.5.4**). Transfected cells were ICC processed (**Section 2.2.7**) and probed with RyR2 1093 and cMyBP-C N-t primary Abs together with Alexa Fluor 488 and 594 labelled secondary Abs (**Section 2.2.11)**, and 3D co-localisation analysis was performed as described in detail in **Section 2.2.8**.

3.3.6 Co-immunoprecipitation of recombinant human proteins

3.3.6.1 Recombinant full-length proteins

To assess the interaction between the recombinant human RyR2 and cMyBP-C, HEK293 cells were co-transfected using calcium phosphate transfection (**Section 2.2.5.3**) with the two plasmid constructs: RyR2 and the cMyBP-C HA-tagged FL (at 3:1 molar ratio, with 24 µg DNA in total per dish). Co-immunoprecipitation was performed as described in **Section 2.2.2.3**. RyR2 specific antibody or non-immune Ab (rabbit polyclonal Ab 1093 and normal rabbit IgG, see **Section 2.2.11**) were used to immunoprecipitate RyR2 (**Section 2.2.2.3)** and tested by Western Blot analysis (**Section 2.2.2.5**) using mouse monoclonal HA antibody (Ab HA, see **Section 2.2.11**). In parallel experiments, successful precipitation of RyR2 was confirmed by WB analysis with RyR2 specific mouse monoclonal antibody P12 (**Section 2.2.11)**. The level of co-precipitated proteins was determined by densitometry (**Section 2.2.10)** and statistical analysis was analysis conducted using GraphPad Prism (**Section 2.2.11**).

Reciprocal co-IP experiments with direct precipitation of cMyBP-C FL (with Ab HA) were also attempted, but in those we failed to detect significant co-precipitated RyR2 amounts (immunoblotting with Ab 1093) (see **Section 3.4.4**), similarly to previously attempted native reciprocal co-IP experiments (**Section 3.3.2**).

3.3.6.2 Recombinant truncated protein fragments

To assess the interaction between recombinant human RyR2 constructs (c-Myc-tagged BT4L or BT7) and the HA-tagged cMyBP-C constructs (NT, FL or CT), HEK293 were co-transfected using calcium phosphate transfection (**Section 2.2.5.3**) with the RyR2:cMyBP-C pair of interest (at approximate 1:1 molar ratio, with 24 µg DNA in total per dish). Co-immunoprecipitation was performed as described in **Section 2.2.2.3**. Rabbit polyclonal HA antibody (**Section 2.2.11**) and protein A Sepharose beads were used to immunoprecipitate the cMyBP-C protein fragment, while the mouse monoclonal c-Myc Ab (**Section 2.2.11**) was used in WB to detect the presence of co-precipitated RyR2 protein fragment and assessed by densitometry (**Section 2.2.10)** and statistical analysis was analysis conducted using GraphPad Prism (**Section 2.2.11**).

3.4 Results

3.4.1 Native cMyBP-C can be detected in pig, guinea pig and rabbit cardiac fractions with both cMyBP-C antibodies.

Cardiac fraction preparations from 5 different animal species were used to screen for cMyBP-C expression in order to assess its presence in the homogenate and cytosolic and SR compartments. Since the coding sequence for extreme N-terminus and C-terminus of cMyBP-C appears to be highly conserved amongst the different mammalian isoforms (for homology comparison of each region see **Appendix**, **Figure 8.1**), it was expected that both Ab N-t (raised against the N-terminus of cMyBP-C of human origin, amino acids 1-120) and Ab C-t (raised against recombinant mouse cMyBP-C, amino acids 988-1100) would detect cMyBP-C in all animal samples tested. The predicted size of a band corresponding to the wild type cMyBP-C for all species is ~140 kDa. As shown in **Figure 3.1**, **panel A**, cMyBP-C was successfully detected following immunoblotting (n=3) with the N-t Ab from pig and rabbit homogenates equally well, while in lesser extent from guinea pig (G/P) and with the weakest signal for mouse and rat homogenates. The C-t Ab was able to detect cMyBP-C from all tested homogenates (**Figure 3.1**, **panel B**), with somewhat weaker signal for guinea pig, probably due to general lower abundance of cMyBP-C in this species, in line with N-t Ab immunoblotting results. Overall, highest expression for full-length cMyBP-C was observed in pig and rabbit obtained with both N-t and C-t Abs. The N-t Ab was found to cross-react with additional lower molecular mass protein bands, especially in rat and mouse, whereas the C-t Ab was very specific for cMyBP-C irrespective of species. In the case of pig, additional bands were present at

30 and 40 kDa when probed with N-t Ab (**Figure 3.1**, **panel A1**), probably due to cMyBP-C degradation products and/or Ab non-specificity.

In terms of cMyBP-C presence in the cytosol, rather surprisingly, both N-t and C-t Abs detected the ~140 kDa band corresponding to full-length cMyBP-C in all five species tested. The amount of cMyBP-C detected in the cytosolic fraction, which was prepared by ultra-centrifugation at 100,000 xg for 1 h to pellet microsomal membranes and contractile sarcomeric components, was in fact equivalent to that seen in whole cell homogenate. This suggests that cMyBP-C is normally found in the cytosol or it easily dissociated from the sarcomere (i.e. during this preparation). The results obtained for cMyBP-C presence in the SR were species dependent, but there was a general agreement between N-t and C-t Abs. High levels of full-length cMyBP-C (~140 kDa band) was detected in pig SR WB, whereas its levels in mouse and rat cardiac SR were negligible. In particular, cMyBP-C levels found in the five species tested were in the following order: pig >> guinea-pig > rabbit > mouse ≈ rat. The SR was prepared by sucrose density gradient centrifugation of microsomal membranes,

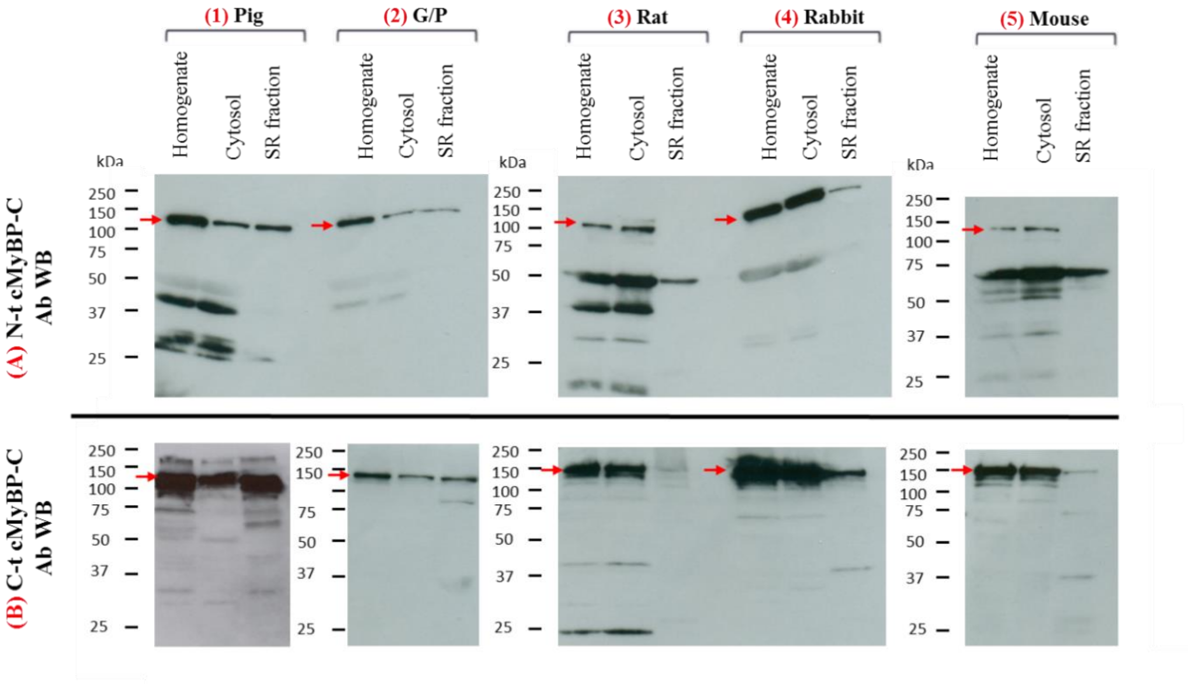

Figure 3.1 Representative blots of cMyBP-C distribution in different animal subcellular fractions. 50 µg of homogenate, cytosol and SR fraction per each lane was loaded onto 10% SDS-PAGE gels and probed using Ab N-t (A, upper panel) or Ab C-t (B, lower pane) (n=3 for all tested samples). The following animal cardiac tissues were used (columns from left to right): (1) pig, (2) guinea pig (G/P), (3) rat, (4) rabbit and (5) mouse. Band of ~140 kDa corresponding to full-length cMyBP-C was detected in all animal fractions (red arrows), except of rat and mouse SR N-t Ab WB.

however contamination by contractile sarcomeric components cannot be excluded. Nonetheless, the presence of cMyBP-C in the SR, where RyR2 is located, could enable the interaction between the two proteins. Based on the obtained results, it was decided to proceed for *in vitro* co-IP experiments with pig and rabbit cardiac muscle homogenates, as they scored for the highest cMyBP-C detection using both antibodies.

3.4.2 Endogenous cardiac cMyBP-C and RyR2 are capable of *in vitro* interaction

To determine the physiological relevance of the RyR2:cMyBP-C association, co-IP experiments were performed using pig or rabbit cardiac muscle homogenates. RyR2 was immunoprecipitated with 1093 Ab and the presence of co-precipitated cMyBP-C was analysed by WB using C-t Ab. Due to low expression levels of RyR2 and difficulty of purification compared to skeletal muscle RyR1 preparations (Lanner et al. 2010), the task of obtaining sufficient quantities of native RyR2 by direct immunoprecipitation proved difficult. At the same time, there were problems with high non-specific binding for cMyBP-C. To overcome these issues, several optimising steps were taken, detailed in **Table 3.1**. Best results were obtained when the amount of pig homogenate used was increased two fold (from 1 mg to 2 mg). RyR2 immunoprecipitation was performed in the presence of BSA and with introduction of Protein A beads pre-clearing steps. This optimised protocol (**Table 3.1**; **experiment 6**) allowed for a successful direct immunoprecipitation of RyR2 and cMyBP-C co-precipitation (560 kDa and 140 kDa immunoreactive bands, respectively). We could not obtain significant detection of cMyBP-C with N-t Ab for WB, due to the lower sensitivity of this Ab compared to C-t Ab (see **Figure 3.1**).

Representative pig homogenate blots are shown in **Figure 3.2**. By applying the optimised conditions, cMyBP-C (~140 kDa) was successfully recovered from RyR2 IP following WB with C-t Ab (**Figure 3.2 A, 2nd lane**) but not in the negative control using non-immune rabbit IgG (3rd lane). As shown in **Figure 3.2 B**, a control WB for RyR2 detection, low amounts of RyR2 were directly precipitated in the Ab 1093 IP (2nd lane) as expected, with no detectable non-specific binding (3rd lane). Co-precipitated cMyBP-C protein band was considerably less intense than that of input lysate (1st lane for both A and B), indicating weak RyR2:cMyBP-C interaction. Quantitative analysis (n=7) by densitometry (**Figure 3.2 C**) shows that the observed difference (approximately 20% higher) between specific and non-specific binding was statistically significant ($p \leq 0.05$, compared using paired, 2-tailed Student's t-test, n=7), indicating that native pig RyR2 is capable of cMyBP-C interaction.

Unfortunately, reciprocal co-IP experiments i.e. direct precipitation of cMyBP-C and testing for RyR2, failed to detect RyR2. The reason was simple in the case of the C-t Ab, since this Ab could not directly immunoprecipitate cMyBP-C, but not obvious in the case of N-t Ab, which resulted in reasonably high amounts of cMyBP-C being precipitated. The most likely explanation is that cMyBP-C exists in a large cytoplasmic pool (see **Figure 3.1**) and only a small proportion of it is associated with RyR2 in the SR compartment. Therefore, when immunoprecipitating cMyBP-C first, the RyR2-bound proportion is further diluted and co-precipitated RyR2 may be beyond the levels of WB detection. Further, despite several attempts with different experimental conditions, obtaining meaningful co-precipitation of cMyBP-C in direct RyR2 IP from rabbit homogenate was not possible due to much higher amounts of observed non-specific binding in this species compared to pig.

In order to improve the signal of co-precipitated cMyBP-C in direct RyR2 IP from pig, it was speculated that co-IP experiments using the SR fraction would help. The reasoning was that the increased concertation of RyR2 in the SR compared to whole cell homogenate will enable higher amounts of cMyBP-C being co-precipitated, especially from pig SR found to have the highest amount of detected cMyBP-C (**Figure 3.1**). Contrary to expectations, cMyBP-C and RyR2 exhibited only occasional binding which failed to reach statistical significance (n=3), possibly because of lower cMyBP-C abundance in the SR fraction compared to homogenate, which might alter the native RyR2:cMyBP-C interaction and accelerate dissociation rates. As the rate of the binding is proportional to the concentrations of the reactants, at equilibrium, the rate of RyR2:cMyBP-C complex formation is equal to the rate of dissociation into its single components. Thus, higher RyR2 availability is SR sample, without simultaneous increase in concentration of cMyBP-C, will not result in greater propensity of the complexes formation, but rather a lower binding will be observed due to lower amount of cMyBP-C available for the interaction. Due to this

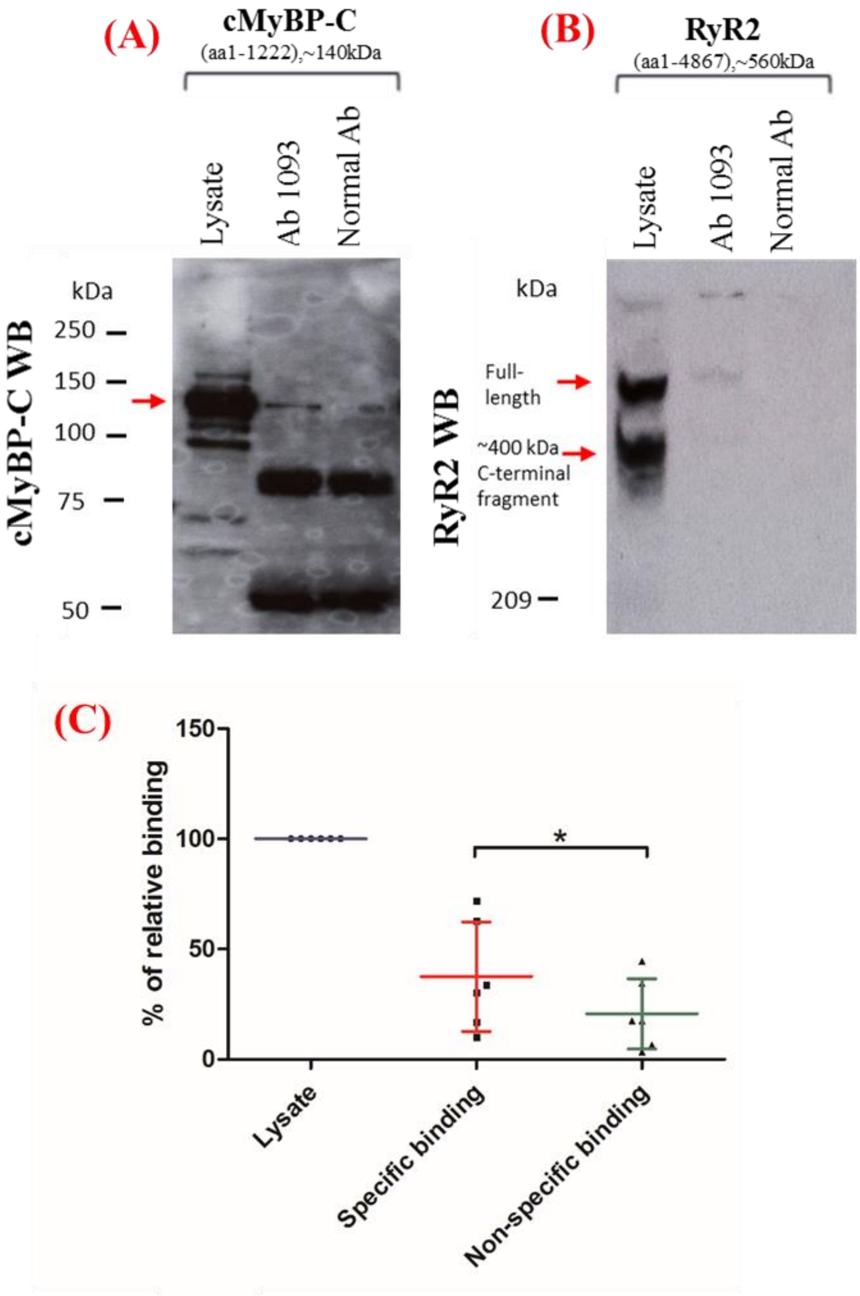

*Figure 3.2 Representative blots of Co-IP and WB results illustrating native RyR2:cMyBP-C interaction and cumulative densitometry analysis. (A-B) RyR2 was immunoprecipitated from cardiac pig homogenate (2 mg per IP lane) and the presence of associated native cMyBP-C were analysed (A: 6% gel). The loading controls represent 1/200th and 1/10th of the processed sample for (A) and (B), respectively. The intense dark bands at ~100 kDa and ~50kDa of the blot in panel A are the IgG heavy chains of the immunoprecipitating Ab1093. In parallel experiment, the presence of directly precipitated RyR2 was also analysed (B: 4%/0.5% gel). Bands corresponding to native cMyBP-C (~140 kDa) and RyR2 subunit (~560 kDa) are shown (red arrows). RyR2 is partially cleaved by the endogenous calpain protease to generate a ~400 kDa C-terminal fragment as indicated (black arrow). The amino acids coordinates are for pig cMyBP-C isoform ([Sus scrofa] (accession number: XP_013849807.1) and RyR2 C ([Sus scrofa] accession number: XP_013838665);(C) Densitometry analysis of native RyR2 and cMyBP-C binding in co-IP assay from pig heart homogenate. Percentage of relative binding corrected for the difference in expression levels are presented relative to lysate input (1/200th of the processed sample). Data are shown as mean ±SD, n=7; * statistical significance at $p<0.05$ calculated using paired, 2-tailed Student's t-test*

experimental variability, the native-based co-IP approach was not pursued further and instead the recombinant mammalian expression system was employed. It was hypothesised that native cMyBP-C binding might be affected by the presence of other RyR2-associated proteins, thus assessment of binding between recombinant human proteins would help to further verify the results obtained from native tissue.

3.4.3 Generation of HA-tagged cMyBP-C constructs

Both plasmid DNA constructs designed to express full length and the N-terminal part of cMyBP-C (FL and NT, respectively, see **Table 3.2**) were successfully generated and their DNA sequences were confirmed. A typical set of results representing intermediate steps of the cloning process is shown in **Figure 3.3**

Table 3.2 List of cMyBP-C constructs and restriction nucleases used. Coordinates correspond to the human cMyBP-C mRNA, accession number: X84075.

Construct	Coordinates	Length	PCR primers	Cloning sites
cMyBP-C CT	2483-3857 (b) 817-1274 (aa)	374 (b) 456 (aa)	-	*EcorI* *XhoI*
cMyBP-C FL	33-3857 (b) 1-1274 (aa)	3824 (b) 1273 (aa)	HcMyBPC.FOR.27-56 HcMyBPC.REV.3849-76	*BamHI* *XhoI*
cMyBP-C NT	33-2630 (b) 1-866 (aa)	2597 (b) 866 (aa)	HcMyBPC.FOR.27-56 HcMyBPC.REV.2611-30	*BamHI* *XhoI*

3.4.4 Recombinant human full-length RyR2 and cMyBP-C can be successfully co-expressed in HEK293 cells.

In order to assess the interaction between recombinant human proteins, HEK293 cells were used, an immortalised cell lineage that do not express endogenous RyR2 nor cMyBP-C. Immunofluorescence analysis was first conducted to confirm that recombinant proteins were co-expressed within the same co-transfected cell and correctly localised *in vivo*. Both proteins were expressed to a levels clearly distinguishable from the background and yielded similar transfection efficiencies (~20%) as illustrated in **Figure 3.4** and **Appendix, Figure 8.2**. Low transfection number was expected, and was linked to (1) low cell plating density, (2) poor RyR2

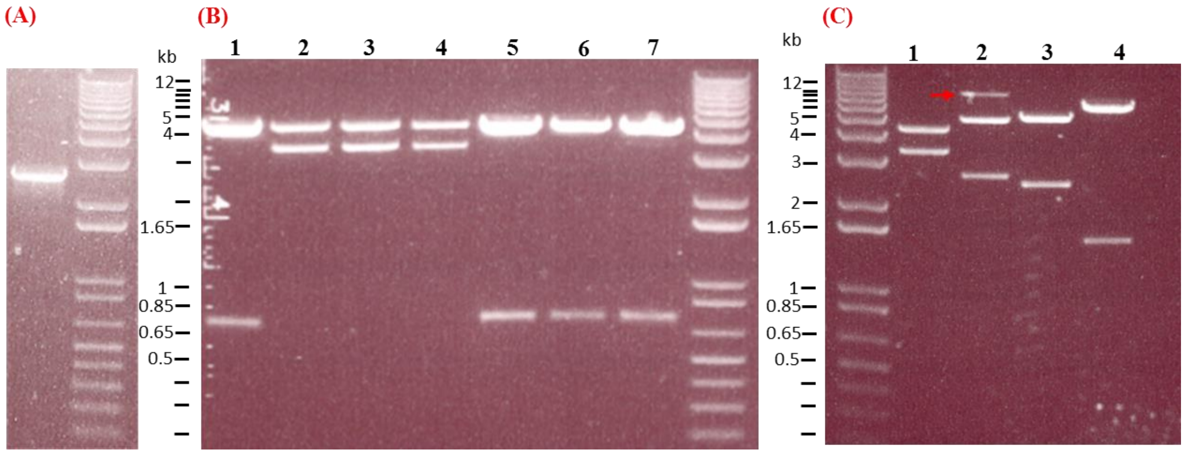

Figure 3.3 Intermediate steps of the experimental procedure generating the cMyBP-C NT construct. (A) DNA gel showing the amplification product obtained in the PCR amplification (expected band: 2.6 kb); (B) DNA gel showing indicative digest of clones following bacteria transformation with the ligated PCR product and the pCR3 vector (1-7: restriction digest of plasmid DNA preparations obtained from seven clones and cut with SpeI/XhoI, expected bands:3.3 and 4.4 kb as seen in 2,3 and 4); (C): restriction digest of the selected positive clone verified by sequencing. From left to right: Lane 1: SpeI/XhoI (expected bands: 3.3 and 4.4 kb), 2: BamHI/XhoI (expected bands: 2.6 and 5.1 kb), 3: ApaI (expected bands: 1, 2.4 and 5.3 kb), 4: SmaI (expected bands:1.5 and 6.2 kb). The partially digested plasmid in (C) 2 is shown with red arrow.

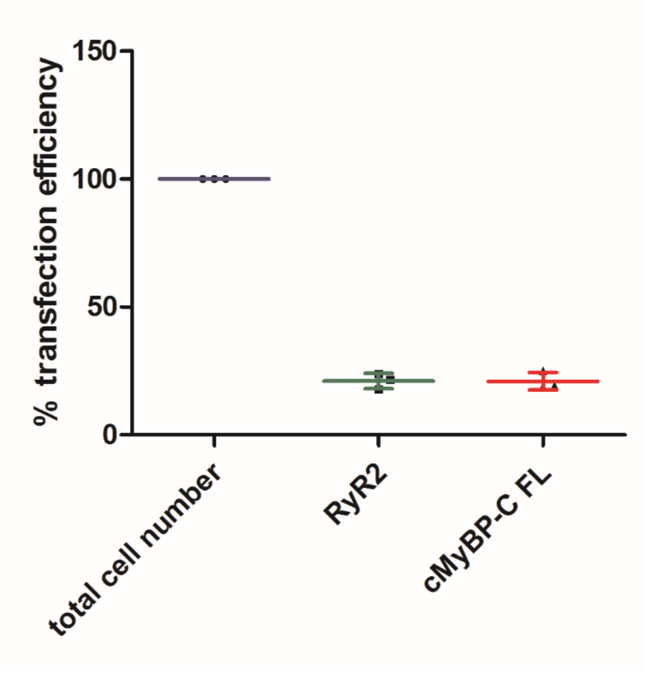

Figure 3.4 Comparable transfection efficiencies of HEK293 cell populations expressing RyR2 and cMyBP-C, assessed with LEICA software. The transfection efficiencies of RyR2 and cMyBP-C were obtained by qualitative determination of number of positive cells (showing detectable fluorescent signal for either cMyBP-C or RyR2) within selected field of view and normalized towards the total number of cells present in given view. Data are shown as mean ±SD, n=3 populations, in average 28 cells in each field of view were analysed.

plasmid uptake by HEK293 cells and (3) lower amount of cMyBP-C FL plasmid used for co-transfection (to yield comparable protein levels to RyR2).

Nevertheless, a high number of co-transfected cells was obtained, labelled both green (for RyR2) and red (for cMyBP-C), calculated to be ~88% of all transfected cells. **Figure 3.5 A** and **A'** shows a representative pair of images acquired from an identical field of view, visualising the level of non-specific signal present in the processed images of co-transfected cells (labelled with both primary and secondary Abs, 1093 + 488 and N-t + 594, for RyR2 and cMyBP-C, respectively). In order to easily distinguish the specific signal from non-specific (calculated as <15% of mean fluorescent intensity) from the background, the image intensity palette width in each image was adjusted form original 0-255 grey levels (8-bits colour depth) to the full dynamic range (**A**) or to the lower intensity range, causing over-saturation of the specific signal (**A', dashed region**). Panels **B** and **C** show representative field of views acquired from co-transfected control specimens with the use of only one primary Ab at time (either N-t only, as in **B**; or 1093 only, as in **C**) and both secondary Abs (488 and 594), again with intensity palette adjusted as in (**A'**). Generally, fluorescence detected in those images was <10% of mean fluorescent intensity for un-labelled protein, either due to low levels of green autofluorescence (**B, Ab 488 panel**), or green to red cross-talk between fluorophores (**C, dashed region**) or non-specific binding of primary Abs (**B, cMyBP-C panel** and **C, RyR2 panel**), whereas green autofluorescence levels in no-primary, double labelled secondary Abs control was measured as <5% of mean fluorescent intensity for green channel (**D, Ab 488 panel**). No detectable red autofluorescence was obtained (**D, Ab 594 panel**).

As demonstrated in **Figure 3.6**, RyR2 (green) signals could be detected throughout the ER of the transfected HEK293 cells, both surrounding the nuclear envelope and extending towards the peripheral part of the cell (**A-C, RyR2 panel**). On the other hand, cMyBP-C (red) signal was found to be distributed throughout the cytoplasm (**A-C, cMyBP-C panel**), with significant cMyBP-C expression being detected in peripheral lamellipodia (**D, white arrows**). Interestingly, cMyBP-C signal could not be detected in the cytoplasmic region spanning from bottom side of the nucleus to the areas of the cell surface in direct contact with the coverslip (**D, dashed box**), either due to cMyBP-C not being well expressed in this site or due to failure of N-t Ab to reach the cMyBP-C epitope. A proportion of cMyBP-C also seemed to co-localise

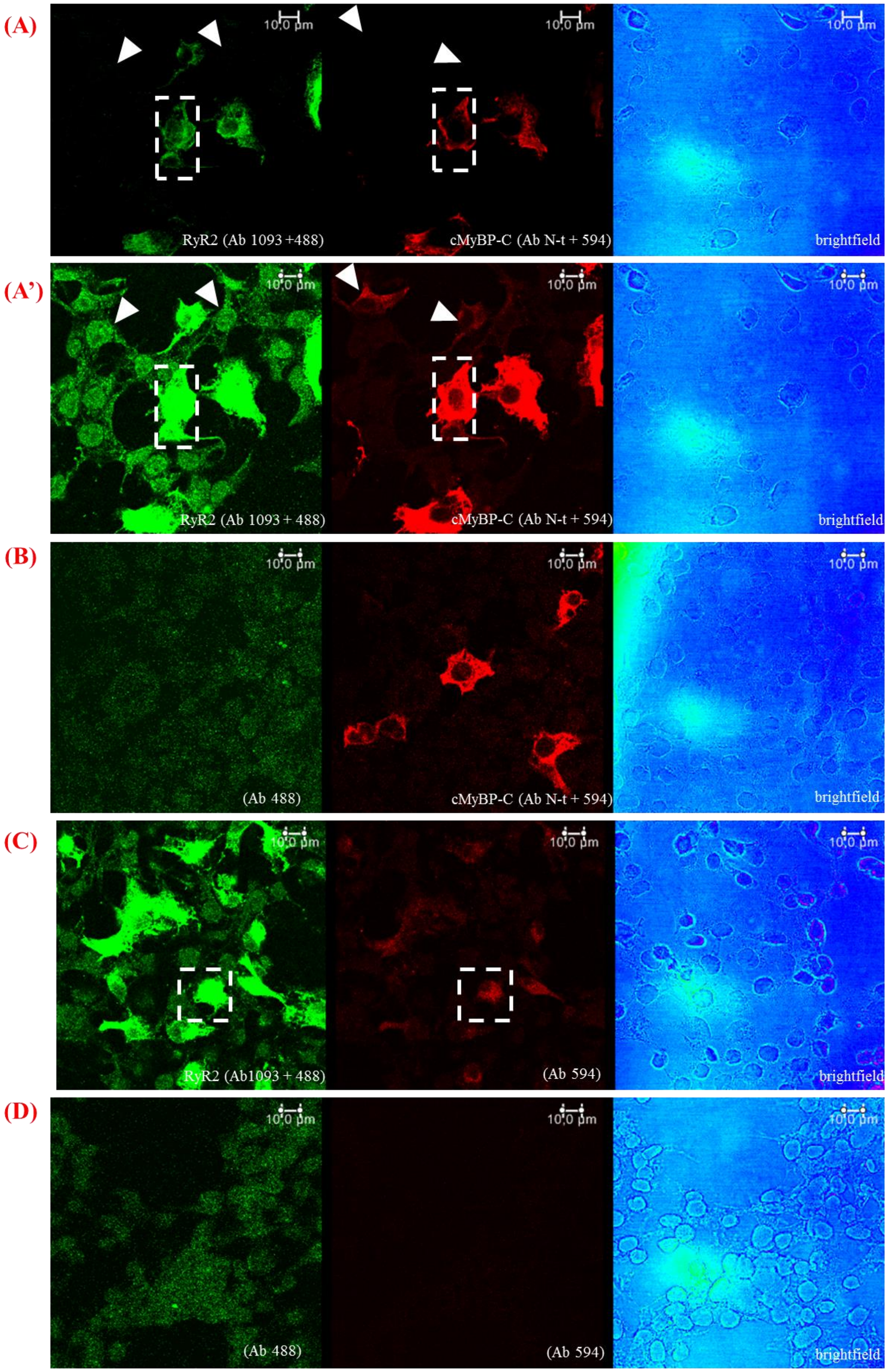
(A)
10.0 µm
RyR2 (Ab 1093 +488)
cMyBP-C (Ab N-t + 594)
brightfield
(A')
RyR2 (Ab 1093 + 488)
cMyBP-C (Ab N-t + 594)
brightfield
(B)
(Ab 488)
cMyBP-C (Ab N-t + 594)
brightfield
(C)
RyR2 (Ab1093 + 488)
(Ab 594)
brightfield
(D)
(Ab 488)
(Ab 594)
brightfield

Figure 3.4 (previous page) Imaging of RyR2 co-expression with cMyBP-C in co-transfected HEK293 cell populations(A-D); (RyR2) RyR2 green signal detection, (cMyBP-C) cMyBP-C red signal detection and (brightfield) corresponding bright field image. (A and A') typical field of view of cells labelled with Ab 1093 and Alexa Fluor 488 and Ab N-t and Alexa Fluor 594. (A) representative image used for co-localisation analysis and (A') corresponding image with intensity level adjusted to show the non-specific signal. Compare arrows pointing to cells without detectable green signal and red signal in A versus the same cells in A'. Dashed regions indicate cell used for co-localisation analysis. (B) typical field of view of cells labelled with Alexa Fluor 488 and Ab N-t and Alexa Fluor 594, or (C) Ab 1093 and Alexa Fluor 488 and Alexa Fluor 594 or (D) Alexa Fluor 488 and Alexa Fluor 594, all (B-D) images had LUT table adjusted as in (A') to show the non-specific signal. Dashed boxes in C show the cross-talk between the green and red channel.

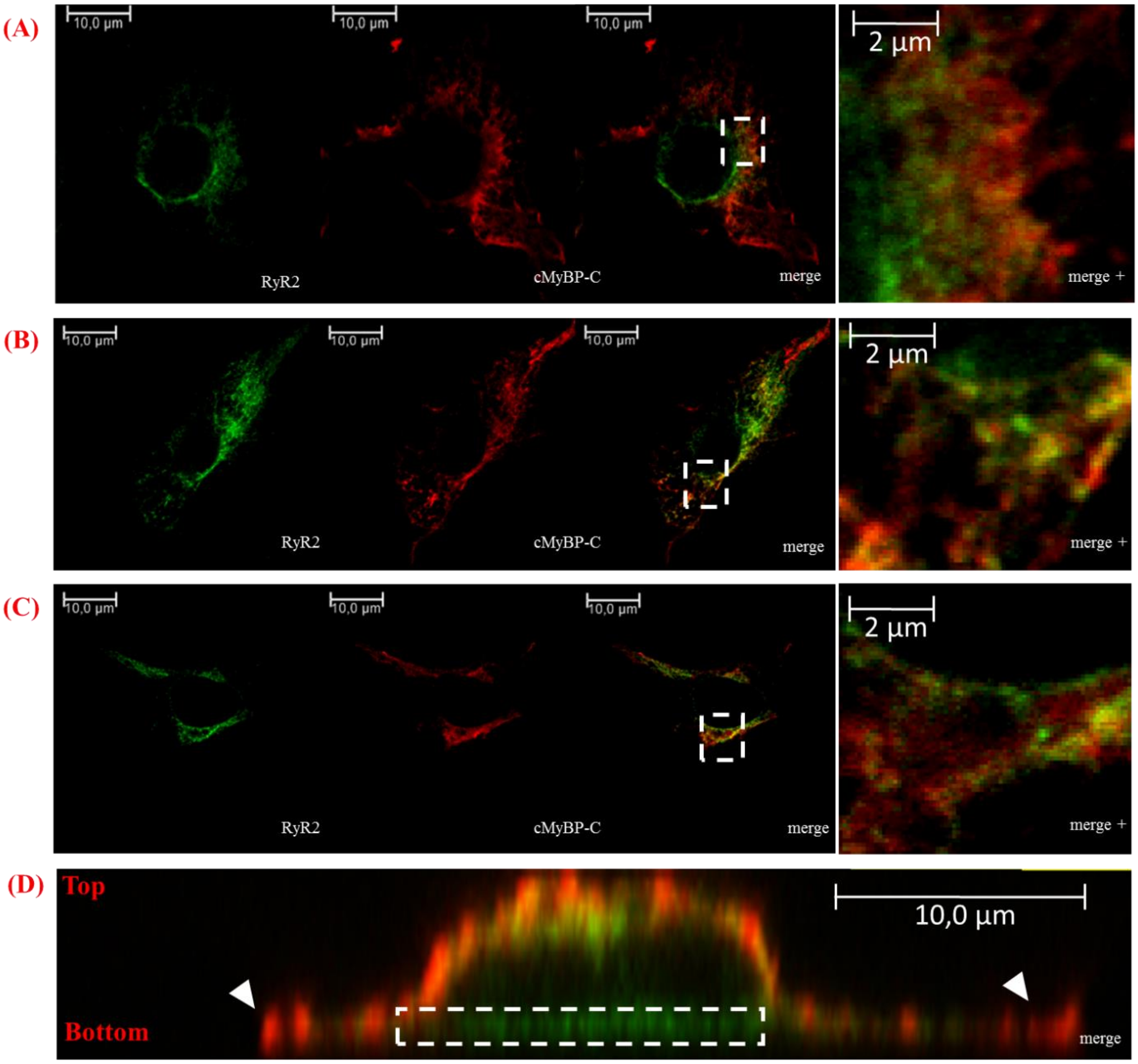

Figure 3.6 2D (x-y) slice representation of the immunofluorescence images of RyR2 and cMyBP-C localisation within the co-transfected HEK293. Shown are typical fields of view of three individual cells (A-C), taken in the middle of z-axis direction. (RyR2) detection of RyR2 with Ab 1092 and Alexa Fluor 488, (cMyBP-C) detection of cMyBP-C with Ab N-t and Alexa Fluor 594, (merge) overlay images and (merge +) higher magnification of dashed box region from (merge). (D) Higher magnification image of the orthogonal section (z axis) from (C), dashed box indicates region where no red cMyBP-C signal could be detected; white arrows show distal cMyBP-C distribution. Yellow colour shows RyR2 and cMyBP-C pixel overlap, and is indicative of co-localisation.

with RyR2, visible as yellow signal from green and red overlap (**A-C**, merge and merge +).

3.4.5 Recombinant human RyR2 and cMyBP-C co-localise in HEK293 cells

To quantify the degree of co-localisation in 3D cell volume, IMARIS software Coloc module was used, as outlined in following **Section 3.3.5**. Fluorescence labelling of RyR2 and cMyBP-C using secondary Alexa Fluor Ab enabled the degree of co-localisation between the two recombinant proteins to be calculated. The extent of Alexa 488 green channel (RyR2) and Alexa 594 red channel (cMyBP-C) 3D co-localisation was quantified from confocal fluorescence image z-stacks and used to generate a new channel corresponding to the co-localised voxels (**Figure 3.7**).

Consistent with simple 2D observations shown above, most of RyR2:cMyBP-C voxel overlap was identified in proximal ER regions (through the body of the cell but not immediately adjacent to the nucleus), with very little signal detected in distal regions and in the space between the bottom of peri-nuclear membrane and cell attachment site. Summary and statistical analysis of IMARIS generated results is presented in **Figure 3.8**. Overall, 2.04% total voxel co-localisation could be detected in the total z-stack volume being assessed, which corresponded to 4.82% of cell volume (after normalisation to each respectable cell size, **A** and **H**). Importantly, this analysis demonstrated that 71.4% of total green (RyR2 signal) voxels present in the dataset (**B**) and 73.3% of total green intensity material (**E**) is co-localized with 29.9% of total red (cMyBP-C signal) voxels (**D**) and 34.62% of total red intensity material (**F**), respectively. The PCC intensity correlation analysis was performed to detect the synchrony of the two proteins and scored for PCC= 0.68 (**G**) and, r^2 =0.46, which can be interpreted as positive co-localisation between RyR2 and cMyBP-C (PCC value of 1 for full co-localisation) with 46% of RyR2 and cMyBP-C follow perfect linear regression. All assessed parameters were statistically significant when compared to their non-specific counterparts obtained from scrambled images (calculated using unpaired, 2-tailed Student’s t-test, **Figure 3.8**), i.e. with values of 0.75% total voxel co-localisation, PCC=0.25 (**G**) and r^2 =0.06 were calculated for non-specific co-localisation results.

Further, obtained data were not dependent on region of interest selection (the approximate size of cell, $r^2 = 0.001$, PCC= 0.04, **Figure 3.9, A**). Weak correlation was detected for co-localisation results with either green channel intensity (relative RyR expression, $r^2 = 0.12$, PCC= 0.35, (**B)**) or red channel intensity (relative cMyBP-C expression, $r^2 = 0.18$, PCC= 0.43, **(C)**). It can be interpreted as 12% of green signal and 18% of red signal fraction of variability, respectively, that can be explained by linear regression with co-localisation result.

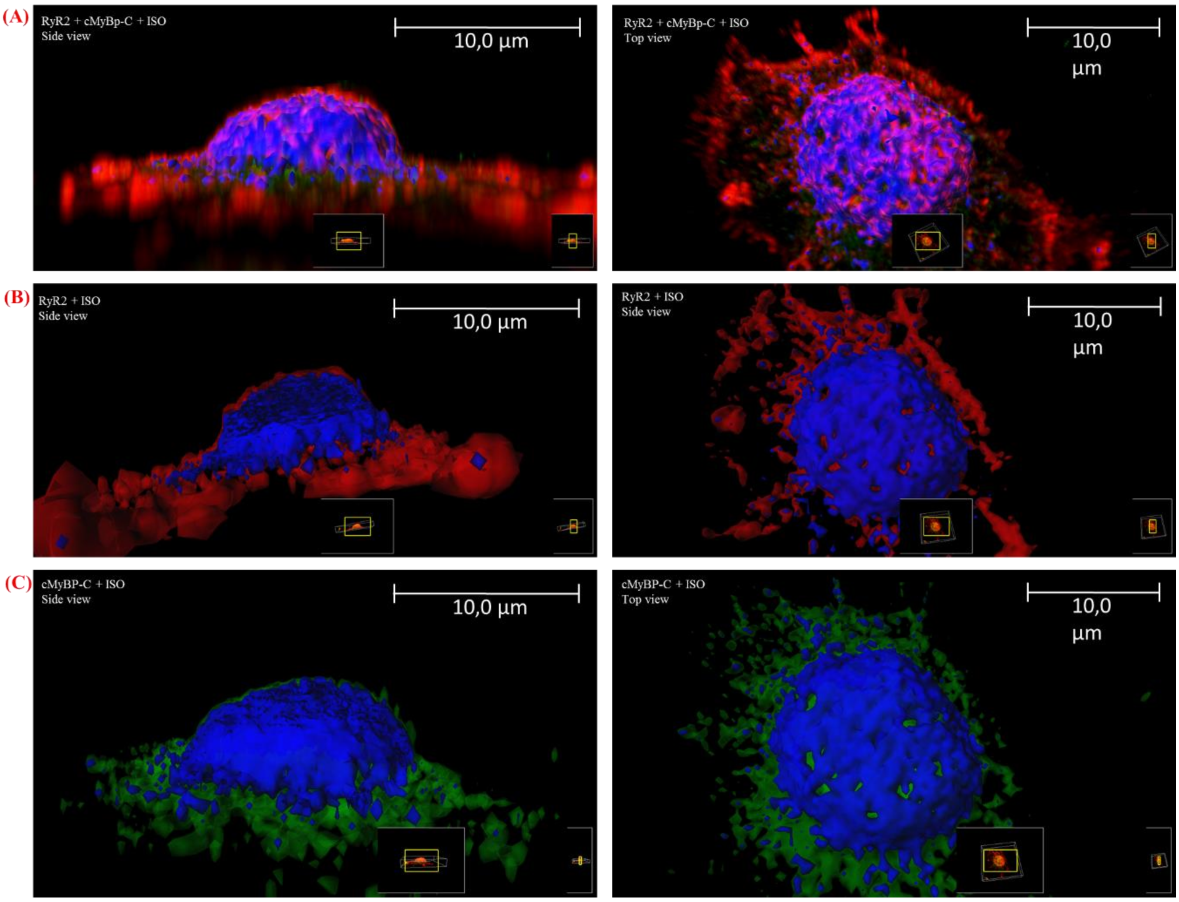

Figure 3.7 Visualisation of RyR2 and cMyBP-C partial co-localisation. (A) side and top view of 3D maximum intensity projection of RyR2 (green) and cMyBP-C (red) signal overlay, with IMARIS generated isosurface (ISO, in blue) corresponding to co-localised region; (B) side and top view of 3D projection of IMARIS generated isosurface corresponding to cMyBP-C signal (red) and co-localised region (ISO); (C) side and top view of 3D projection of IMARIS generated isosurfaces corresponding to RyR2 signal (green) and co-localised region (ISO).

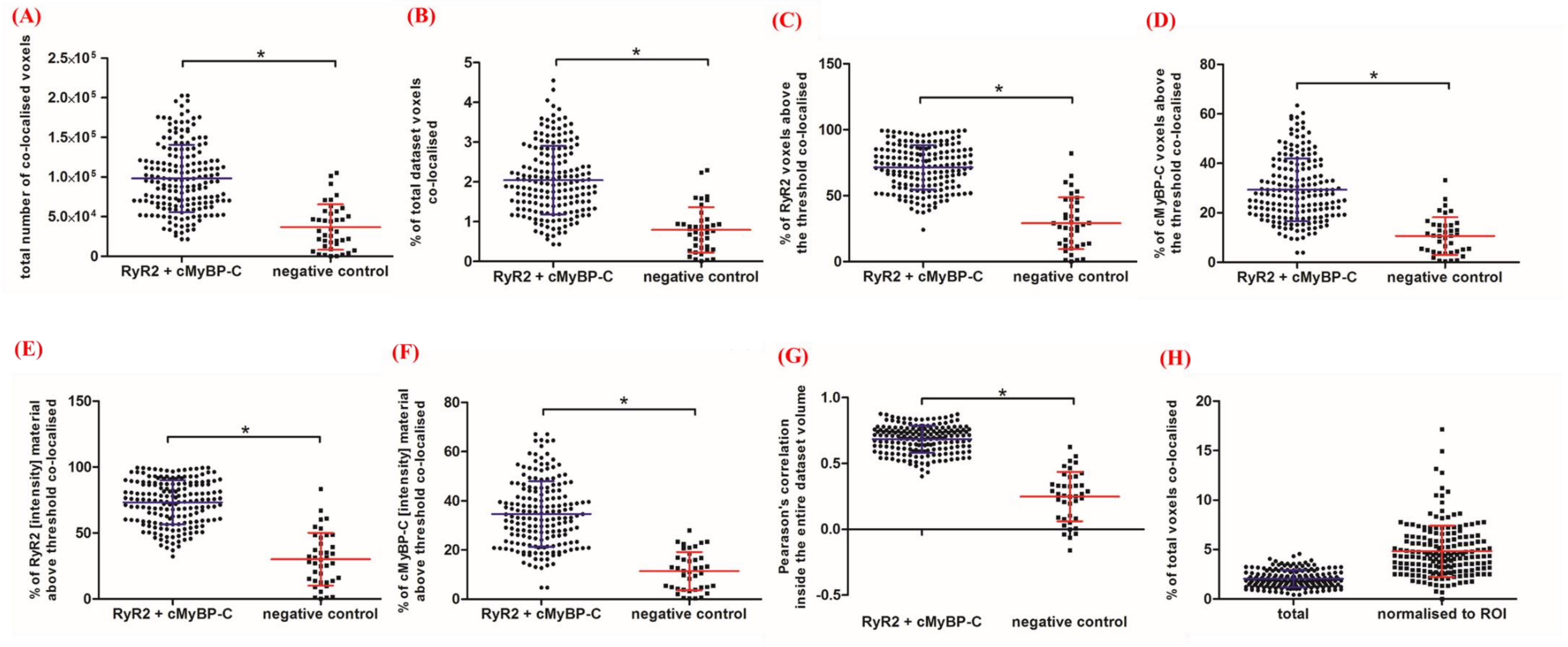

*Figure 3.8 Summary of IMARIS generated results of RyR2 and cMyBP-C co-localisation. (A-H) Data are shown as mean ±SEM, Samples: RyR2 + cMyBP-C n=184, negative control (representing the non-specific co-localisation results) n=40 fields of view, from four independent experiments; * statistical significance at p<0.05 calculated using unpaired, 2-tailed Student's t-test.*

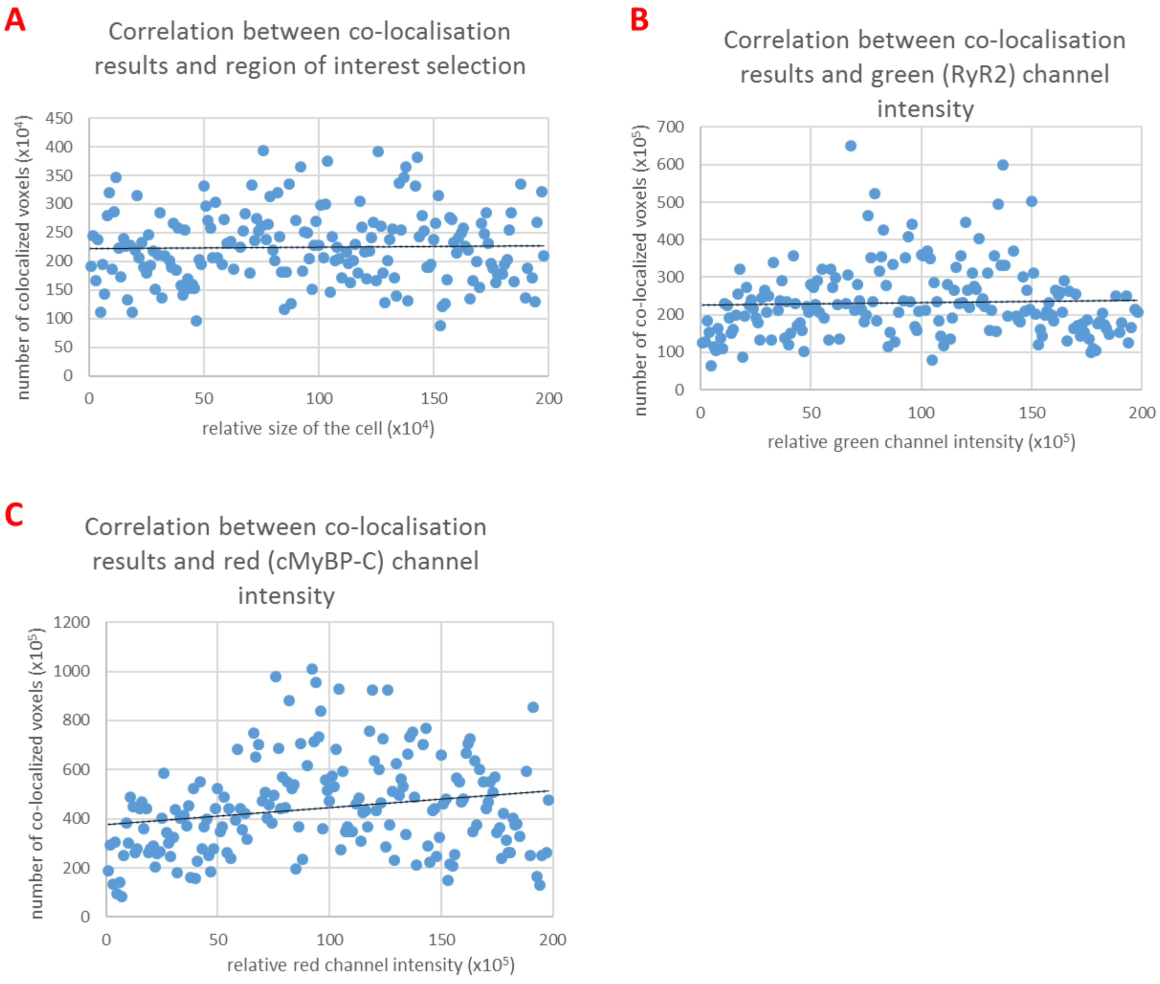

Figure 3.9 Distribution of data used for correlation analysis using Pearson's correlation coefficient (PCC) and square of PCC (denoted as r^2) calculated using GraphPad Prism. (A) Correlation between co-localisation results and region of interest selection, $r^2 = 0.001$, PCC= 0.04, (B) Correlation between co-localisation results and green (RyR2) channel intensity, $r^2 = 0.12$, PCC= 0.35 and (C) Correlation between co-localisation results and red (cMyBP-C) channel intensity, $r^2 = 0.18$, PCC= 0.43. Trend lines are shown in black.

3.4.6 RyR2:cMyBP-C interaction detected between recombinant human proteins

RyR2 and cMyBP-C were co-expressed in HEK293 cells, RyR2 was immunoprecipitated from solubilised HEK293 homogenate and the presence of co-precipitated HA-cMyBP-C was tested by WB analysis using HA-specific antibody. Representative blots presented in **Figure 3.10, A-B**, show that cMyBP-C was recovered in the RyR2 immunoprecipitate, indicative of positive recombinant

RyR2:cMyBP-C binding. Cumulative data (n=5) following densitometry analysis are presented in **panel C**. The detected difference between specific and non-specific binding was comparable to the binding ability detected in native pig homogenates (~20% difference between specific vs non-specific), reinforcing that both native pig and recombinant human RyR2 are capable of cMyBP-C interaction.

In similar way to native pig cardiac proteins, obtaining significant results from reciprocal co-IP experiments where HA-cMyBP-C was immunoprecipitated with HA Ab and the presence of co-precipitated RyR2 was tested by WB using 1093 Ab, were largely unsuccessful, most probably due to the large cytoplasmic cMyBP-C pool (see **Section 3.3.2**)

3.4.7 The recombinant N-terminal region of RyR2 is responsible for the interaction with the C-terminus cMyBP-C

To further assess the specificity of the interaction, the same mammalian expression system was employed to co-express either RyR2 c-Myc-tagged BT4L (N-terminal fragment, corresponding to RyR2 1-906 amino acids) or BT7 (residues 3071-3940; a similar size construct from RyR2 central region) with either the HA-tagged cMyBP-C C-terminal fragment (CT, residues 817-1274) or N-terminal fragment (NT, residues 1-865) or FL (full length cMyBP-C). Co-IP experiments were carried out using HA Ab to immunoprecipitate HA-cMyBP-C constructs, while the presence of co-precipitated c-Myc-tagged RyR2 constructs was analysed by WB with c-Myc Ab. These experiments resulted in the BT4L fragment reproducibly positive for robust cMyBP-C CT and FL interaction (**Figure 3.11, B: (1) and (2)**) and very weak positive signal for cMyBP-C NT (**B:(3)**); also neither of cMyBP-C constructs co- precipitated BT7 (used as a negative control). Cumulative results were further quantitatively evaluated by densitometry and statistical significance was calculated using paired, 2-tailed Student’s t-test (**Figure 3.12**). The difference between specific versus non-specific binding was statistically significant only for pairs CT + BT4L and FL+ BT4L and not for NT + BT4L. Further, the observed relative binding ability (calculated as the significant binding subtracted of the non-specific binding) of CT + BT4L was comparable to that of FL + BT4L (no significant difference calculated using Kruskal-Wallis test with Dunn’s post-test, see **Appendix, Table 8.1**). Overall, the obtained

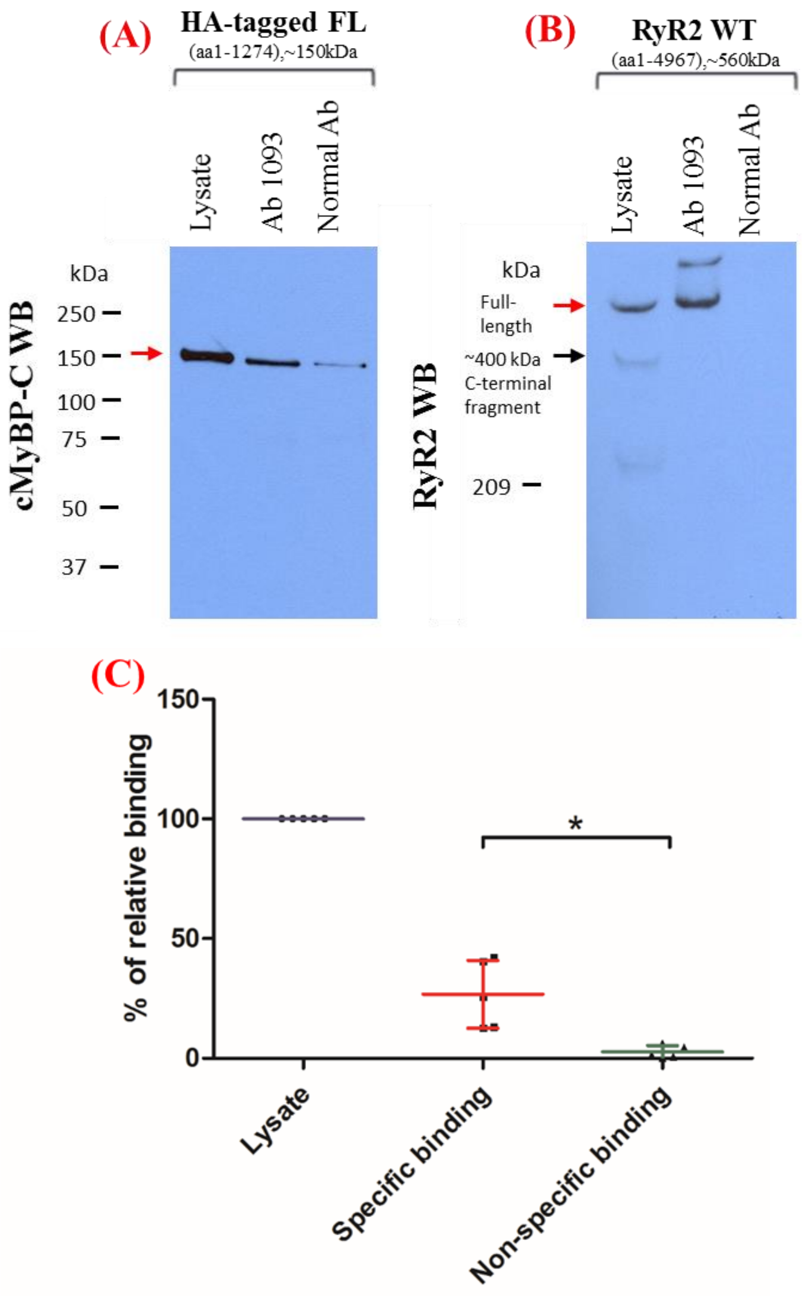

*Figure 3.10 Representative blots of Co-IP and WB results illustrating recombinant RyR2:cMyBP-C association and cumulative densitometric analysis. (A-B). HEK293 expressed recombinant human RyR2 was immunoprecipitated with Ab1093 from CHAPS-solubilised HEK293 cell lysate (2 mg per IP sample) analysed by immunoblotting with Ab HA (A: 12% gel) and Ab P12 (B: 4% gel), respectively. Bands corresponding to full-length cMyBP-C FL (~150 kDa) and RyR2 subunit (~560 kDa) are shown (red arrows). The loading controls represent 1/200th and 1/10th of the processed sample for (A) and (B), respectively. RyR2 is partially cleaved by the endogenous calpain protease to generate a ~400 kDa C-terminal fragment as indicated (black arrow). The amino acids coordinates are for human cMyBP-C (accession number: CAA58882.1) and RyR2 (accession number: X98330; (C) Densitometry analysis of recombinant full-length RyR2 and cMyBP-C binding in co-IP assay from HEK 293 homogenate. Percentage of relative binding corrected for the difference in expression levels are presented relative to lysate input (1/200th of the processed sample). Data are shown as mean ±SD, n=5; * statistical significance at $p<0.05$ calculated using paired, 2-tailed Student's t-test.*

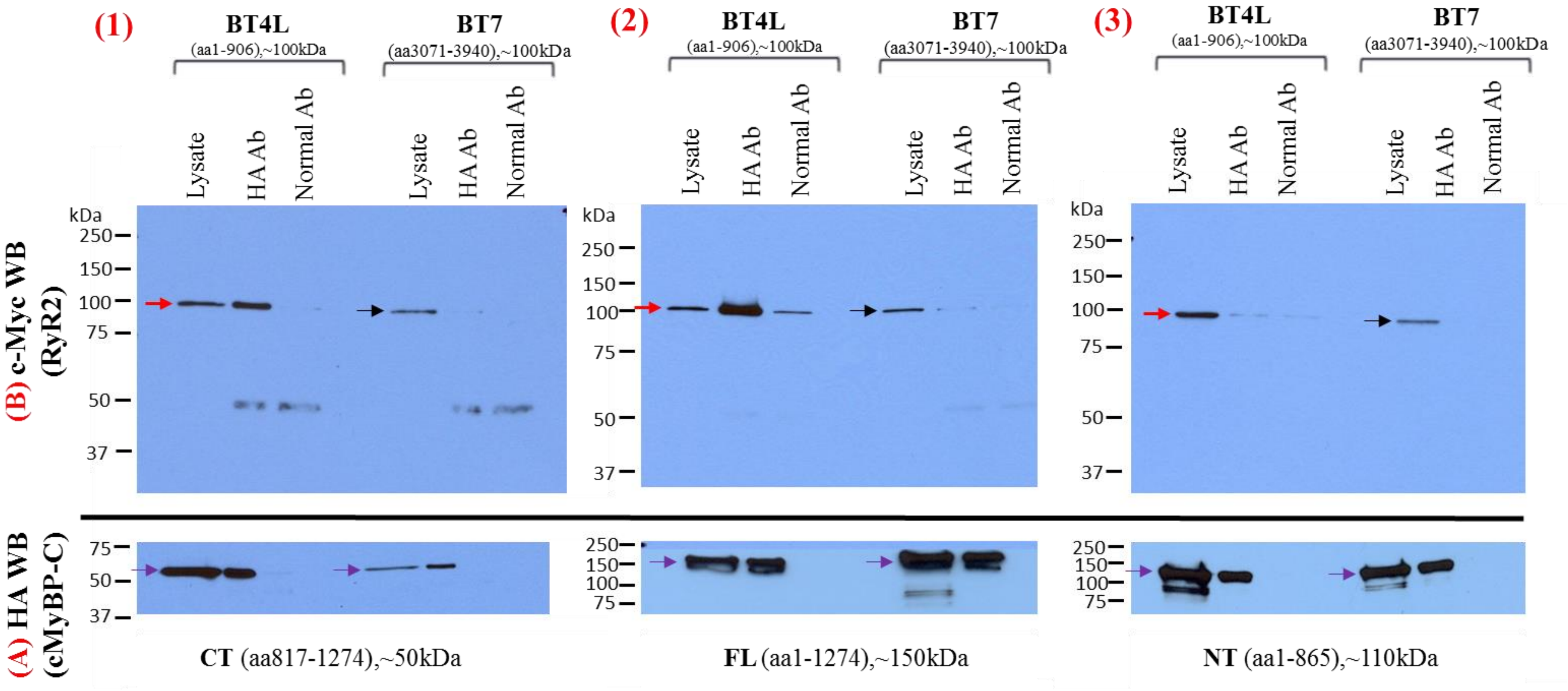

Figure 3.11 Representative results (n≥5)of c-Myc- tagged RyR fragments (BT4L or BT7) co-IP with HA-tagged cMyBP-C constructs (CT or FL or NT). cMyBP-C fragment of interest was immunoprecipitated with HA Ab from CHAPS-solubilised HEK293 cell lysate (2 mg) and normal, non-immune rabbit IgG was used as negative control. Co-IP samples were loaded on two separate SDS-PAGE gels (1/10th and 9/10th split) and analysed by immunoblotting with Ab HA and Ab c- Myc, respectively. upper panels (A), 1-3: WB using c-Myc Ab detecting c-Myc tagged BT4L and BT7; lower panes (B), corresponding WB using HA Ab detecting HA-tagged cMyBP-C CT (1), or cMyBP-C FL (2), or cMyBP-C NT (3). A cell lysate aliquot was loaded on the gels to verify expression in HEK293; in c-Myc WB, 1/200th of the volume processed in co-IP samples; in HA WB 1/100th of the volume processed in co-IP samples. All fragments are indicated as follows: BT4L, red arrows; BT7, black arrows, cMyBP-C fragments, violet arrows. 8% reducing SDS-PAGE gels were used for c-Myc WB and 12% gels for HA WB.

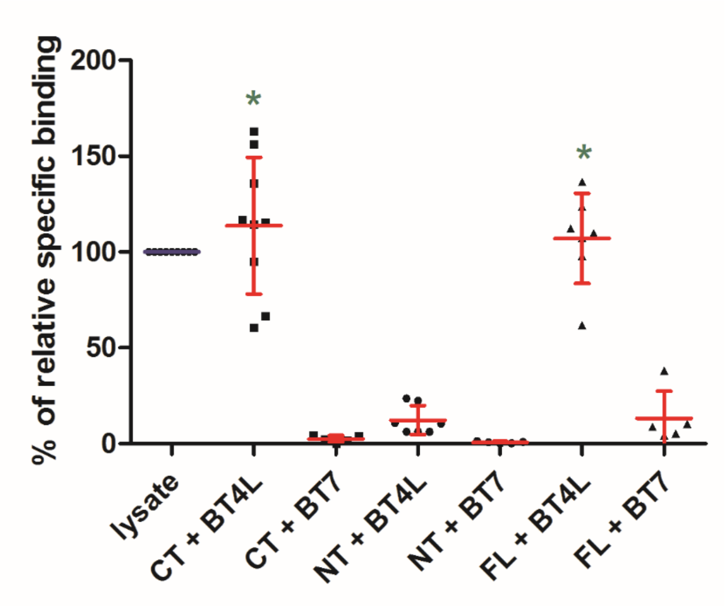

*Figure 3.12 Densitometry analysis of recombinant RyR2 and cMyBP-C constructs binding in co-IP assay from HEK 293 homogenate. Results shown are presented as relative binding (the specific binding subtracted of the non-specific binding) and normalised to each fragments respectable lysate input (corresponding to 1/200th of the processed sample). Data are shown as mean ±SD, n≥5; * statistical significance at $p<0.05$ calculated using paired, 2-tailed Student's t-test.*

data confirmed that RyR2 and cMyBP-C are able to form a complex *in vitro* and also highlighted the importance of the RyR2 N-terminal in cMyBP-C C-terminal binding.

3.5 Discussion

3.5.1 RyR2:cMyBP-C association may be applicable to larger mammal species

The goal the work presented in this chapter was to verify the putative RyR2:cMyBP-C association between (1) the native proteins from animal cardiac tissue and (2) the recombinant human proteins. The most significant finding presented in this Chapter is the positive co-precipitation of endogenous pig cMyBP-C with RyR2 complex, pointing to the physiological significance of the observed association. However, the inconsistency between the positive interaction detected in pig cardiac homogenate (**Figure 3.2**) versus somewhat ambiguous results from SR preparations, and the high non-specific binding observed for native cMyBP-C, particularly in the case of rabbit, could reflect limitations of the applied co-IP technique.

As part of the normal sarcomeric protein turnover, cMyBP-C exists in two different forms *in vivo*, the predominant phosphorylated (associated with greater thick filament stability) and second, the dephosphorylated form (Kulikovskaya et al. 2007). The latter is relatively sensitive to release from the sarcomere, with detectable low levels of full-length cMyBP-C in the cytosol (Decker et al. 2012; Kuster et al. 2014; Baker et al. 2015). Notably, the increased rate of cMyBP-C dephosphorylation and subsequent degradation has been associated with pathological conditions, as observed in patients with heart failure, MI and ischemia-reperfusion injury, and pathological hypertrophy (Decker et al. 2012; Govindan et al. 2012; Kuster et al. 2014; Baker et al. 2015). It has been shown that the proteolysis occurs in the C-terminal region, involving domains C5 and C10, resulting in detection of anti-C0C2, but not anti-C5 or anti-C8-C9 bands (Kulikovskaya et al. 2007). Importantly, animal model study by (Decker et al. 2012) have shown that proteolytic fragments of cMyBP-C are generated during MI and ischemia that were not present in either the myofibrillar or cytoplasmic myocardium from healthy, sham-operated hearts, whereas substantial degradation was observed after reperfusion. Therefore, at least under pathophysiological conditions, it is possible for full-length cMyBP-C and/or its proteolytic fragments to dissociate from the thick filament and be readily available for RyR2 binding. This observation is in line with our WB results of cardiac sub-cellular fractions indicating substantial amounts of intact full-length cMyBP-C in the cytosol and partly in the SR fraction, at least for pig, guinea pig and rabbit (**Figure 3.1**). Cytosolic and/or SR localisation for cMyBP-C may enable its interaction with RyR2 as observed in our co-IP experiments, probed with Ab C-t (detecting the epitope 988-1100 within the C8 domain), resulting in co-precipitation of a single 140kDa band **(Figure 3.2)**, indicating that cMyBP-C protein is intact and capable of interaction with RyR2. Given the fact that up to fifth part of RyR2 population can be localized outside the Z-line (Shacklock et al. 1995; Lukyanenko et al. 2007; Asghari et al. 2009; Jayasinghe et al. 2009), with non-junctional RyR2s detected between the Z-disks (Salnikov et al. 2009), present in the axial tubular system (Asghari et al. 2009) and/or on the periphery immediately under the sarcolemma but absent in the cell interior (Chen-Izu et al. 2006; Lukyanenko et al. 2007; Hiess et al. 2015), those RyR2s

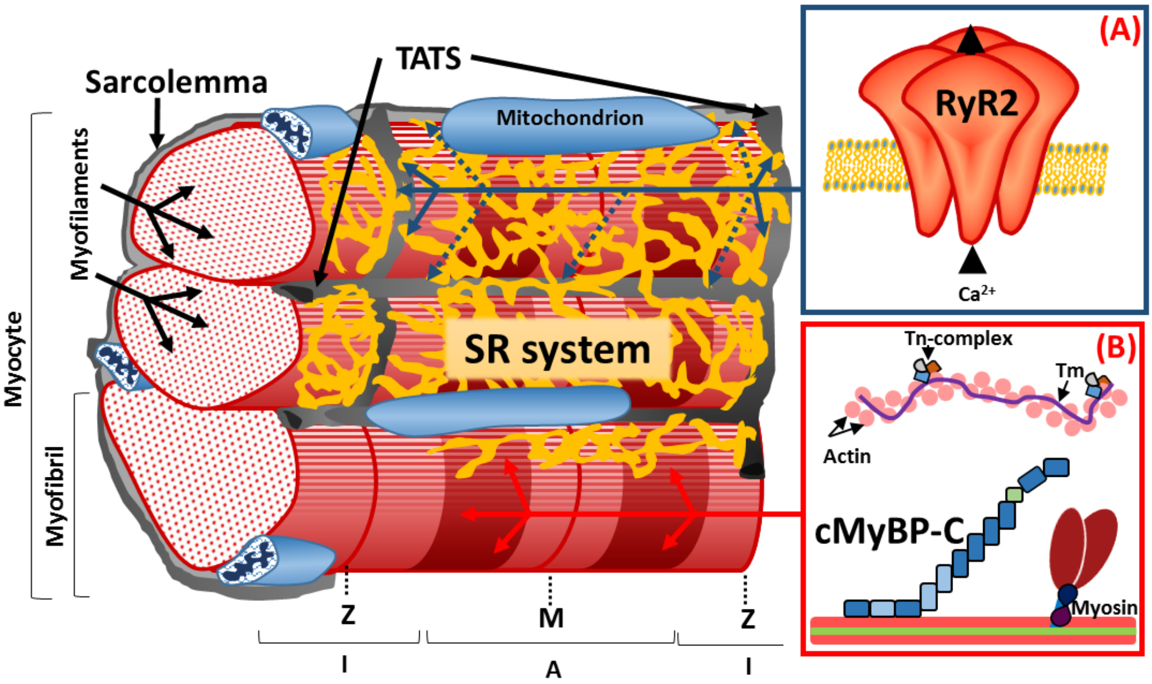

Figure 3.13 Graphical representation of RyR2 and cMyBP-C localisation within ventricular myocyte. T-tubules are depicted as regular invaginations of the sarcolemma perpendicular to the long axis of the myocyte and their relationship to the Z-line (Z) of sarcomere. The T-tubular lattice is crucial for the efficient spread of action potential and facilitates the spatiotemporal synchronisation of intracellular Ca^{2+} release. Adapted from (Bers and Shannon 2013).

positioned close to the C-zone may participate in the interaction with cMyBP-C. The **Figure 3.13** depicts the proposed model of cMyBP-C and RyR2 location in the sarcomere.

In order to assess the interaction between the human proteins, recombinant proteins had to be used, expressed in mammalian HEK293 cells. First of all, immunofluorescent staining assessment allowed to positively identify cells co-expressing recombinant cMyBP-C and RyR2 (**Figure 3.5**). In agreement with previous reports (George et al. 2003b; Stange et al. 2003; Thomas et al. 2004), recombinant RyR2 displayed correct targeting to the endoplasmic reticulum according to the characteristic lattice-like morphology (**Figure 3.6**). By contrast, cMyBP-C, was distributed diffusely throughout the cytoplasm (**Figure 3.6**), in conformity with findings of transient expression observed in COS cells (Sebillon et al. 2001; Welikson and Fischman 2002), HEK293 cells (Gedicke 2011) and also in agreement with the pattern described previously with the skeletal isoform (Seiler et al. 1996). Any additional nuclear localisation as reported by (Welikson and Fischman

2002) in COS cells was not observed, probably due to use of different cell line and/or Abs.

Initial inspection of obtained co-labelled RyR2/cMyBP-C 2D pictures showed potential overlap of detected signals (**Figure 3.6**), which was further verified by 3D quantification and scored as co-localisation (**Figure 3.8**). In the course of cell topological analysis, it became evident that the cMyBP-C signal was not visible in a substantial proportion of cytoplasmic region, in particular the area spanning from bottom side of the nucleus to the cell surface in direct contact with the coverslip (**Figure 3.6**, **D, dashed box**). Later experimental analysis with mCherry tagged cMyBP-C (see **Section 5.4.4**) proved it to be caused not by the absence of protein in this region, but by failure of N-t Ab to reach the cMyBP-C epitope. Therefore, the obtained 2.04% total and 4.82% of volume of cell (selected region of interest, ROI) voxel co-localisation accounts only for part of the true cMyBP-C:RyR2 overlap, which should yield higher values with appropriate Ab detection. This error could be avoided by further optimization of the immunofluorescence staining protocol or by use of another primary, cMyBP-C specific antibody.

The binding between the recombinant human full-length proteins was investigated following expression in HEK293 cells by the co-IP assay. The densitometric analysis revealed rather weak but reproducible and statistically significant interaction between human recombinant RyR2 and cMyBP-C proteins, comparable to native pig cardiac homogenate results (see **Figure 3.2, C** and **3.10,C** respectively), The quantitative accuracy of densitometric analysis could have been further improved by use of an additional internal loading control (such as α actinin or β myosin heavy chain) alongside samples to correct for possible errors in loading/transfer efficiencies, or by generating a standard curve from serial dilutions of used sample and subsequent immunoblotting detection (Taylor et al. 2013). Cumulatively, the obtained data support the presence of cMyBP-C and RyR2 protein-protein interaction in larger mammal species, in particular pig and human.

It should be noted that the phosphorylation levels of cMyBP-C have not been assessed in our experimental conditions, neither for native nor recombinant protein. Notably, it is widely accepted that the major cMyBP-C phosphorylation region is localized in the N-terminal domains C0-C2 (Sadayappan et al. 2005), with only a single phosphorylation site of unknown function reported in C9 domain (amino acids

S1066) (Kooij et al. 2013). Thus, is rather unlikely that phosphorylation state of cMyBP-C directly mediates the interaction with RyR2. Instead, considering that the requirement of cMyBP-C translocation to the sarcomere is the initial cMyBP-C dephosphotylation, it would be intriguing to speculate that it is a predominant from associated with RyR2.

Structural arrangement for RyR2 coupling is markedly different in cells lacking a T-tubules such as adult atrial myocytes, neonatal cardiac myocytes, sino-atrial node and Purkinje cells, where the junctional coupling exists at the cell periphery immediately under the sarcolemma (Bootman et al. 2006), thus the putative RyR2:cMyBP-C association may display different affinity than in ventricular myocytes. Further, the loss and disorganization of T-tubules is known to be causative of asynchronous and inhomogeneous Ca^{2+} release, due to the presence of orphan RyRs that have lost their coupling with the LTCC and are either not activated or activated with a delay (Song et al. 2006). Disease-related remodelling of the TATS can be found in a number of pathological conditions including human heart failure and dilated and hypertrophic cardiomyopathies, as well as in animal models of heart failure, chronic ischemia and atrial fibrillation (Biesmans et al. 2011; Guo et al. 2013; Zhang et al. 2013). Recently, several RyR2 mutations have been linked to the DCM phenotype (Haas et al. 2014), with arrhythmogenic phenotype emerging to be present in up to one-third of DCM cases (Spezzacatene et al. 2015). cMyBP-C is also involved in DCM pathology with arrhythmic events, thus, it is tempting to speculate that certain disease phenotypes may be linked to perturbation of the cMyBP-C:RyR2 association.

3.5.2 The regions responsible for the interaction are the RyR2 N-terminus and cMyBP-C C-terminus.

To reinforce the initial Y2H observation of interaction between cMyBP-C C-terminus (residues 817-1274) and RyR2 N-terminal region (residues 1-906), these protein fragments were co-expressed in the HEK293 cells and co-IP experiments were carried out. Densitometric analysis indicated strong binding between cMyBP-C CT (residues 817-1274) and RyR2 BT4L (residues 1-906) (**Figure 3.12**). Interestingly, the relative binding ability of cMyBP-C CT seems to be equal to the FL + BT4L, pointing that the cMyBP-C region 817-1274 contains the specific binding site responsible for the interaction with RyR2 BT4L. Importantly, BT7, an unrelated but similar size fragment form the central domain of RyR2, did not score for an interaction with any of the tested cMyBP-C constructs (NT, CT or FL), further highlighting the specificity of the interaction.

The 3D visualization in published high-resolution cryo-EM RyR1 structure (Yan et al. 2015) places BT4L (RyR2 residues 1-906, coordinates for RyR1: 1-894) at the very top of the cytoplasmic assembly forming a ring structure around the fourfold axis of the RyR channel, spreading towards the clamp region, whereas BT7 is located near transmembrane region (RyR2 residues 3071-3940, RyR1 coordinates 3071-3940), highlighting the spatial distance between the two regions (**Figure 3.14 A-C**). When compared to the RyR1 domain sequence boundaries proposed by (Yan et al. 2015), the BT4L appears to contain the sequences corresponding to that of NTD region (residues 1-631), part of the SPRY1 core β-sandwich (residues 632-826) and part of domain SPRY2 (residues 827–845) followed by sequence of the P1 domain (residues 851-1055). Notably, BT4L construct lacks the remaining SPRY1 two pairs of anti-parallel β-strands (residues 1466–1491 and 1615–1634), the primary sequences of which are connected to those of SPRY3 (see **Figure 3.14, D**), indicating that the latter does not directly participate in the interaction with cMyBP-C.

As each of the RyR2 domain seems to control different aspect of channel function, i.e. the NTD region is involved in regulation of channel gating whereas SPRY domains have been proposed to maintain channel structural integrity (Efremov et al. 2015), mapping of the minimal RyR2 binding region would allow to shed some light on the potential effect of cMyBP-C interaction with RyR2.

Many studies of cMyBP-C to date have focused on the N-terminal part of the protein, as it is involved in the interaction with both actin and myosin to regulate contraction, and to lesser extent on the C-terminal modules that anchors the protein to the thick filament. It has been shown that domains C5-C7 and C8-C10 interact with each other, based on which the collar model of cMyBP-C arrangement in the sarcomere was proposed (Moolman-Smook et al. 2002). Currently, there are no crystal structures for human cMyBP-C C6-C10 domains available, however NMR structure of human fMyBP-C C6 domain (PDB:2E7C), C7 (PDB:2YUW), C9 (PDB:2YUX) and

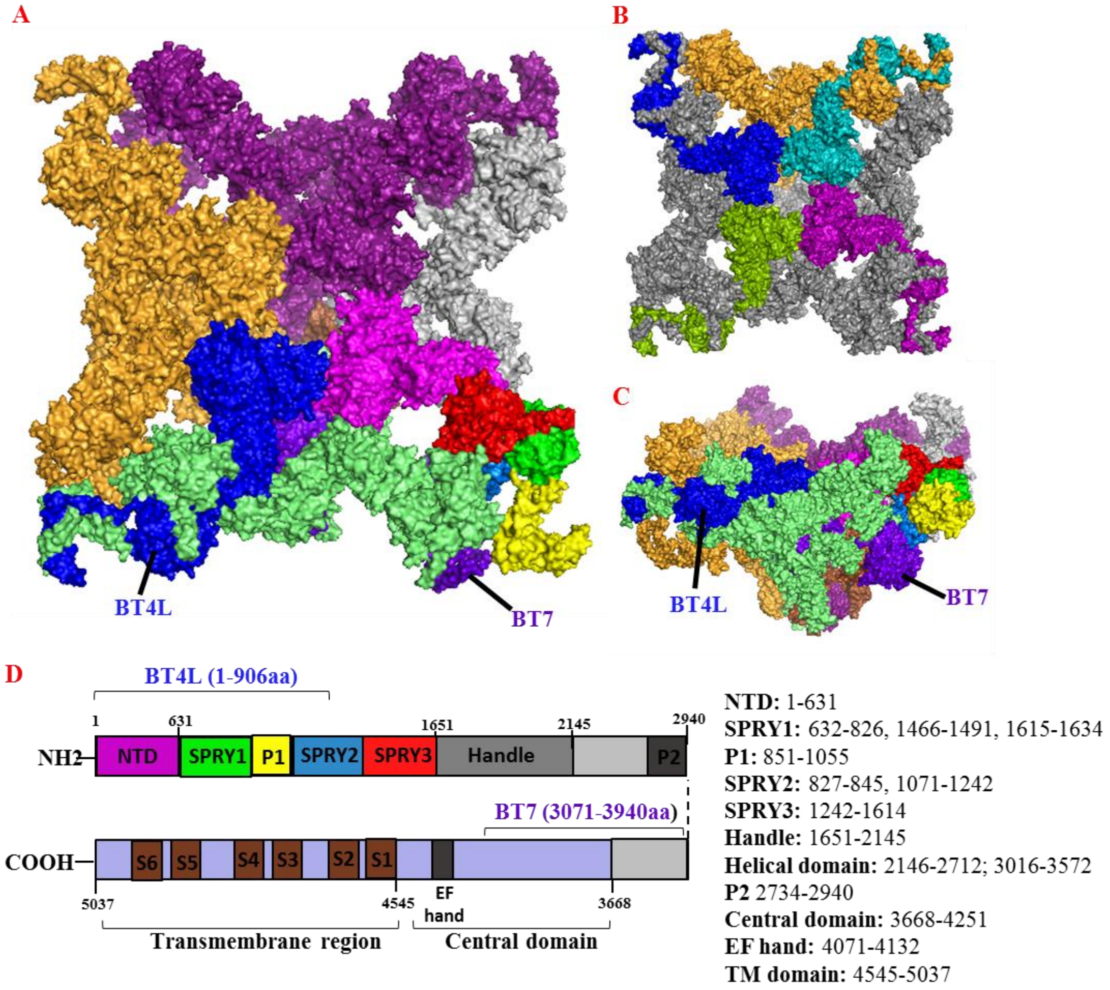

Figure 3.54 BT4L (RyR2 residues 1-906, coordinates for RyR1: 1-894) and BT7 (RyR2 residues 3071-3940, RyR1 coordinates 3071-3940) location in 3D structure of the rabbit RyR1 at 3.8 Å. (A) The top view shows the large cytoplasmic assembly and its previously assigned N-terminal domains (see the color-coded regions in D). Single RyR1 subunits are depicted in orange, purple, grey and light green, respectively. BT4L and BT7 are indicated with navy blue and violet (see labels); (B)The same top view with four BT4L (navy blue, teal, purple and lime) indicated in each subdomain, forming ring-like structure around the fourfold axis of the RyR channel. Single RyR1 subdomain indicated in orange; (C) the side view of image presented in A; (D) A schematic illustration of domain organization in one RyR1, with indicated sequences corresponding to BT4L and BT7. Images created using The PyMOL Molecular Graphic Software (based on ((Yan et al. 2015), accession number 3J8H).

mouse fMyBP-C C7 (PDB:1X5Y) have been deposited in PDB and they display overall predicted Fn β-sandwich fold (**Figure 3.15**). The cMyBP-C fragment testedpositive for RyR2 interaction, CT (residues 817-1274), includes the Fn domains C6, C7 and C9, with the Ig domains C8 and C10. cMyBP-C Ig domains belong to the I-set, which can be found in several cell adhesion molecules (including vascular, intercellular and neural), as well as several tyrosine kinase receptors. More importantly, the Ig I-set is present in other Z- and M-line sarcomeric proteins, including titin and obscurin (Harpaz and Chothia 1994; Benian and Mayans 2015; NCBI 2016b). Notably, those muscle proteins, similarly to cMyBP-C, also have the Fn type 3 domains, topologically very similar to the Ig fold, with a notable difference being the lack of a conserved disulfide bond in the Fn domains (Leahy et al. 1992). Fn type 3 repeat homologs have also been found in various animal protein families including extracellular-matrix molecules and cell-surface receptors (tyrosine phosphatase, cytokine and growth hormone receptors) (Koide et al. 1998; NCBI 2016a).

Unlike titin, which is an integral component of sarcomeres, obscurin is not present within sarcomeres but intimately surrounds them, primarily at the level of the M-band and Z-disk, where it is appropriately positioned to participate in their assembly and integration with other sarcoplasmic elements. Notably, the first Ig domain within the 11-domain super-repeats of titin in the C-zone has been shown to interact with MyBP-C C8-C10 domains, whereas N-terminal titin Ig domains Z8-9, which are more distal in the Z-disk, can associate with obscurin Ig domains 58-59 (Linke 2008). Further, invertebrate obscurin mutants lacking the large Ig domain-rich isoforms have

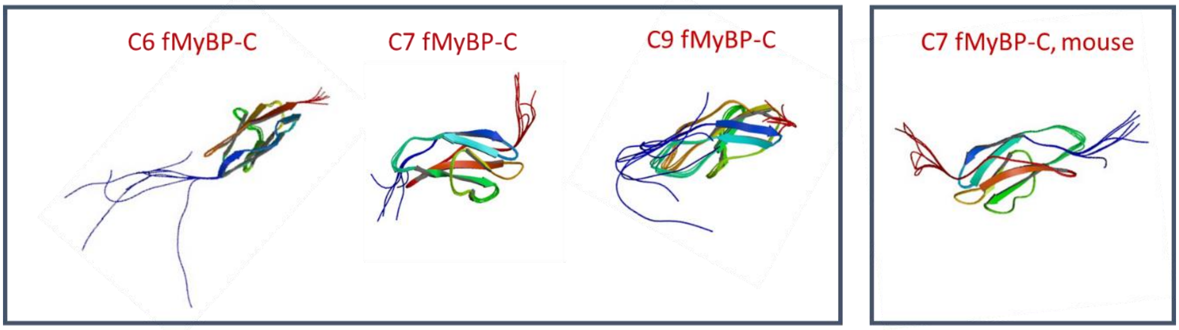

Figure 3.65 Available NMR structures of fMyBP-C C-terminal Fn domains. From left to right: human C6 domain (PDB:2E7C), C7 (PDB:2YUW), C9 (PDB:2YUX) and mouse fMyBP-C C7 (PDB:1X5Y). Images shown were taken from the PDB website (www.rcsb.org/pdb/home/home.do)using appropriate accession numbers and modified.

been reported to display reduced Ca^{2+} signalling and reduced muscle activity (Spooner et al. 2012) suggesting a role of Ig domains in connectivity between the SR, the Z-disk, and other cytoskeletal structures. Further, work by (Ackermann et al. 2009) has shown that disarray of the A-band and M-line of primary rat skeletal myocytes caused by overexpression of the single Ig type 2 domain of obscurin is mediated by direct interaction of this domain with Ig C10 domain of sMyBP-C variant 1, but not by the corresponding C10 domains of the fMyBP-C and cMyBP-C. This sMyBP-C splice variant, which has a unique C-terminus containing a total of 26 new amino acids, was shown to be expressed in significantly lower amounts than other sMyBP-C variants, and notably was the only one demonstrated to localize preferentially to the M-band of the sarcomere instead of the C-zone, generally accepted for MyBP-Cs (Ackermann et al. 2009). This distinct localization of sMyBP-C due to changes in its C-terminus is not without a precedent, as an alternatively spliced form of mouse cMyBP-C, containing 10 additional amino acids in the Fn C9 domain (30 bases insertion located in the exon 31) was also shown to not localize at the A-bands, but instead exhibited a diffuse distribution throughout the cardiomyocyte. Further, it also had a markedly decreased affinity for myosin and titin, and was reported to be the predominant form of cMyBP-C in aged atrial muscle (Sato et al. 2003). Interestingly, (Kuster et al. 2015) have recently reported that a human HCM-associated cMyBP-C C10 mutation (caused by a 25-basepair deletion in the MYBPC3 gene) resulted in improper localisation of this variant to the Z-line. An increased concertation of mutant protein in the cytosolic fraction was also shown (when compared to WT cMyBP-C), which was predicted to be the main cause of contractile dysfunction induced by this variant, as detected in the cultured adult rat cardiomyocytes. Notably, it has been shown that a significant portion of HCM-linked cMyBP-C sequence variants occur in the C-terminus domains, with variable phenotypic patterns and the mechanisms by which they cause disease only partly understood (Harris et al. 2011). A recent study by (Nadvi et al. 2016) assessed three HCM variants: D745G in C5, P873H in C7 and R820Q in C6, the latter being associated also with the DCM phenotype (Konno et al. 2003). Using bioinformatics and NMR modelling, it was predicted that those variants confer different disease outcomes based on their divergent structural consequences, with R820Q being surface exposed and proposed to interfere with interactions within the sarcomere, whereas the other two were shown to disrupt domain folding. Thus, since both Ig and

Fn domains appear to exhibit broad functional modularity, with the alterations in cMyBP-C C-terminal domains shown to be implicated in cMyBP-C-linked pathology, we decided to evaluate in the subsequent Chapter which one of the cMyBP-C domain/s are directly involved in the RyR2 N-terminal interaction.

3.5.3 Conclusions

Overall, obtained data support the conclusion that the cMyBP-C and RyR2 can readily form protein complexes, in particular in higher mammals, and that the regions responsible for the binding are RyR2 N-terminus and cMyBP-C C-terminus.

Chapter 4

Mapping of RyR2 and cMyBP-C interaction sites

4 Mapping of RyR2 and cMyBP-C interaction sites

4.1 Introduction

Having established a gross mapping of RyR2 N-terminus interaction with cMyBP-C C-terminus in the previous Chapter, the subsequent aim was to further refine the region/domain/residues participating in the association. Therefore, a series of truncated cMyBP-C constructs spanning the entire length of the protein were generated by PCR amplification and cloning, and used to co-transfect HEK293 cells with BT4L (RyR2 construct, residues 1-906), followed by co-IP analysis for protein-protein interaction. In a similar way, a series of truncated RyR2 N-terminal overlapping constructs within BT4L (previously made in our lab) were used to map the binding site within RyR2 by co-expression with CT (cMyBP-C construct, residues 817-1274) and the binding was assessed by co-IP. To ease the detection of recombinant protein fragments, each cMyBP-C construct was cloned with immunoaffinity tag HA at the N-terminus, whereas each RyR2 construct was expressed as N-terminal c-Myc fusion protein. Since one of the disadvantages of the epitope-tagging approach is that the artificially introduced tag may interfere with protein stability and/or expression (Yang et al. 2008), the presence and expected molecular weight of all prepared new constructs in transfected HEK293 cells was verified by WB prior to commencing to the mapping studies. Notably, HA and c-Myc peptide epitopes have been used previously in our lab in connection with co-IP assay (Stewart et al. 2003; Zissimopoulos and Lai 2005; Zissimopoulos et al. 2013; Zissimopoulos et al. 2014).

To extend the co-IP observations, an independent *in vivo* technique was employed, namely the Y2H system. In this approach, the interaction between two proteins (i.e. X and Y) is measured by the reconstitution of a functional hybrid transcription factor GAL4 and the concurrent activation of a reporter gene by introducing in yeast the following two fusion proteins: GAL4 DNA-Binding Domain (DNA-BD)/protein X fusion (bait) and GAL4 Activation Domain (AD)/protein Y fusion (target) (Stynen et al. 2012). When the recombinant DNA-BD and AD protein fusions are co-expressed in the yeast nucleus, the separated DNA-BD and AD peptides do not directly interact with each other unless they are brought into close physical proximity by X and Y interaction to produce a hybrid GAL4 transcription factor. Positive growth selection of those colonies expressing prey which interacts with the bait is achieved using a prototrophic reporter gene, such as HIS3, which is transcribed in response to the bait–prey interaction. Parallel transcriptional activation of a colorimetric reporter, such as lacZ encoding β-galactosidase (β-gal), serves to confirm the specificity of the activation. The main advantage of the Y2H is that it detects even weak or transient protein-protein interactions, because it is amplified many-fold through a transcriptional process (Fashena et al. 2000; Stynen et al. 2012). In our study, the colony-lift filter paper β-gal assay was used as means to qualitatively measure the β-gal activity of positive interaction between a series of RyR2 N-terminal construct with cMyBP-C CT.

RyR2 N-terminus is known to self-associate in a tetrameric fashion (Tung et al. 2010; Zissimopoulos et al. 2013). This raises the possibility that cMyBP-C may be interacting with an RyR2 interface either provided entirely by the monomer or be composed of binding determinants provided by two adjacent RyR2 subunits. To test this, we used a BT4L construct with a small internal deletion of (residues 167-178, corresponding to the loop connecting β-strand 8 and 9 in NTD subdomain A) shown to disrupt RyR2 N-terminus tetramerisation (Seidel 2014). The BT4L$^{\Delta\beta8\text{-}\beta9}$ was co-transfected HEK293 cells with cMyBP-C CT, followed by co-IP analysis for protein-protein interaction. The detected binding ability was directly compared to that of the original BT4L + CT.

Analysis of RyR mRNA expression pattern in adult atrial and ventricular myocytes by (Gorza et al. 1997) revealed that in fact the most abundant isoform in the heart is RyR2 while RyR3 was shown to be widely co-expressed in the same cell at relatively low levels. Further, a concomitant expression of all three isoforms was reported to take place in the vascular smooth muscle (Neylon et al. 1995). Notably, cMyBP-C C-terminus has high sequence homology with two other mammalian MyBP-C isoforms, fMyBP-C and sMyBP-C (~70%, for the residues 817-1274, similarity between sequences was calculated with NCBI BLAST tool), both being expressed in abundance in skeletal muscle (Dhoot et al. 1985), where RyR1 is the main RyR isoform involved in ECC. Further, since the RyR2 N-terminal region shares high homology with the two remaining RyR isoforms (~85% for the first 900 residues, NCBI BLAST tool), we tested the cMyBP-C CT interaction with RyR1 and RyR3 in parallel experiments, both *in vitro* (co-IP assay) and *in vivo* (Y2H analysis), in order to get some insights whether the MyBP-C:RyR interaction could also occur between different RyR isoforms.

4.2 Chapter objectives

The main aim of this Chapter was to identify the cMyBP-C and RyR2 binding sites. In particular, the following points will be addressed:

- mapping of RyR2 region responsible for cMyBP-C binding using co-IP and Y2H assays;
- assessment of cMyBP-C binding to monomeric N-terminal RyR2 construct using the co-IP assay;
- mapping of cMyBP-C region responsible for RyR2 interaction using the co-IP assay;
- verification of the RyR isoform-specificity of cMyBP-C association using co-IP and Y2H assays.

4.3 Methods

4.3.1 Generation of a series of truncated HA-tagged cMyBP-C constructs

Truncated cMyBP-C cDNA fragments were generated by PCR from cMyBP-C FL construct as a template in the presence of the appropriate forward and reverse primer (see **Table 2.1**), designed to introduce suitable cloning sites at both 5’ and 3’ end of the PCR product. To ensure proper peptide folding, protein fragments were designed to start/stop within the linker sequences between individual cMyBP-C Ig or Fn domains, therefore, oligonucleotide primers annealing at the selected, corresponding cDNA sequences were used. Obtained products were cloned into HA-modified pCR3 vector and used for large scale plasmid isolation (for details, see **Sections 2.2.1.2-2.2.1.4,** and **2.2.3.1-2**). Summary of all generated constructs can be found in **Table 4.1** and **Figure 4.1.**

Table 4.1 List of generated HA-tagged cMyBP-C constructs and corresponding primers and restriction nucleases used in this study. Coordinates correspond to the human cMyBP-C mRNA, accession number: X84075.

Construct	Coordinates	Length	PCR Primers	Cloning Sites
C6-C8	2490-3237 (b) 820-1068 (aa)	747 (b) 248 (aa)	HcMyBPC.FOR.2481-2508 HcMyBPC.REV.3217-3237	*EcoRI* *XhoI*
C8-C10	2931-3857 (b) 967-1274 (aa)	926 (b) 307 (aa)	HcMyBPC.FOR.2925-2949 HcMyBPC.REV.3849-3876	*BamHI* *XhoI*
fC6-C7	2337-2952 (b) 771-972 (aa)	615 (b) 201 (aa)	HcMyBP-C.FOR.2331-2360 HcMyBP-C.REV.2931-2958	*BamHI* *XhoI*
C6-C7	2490-2952 (b) 820-972 (aa)	462 (b) 152 (aa)	HcMyBPC.FOR.2481-2508 HcMyBP-C.REV.2931-2958	*EcoRI* *XhoI*
fC6	2337-2630 (b) 771-866 (aa)	293 (b) 95 (aa)	HcMyBP-C.FOR.2331-2360 HcMyBPC.REV.2611-30	*BamHI* *XhoI*
C7	2635-2952 (b) 869-972 (aa)	307 (b) 103 (aa)	HcMyBP-C.FOR.2625-56 HcMyBP-C.REV.2931-2958	*BamHI* *XhoI*
C8	2931-3237 (b) 967-1068 (aa)	306 (b) 101 (aa)	HcMyBPC.FOR.2925-2949 HcMyBPC.REV.3217-3237	*BamHI* *XhoI*
C9	3213-3512 (b) 1061-1160 (aa)	299 (b) 99 (aa)	HcMyBPC.FOR.3204-3235 HcMyBPC.REV.3519-3488	*BamHI* *XbaI*
C8-C9	2931-3512 (b) 967-1160 (aa)	581 (b) 193 (aa)	HcMyBPC.FOR.2925-2949 HcMyBPC.REV.3519-3488	*BamHI* *XbaI*
C9-C10	3213-3857 (b) 1061-1274 (aa)	644 (b) 213 (aa)	HcMyBPC.FOR.3204-35 HcMyBPC.REV.3849-3876	*BamHI* *XhoI*

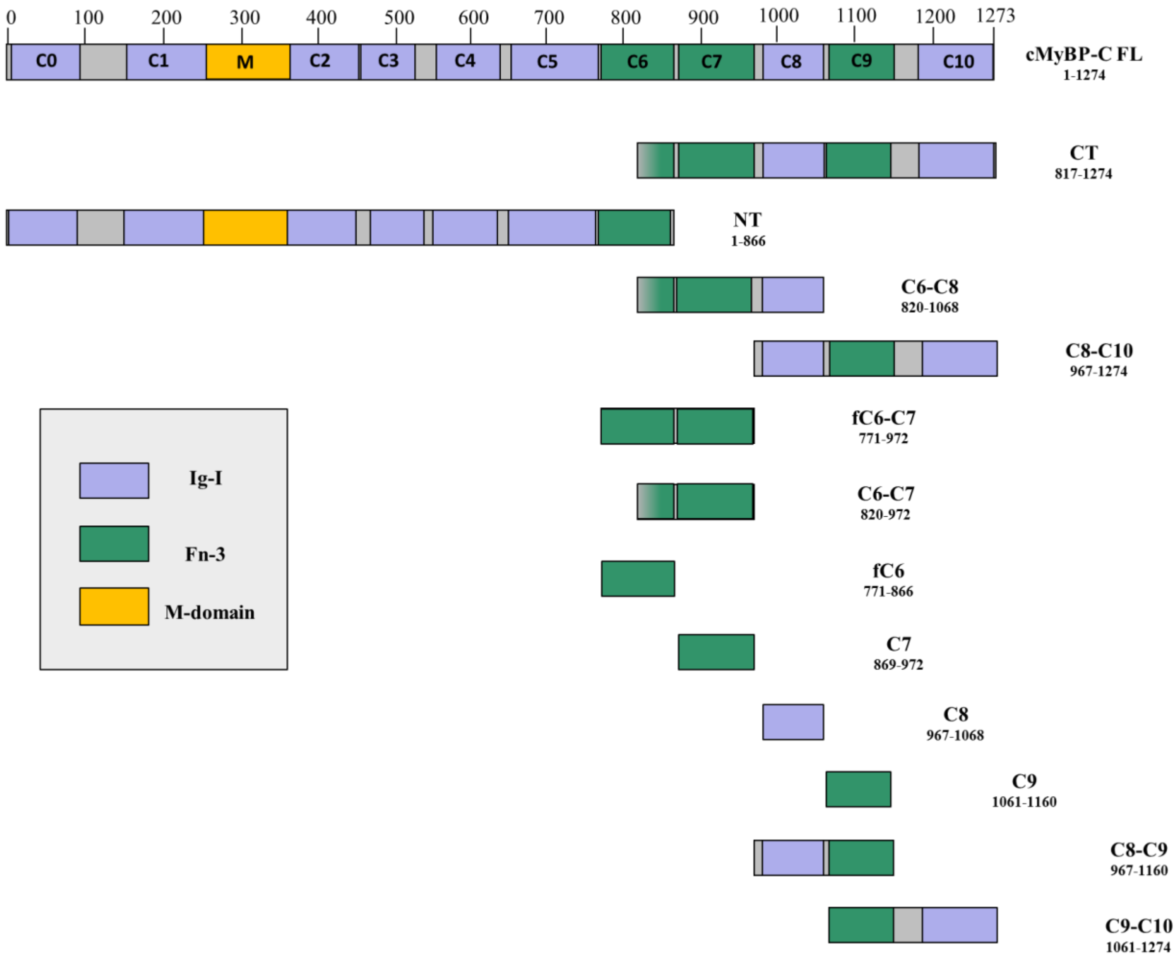

Figure 4.1 Graphical representation of generated HA-tagged cMyBP-C constructs. Coordinates correspond to the human cMyBP-C cDNA, accession number: X84075

4.3.2 Co-immunoprecipitation

Mammalian (c-Myc tagged) RyR constructs (BT fragments, obtained from Dr S. Zissimopoulos, see **Table 4.2** and **Figure 4.2** for summary) and (HA-tagged) cMyBP-C plasmids were used to co-transfect HEK293 cells growing on 100 mm Petri dishes as described in (**Section 2.2.5.3**). RyR2 BT4L was used to screen the series of cMyBP-C truncated fragments, whereas cMyBP-C CT fragment was used to screen the series of RyR2 fragments (BT constructs). All plasmids were co-transfected in ~1:1 molar ratio (12 µg + 12 µg per dish), apart from BT4C+ CT (4 µg +20 µg), BT4EL+CT (20 µg +4 µg), BT4B + CT (22 µg +2 µg) and BT4D + CT (22 µg +2 µg). Those adjustments were required due to higher (BT4C) or lower expression levels (BT4EL, BT4B, BT4D) in HEK293 when compared to other BT constructs. All subsequent statistical analysis was conducted using GraphPad Prism (see **Section 2.2.11**).

Table 4.2 List of all RyR2 plasmids used. Coordinates correspond to the human RyR2 mRNA (accession number: X98330).

Construct	Coordinates	Length
BT4L	122-2840 (b) 1-906 (aa)	2718 (b) 906 (aa)
BT4	122-2398 (b) 1-759 (aa)	2276 (b) 759 (aa)
BT4L$^{\Delta\beta8\text{-}\beta9}$	BT4L deletion, without 167-178 (aa)	896 (aa)
BT4A	122-1711 (b) 1-530 (aa)	1589 (b) 530 (aa)
BT4B	1160-2398 (b) 346-759 (aa)	1238 (b) 413 (aa)
BT4C	122-2084 (b) 1-654 (aa)	962 (b) 654 (aa)
BT4D	605-2398 (b) 161-759 (aa)	793 (b) 598 (aa)
BT4BL	1160-2840 (b) 346-906 (aa)	1680 (b) 560 (aa)
BT4DL	605-2840 (b) 161-906 (aa)	2235 (b) 745 (aa)
BT4EL	1818-2840 (b) 565-906 (aa)	1022 (b) 341 (aa)
RyR1 BT4L	1-915 (aa)	915 (aa)
RyR3 BT4L	1-911 (aa)	911 (aa)

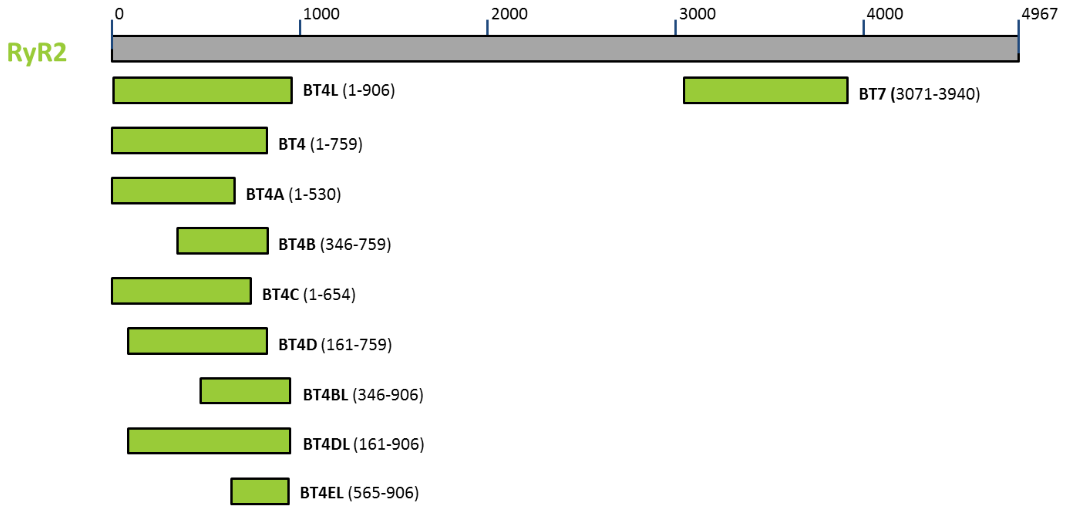

Figure 4.2 . Graphical representation of BT fragments relative to RyR2 cDNA sequence (accession number: X98330).

Cell pellets obtained 24 hours after transfection were homogenised (**Section 2.2.2.1**) and co-IP was performed as described in **Section 2.2.2.3**. Polyclonal HA antibody (**Section 2.1.11**) were used to immunoprecipitate the HA-tagged cMyBP-C fragment of interest. Non-immune rabbit IgG served as negative control. DTSSP was used to cross-link the immunoprecipitating Ab onto Protein A beads for BT4A + CT, BT4B + CT and BT4EL + CT pairs, and samples were co-immunoprecipitated (see **Section 2.2.2.3)**, due to the similar size of Ab heavy chain to that of BT4A/B/EL. For immunoblotting, Ab HA and Ab c-Myc (**Section 2.2.11**) were used to detect directly precipitated cMyBP-C fragment and indirectly co-precipitated RyR2 fragment, respectively. The level of co-precipitated proteins was determined by densitometry (**Section 2.2.10**).

4.3.3 Yeast-two hybrid

The C-terminus interaction of cMyBP-C with the series of truncated RyR2 N-terminus fragments was assessed *in vivo* using the yeast two-hybrid system. The series of bait plasmids containing the truncated N-terminal RyR2 fragments (BT fragments, spanning the RyR2 residues 1-906) fused to the GAL4 DNA-BD and c-Myc epitope (in pGBKT7 vector), and the prey plasmid (AD-CT) containing the C-terminal of cMyBP-C (CT) expressed as fusion protein with GAL4 AD and HA epitope (in pACT2 vector) were obtained from Dr S. Zissimopoulos. Yeast co-transformations and β-galactosidase colony-lift filter assay were performed as described in **Section 2.2.4.1** and **2.2.4.2** respectively. **Table 4.3** enlist all tested combinations (pairs 1-10). The interaction between pVA3-1 coding for a DNA-BD/murine p53 fusion protein and pTD1-1 coding for an AD/SV40 large T-antigen fusion protein was used as assay quality positive control. The expression levels of all constructs used in this study were investigated with immunoblotting (**Section 2.2.4.3**). The Y2H obtained data were expressed relative to the positive interaction observed between the control proteins (pVA3 + pTD1).

Table 4.3 Summary of all tested RyR2:cMyBP-C pairs used in Y2H assay.

Pair	GAL 4 DNA-BD	GAL4 AD
Control	pVA3	pTD1
1	BT4L	CT
2	BT4	CT
3	BT4A	CT
4	BT4B	CT
5	BT4C	CT
6	BT4D	CT
7	BT4BL	CT
8	BT4DL	CT
9	RyR1 BT4L	CT
10	RyR3 BT4L	CT

4.4 Results

4.4.1 Generation of a series of cMyBP-C truncated constructs

All cMyBP-C constructs (see **Table 4.1**) were successfully generated and their DNA sequence was confirmed. For a typical set of results representing intermediate steps of the cloning process, see **Section 3.4.3** and **Figure 3.3.**

4.4.2 Mapping of the minimal interacting region of RyR2 N-terminus involved in association with cMyBP-C C-terminus

4.4.2.1 Several RyR2 binding determinants can be detected using in vitro co-IP assays

To further localise the cMyBP-C binding site within BT4L (RyR2 residues 1-906), a series of eight overlapping BT sub-fragments (c-Myc-tagged) were co-expressed together with the same HA-tagged cMyBP-C CT fragment and used in co-IP. Representative blots are shown in **Figure 4.3** and summary of the results following quantitative densitometry analysis is presented in **Figure 4.4 A** (shown as relative binding, calculated by subtracting the non-specific binding form the specific binding of given BT construct). Obtained data indicated that fragments BT4 (residues 1-759), BT4D (residues 161-759), BT4DL (residues 161-906), BT4EL (residues 565-906) scored as positive with CT when compared to their respective non-specific binding (calculated using paired, 2-tailed Student’s t-test, **Figure 4.4 A**), with BT4EL being the smallest but also the weakest of all obtained positive constructs. Interestingly, both BT4EL and a fragment consisting of additional 346-565 amino acids, BT4BL (residues 346-906) exhibited only an occasional interaction with CT (which did not reach the statistical significance in the case of BT4BL), whereas the smaller fragments within RyR2 residues 1-906 were negative, namely BT4A (residues 1-530), BT4B (residues 346-759) and BT4C (residues 1-654) (**Figure 4.4 A**). Notably, lack of amino acids 1-161 or 755-906 appeared to result in a substantial reduction in the relative binding ability (BT4, residues 1-755; BT4D, residues 161-759, BT4DL, residues 161-906, BT4EL, residues 565-906) when compared to BT4L (~50%, ~70%, ~30% and ~80%, respectively, **Figure 4.4 A**). Further, monomeric BT4L$^{\Delta\beta8\text{-}\beta9}$ (BT4L lacking residues 167-178) displayed comparable cMyBP-C relative binding to tetrameric BT4L (**Figure 4.4 A and B**), with only those two constructs (BT4L and BT4L$^{\Delta\beta8\text{-}\beta9}$) having the statistically significant difference in the relative binding ability across all tested BT RyR2 fragments when compared to the negative construct BT7 ($p< 0.0001$ using Kruskal-Wallis test, with Dunn's multiple comparisons test, see **Appendix, Table 8.2**).

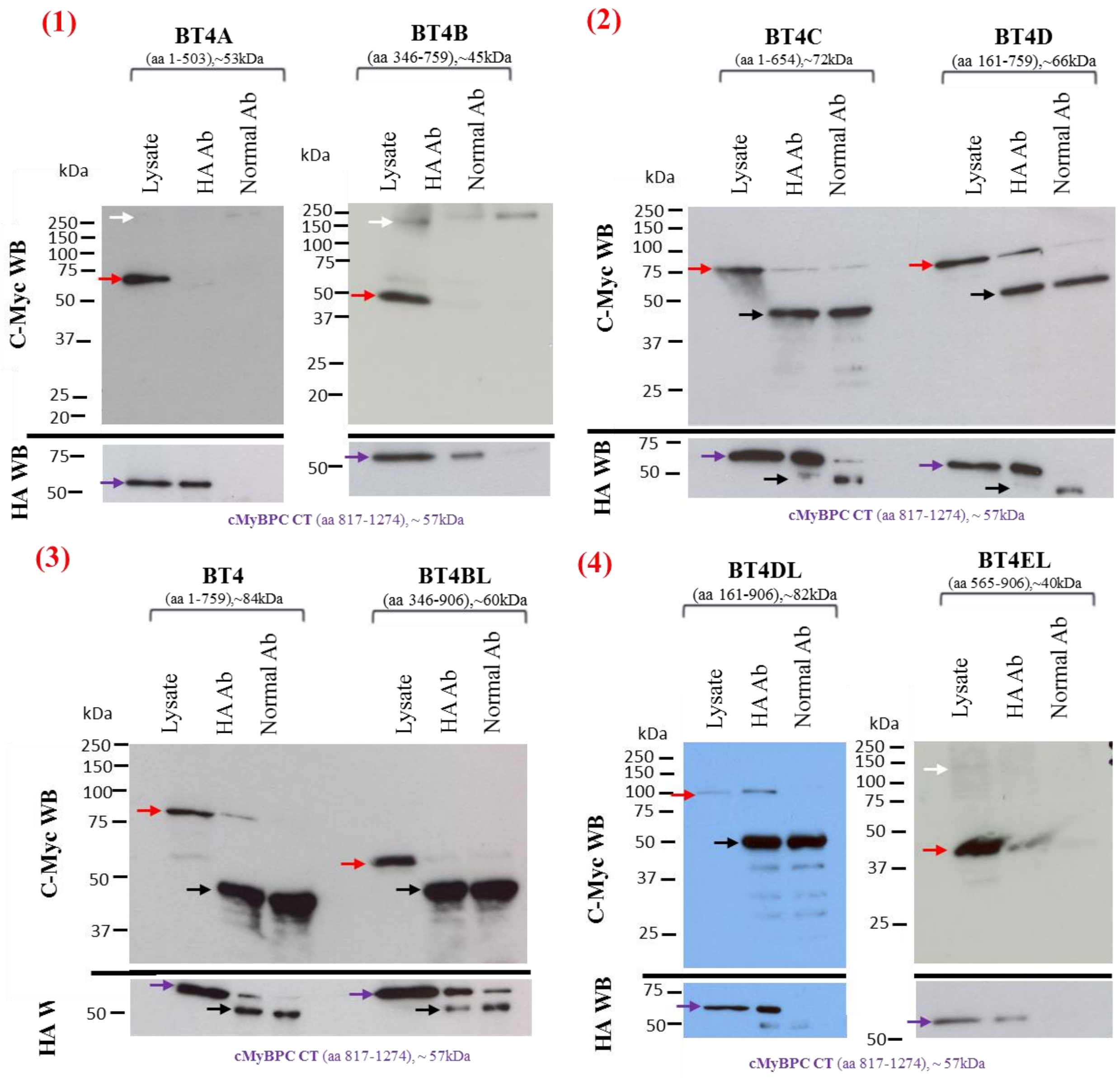

Figure 4.3 Representative results (n≥4) of a series of BT c-Myc- tagged RyR fragments co-IP with HA-tagged cMyBP-C CT construct. CT was immunoprecipitated with HA Ab from CHAPS-solubilised HEK293 cell lysate (2 mg) and normal, non-immune rabbit IgG was used as negative control. Co-IP samples were loaded on two separate SDS-PAGE gels (1/10th and 9/10th split, lower and upper panel, respectively) and analysed by immunoblotting with Ab HA (HA WB for CT, lower panels) and Ab c-Myc (c-Myc WB for BT, upper panels). A cell lysate aliquot was loaded on the gels to verify expression in HEK293; in c-Myc WB, 1/200th of the volume processed in co-IP samples; in HA WB 1/100th of the volume processed in co-IP samples. All bands corresponding to appropriate fragments are indicated as follows: BT of interest, red arrow; CT, violet arrow. 8-12% reducing SDS-PAGE gels were used for c-Myc WB and 12% gels for all HA WB. Black arrows show Ab heavy chain and white arrows in BT4A, BT4B and BT4EL WB show bands corresponding to aggregates formation (due to non-reducing conditions required for Abs DTSSP cross-linking).

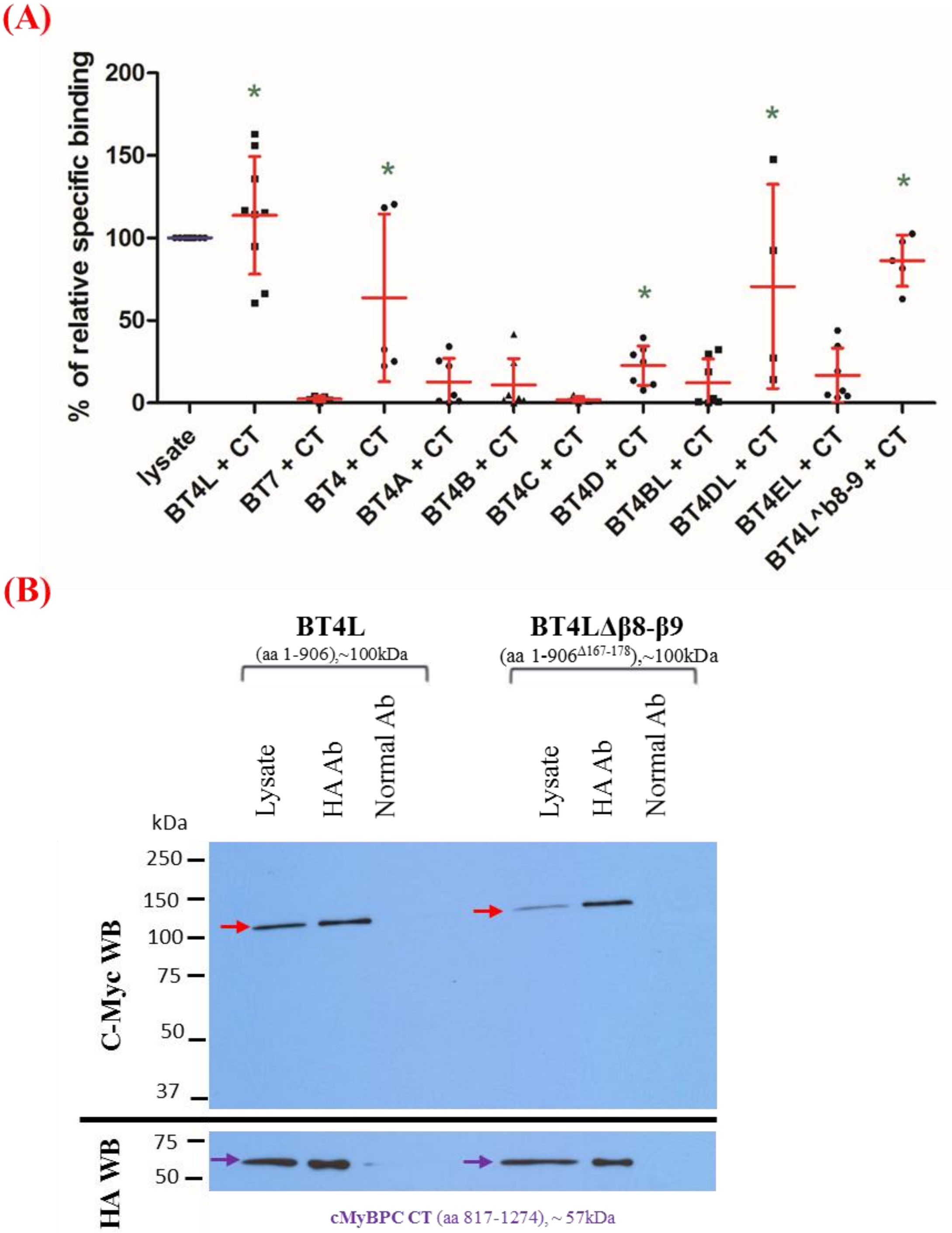

*Figure 4.4 Densitometry analysis of a series of recombinant RyR2 BT truncated fragments with cMyBP-C CT construct binding in co-IP assay from HEK293 homogenates and representative blot showing co-IP results of BT4L + CT and BT4LΔβ8-β9 + CT. (A) Results shown are presented as relative specific binding (specific binding subtracted of non-specific binding) and normalised to each fragments respectable lysate input (corresponding to 1/200th of the processed sample). Data are shown as mean ±SD, n≥4; * statistical significance at $p<0.05$ calculated using paired, 2-tailed Student's t-test. For comparison, BT4L + CT and BT7 + CT relative binding (from Figure 3.10) are also included. (B, top panel) WB using c-Myc Ab detecting c-Myc tagged BT construct of interest; (B,lower panel) corresponding WB using HA Ab detecting HA-tagged cMyBP-C CT. A cell lysate aliquot was loaded on the gels to verify expression in HEK293; in c-Myc WB, 1/200th of the volume processed in co-IP samples; in HA WB 1/100th of the volume processed in co-IP samples. All fragments are indicated as follows: BT of interest, red arrow; CT fragment, violet arrow. 8% reducing SDS-PAGE gel was used for c-Myc WB and 12% gel for HA WB.*

Importantly, when all used truncated BT fragments were compared to the positive BT4L, significant difference was observed for BT4A, BT4B, BT4C and BT4BL, which indicates that those constructs are negative, but not for BT4, BT4D, BT4DL and BT4EL, which appear to be positive for cMyBP-C interaction (**Appendix, Table 8.2)**. Overall, the obtained data shown that although BT4L (residues 1-906) displays the strongest cMyBP-C interaction *in vitro*, the residues 1-346 and 654-906 (present in the weaker, positive BT constructs) appear to be the important determinants of the association. Importantly, none of the smaller BT constructs could retain comparable relative binding to BT4L, indicating the presence of several binding sites and/or regions important for the association within amino acids 1-906, which seems to be indispensable for comparable BT4L + CT binding ability.

4.4.2.2 RyR2 binding site is contained within BT4L as assessed using in vivo Y2H assays

The findings described in the previous sections, indicated that residues 654-759 and 165-346 from RyR2 might be the important determinants of cMyBP-C C-terminus binding. The experiments described in previous section tested RyR2:cMyBP-C association in a test tube outside of the cell, an environment which substantially differs from the tightly controlled and intact cellular milieu. The Y2H system, where detection of protein-protein interactions takes place in living yeast, was employed to evaluate whether the *in vitro* observed effects can be reproduced in in *vivo* conditions. The cMyBP-C CT fragment was expressed in yeast strain Y190 as a fusion with GAL4 AD, co-transformed with one of the RyR2 truncated fragments, expressed as fusions with DNA-BD. The expression of all constructs used in this Y2H study was investigated by WB, as substantial differences in protein levels would affect the outcome of the assay. As shown in **Figure 4.5**, all recombinant proteins were successfully expressed, but to various levels. Summary of obtained Y2H results is shown in **Table 4.4**. The β-galactosidase colony-lift filter paper assay confirmed that interaction between CT and BT4L indeed takes place *in vivo* and also scored for an interaction for the CT + BT4 pair, albeit considerably weaker. Interaction with smaller RyR2 BT fragments could not be detected, also for BT4DL, probably due to

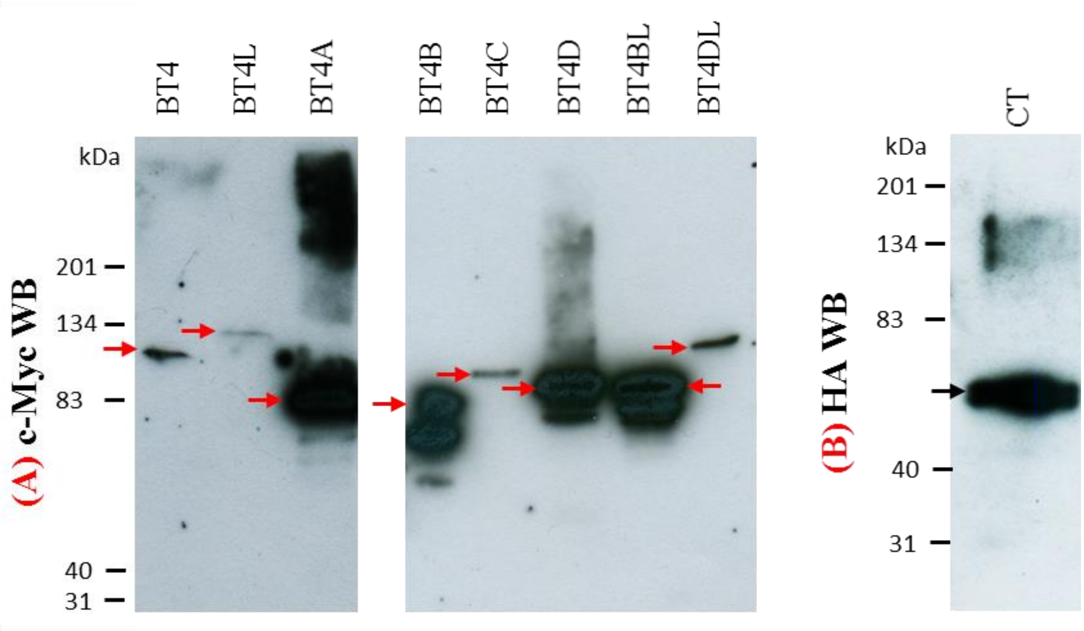

Figure 4.5 Representative western blots showing expression levels of recombinant proteins tested in Y2H system (n≥3); (A): c-Myc WB of recombinant proteins fused with DNA-BD, respective bands are shown with red arrows; (B): HA WB of recombinant CT fused with GAL4 AD, indicated with black arrow.

Table 4.4 Summary of Y2H results for RyR2:cMyBP-C interaction.

Pair	GAL 4 DNA-BD	GAL4 AD	Y2H Results
Control	pVA3	pTD1	+++
1	BT4L	CT	++
2	BT4	CT	+
3	BT4A	CT	-
4	BT4B	CT	-
5	BT4C	CT	-
6	BT4D	CT	-
7	BT4BL	CT	-
8	BT4DL	CT	-
9	BT4L RyR1	CT	++
10	BT4L RyR3	CT	-

Note: The 2nd column lists fusion proteins with the GAL4 DNA binding domain (BD) and the 3rd column lists fusion proteins with the GAL4 activation domain (AD). Interactions between two fusion proteins is shown in the third (β-galactosidase activity = lacZ Assay) column. Qualitative relative binding affinities after ~4 h are expressed as pluses in the table (+Light blue; ++Blue; +++Deep blue). Interaction between pVA3 and pTD1 served as the positive control.

general high variability of the BT4DL + CT binding when compared to BT4 + CT as seen in co-IP experiments (**Figure 4.4 A**), which likely was beyond sensitivity of Y2H assay. Further, despite several attempts successful BT4EL + CT co-transformation could not be achieved, thus results for this construct are not shown.

4.4.2.3 Corresponding RyR1 and RyR3 N-terminal fragments can interact with MyBP-C

Since both the C-terminal primary sequence of the mammalian MyBP-C isoforms and N-terminal sequence of RyR isoforms show high sequence homology, attempts were made to verify if cMyBP-C CT is capable of interaction with two other mammalian RyR isoforms, RyR1 and RyR3.

Parallel Y2H and co-IP experiments with the corresponding RyR1/3 N-terminal fragments (RyR1 BT4L, amino acids 1-915 and RyR3 BT4L, amino acids 1-911) were conducted to test if MyBP-C interaction is RyR isoform specific. Robust interaction was detected only between cMyBP-C CT and RyR1 BT4L from Y2H experiments comparable to that of RyR2 (**Table 4.4**, **9-10**). RyR1 BT4L interaction with cMyBP-C, equivalent to RyR2, was also found from co-IP experiments (**Figure 4.6, A**). Unlike the Y2H, co-IP experiments showed that RyR3 isoform is also capable of interaction with cMyBP-C CT (when compared to their respective non-specific binding calculated using paired, 2-tailed Student's t-test, **Figure 4.2, B**), and the relative binding ability (the specific binding subtracted of the non-specific binding) is comparable (no statistical difference) to those detected for BT4L and RyR1 BT4L (p= 0.2626 using one-way ANOVA, with Bonferroni's post-test, see **Appendix, Table 8.3**). In conclusion, these results might suggest that MyBP-C could be relevant in regulation of RyR not only in cardiac, but it also in skeletal muscle.

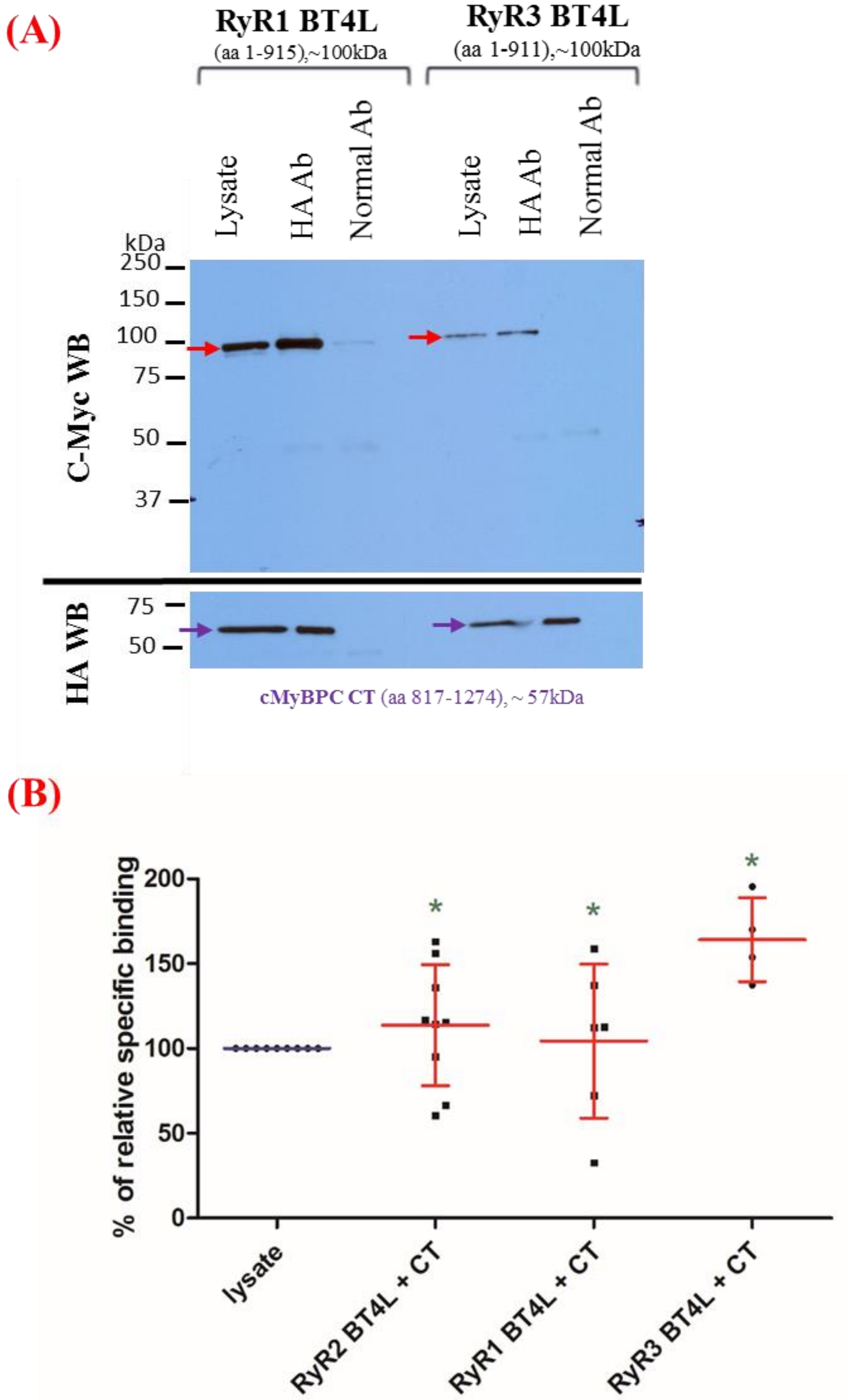

*Figure 4.6 Representative blot showing co-IP results of RyR1 BT4L + CT and RyR3 BT4L + CT and cumulative densitometric analysis. (A, top panel) WB using c-Myc Ab detecting c-Myc tagged BT construct of interest; (A, lower panel) corresponding WB using HA Ab detecting HA-tagged cMyBP-C CT. A cell lysate aliquot was loaded on the gels to verify expression in HEK293; in c-Myc WB, 1/200th of the volume processed in co-IP samples; in HA WB 1/100th of the volume processed in co-IP samples. All fragments are indicated as follows: BT of interest, red arrow; CT fragment, violet arrow. 12% reducing SDS-PAGE gel was used for both c-Myc and HA WB. (B)Densitometry analysis of recombinant cMyBP-C CT constructs binding with different N-terminal RyR isoforms in co-IP assay from HEK 293 homogenate. Results shown are presented as relative specific binding (specific binding subtracted of non-specific binding) and normalised to each fragments respectable lysate input (corresponding to 1/200th of the processed sample). Data are shown as mean ±SD, n≥5; * statistical significance at p<0.05 calculated using paired, 2-tailed Student's t-test. For comparison, BT4L + CT relative binding (from Figure 3.10) is also shown.*

4.4.3 Mapping of the minimal interacting region of cMyBP-C C-terminus involved in association with RyR2 N-terminus

4.4.3.1 Domains C6-C7 and C9-C10 are important for the interaction with RyR2 as assessed using in vitro co-IP assays

To further examine the RyR2-binding site within the cMyBP-C CT fragment (consisting of half of C6 domain and whole domains C7-C10, residues 817-1274), initially two overlapping sub-fragments C6-C8 (consisting of half of C6 domain and whole domains C7 and C8, residues 820-1068) and C8-C10 (consisting of whole domains C8-C10, residues 967-1274) were co-expressed with BT4L (RyR2 construct, residues 1-906) and used in co-IP experiments. Representative blot is shown in **Figure 4.7, A**. Statistical analysis with paired, 2-tailed Student’s t-test indicated that both construct retain the interaction with BT4L when compared to their respective non-specific binding with C6-C8 displaying ~2-fold stronger binding ability with BT4L than either C8-C10 or the original CT fragment (**Figure 4.7, B**), which did not reach the statistical significance when the relative binding abilities (the specific binding subtracted of the non-specific binding) of (1) C6-C8 + BT4L versus C8-C10 + BT4L or (2) C6-C8 + BT4L versus CT + BT4L or (3) C8-C10 + BT4L versus CT + BT4L were compared (calculated using Kruskal-Wallis test, with Dunn's multiple comparisons test, see **Appendix, Table 8.4**). This allowed for some preliminary conclusions regarding the possible location of the RyR2 binding site: (1) the candidate region could be the C8 domain (residues 967-1068) since it was present in both tested constructs; and/or (2) Fn domains could be required to mediate the interaction, as C6-C8 containing two Fn domains (C6 and C7) shown the strongest binding.

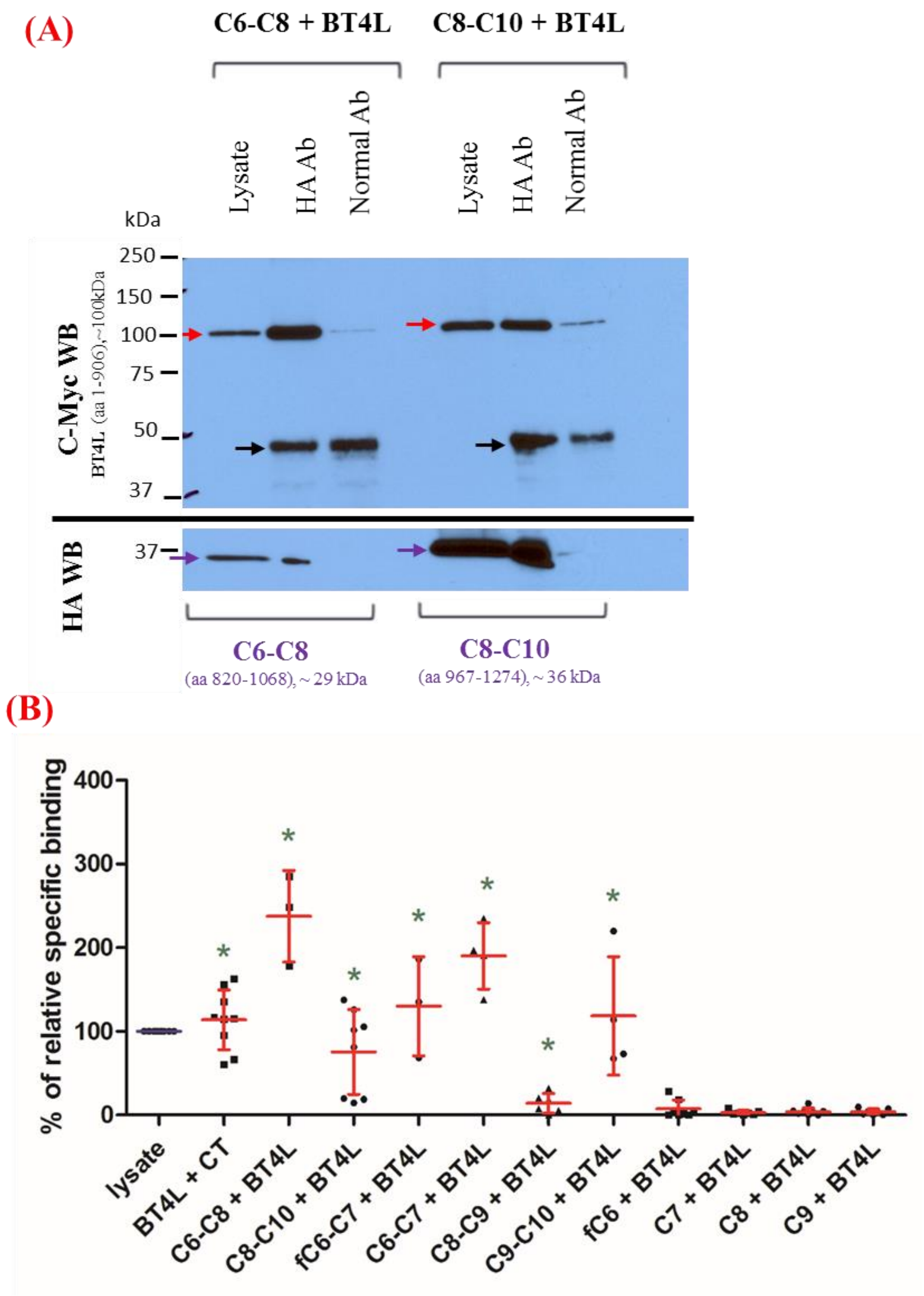

*Figure 4.7 Representative blot showing co-IP results of C6-C8 + BT4L and C8-C10 + BT4L and cumulative densitometric analysis. (A, top panel) WB using c-Myc Ab detecting c-Myc tagged BT4L; (B, lower panel) corresponding WB using HA Ab detecting HA-tagged cMyBP-C construct of interest. A cell lysate aliquot was loaded on the gels to verify expression in HEK293; in c-Myc WB, 1/200th of the volume processed in co-IP samples; in HA WB 1/100th of the volume processed in co-IP samples. Band corresponding to BT4L is shown with red arrow; whereas cMyBP-C fragment of interest with violet arrow, 12% reducing SDS-PAGE gel was used for both c-Myc WB and HA WB. Black arrows show bands corresponding to Ab heavy chain. Densitometry analysis of a series of recombinant cMyBP-C truncated fragments with RyR2 BT4L constructs (residues 1-906) binding in co-IP assay from HEK 293 homogenate. Results shown are presented as relative specific binding (specific binding subtracted of non-specific binding) and normalised to each fragments respectable lysate input (corresponding to 1/200th of the processed sample). Data are shown as mean ±SD, n≥5; * statistical significance at $p<0.05$ calculated using paired, 2-tailed Student's t-test. For comparison, BT4L + CT relative binding (from Figure 3.10) is also shown.*

Since the CT fragment, originally isolated from the Y2H screen, starts in the middle of the C6 domain sequence, it is possible that the C6 domain is not correctly folded. In order to test it, two new constructs fC6-C7 (consisting of whole domains C6-C7, residues 771-972) and C6-C7 (consisting of half of C6 domain and whole domain C7, residues 820-972) were generated. Representative blot is shown in **Figure 4.8, (1)**. Both new constructs displayed positive interaction with BT4L when compared to their non-specific binding with paired, 2-tailed Student's t-test (**Figure 4.7, B**). The introduction of the missing sequence at the start of the C6 domain had no statistically significant effect when (1) C6-C7 + BT4L versus fC6-C7 + BT4L or (2) CT + BT4L versus fC6-C7 + BT4L or (3) CT + BT4L versus C6-C7 + BT4L relative binding abilities (the specific binding subtracted of the non-specific binding of each tested pair) were compared (calculated using Kruskal-Wallis test, with Dunn's multiple comparisons test, see **Appendix, Table 8.4**). These results suggested that the truncated C6 domain did not have an effect on the cMyBP-C:RyR2 binding ability and highlighted possible role for Fn domain C7.

In order to further assess the involvement of individual cMyBP-C Ig/Fn C-terminal domains in the interaction with RyR2, six new constructs were made: single domain fC6, C7, C8 and C9 (residues 771-866, 869-97, 967-1068 and 1061-1160, respectively) and double domains C8-C9 (residues 967-1160) and C9-C10 (residues 1061-1274). Representative blots are shown in **Figure 4.8, (2-4)**. When the specific binding was compared to the non-specific binging using paired, 2-tailed Student's t-test, none of the single domain constructs scored for an interaction with BT4L, whereas both C8-C9 + BT4L and C9-C10 + BT4L were positive (significance at $p<0.05$ calculated using paired, 2-tailed Student's t-test, **Figure 4.7, B**). It appears that C9-C10 + BT4L display ~3x stronger relative binding ability than C8-C9 + BT4L, although this difference is not statistically significant (calculated using Kruskal-Wallis test, with Dunn's multiple comparisons test, see **Appendix, Table 8.4**). However, when considering only CT + BT4L, C9-C10 + BT4L and C8-C9 + BT4L, equal variance between populations enabled to use more powerful than non-parametric Kruskal-Wallis test, the one-way ANOVA test, which indeed, shown (1) a statistically significant difference between C8-C9 and C9-C10 binding and (2) comparable binding between CT and C9-C10 (see **Appendix, Table 8.4**). This suggests that the

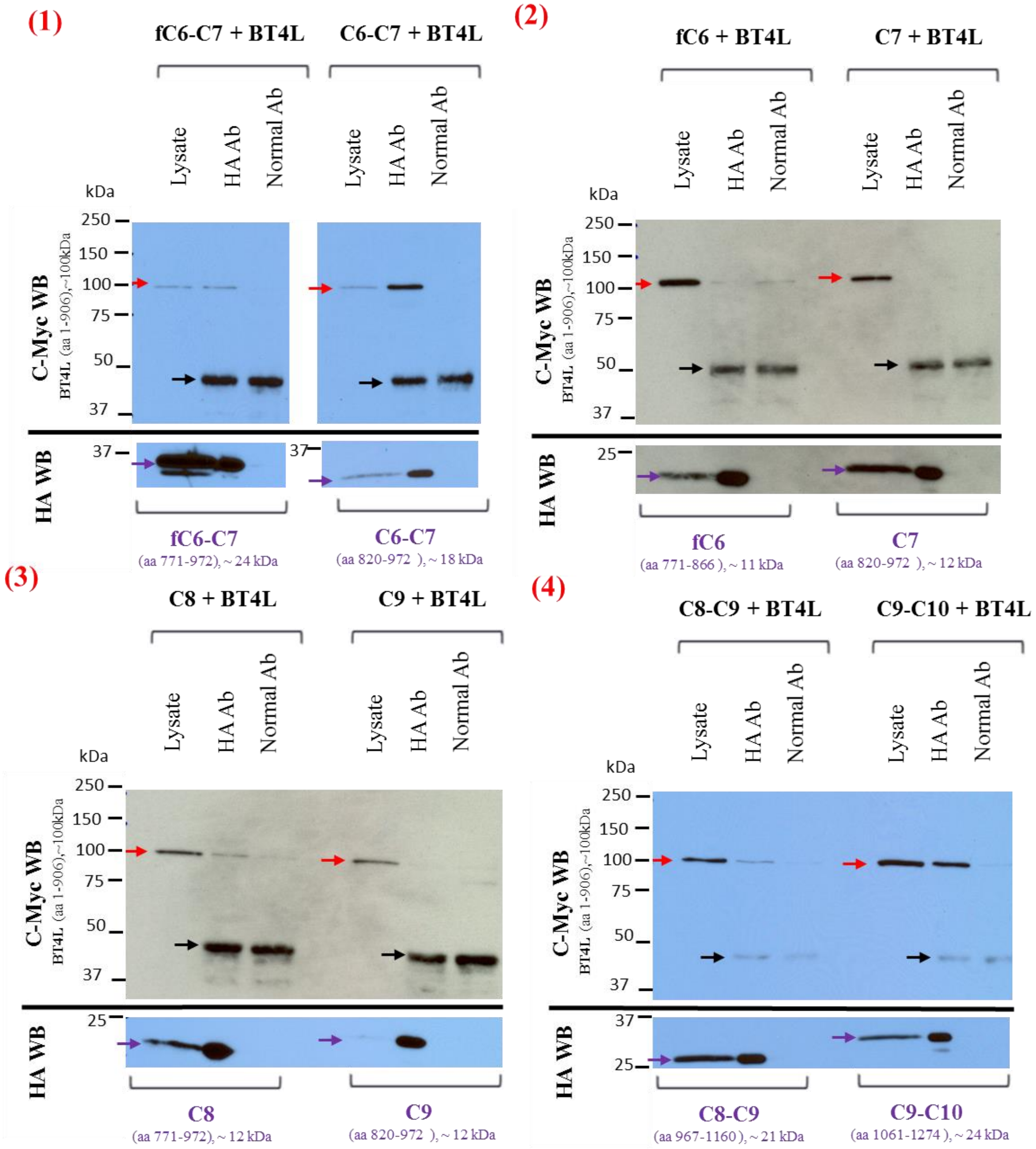

Figure 4.8 Representative results of a series of HA-tagged cMyBP-C construcs co-IP with c-Myc-tagged BT4L (n≥5). cMyBP-C fragment of interest was immunoprecipitated with HA Ab from CHAPS-solubilised HEK293 cell lysate (2 mg) and normal, non-immune rabbit IgG was used as negative control. Co-IP samples were loaded on two separate SDS-PAGE gels (1/10th and 9/10th split, lower and upper panel, respectively) and analysed by immunoblotting with Ab HA and Ab c-Myc. A cell lysate aliquot was loaded on the gels to verify expression in HEK293; in c-Myc WB, 1/200th of the volume processed in co-IP samples; in HA WB 1/100th of the volume processed in co-IP samples. All fragments are indicated as follows: BT4L, red arrow; cMyBP-C construct of interest, violet arrow. 12% reducing SDS-PAGE gels were used for both c-Myc and HA WB. Black arrows show bands corresponding to Ab heavy chain.

C8 domain is unlikely to be involved in the interaction, and reinforced the notion that the Fn domain/s mediate/s the RyR2 binding.

Overall, two truncated C-terminal cMyBP-C constructs retained comparable strong RyR2 interaction, namely C6-C7 and C9-C10. Both fragments consist of Fn domains, either C6 and C7 or C9, suggesting the possible importance of a Fn domain as responsible for RyR2 binding, with the presence of minimum one of neighbour (either another Fn or Ig) domain being required for detectable BT4L association.

4.5 Discussion

4.5.1 The regions responsible for cMyBP-C binding are contained within the cytosolic RyR2 NTD subdomains A and B, and SPRY1 and P1

The presented data provide several lines of evidence for a specific protein–protein interaction between RyR2 and cMyBP-C, further reinforcing findings reported in **Chapter 3**. Using complementary *in vitro* and *in vivo* assays, mapping of the binding region responsible for cMyBP-C:RyR2 interaction in each protein was attempted. The smallest positive RyR2 interacting construct obtained *in vitro* was the BT4EL fragment (residues 565-906) (**Figure 4.4 A**), indicating that this fragment may include the part of the cMyBP-C binding region. Notably, detected BT4EL relative binding ability was the weakest of all positive fragments (BT4, BT4D and BT4DL), implying that other region/s present in the missing 1-565, corresponding to the NTD subdomain A and B (residues 10-223 and 224-408 for RyR2 coordinates (Borko et al. 2014)) contribute to the interaction. The summary of RyR2 residues mapped to be important for association with cMyBP-C CT are show in **Figure 4.9** and **Table 4.5**. It appears that RyR2 residues 1-161, 161-346, 654-759 and 759-906 are involved in the interaction, with residues 654-759 most likely being the most important as this region is present in all positive constructs. Notably, presence of all four regions is indispensable for strong RyR2:cMyBP-C binding, as observed for BT4L + CT. Thus, lack of residues 1-161 results in ~30% reduction of relative binding ability of BT4DL + CT, deletion of residues 759-906 decreases relative binding ability of BT4 + CT by

~50%, lack of residues 1-161 and 759-906 causes ~70% reduction of relative binding ability of BT4D + CT, and amino acids 1-346 truncation seems to inhibit the BT4EL + CT binding by ~50% (all relative to positive BT4L + CT). Interestingly, BT4B (residues 346-759) and BT4BL (residues 346-906) which also have amino acids 654-759, scored as negative, with the latter displaying weakly positive, but not reproducible results.

It is possible that residues 346-530, without presence of flanking residues 161-346 and 565-654, are responsible for the incorrect secondary structure of this region (**Table 4.5, highlighted in orange**), which appears to completely inhibit the interaction with CT. Also, residues 1-346 and 565-654 on their own are not sufficient to mediate the interaction, as observed for BT4C + CT. Further, deletion construct BT4L$^{\Delta\beta8\text{-}\beta9}$ lacking residues 167-175 did not display any difference in binding ability with CT when compared to BT4L + CT (**Figure 4.1 A**), therefore it seems that those residues are not important for RyR2:cMyBP-C association (for further explanation see **Section 4.5.2**). In conclusion, the determinants for the cMyBP-C:RyR2 binding are residues 1-167, 175-346, 654-759 and 759-906. As the residues 165-223 are included in the two β strands of the surface exposed region of subdomain A (**Figure 4.10, A' and B', black arrow**), it is possible that those are directly involved in mediating the interaction, as observed in case of positive constructs BT4, BT4D and BT4DL (**Table 4.5**).

Mapped RyR2 residues 654-906 (coordinates for RyR1: 642-894) are contained within the first part of SPRY1 domain and also overlap with first 43 amino acids of P1 (residues 632-826 and 851-1055, respectively, RyR1 coordinates by (Yan et al. 2015), residues 650-844 and 844-1054, RyR2 coordinates by (Borko et al. 2014)), whereas RyR2 residues 1-167 (coordinates for RyR1: 1-154) and 175-346 (coordinates for RyR1: 162-330) belong to NTD subdomain A and B (residues 1- 205 and 206–394, respectively, RyR1 coordinates by (Tung et al. 2010; Yan et al. 2015); and 10-223 and 224–408, respectively, for RyR2 (Borko et al. 2014)), which appear to be ~190Å apart in single RyR1 subunit (**Figure 4.11**). Notably, all regions seem to be surface exposed towards cytosol, thus physically accessible for the interaction to take place. Interestingly, (Borko et al. 2014) reported that while NTD subdomains A and C are structurally very similar in all published structures of human RyR2 (4JKQ, amino acids 1-606), rabbit RyR1 (2XOA; amino acids 1–559; (Tung et al. 2010))

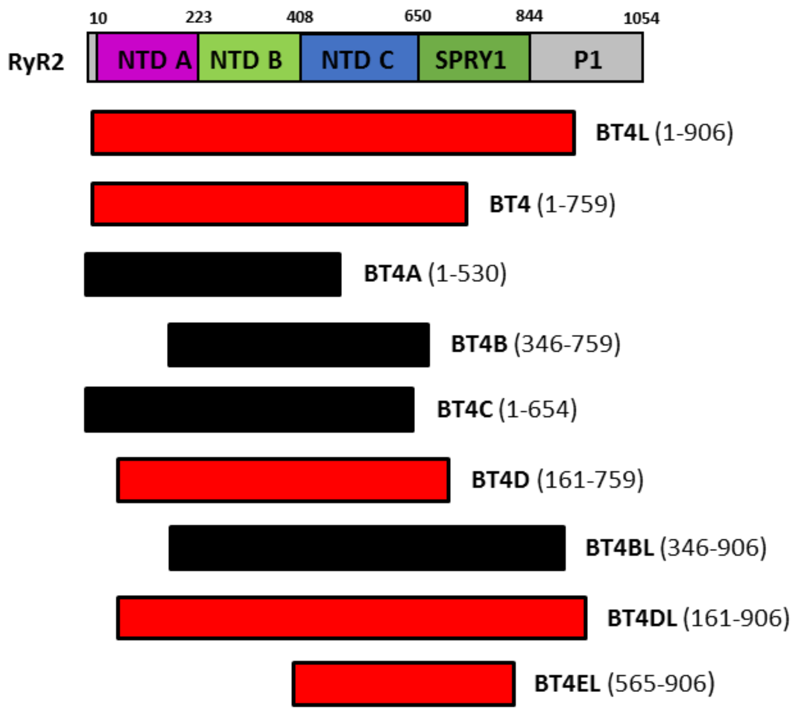

Figure 4.9 Graphical representation of fragments used in mapping of the minimal RyR2 region interaction with cMyBP-C CT using co-IP assays. Upper rectangle is the N-terminal 1-1054 amino acids RyR2 sequence, with depicted domain organisation according to (Borko et al. 2014). Rectangles below are RyR2 overlapping fragments tested for cMyBP-C binding. Rectangles in red (BT4L, BT4, BT4D, BT4DL, BT4EL) are fragments positive for the interaction with cMyBP-C CT.

Table 4.5 Summary of RyR2 residues mapped to be important for the association

construct	**1-161**	**161-346**	**346-530**	**565-654**	**654-759**	**759-906**	**+ CT binding description (versus BT4L + CT)**
BT4DL	no	yes	yes	yes	yes	yes	positive, ~30 % reduction
BT4	yes	yes	yes	yes	yes	no	positive, ~50% reduction
BT4D	no	yes	yes	yes	yes	no	positive, ~70% reduction
BT4EL	no	no	no	yes	yes	yes	variable, positive, ~80% reduction
BT4BL	no	no	yes	yes	yes	yes	variable, negative
BT4A	yes	yes	yes	no	no	no	negative
BT4B	no	no	yes	yes	yes	no	negative
BT4C	yes	yes	yes	yes	no	no	negative

Notes: regions included in the mapped fragment are shown in green, proposed misfolded region contained within residues 346-530 is shown in orange,

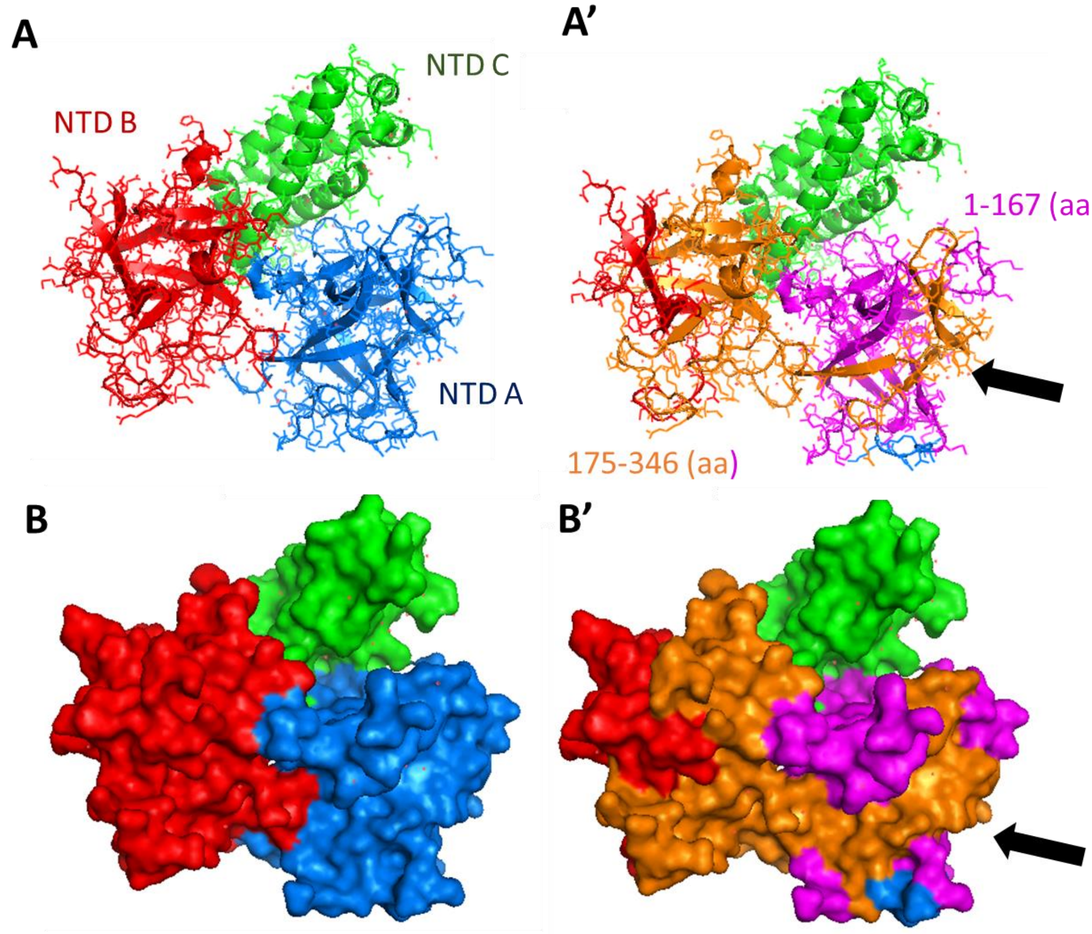

Figure 4.10 Location of mapped cMyBP-C CT regions in 3D structure of the human RyR2 NTD residues 1-606 at 2.39 Å. A depicts the structure as cartoon and B as sphere. A’ and B’ show corresponding mapped region. Subdomain NTD A is labelled in blue (residues 10-223), NTD B in red (residues 224-408) and NTD C in green (residues 409-544), whereas mapped regions are shown in pink (residues 1-167) and orange (residues 175-346). Residues 165-223 exposed on the surface of subdomain A are indicated with black arrow. Images created using The PyMOL Molecular Graphic Software (based on (Borko et al. 2014), accession number 4JKQ).

and mouse RyR2 (4l4H; amino acids 1–547; (Kimlicka et al. 2013)), they show large differences between the structures of subdomain B. The largest dissimilarity can be observed in the region of the long loop composed of residues 333–361 in subdomain B, which are contained in our mapped 175-346 binding site.

The N-terminal formed ring-like region has been shown to undergo large conformational changes upon channel activation (Samso et al. 2009; Efremov et al. 2015; Zheng 2015), with this region known to harbour more than 50 disease mutations, almost all located at domain interfaces (Amador et al. 2009; Tung et al. 2010). Based on these observations, it has been proposed that these disease

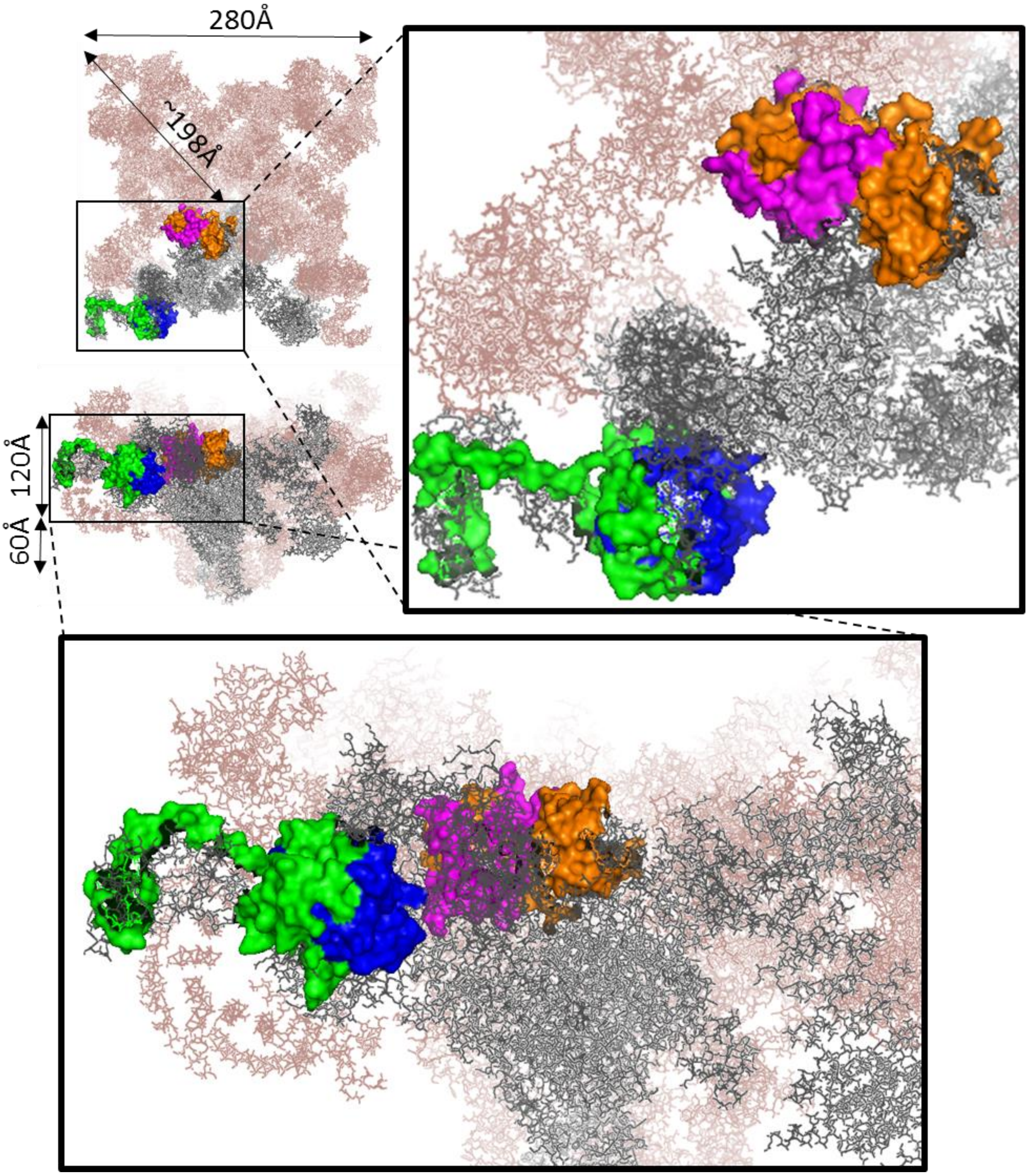

Figure 4.11 Location of mapped cMyBP-C CT interaction regions in 3D structure of the rabbit RyR1 at 3.8 Å. Proposed residues are labelled with pink (RyR2 residues 1-167, coordinates for RyR1: 1-154), orange (RyR2 residues 175-346, coordinates for RyR1: 162-330), blue (RyR2 residues 654-759, coordinates for RyR1: 642-747) and green (RyR2 residues 759-906, coordinates for RyR1: 742-894) within single RyR1 subunit (grey). Images created using The PyMOL Molecular Graphic Software (based on ((Yan et al. 2015), accession number 3J8H).

mutations might destabilize domain interfaces, which, in turn, would alter the conformational changes that are important in regulation of channel gating (Lobo and Van Petegem 2009; Lobo et al. 2011; Amador et al. 2013). Consistently, the RyR2 N-terminal disease mutations have been shown to enhance the activation of the channel (Jiang et al. 2005; Jiang et al. 2010; Tang et al. 2012; Liu et al. 2013). Additionally, recent work of (Liu et al. 2015) found that each domain of NTD has a specific role in governing the RyR2 channel activity, with the NTD subdomain A (residues 1-217) being important for termination, but not for activation of Ca^{2+} release, with the subdomain B (residues 218-409) being involved in stabilizing the closed state of the channel important for both activation and termination of Ca^{2+} release, and subdomain C (residues 410-543) being critical for channel activation and expression. Thus, since part of the mapped RyR2 + CT binding region is contained within the NTD subdomains A and B (residues 1-346), it could be possible for cMyBP-C to affect channel function by directly altering channel gating, i.e. by inhibiting the RyR2 activity.

The SPRY domains have one of the most common β-sandwich folds in eukaryotes and a broad range of functions, with the role in RyRs still poorly understood. In general, SPRY can be found as central domains in ligases, where they act as binders of regulatory proteins (Perfetto et al. 2013). Their positions in RyR1 suggest that among other possible functions, they might maintain channel structural integrity by mediating contacts between two large α-solenoid domains (helical and central) and provide a scaffold for the P1 domain (Efremov et al. 2015). Notably, the recently obtained crystal structures of SPRY1 and P1 region indicates that SPRY1 loop is a major FKBP binding determinant, with disease mutation in the SPRY1 domain affecting the FKBP binding (Yuchi et al. 2015). The same authors propose that those mutations, through interfering with the folding, might affect the closed state of the channel and decrease the appearance of RyR subconductance states. Therefore, cMyBP-C may either directly compete for FKBP binding site and/or disrupt the RyR2 N-terminal and central region interactions.

To test whether observed *in vitro* results can be reproduced in a living cell, the Y2H system was employed to verify binding of C-T fragment and the same set of truncated RyR2 fragments (**Table 4.4**). Detected with WB expression levels were not homogenous, with the smaller BT fragments expressed at higher levels than the bigger fragments BT4L and BT4. Interestingly, β-galactosidase assays indicated an interaction between CT + BT4L and weaker CT + BT4, whereas interaction with smaller RyR2 BT fragments could not be detected. These findings emphasize that protein abundancy does not have any bearing on the detection of interaction, with the identity of interacting fragments linked to true relative binding ability and specificity of cMyBP-C:RyR2 interaction.

4.5.2 cMyBP-C appears to interact with single RyR2 subunit

The NTDs are known to make key interactions stabilizing the cytosolic assembly of the channel, both with other domains in the same protomer, and with N-terminal domains contributed by neighbouring subunits. A major feature of this cytosolic assembly interaction is the apparent homotetramer formation by the RyR2 N-terminal region (Zissimopoulos et al. 2013), a property that is conserved in the inositol 1,4,5-trisphosphate receptors, another Ca^{2+} release channel family that share ~30% homology with RyRs and display high conservation of structure-function relationship (Zissimopoulos et al., 2014). The interacting surfaces of subdomains A and B have been shown to display a prevalence of positive (D18, E22, D61) and negative (R276, R281, H288, R298, K319) electrostatic potentials distribution of amino acid sequences, respectively, suggesting a significant role of electrostatic interactions in RyR2 central rim tetramerization (Borko et al. 2014). For the RyR1, those sites included flexible loops connecting β-strand 20 and 21, β22-23 and a part of loop connecting β-strand 8 and 9, with the two latter proposed to mediate the homotetramer formation. Further, the β8-β9 loop contains three arrhythmia associated mutations (P164S, R169Q and R176Q) implying the functional importance of residues contained within this loop (Seidel 2014). Importantly, disruption of N-terminal inter-subunit interactions within RyR2 has been reported to increase channel activity at low Ca^{2+} concentrations, suggesting that N-terminus tetramerization is involved in RyR2 channel closure (Zissimopoulos et al. 2013). Since the part of the initial mapped CT binding region spans residues 1-346, we hypothesized that RyR2 N-terminus tetramerisation may be required for RyR2:cMyBP-C interaction to occur. However, deletion construct $BT4L^{\Delta\beta8\text{-}\beta9}$ lacking residues 165-195 did not display any difference in binding ability with CT when compared to BT4L + CT (**Figure 4.4 A and B**), thus it is likely that cMyBP-C is interacting with an RyR2 interface provided by the single monomer rather than by two adjacent RyR2 subunits.

4.5.3 RyR1:MyBP-C interaction may occur in skeletal muscle

Parallel experiments with the corresponding N-terminal fragments from the skeletal muscle isoform RyR1 (amino acids 1-915) indicated robust interaction with cMyBP-C C-T by Y2H (**Table 4.4**) and form co-IP analysis (**Figure 4.6**). These results suggest that MyBP-C binding is conserved in other RyR isoforms and thus could be relevant in regulation of ECC coupling not only in cardiac muscle, but also in skeletal muscle. Further studies should help to unravel the precise molecular mechanism(s) by which MyBP-C binding is involved in the possibly dynamic, RyR isoform specific regulation of intracellular Ca^{2+} release.

4.5.4 The cMyBP-C Fn domains are responsible for RyR2 binding

The smallest cMyBP-C constructs retaining RyR2 BT4L interaction were C6-C7 (residues 820-972) and C9-C10 (residues 1061-1274), which displayed comparable binding ability to the original cMyBP-C CT fragment isolated from the Y2H screen (**Figure 4.7 B** and **Figure 4.12**). Both fragments have Fn domains, and especially C7 or C9 seem to be important for RyR2 interaction. C6 also belongs to the Fn fold, but it is unlikely to be as important because only half of it is present in the C6-C7 construct and also because the NT construct that contains the whole C6 domain does not interact with BT4L (see **Section 3.4.5.).** Comparable BT4L binding was obtained between C6-C7 and fC6-C7, which contains the whole C6 domain, further indicating that C7 rather than C6 is the main contributor to the interaction. Importantly, none of single domain constructs (fC6, C7, C8 or C9) could retain the interaction, suggesting that at least two domains are required to sustain the binding, one Fn and one additional neighbour being either Ig or Fn domain, and with each additional domain further strengthening the binding.

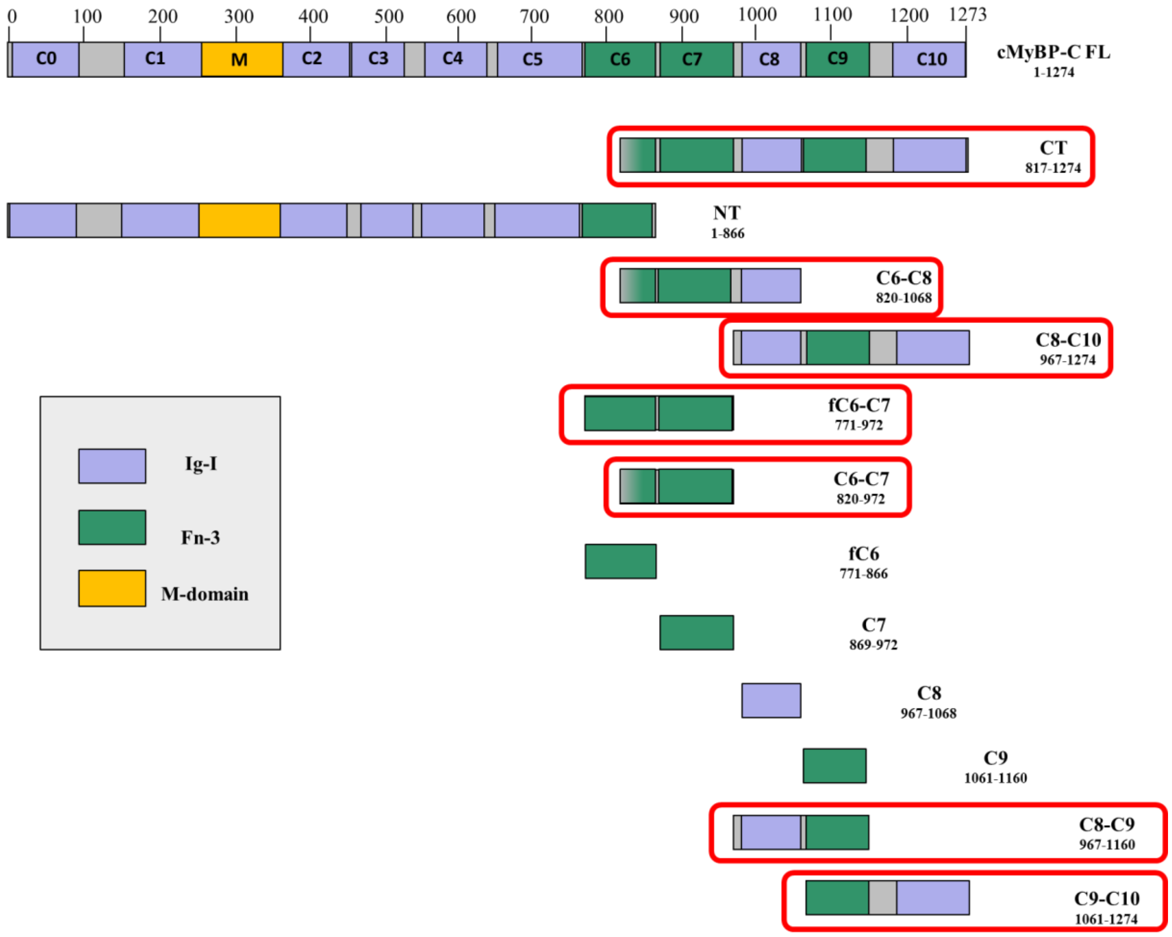

Figure 4.12 Graphical representation of fragments used in mapping of the minimal cMyBP-C region interaction with RyR2 BT4L using co-IP assays. Top rectangle represents the whole cMyBP-C FL sequence, while subsequent rectangles are cMyBP-C overlapping fragments tested for RyR2 binding. Rectangles encircled in red (CT, C6-C8, C8-C10, fC6-C7, C6-C7, C8-C9, C9-C10) are fragments positive for the interaction.

The requirement for an additional domain may simply be to enable and/or stabilise the correct folding of the C7/C9 domains, which are the primary RyR2 binding sites. Alternatively, secondary interaction may occur with this additional domain or within the linker sequence between the two domains. Altogether, Ig and Fn domains are connected linearly with ~4nm repeats, creating a full-length cMyBP-C molecule of ~50nm (~500Å) long (Furst et al. 1992). Crystal and NMR structures of cMyBP-C domains show that each Ig and Fn domain displays a compact, ~10kDa globular fold with dimensions ~2x3x4nm (Nadvi et al. 2016), thus the predicted length of cMyBP-C CT fragment, considering linear alignment of each globular domain, would appear to be ~180Å (~18nm), in line with the ~190Å distance calculated for the RyR binding site within the same protomer (**Figure 4.11**).

Approximately 2% of all animal proteins contain the Fn type 3 repeat (Koide et al. 1998). It belongs to one of the three types of internal Fn repeats found in the plasma protein fibronectin, with the 10th Fn type 3 domain shown to be directly involved in the interaction between fibronectin and its cell-surface receptors, integrins, a signalling process which is important for the wound healing (Pierschbacher and Ruoslahti 1984). Further, (Martino and Hubbell 2010) reported that the fibronectin region spanning the 12th to 14th Fn type 3 repeats acts as growth factor-binding site, with recent evidence suggesting that the close proximity of this region to the Fn 12th to 14th allows strong cross talk between the integrins and growth factor receptors (Lin et al. 2011). Further, it has also been shown that domains Ig 53 to Fn 2 of molluscs obscurin interacts with MEL-26 protein, pathway important for regulation of microtubule length (Wilson et al. 2012), whereas domains Ig-Ig-Fn 168-70 of titin are important its proteasome-dependent degradation by serving as direct binding site for an E3 ubiquitin ligase MURF1 (Mrosek et al. 2007). Thus, the proposed by us Fn/Ig or Fn/Fn domains cMyBP-C interaction with RyR2 would add to the already established functional diversity of Fn type 3 domain.

4.5.5 Conclusions

In conclusion, we have identified the C-terminus of MyBP-C as a novel interacting partner for mammalian RyR1/3 isoforms. Next, mapping of minimal binding regions of both proteins have shown that cMyBP-C residues 820-972 and 1061-1274, and RyR2 amino acids 1-167, 175-346 and 654-906 are important for RyR2:cMyBP-C interaction. We propose that cMyBP-C domains C6-C7 and C9-C10 mediate RyR2 interaction, presumably by binding to both NTD A-B and SPRY1-P1 regions of single subunit simultaneously.

Chapter 5

Functional modulation of RyR2 channel by cMyBP-C

5 Functional modulation of RyR2 channel by cMyBP-C

5.1 Introduction

As discussed in **Chapter 1**, intracellular Ca^{2+} release from the SR store through RyR2 channels is a crucial event during ECC, which must be carefully regulated for normal contraction and subsequent relaxation of the mammalian heart (Bers 2004). It is well known that RyR2 activation is governed predominantly by cytosolic Ca^{2+}, but also by Ca^{2+} accumulated within the SR lumen, where small increases in luminal Ca^{2+} load have been shown to generate large elevations in Ca^{2+} efflux (Gyorke et al. 2004). RyR2 Ca^{2+} release is also modulated by several accessory proteins (see **Section 1.2.3**), and the findings presented in **Chapters 3** and **4** highlight for the first time the possible link between the predominantly sarcomeric protein cMyBP-C and RyR2. The functional characterisation of the possible cMyBP-C impact on RyR2 regulation was pursued in this Chapter.

The possible implication with regards to the role that cMyBP-C plays in the shaping of myoplasmic Ca^{2+} transient can be deduced from the evidence provided by three independent cMyBP-C KO models reporting impaired relaxation and altered Ca^{2+} transients due to lack of cMyBP-C (Song et al. 2003; Brickson et al. 2007; Pohlmann et al. 2007). All of the aforementioned papers have shown that isolated cMyBP-C deficient cardiomyocytes exhibit prolonged Ca^{2+} transient decay time when compared with their wildtype counterparts, while (Pohlmann et al. 2007) also reported increased rate of Ca^{2+} transient activation (~27%). The study by (Song et al. 2003) using a homozygous mouse DCM model developed by (McConnell et al. 1999) (generated by the insertion of a neomycin resistance gene into exon 30 resulting in exon-skipping and a C-terminal truncated cMyBP-C, where little or no mutant protein is expressed) demonstrated 33% increase in Ca^{2+} transient decay. An increase by 19% was reported in the second study by (Brickson et al. 2007) using functional cMyBP-C KO (developed by (Harris et al. 2002) in which exons 3-10 of the endogenous cMyBP-C were replaced by a neomycin resistance gene), whereas a smaller but statistically significant increase of 11% was found in the third study by (Pohlmann et al. 2007) (employing transcriptional KO generated by (Carrier et al. 2004) with targeted deletion of exons 1-2 of the mouse MYBPC3 gene, which includes the translation initiation site), without any evident changes reported in peak Ca^{2+} transient amplitude. As already outlined in **Chapter 1**, the rate of cytoplasmic Ca^{2+} transient decay is dictated by the actions of SERCA (which pumps Ca^{2+} into the SR) the NCX, (which is responsible for Ca^{2+} extrusion out of the cell), and the possible SR Ca^{2+} leak through the RyR2, which normally is minimal but could be substantial in pathological conditions (Marx et al. 2000; Kubalova et al. 2005). In the mouse heart, the contribution of SERCA is ~92% whereas that of the NCX is ~7% (Li et al. 1998; Yao et al. 1998; Fearnley et al. 2011), with phosphorylation of PLB known to relieve its inhibition on SERCA Ca^{2+} uptake activity (Bers 2002). While RyR2 expression and/or channel activity was not investigated in any of the aforementioned three papers, (Song et al. 2003) reported diminished SERCA levels (~20%) when compared to WT, with no difference in PLB expression, which could account for the increased SERCA-PLB inhibition and observed prolonged Ca^{2+} transient. However, they did not assess the PLB phosphorylation level, thus whether diminished SERCA activity is indeed exclusively responsible for the observed effect requires further investigation. Further, (Pohlmann et al. 2007) reported that the amount of NCX was 34% lower, while SERCA and PLB expression was identical between both KO models versus wildtype, but the level of phosphorylated PLB was 3-fold higher in knockout than in WT. Therefore, the Ca^{2+} transient decay time would be expected to be reduced rather than increased, with the observed prolonged Ca^{2+} transient seen in cMyBP-C KO mice rather unlikely to be solely due to lower NCX levels given the relative contribution of SERCA (~92%) and NCX (~7%) in diastolic Ca^{2+} removal, thus it could involve potential SR Ca^{2+} leak through the RyR2. Interestingly, when cMyBP-C KO cardiomyocytes were stimulated with an β-AR agonist isoproterenol, the calcium transients in cMyBP-C KO cardiomyocytes appeared to be no different than WT (Brickson et al. 2007), which highlights the possibility that flight-or-fight response is capable of attenuation cMyBP-C KO phenotype. Therefore, it is possible that cMyBP-C may be involved in suppression of diastolic SR Ca^{2+} leak through its interaction with RyR2, thus be normally required to inhibit RyR2 function. On the other hand, a study by (Fraysse et al. 2012) showed faster Ca^{2+} transient decay in myocytes isolated from a KI mouse model expressing an HCM missense mutation (developed by (Vignier et al. 2009), where point mutation G to A transition in exon 6 in MYBPC3 gene that resulted in decreased cMyBP-C expression by ~20% in HET and by ~90% in homozygous animals versus WT). Interestingly, (Cheng et al. 2013) have shown that an HET mice model (developed by (Harris et al. 2002)) with decreased cMyBP-C expression similar to those of HET human HCM (~32% when compared to WT) displayed unchanged Ca^{2+} transient kinetics without any evident alterations in Ca^{2+} handling proteins (RyR2, SERCA, NCX, PLB or phosphorylated PLB). These data indicate the presence of several compensatory mechanism(s) required to improve diastolic relaxation in the cMyBP-C KO and HCM cMyBP-C mutant hearts, with observed changes directly linked to altered Ca^{2+} transients. The reported alterations may be also part of the adaptive process, and not be directly linked to cMyBP-C Ca^{2+} homeostasis regulation, since cMyBP-C phosphorylation is also known to influence the rate of thin filament deactivation and cross-bridge cycling (Moss et al. 2015), both of which contribute towards muscle relaxation (Biesiadecki et al. 2014). The above studies suggest that cMyBP-C can affect the Ca^{2+} transient through a possible inhibitory role on RyR2. We therefore assessed the action of cMyBP-C on RyR2 function using two independent functional assays: equilibrium $[^3H]$ryanodine binding and single cell Ca^{2+} imaging.

Ryanodine is known to have a complex effect on the conductance and the gating of single RyR channels. In particular, ryanodine at submicromolar to micromolar concentrations (up to 1 μM) results in the channel exhibiting partially conducting or subconductance states (approximately 40-50% of the full conductance state), whereas prolonged exposure to micromolar concentrations (>10 μM) has inhibitory effect on RyR (Sutko et al. 1997). These effects are observed consistently and have become a signature for ryanodine:RyR binding, with the mechanism of interaction proposed to alter the conductance state of the RyR by stabilizing a specific conformation of the channel via allosteric effect. The complexity of ryanodine:RyR binding is most likely due to the presence of several binding sites exhibiting high (K_d ∼1-10 nM) and low (K_d ∼1-10 μM) affinities (Lai et al. 1988). It is also generally accepted that the low affinity binding causes channel inhibition (with up to three sites being proposed), while binding to a single high affinity site per tetrameric channel results in RyR activation and conductance sub-states, indicating that ryanodine binds to a RyR conformation associated with an open state of the channel. This ryanodine property has proven to be useful as a tool for channel characterisation, because any detected changes in the ryanodine binding levels would also reflect changes in channel function. Therefore, ryanodine binding can be used as an index of channel activation, with the introduction of radiolabelled [^{3}H]ryanodine allowing an indirect quantification of Ca^{2+} sensitivity of channel populations (Pessah et al. 1985; Meissner and el-Hashem 1992). This method involves mixing SR vesicles or other RyR-containing sample (i.e. HEK293 cell homogenates expressing recombinant RyR2) in buffered Ca^{2+} assay medium with the isotope-labelled (8 nM final concentration), while an excess of un-labelled ryanodine (10 µM final concentration) is used for determination of non-specific binding, followed by incubation period to allow equilibrium ryanodine binding. The bound [^{3}H]ryanodine is further collected using a filtration device and the remaining radioactivity is determined by liquid scintillation counting (Du et al. 1998). Our experimental approach involved comparison of RyR2 activation profile in the presence and absence of cMyBP-C in a wide range of calcium concentrations. The reasoning behind this was that cytosolic cMyBP-C could interact with the RyR2 at the N-terminus binding sites of single subunit and thus possibly alter channel function.

Due to RyR intracellular location, techniques developed to study the channel behaviour both *in situ* (primary cells and tissues) and *in vivo* (heterologous systems) are based on the visualization of Ca^{2+} flux passing from SR/ER into the cytosol with the aid of fluorescent Ca^{2+} indicators. The changes in fluorescence intensity, captured with confocal laser scanning microscopy, reflect the changes in binding of free Ca^{2+} to the indicator, hence it becomes possible to monitor global variations of the $[Ca^{2+}]_i$ (Cannell and Cody 2006). For this purpose, Fluo-3 AM was employed in this study as it is one of the most widely used Ca^{2+} probes, since it displays a large dynamic range, low compartmentalization and high Ca^{2+} binding affinity (Thomas et al. 2000). To assess the effect of cMyBP-C on RyR2-mediated intracellular Ca^{2+} handling in a more physiological context than equilibrium [^{3}H]ryanodine binding, a cellular assay developed by (Jiang et al. 2002) was used, as it enables the recombinant proteins to be studied in a background not complicated by endogenous expression of RyR2 or its cardiac-specific accessory proteins (Chen et al. 1997). The paper by (Jiang et al. 2002) has shown that HEK293 cells expressing RyR2 display spontaneous Ca^{2+} release events in a manner indistinguishable from cardiac myocytes. Notably, this phenomenon is directly linked to RyR2 expression, as untransfected cells that do not have recombinant RyR2, neither display Ca^{2+}

transients nor respond to caffeine. Using this technique, parameters of spontaneous Ca^{2+} release (SCR), such as amplitude, duration and frequency can be monitored to establish any differences in Ca^{2+} handling between HEK293 cells expressing RyR2 channels in conditions of interest, i.e. with or without cMyBP-C presence.

More than 150 disease-associated RyR2 mutations have been identified to date, with the majority shown to be clustered in four hotspots in the linear sequence of the channel. Notably, N-terminal hot-spot (amino acids 44-466) variants account for ~18% of all cases reported (Priori and Chen 2011), demonstrated to be causative by aberrant activation and/or termination of Ca^{2+} release (Jiang et al. 2010; Tang et al. 2012; Liu et al. 2013). It has been proposed that the functional impact of those variants is linked to destabilization of NTD domain interfaces, which, in turn, alters conformational changes in the N-terminal region that are important for channel gating (Tung et al. 2010; Lobo et al. 2011; Kimlicka et al. 2013). Consistent with this hypothesis, recent study by (Liu et al. 2015) using NTD deletion mutants shown for the first time that individual NTD subdomains of RyR2 are involved in distinct roles in channel function (with NTD A being important for Ca^{2+} release termination; NTD B-stabilization of the closed state and thus crucial for both activation and termination of Ca^{2+} release; and NTD C involved in channel activation) and thus providing valuable insights into the possible molecular basis of different functional phenotypes of N-terminal RyR2 mutations pathogenesis. Notably, an increasing body of evidence suggests that defective RyR2 function can lead not only to cardiac arrhythmias but also cardiomyopathies. A recent multiscale DCM genotyping study by (Haas et al. 2014) has shown for the first time that RyR2 mutations can be readily found in patients with DCM, with the majority of identified missense mutations located in the first 1100 residues of RyR2. In order to assess whether impaired cMyBP-C:RyR2 interaction could contribute towards the reported functional variability of RyR2 N-terminus-linked mutations, four missense variants were investigated in this study: S166C, R176Q, R420Q and L433P (previously made in our lab in BT4L construct). S166C is a newly-identified DCM variant found in the N-terminal hot-spot with unknown impact on channel function (Haas et al. 2014), while R176Q and L433P are known to be causative of ARVD/CPVT and ARVD, respectively (Tiso et al. 2001). Interestingly, while heterologously expressed $RyR2^{R176Q}$ have been reported to display hyper-sensitised caffeine activation (Thomas et al. 2004) and enhanced sensitivity to luminal calcium (Jiang et al. 2005), the phenotype associated with the L433P mutation leads to a substantially desensitised response (Thomas et al. 2004), prolonged Ca^{2+} transients and reduced Ca^{2+} store content indicating defective channel closure (Tang et al. 2012; Seidel et al. 2015). Further, the missense $RyR2^{R420Q}$ variant linked to CPVT has been shown to have decreased amplitude and frequency of Ca^{2+} oscillations when compared to RyR2 wild-type cells (Domingo et al. 2014). In light of apparently different mechanisms of channel regulation by NTD domains and since the cMyBP-C binding region is contained within subdomains A and B, we employed the recombinant HEK293 expression system and the co-IP binding assay to biochemically test whether the presence of those mutations alters cMyBP-C:RyR2 binding.

5.2 Chapter objectives

In this Chapter studies were undertaken to elucidate whether cMyBP-C binding could affect RyR2 channel activity. In particular, the following points will be addressed:

- assessment of cMyBP-C impact on Ca^{2+} dependent RyR2 activation using equilibrium [^{3}H]ryanodine binding assay;
- assessment of cMyBP-C influence on spontaneous RyR2-mediated Ca^{2+} oscillations in HEK293 cells using single cell Ca^{2+} imaging;
- test whether cMyBP-C interaction with RyR2 could be affected in disease-causing point mutations in RyR2 N-terminus (S166C, R176Q, R420Q and L433P) using the co-IP assay.

5.3 Methods

5.3.1 [^{3}H]ryanodine binding

For the [^{3}H]ryanodine binding assay, ten 100 mm Petri dishes were co-transfected with either (1) the full length RyR2 and the empty HA-pCR3 vector or (2) with the full length RyR2 in combination with the full length cMyBP-C HA-tagged (FL) construct, using calcium phosphate transfection (**Section 2.2.5.3**). After 24 hours, cells were collected and each sample was homogenised (**Section 2.2.2.1**) and total protein content was measured with the BCA assay (**Section 2.2.2.2**). The recombinant protein expression was confirmed by SDS-PAGE and Western blotting (**Sections 2.2.2.4** and **2.2.2.5**, respectively) using Ab 1093 (anti-RyR2) and Ab HA (anti HA-tagged cMyBP-C). To estimate channel activation of each sample at a specific free Ca^{2+} concentration (**Section 2.2.9**), six Ca^{2+} concentration points were used: 100 nM, 250 nM, 500 nM, 1 µM, 5 µM and 100 µM. All subsequent statistical analysis was conducted using GraphPad Prism (see **Section 2.2.9** and **2.2.11**).

5.3.2 Generation of mCherry-modified pCR3 vector and mCherry-tagged full length (mCherry-FL) cMyBP-C construct

The full length mCherry cDNA coding sequence (accession number: AJN91097) was amplified using forward and reverse primers (mCherry.FOR.1-27 and mCherry.REV.689-708, respectively, **Table 2.1**) and obtained PCR product (708 b, with new *HindIII* restriction site at the 5' end and *NheI* restriction site at the 3' end, introduced by the primers) was cloned into the pCR3-HA-cMyBP-C (containing the full length cMyBP-C cDNA coding sequence, as described in **Sections 2.2.1.2-2.2.1.4**, and **2.2.3.1-2**).

5.3.3 ICC

RyR2 co-expression with mCherry-FL cMyBP-C or mCherry alone following Effectene-mediated co-transfection in HEK293 cells was further verified by ICC as described in **Sections 2.2.5.5** and **2.2.7**, with additional optimization, as all incubation steps in ICC were conducted in the dark to avoid mCherry photobleaching. For recombinant RyR2 detection, Ab 1093 and Alexa Fluor 488 were used, whereas mCherry fluorescence from co-transfected cells was excited using HeNe 594 laser at a wavelength of 594 nm and collected by a PMT set at 600-650 nm. To visualise the transfection efficiencies of (1) RyR2 with mCherry-FL cMyBP-C and (2) RyR2 with mCherry alone, the cells were imaged using an SP5 confocal microscope (Leica) with an oil immersion, x63 objective lens. HEK293 cells expressing the proteins of interest were counted using LEICA software and obtained values were further normalized towards the total number of all cells present in the selected field of view, represented as % transfection efficiency. All subsequent statistical analysis was conducted using GraphPad Prism (see **Section 2.2.11**).

5.3.4 Co-IP of mCherry-cMyBP-C and RyR2

The possible influence of a new tag, the mCherry protein, on recombinant human cMyBP-C conformation and its association with RyR2 was tested by HEK293 calcium phosphate co-transfection, followed by cell homogenization (**Sections 2.2.5.3** and **2.2.2.1,** respectively), co-IP, SDS-PAGE and WB (**Section 2.2.2.3-5)**. To enable the direct comparison of relative binding ability, HA-FL cMyBP-C + RyR2 samples were co-expressed in HEK293 and processed in parallel to mCherry-FL cMyBP-C + RyR2. For immunoblotting, Ab 1093 and Ab C-t (**Section 2.2.11**) were used to detect directly precipitated RyR2 and indirectly co-precipitated cMyBP-C of interest, respectively. The level of co-precipitated proteins was determined by densitometry (**Section 2.2.10**). All subsequent statistical analysis was conducted using GraphPad Prism (see **Section 2.2.11**).

5.3.5 Ca^{2+} imaging

HEK293 growing on 35 mm glass bottom dishes were transfected using Effectene reagent (**Sections 2.2.5.5**) with either (1) RyR2 alone or (2) RyR2 + mCherry-FL cMyBP-C or (3) RyR2 + mCherry. Subsequently, cells were loaded with Fluo3-AM and imaged in KHR buffer using a laser scanning confocal microscope (**Section 2.2.6**). Data were acquired as regions of interest from all cells displaying SCR (visualised as calcium oscillations) and/or caffeine dependent Ca^{2+} release events. Obtained traces were further exported to Microsoft Excel for off-line examination and subsequent statistical analysis was conducted using GraphPad prism (see Sections **2.2.6** and **2.2.11**).

5.3.6 Co-IP binding analysis of mutant RyR2 N-terminal constructs ($BT4L^{S166C}$, $BT4L^{R176Q}$, $BT4L^{R420Q}$ and $BT4L^{L433P}$) with cMyBP-C CT

Mammalian c-Myc tagged mutated RyR constructs (BT4L fragments, obtained from Dr S. Zissimopoulos, see **Table 5.1**) and cMyBP-C CT plasmid were used as cMyBP-C:RyR2 pairs to co-transfect HEK293 cells growing on 100 mm Petri dishes as described in (**Section 2.2.5.3**). All plasmids were co-transfected in ~1:1 molar ratio (12 µg + 12 µg per dish), homogenized (**Section 2.2.2.1**) and assayed for protein-protein interaction with co-IP (**Section 2.2.2.3**), followed by SDS-PAGE and WB (**Sections 2.2.2.4-5**). The level of co-precipitated proteins was determined by densitometry (**Section 2.2.10**) and statistical analysis was conducted using GraphPad Prism (**Section 2.2.11**).

Table 5.1 List of mutated BT4L RyR2 plasmids used. Coordinates correspond to the human RyR2 mRNA (accession number: X98330).

Construct	Coordinates	Length
BT4L^{S166C}	122-2840 (b) 1-906 (aa)	2718 (b) 906 (aa)
BT4L^{R176Q}	122-2840 (b) 1-906 (aa)	2718 (b) 906 (aa)
BT4L^{R420Q}	122-2840 (b) 1-906 (aa)	2718 (b) 906 (aa)
BT4L^{L433P}	122-2840 (b) 1-906 (aa)	2718 (b) 906 (aa)

5.4 Results

5.4.1 Optimisation of [^{3}H]ryanodine binding assay

Figure 5.1, A shows representative blot depicting successful cMyBP-C expression in RyR2 + cMyBP-C co-transfected samples (1+/2+/3+) and that remaining samples (1-/2-/3-) did not have any detectable levels of cMyBP-C as predicted, since cMyBP-C is a cardiac specific protein and unlikely to be expressed in an embryonic-kidney-derived cell line. To assure equal amounts of RyR2 in all samples to be tested (both RyR2 + HA-pCR3 and RyR2 + HA-FL cMyBP-C) by [^{3}H]ryanodine binding, RyR2 protein level was assessed by Western blotting and was adjusted accordingly to be comparable between the pairs 1+/1-, 2+/2-, 3+/3- (**Figure 5.1, B).** The paired homogenate sample aliquots (containing approximate equal RyR2 levels) were subjected to [^{3}H]ryanodine binding using conditions promoting maximum channel activation (100 µM Ca^{2+}, 10 mM caffeine, **Figure 5.1 C**). Typically, it enables to evaluate the capacity of cell preparations for maximum [^{3}H]ryanodine binding which reflects the total amount of functional RyR2 protein expressed. Knowing the value of maximum [^{3}H]ryanodine binding is necessary to normalise the data for comparison between samples of different origin. Furthermore, this step ascertains that WB adjustments indeed result in similar levels of RyR2 between the samples, as it can be prone to SDS-PAGE gel loading as well as protein transfer errors.

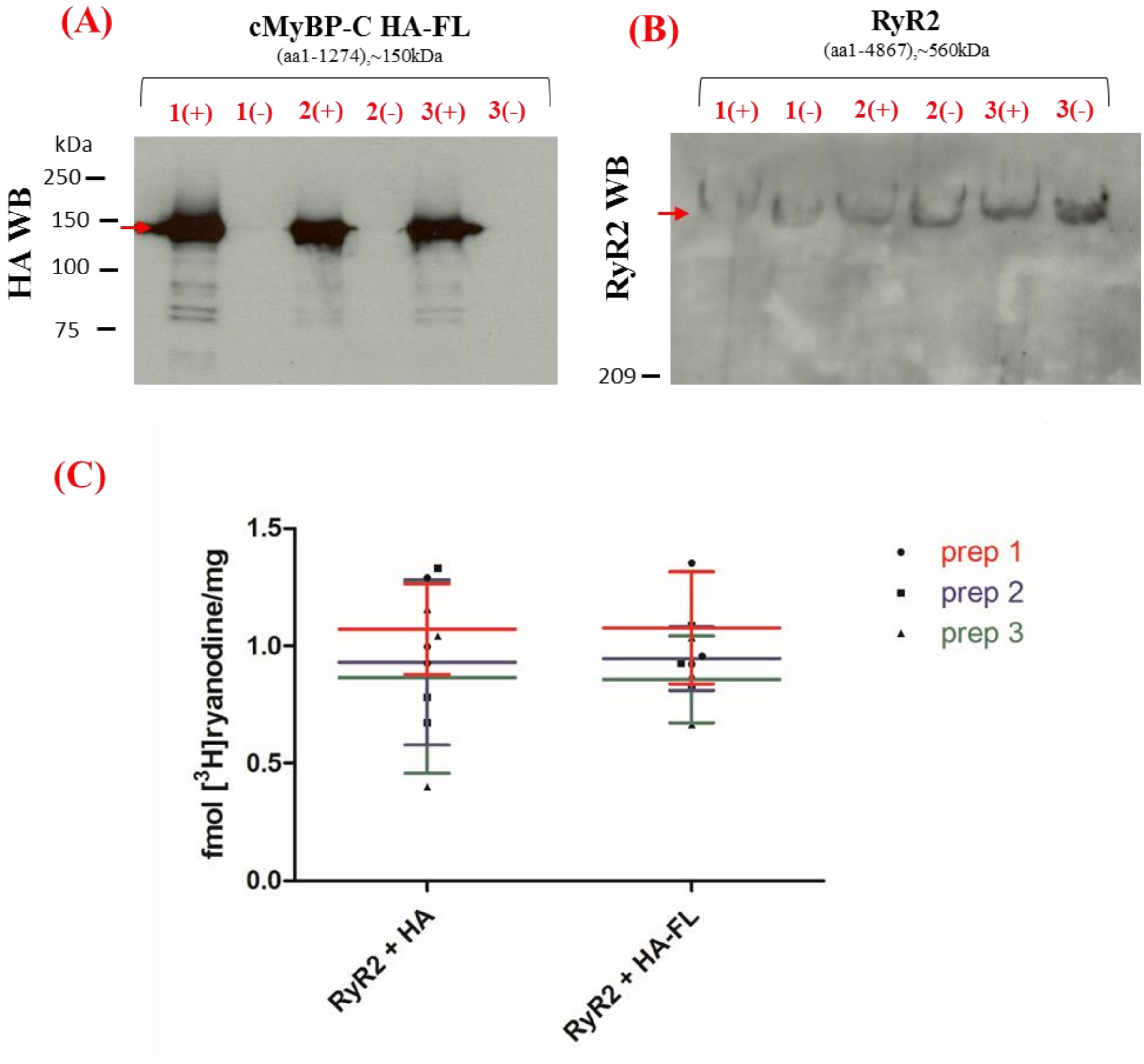

Figure 5.1 Representative blots showing protein expression in six independent homogenate preparations used in [^{3}H]ryanodine binding and graph summarising the cumulative maximum activation with 100 µm Ca^{2+} + 10mM caffeine. (A) WB for cMyBP-C HA-FL expression where equal amount of homogenates was loaded: (25 µg total protein); (B) WB for optimised RyR2 expression (left to right: 30, 40, 50, 40, 40 and 50 µg total protein were loaded). (+) corresponds to homogenates with co-expressed RyR2 + FL (lanes 1,3 and 5), whereas (-) is indicative of RyR2 + HA-pCR3 co-transfected HEK293 cell homogenates (lanes 2,4 and 6). (C) Data presented relative to maximum binding obtained for the each pair RyR2 (+HA) and shown as mean ±SD, n=3 for each preparation (1-3).

5.4.2 [^{3}H]ryanodine binding at different Ca^{2+} concentrations

Figure 5.2 A presents the data obtained for calcium dependence of [^{3}H]ryanodine binding for RyR2 + HA-FL cMyBP-C relative to RyR2 alone (+ HA empty vector). Dose-response curves of the above results are visualised in (**B)** (two model fits with three parameters, fourth parameter being bottom constrained) and best-fit values calculated with GraphPad Prism are outlined in **Table 5.2.** As shown in **Figure 5.2 A**, RyR2 activation appears to be weakly diminished by the presence of cMyBP-C relative to RyR2 at 1 µM Ca^{2+} (~20% decrease in RyR2 alone activity, statistical significance calculated using unpaired, 2-tailed Student's t-test). Interestingly, channel activity appears to be also decreased by a similar extent at 500 nM, 5 µM and 100 µM Ca^{2+} when compared to RyR2, although it did not reach statistical significance at these Ca^{2+} concentrations. Comparison of the dose response curves fitted with GraphPad (**Figure 5.2 B** and **Table 5.2**) showed that for both conditions, calcium concentration threshold for activation was above p[Ca^{2+}] = (-7) and reached plateau at p[Ca^{2+}] ~(-6). Interestingly, cMyBP-C presence did not result in any noticeable shift of the Ca^{2+} activation curve (EC_{50} = 214.7±38.7 nM [Ca^{2+}] for RyR2 alone versus EC_{50} = 163.2±33.7 nM for RyR2 + HA-FL cMyBP-C) or slope factor (Hill slope = 2.955±1.673 for RyR2 alone versus Hill slope = 4.032±1.998 for RyR2 + HA-FL cMyBP-C), but was responsible for lower maximal Ca^{2+} activation when compared to RyR2 only sigmoidal curve. Even though the observed differences for each data fit set scored as statistically significant ($p \leq 0.05$, assessed using the extra-sum of squares F test), high overlap of the error bars for each maximum Ca^{2+} binding point (**Figure 5.2**) made it difficult to provide a meaningful interpretation of the results.

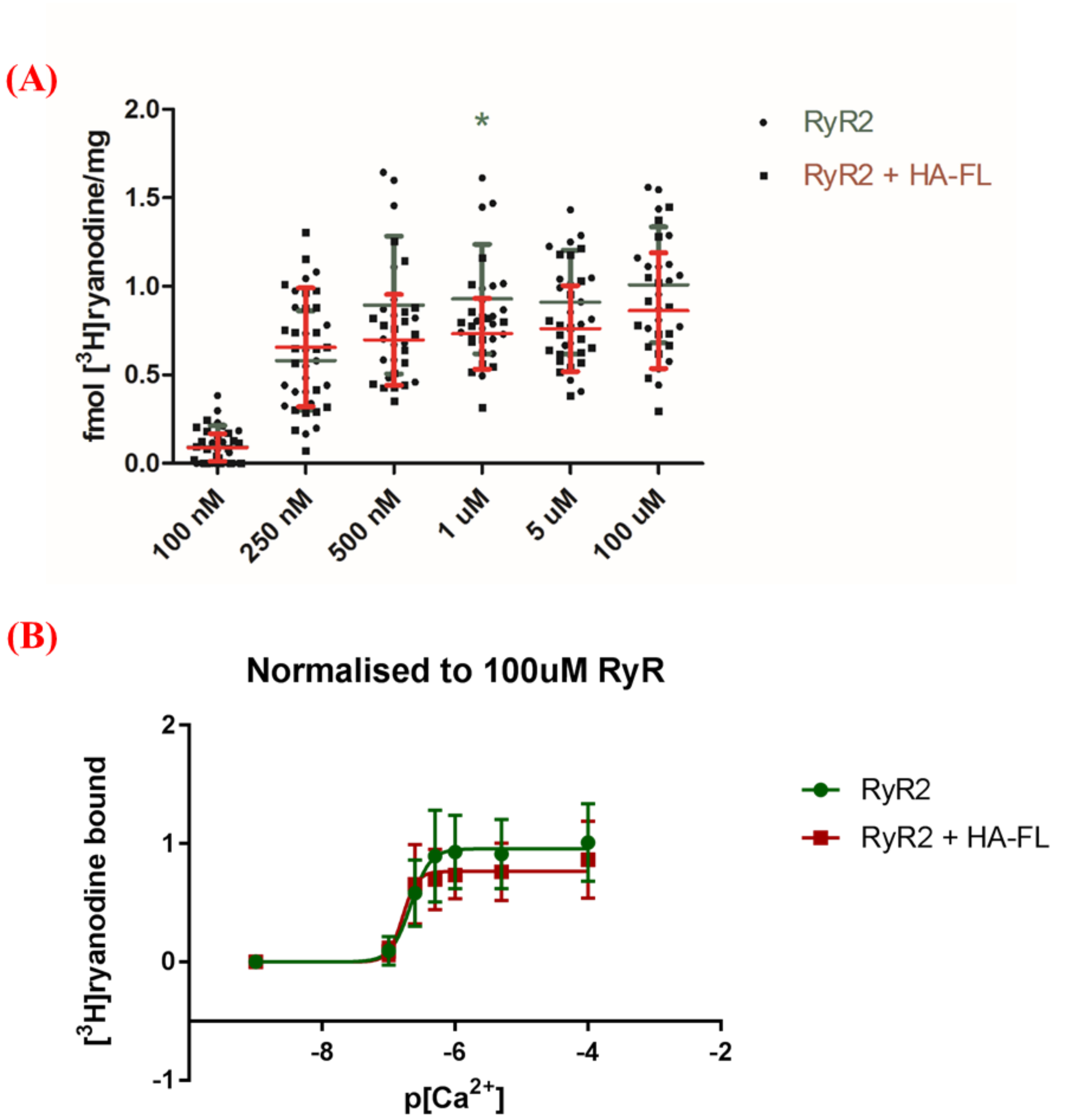

*Figure 5.2 Graph and model fits summarising the effect of the cMyBP-C HA-FL on RyR2 function as assessed in [^{3}H]ryanodine binding assay over a range of free Ca^{2+} concentrations. (A) Data presented relative to maximum binding obtained for the RyR2 (+HA) at 100µmol Ca^{2+} and shown as mean ±SD, * statistical significance at $p<0.05$ calculated using unpaired, 2-tailed Student's t-test, n≥15 for each Ca^{2+} concertation point. (B) Dose-response curve of RyR2 (+HA) and RYR2 + cMyBP-C HA-FL fitted with GraphPad Prism using four-parameter logistic model with bottom constrained to 0. Data shown as shown as mean ±SD, n≥15 for each Ca^{2+} concertation point.*

Table 5.2 Best-fit values obtained for RyR2 (+HA) and RYR2 + cMyBP-C HA-FL presented in Figure 5.2.

Best-fit values	**RyR2 only (+ HA)**	**RyR2 + HA-FL (cMyBP-C)**
Bottom	= 0.0 (constrained)	= 0.0 (constrained)
Top ***(95% Confidence Intervals)***	0.9564 *(0.8786 to 1.03)*	0.7653 *(0.7029 to 0.8276)*
Hill slope ***(95% Confidence Intervals)***	2.955 *(1.322 to 4.588)*	4.032 *(2.034 to 6.030)*
EC_{50} ***(95% Confidence Intervals)***	214.7 nM (176 to 262 nM)	163.2 nM (129.5 to 205.7 nM)

5.4.3 Generation of mCherry-pCR3 vector and mCherry-FL cMyBP-C construct

Both plasmid DNA constructs designed to express mCherry protein and mCherry-tagged full length cMyBP-C (mCherry-FL cMyBP-C) were successfully generated and their DNA sequences were confirmed. A typical set of results representing intermediate steps of the cloning process is shown in **Figure 5.3.**

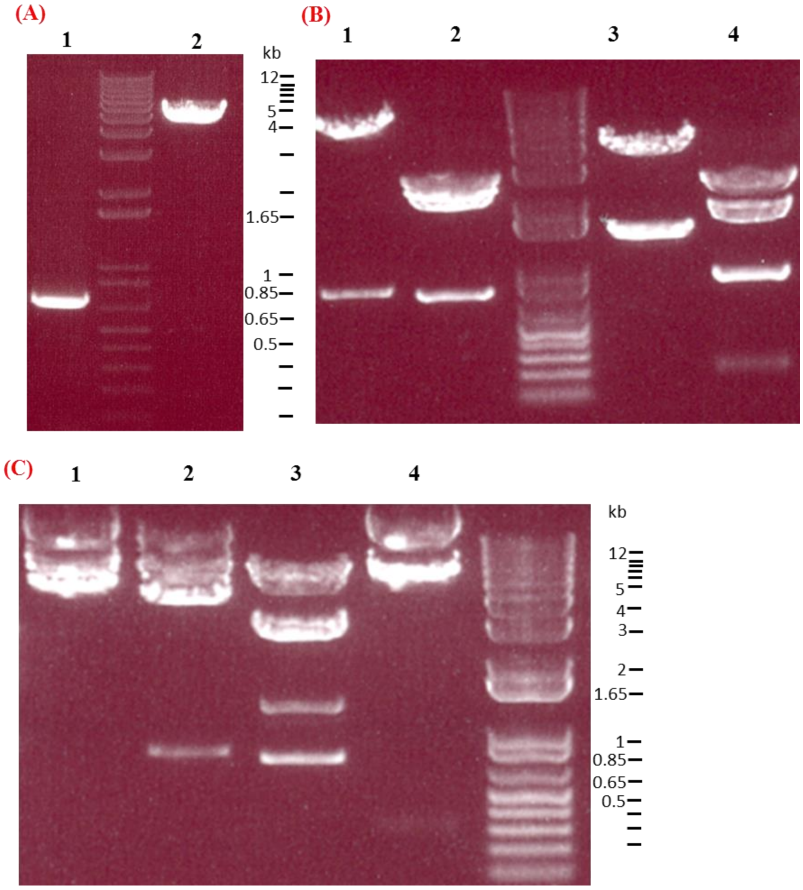

Figure 5.3 Intermediate steps of the experimental procedure generating the mCherry and mCherry-FL constructs. (A) DNA gel showing the amplification product obtained in the mCherry sequence PCR amplification (lane 1, expected band: 700 b) and empty pCR3 vector digested with HindIII/NheI (lane 2, expected size: 5.1 kb); (B) restriction digests of the selected positive clone containing the mCherry insert, verified by sequencing. From left to right: Lane 1: HindIII/NheI (expected bands: 5.1 and 0.7 kb), 2: MscI (expected bands: 2.8, 2.2 and 0.7 kb), 3: SpeI/ApaI (expected bands: 4.4 and 1.4 kb), 4: StuI/SpeI (expected bands: 2.8, 1.9, 0.86 and 0.2 kb); (C) restriction digests of the selected positive clone containing the mCherry-FL, verified by sequencing. From left to right: Lane 1: BamHI/XhoI (expected bands: 5.6 and 3.8 kb), 2: HindIII/NheI (expected bands: 5.3, 3.6 and 0.7 kb), 3: MscI (expected bands: 4.8, 2.8, 1.2 and 0.7 kb), 4: HindIII/XhoI (expected bands: 5.0, 4.3 and 0.3 kb).

5.4.4 mCherry- cMyBP-C can be successfully co-expressed with RyR2 in HEK293 cells

Immunofluorescence analysis was first conducted to confirm that the recombinant mCherry and mCherry-FL cMyBP-C proteins can be co-expressed with RyR2 within the same cell and correctly localised *in vivo*. Secondary Alexa Fluor 488 Ab labelling enabled estimation of transfection efficiency of RyR2, whereas direct excitation of mCherry fluorescent protein allowed to assess the mCherry alone and mCherry-tagged cMyBP-C expression. All proteins were expressed to levels clearly distinguishable from the background (**Figure 5.4 and 5.5; Appendix, Figure 8.3 and 8.4**) and yielded similar transfection efficiencies for both conditions (A: RyR2 + mCherry-FL cMyBP-C; B: RyR2 + mCherry) with Effectene transfection reagent (~20%/~25%, for both A and B, as illustrated in **Figure 5.6**), values almost identical to previous HA-FL cMyBP-C + RyR2 co-transfection results obtained with Turbofect reagent (see **Section 3.4.4**). Further, in similar manner to aforementioned transfection reagent, a high number of co-transfected cells was obtained for both (A) and (B), labelled green (for RyR2) and red (for mCherry or mCherry-FL cMyBP-C), calculated to be ~70% of all transfected cells for both conditions. As demonstrated in **Figures 5.4 and 5.5**, RyR2 (green) signals could be detected throughout the ER of the transfected HEK293 cells in both conditions (**A1, B1, C1**) in line with previous observations described in **Chapter 3.** Notably, the mCherry-FL cMyBP-C (red) signal was found to be distributed throughout the cytoplasm (**Figure 5.4, A2, B2, C2**) and readily detected in the region spanning from bottom side of the nucleus to the areas of the cell surface in direct contact with the coverslip (**A4. B4, C4, dashed box**), which failed to be observed in our RyR2 + cMyBP-C HA-FL co-localisation study in HEK293 cells (see **Section 3.4.5**). On the other hand, the monomeric mCherry protein displayed very low cytoplasmic expression pattern, with the majority of the signal localized in the nucleus (**Figure 5.5**).

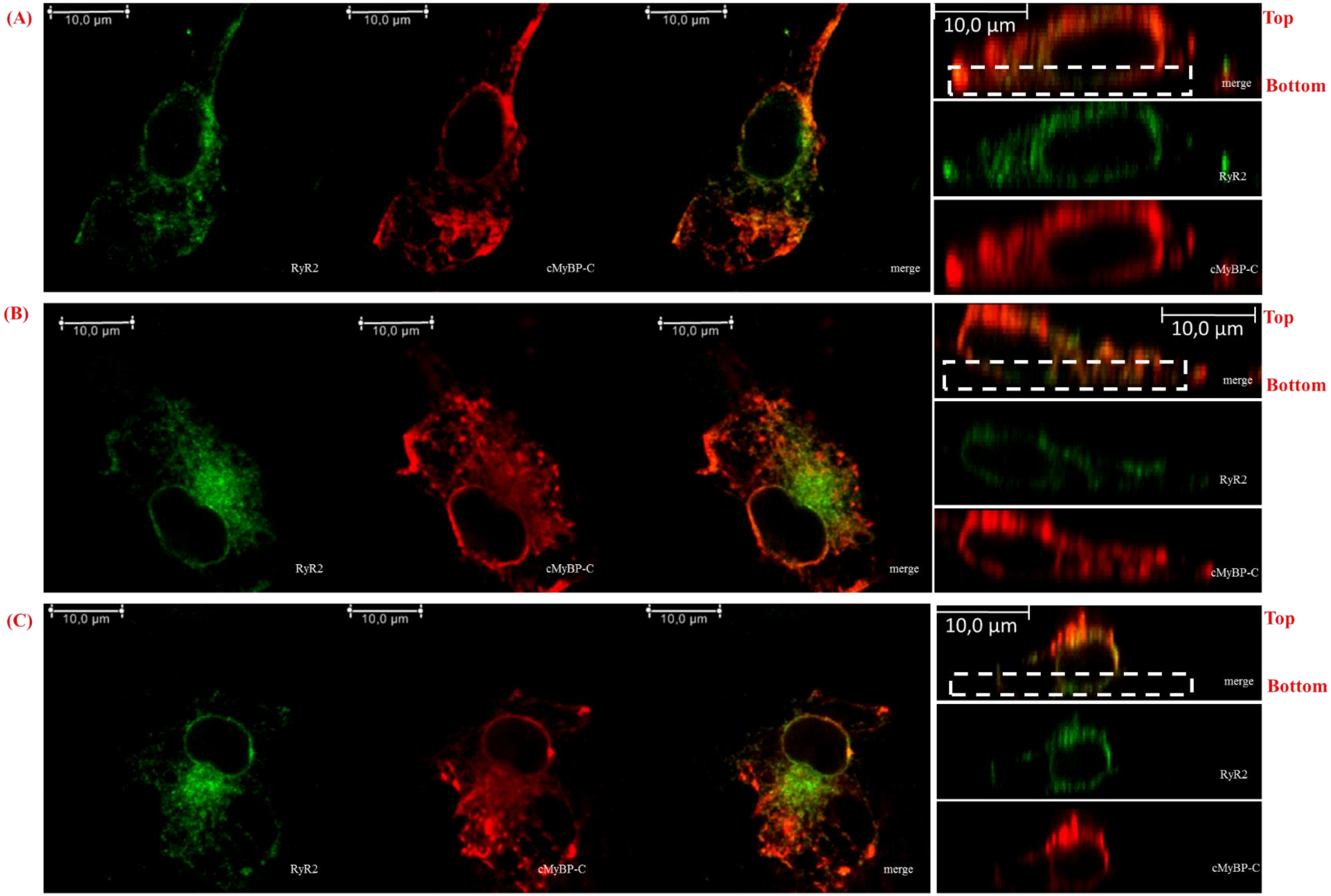

Figure 5.2 2D (x-y) slice representation of the immunofluorescence images of RyR2 and cMyBP-C mCherry-FL localisation within the co-transfected HEK293. Shown are typical fields of view of three individual cells (A-C), taken in the middle of z-axis direction. (1) detection of RyR2 with Ab 1093 and Alexa Fluor 488 (green), (2) detection of mCherry-FL with direct laser He/Ne 594 excitation (red), (3) overlay images and (4-6) the corresponding orthogonal sections (z axis). Dashed box indicates region where previously red signal (cMyBP-C) could not be detected. Yellow colour shows RyR2 and cMyBP-C pixel overlap, and is indicative of co-localisation.

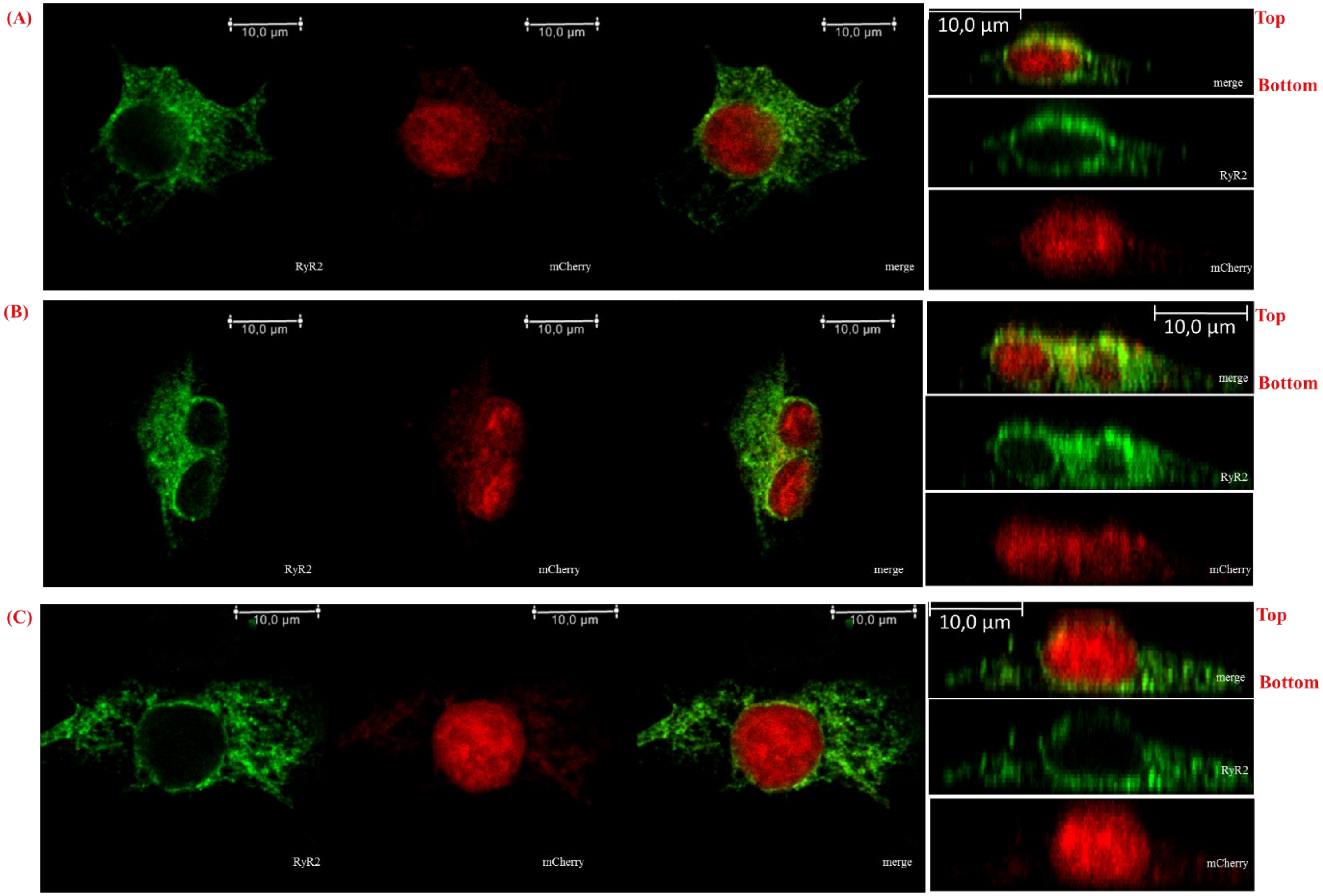

Figure 5.3 2D (x-y) slice representation of the immunofluorescence images of RyR2 and mCherry localisation within the co-transfected HEK293. Shown are typical fields of view of three individual cells (A-C), taken in the middle of z-axis direction. (1) detection of RyR2 with Ab 1093 and Alexa Fluor 488 (green), (2) detection of mCherry with direct laser He/Ne 594 excitation (red), (3) corresponding overlay images and (4-6) the orthogonal sections (z axis).

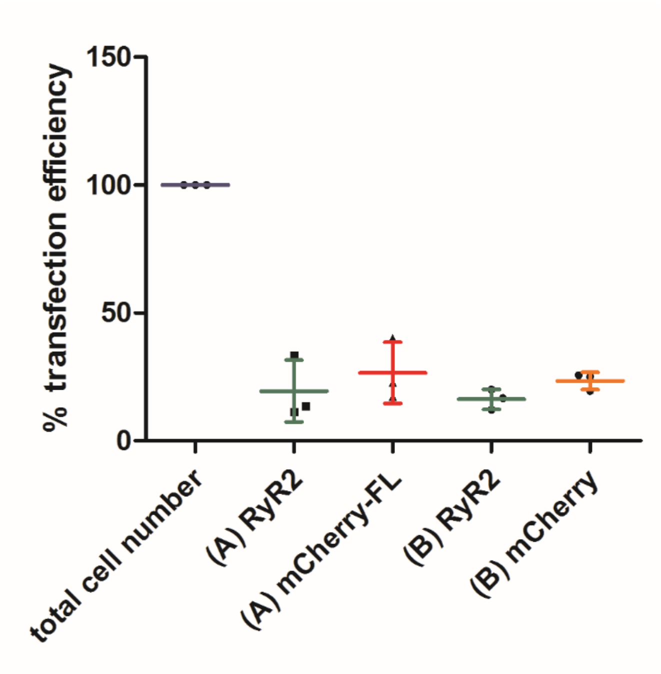

Figure 5.6 Comparable transfection efficiencies of HEK293 cell populations co-expressing RyR2 (A and B) with either cMyBP-C mCherry-FL (A) or mCherry only (B), counted with LEICA software. Percentage of transfection efficiencies were normalized towards total number of cells present in selected field of view (used as 100%). Data are shown as mean ±SD, n=3 populations, in average, n=24 and n=37 cells in each field of view were analysed, for condition A and B, respectively.

5.4.5 The mCherry tag does not affect the recombinant human cMyBP-C:RyR2 interaction

In order to verify whether fusion of cMyBP-C with a mCherry fluorescent protein would affect RyR2:cMyBP-C binding, parallel co-IP experiments were conducted of HEK293 homogenates from either RyR2 + mCherry-FL cMyBP-C or RyR2 + HA-FL cMyBP-C co-transfected cells. **Figure 5.7** shows representative blot together with a summary of densitometric analysis. Statistical analysis using paired, 2-tailed Student’s t-test for specific co-precipitated cMyBP-C protein and negative control (non-specific binding) detected positive interaction for each tested pair, while comparison of relative binding ability (the specific binding subtracted of non-specific binding) of mCherry-FL cMyBP-C + RyR2 to that of HA-FL cMyBP-C + RyR2 did not display any statistical differences (calculated using the same test). In general, mCherry-FL fusion protein was expressed at considerably higher levels than HA-FL cMyBP-C (see **Appendix, Figure 8.5**), but this appeared to not enhance the RyR2 binding, as demonstrated in **Figure 5.7 B**.

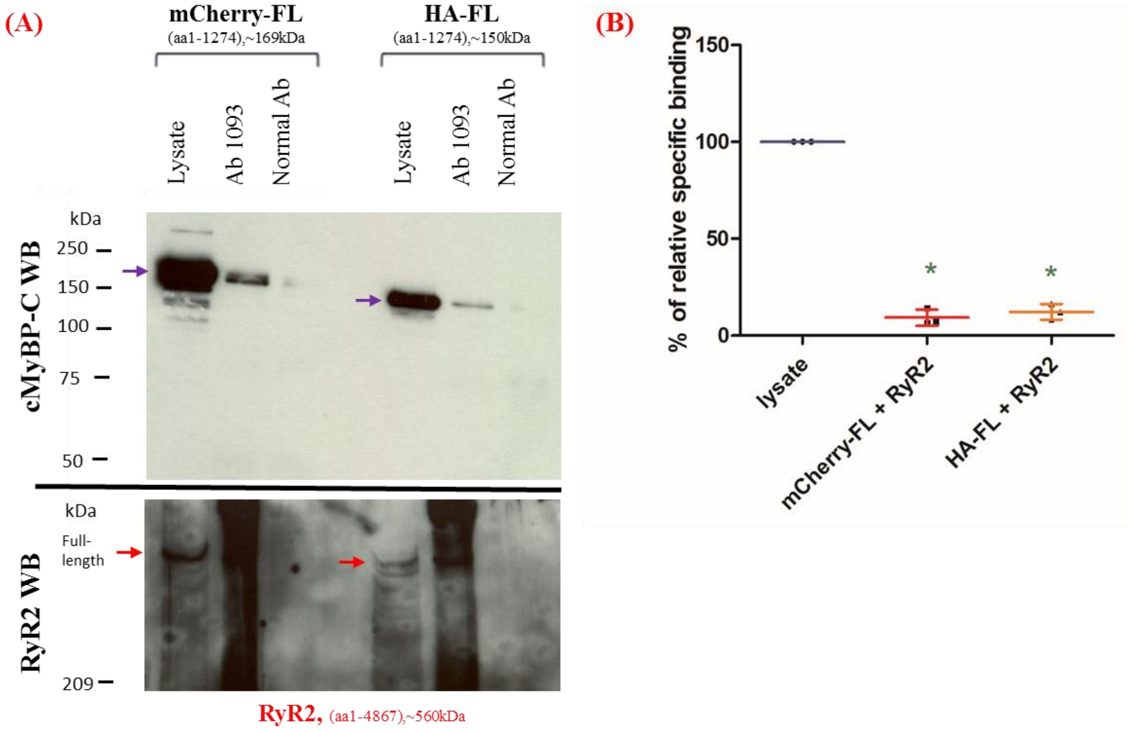

*Figure 5.7 Representative blot of Co-IP and WB results illustrating recombinant RyR2 interaction with one of the two cMyBP-C constructs, either mCherry- or HA-tagged, and cumulative densitometric analysis (A). RyR2 was immunoprecipitated with Ab1093 from CHAPS-solubilised HEK293 homogenate (2 mg per IP lane) and the presence of associated cMyBP-C was analysed with Ab C-t. The loading controls represent 1/200th and 1/10th of the processed sample for (top panel) and (lower panel), respectively. Bands corresponding to cMyBP-C (mCherry-tagged, ~169 kDa; HA-tagged, ~150 kDa; black arrows) and RyR2 subunit (~560 kDa, red arrows) are shown; (B) Densitometry analysis of mCherry-FL + RyR2 and HA-FL + RyR2 binding from parallel co-IP assays of HEK293 homogenates. Percentage of relative specific binding (the specific binding subtracted of the non-specific binding) corrected for the difference in expression levels are presented relative to lysate input (1/200th of the processed sample). Data are shown as mean ±SD,, n=3 for each condition, processed in parallel. * statistical significance calculated using paired, 2-tailed Student's t-test for specific co-precipitated protein and negative control (non-specific binding).*

5.4.6 Detected decreased calcium oscillations frequency is indicative of inhibitory role of cMyBP-C on RyR2 function

Representative traces of SCR events from RyR2 only-expressing HEK293 cells at 1.3 mM extracellular Ca^{2+} and in the presence of either mCherry alone or mCherry-FL cMyBP-C are demonstrated in **Figure 5.8**. Notably, only RyR2 expressing cells were responsive to 10mM caffeine (**C-E**), with the portion of cell population exhibiting spontaneous SCR events (**F**). On the other hand, the RyR2 untransfected cells, but expressing either mCherry-FL or mCherry, neither displayed SCR events nor responded to caffeine (**A** and **B**), in agreement with (Jiang et al. 2002). To assess the effects mCherry-FL cMyBP-C co-expression has on the Ca^{2+} handling dynamics of RyR2 channels, the properties of the SCR-events were examined and compared to both RyR2 only expressing cells as well as to RyR2 + mCherry co-expressing cells, to verify whether any observed changes are not due to mCherry tag presence. Namely, the following cellular calcium handling parameters were examined: the amplitude, duration, rate up/down of each individual Ca^{2+} transient, the time between Ca^{2+} transients (inter-SCR duration), the number of Ca^{2+} transients observed (frequency/number of events), and ER Ca^{2+} store content (see **Section 5.3.5**).

As illustrated in **Figure 5.8**, mCherry-FL cMyBP-C + RyR2 co-expressing HEK293 cells displayed markedly lower frequency of SCR-events (**E**), compared with those observed in cells expressing mCherry + RyR2 (**D**) or RyR2 alone (**C**). Presented as a series of bar graphs in **Figure 5.9**, the kinetic parameters of these three different cell populations were compared. The details of the statistical analysis can be found in the **Appendix, Table 8.6**. When compared to RyR2 alone, the presence of mCherry-FL cMyBP-C caused a significant increase in the mean duration of each Ca^{2+} transient (**Figure 5.9, B**) and also of inter-SCR duration (**E**) as well as decrease in the rate of Ca^{2+} decay (**D**), thereby overall decreasing the number of oscillations (**G**) and thus their frequency (**F**). However, in our experimental conditions, cumulative data indicated that the observed decrease in the rate of Ca^{2+} decay and corresponding increase in mean Ca^{2+} transient SCR duration was due to the mCherry protein (RyR2 alone versus RyR2 + mCherry). Hence the effects directly attributable to cMyBP-C were the decrease in the frequency/number of events and parallel increase in inter-SCR duration (statistically significant when compared to both RyR2 only and RyR2 +

mCherry, calculated using Kruskal-Wallis test with Dunn's multiple comparisons test). Notably, both the amplitude (**A**) and the ER Ca^{2+} store content (**H**) (measured by the Ca^{2+} transient amplitude induced by 10 mM caffeine application) appeared similar in all conditions tested (no statistical difference), which highlights that the observed changes are not due to perturbations in Ca^{2+} load, but specifically because of decrease of RyR2 channel open probability because of interaction with cMyBP-C. In contrast, all the remaining SCR parameters in HEK293 cells co-expressing RyR2 and mCherry appeared similar to cells expressing RyR2 only (apart from mean duration and the rate of Ca^{2+} decay), where no significant differences between the two could be detected.

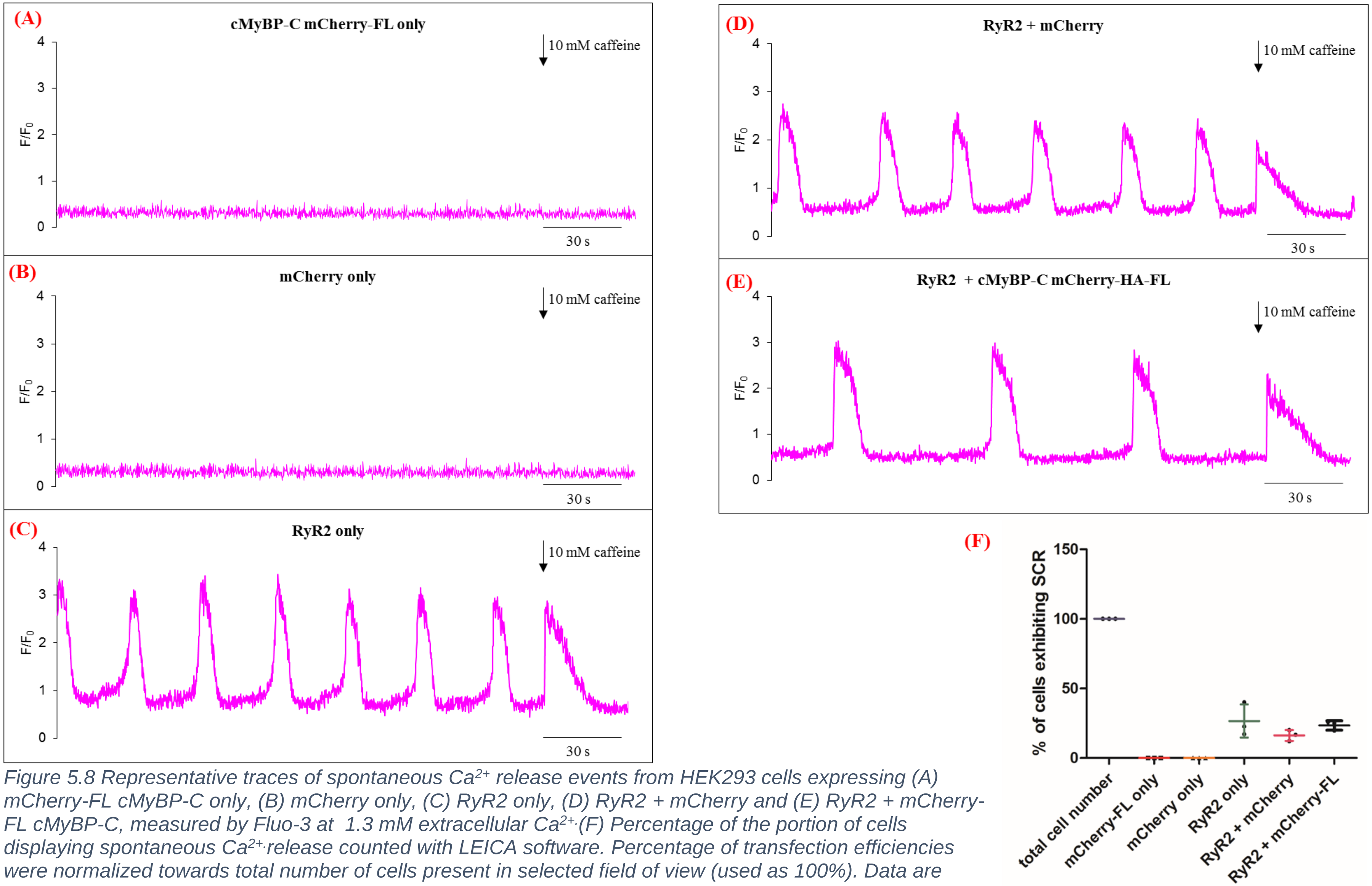

Figure 5.8 Representative traces of spontaneous Ca^{2+} release events from HEK293 cells expressing (A) mCherry-FL cMyBP-C only, (B) mCherry only, (C) RyR2 only, (D) RyR2 + mCherry and (E) RyR2 + mCherry-FL cMyBP-C, measured by Fluo-3 at 1.3 mM extracellular Ca^{2+}. (F) Percentage of the portion of cells displaying spontaneous Ca^{2+} release counted with LEICA software. Percentage of transfection efficiencies were normalized towards total number of cells present in selected field of view (used as 100%). Data are shown as mean ±SD, n=3 populations, in average, n≥27 cells in each field of view were analysed, for each condition A-E.

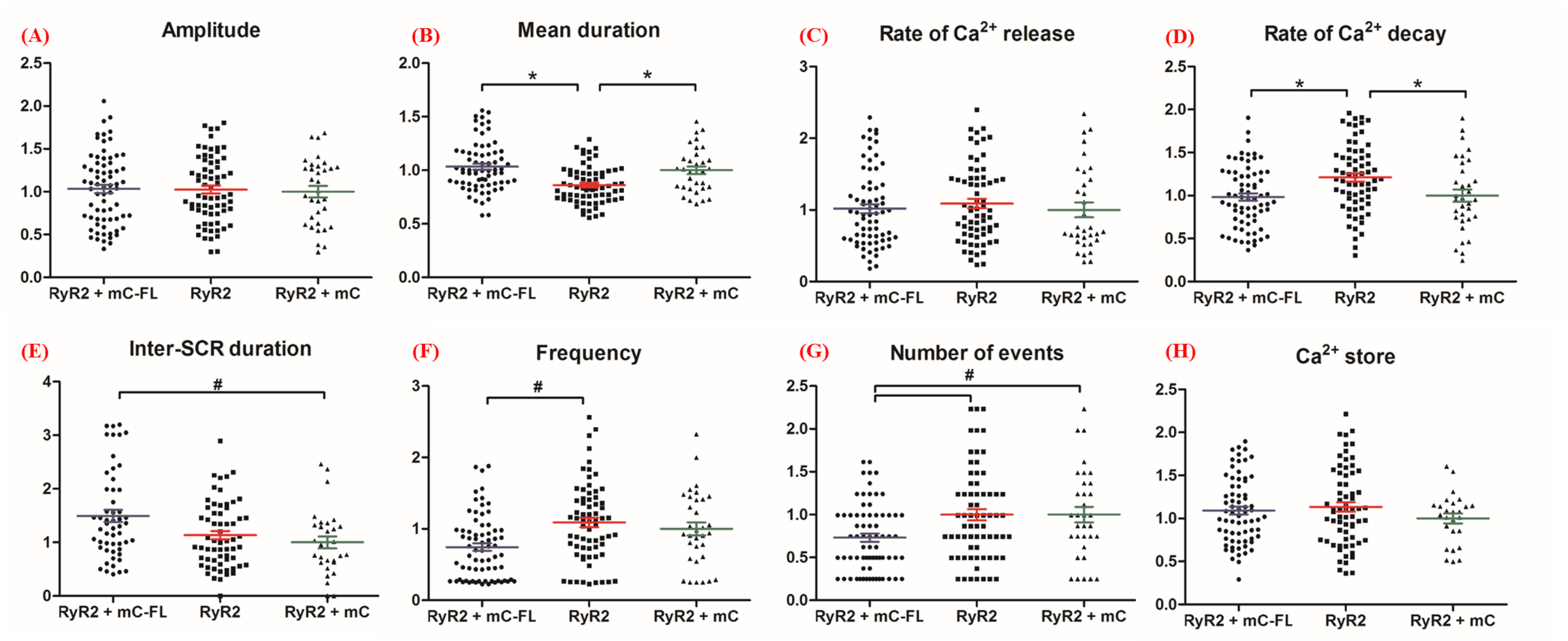

*Figure 5.9 Summary of spontaneous Ca^{2+} release events examination using single cell Ca^{2+} imaging. Data are normalized for RyR2 + mCherry and shown as mean ±SD. Samples: RyR2 + mCherry-FL (cMyBP-C) n=70, RyR2 only n=73, and RyR2 + mCherry n=33, from ≥8 independent experiments; * statistical significance at $p<0.05$ calculated using one-way ANOVA with Bonferroni's multiple comparisons test, # statistical significance at $p<0.05$ calculated using Kruskal-Wallis test with Dunn's multiple comparisons test.*

5.4.7 Tested RyR2 mutations seem to have no effect on RyR2:cMyBP-C interaction

In order to test whether cMyBP-C interaction with RyR2 could be affected by disease-causing point mutations in RyR2 N-terminus, four new BT4L constructs were used: BT4L^{S166C} (where serine 166 was replaced by cysteine), BT4L^{R179Q} (where arginine 179 was replaced by glutamine), BT4L^{R420Q} (where arginine 420 was replaced by glutamine) and BT4L^{L433P} (where leucine 433 was replaced by proline). Each c-Myc tagged mutant plasmid was co-expressed in HEK293 with HA-tagged cMyBP-C CT, and protein interaction was assessed by co-IP as before. Densitometry-based analysis was performed as described in **Section 4.2.2** to quantitatively evaluate the impact of each mutation on the amount of recovered co-precipitated BT4L mutant following HA-cMyBP-C immunoprecipitation. **Figure 5.10 A-B** shows representative blots of obtained co-IP results. All tested constructs scored as positive with cMyBP-C CT when compared to their respective non-specific binding, calculated using unpaired, 2-tailed Student’s t-test (**C**). However, no statistically significant difference between cMyBP-C CT interaction with either of the four mutant BT4L fragments was observed (calculated using one-way ANOVA with Bonferroni's post-test, see **Appendix, Table 8.5**). Obtained results indicate that cMyBP-C:RyR2 binding is not affected by the four tested RyR2-linked mutations.

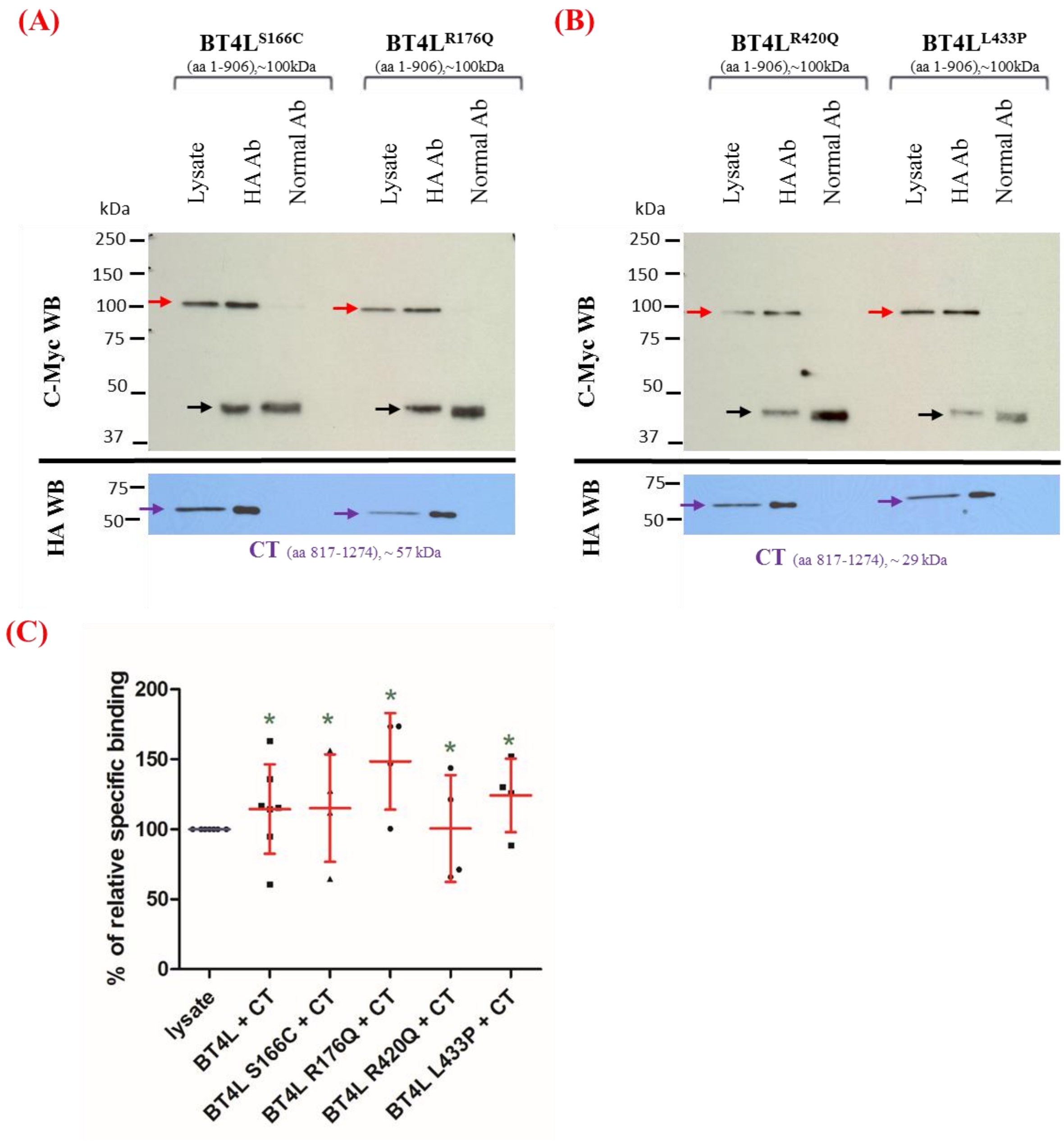

*Figure 5.10 Representative results of a series of BT4L mutated c-Myc- tagged RyR fragments co-IP with HA-tagged cMyBP-C CT constructs, together with cumulative densitometric analysis.(A-B)) cMyBP-C was immunoprecipitated with HA Ab from CHAPS-solubilised HEK293 cell lysate (2 mg) and normal, non-immune rabbit IgG was used as negative control. Co-IP samples were loaded on two separate SDS-PAGE gels (1/10th and 9/10th split, lower and upper panel, respectively) and analysed by immunoblotting with Ab HA (HA WB for CT, lower panels) and Ab c-Myc (c-Myc WB for BT4L mutant of interest, upper panels). A cell lysate aliquot was loaded on the gels to verify expression in HEK293; in c-Myc WB, 1/200th of the volume processed in co-IP samples; in HA WB 1/100th of the volume processed in co-IP samples. All fragments are indicated as follows: BT4L mutant of interest, red arrows; cMyBP-C CT, violet arrows. 12% reducing SDS-PAGE gels were used for c-Myc WB and 12% gels for all HA WB. Black arrows show Ab heavy chains. (C) Densitometry analysis of mutated RyR2 BT4L constructs binding with cMyBP-C CT truncated fragment using co-IP assay from HEK 293 homogenates. Results corrected for the difference in expression levels and non-specific binding are presented relative to each respectable lysate input. Data are shown as mean ±SD, n≥4; * statistical significance at $p<0.05$ calculated using unpaired, 2-tailed Student's t-test.*

5.5 Discussion

5.5.1 Decreased cellular calcium oscillation frequency is indicative of inhibitory role of cMyBP-C on RyR2 function

The principal goal of this study was to investigate the possible functional effect/s that the cMyBP-C protein could exert on recombinant RyR2 channel. Our reasoning was that since each domain of RyR2 NTD governs different aspect of channel activity, with NTD subdomain A (residues 1-217) proposed to be involved in Ca^{2+} release termination and subdomain B (residues 218-409) being involved in stabilizing the closed state of the channel (Liu et al. 2015), it could be possible for cMyBP-C to affect channel function because its RyR2 binding region appears to be contained within those subdomains (residues 1-346, see **Chapter 4**). Another possible impact on RyR2 by cMyBP-C could be an influence on the N-terminal to central region conformational change of the channel, as a second part of the region important for cMyBP-C binding was contained within the SPRY1/P1 domains (mapped RyR2 residues 654-906). Therefore, quantitative [^{3}H]ryanodine binding was used to assess the cytosolic Ca^{2+} sensitivity of RyR2 with or without cMyBP-C co-expression. To directly compare the data, a two-part optimisation step was performed, to ensure that approximately equivalent RyR2 levels were present in the two different HEK293 cell populations co-transfected either HA empty vector of HA-FL cMyBP-C: assessment of RyR2 protein levels by densitometric analysis of Western blot signals (**Figure 5.1 A-B**), and second assessment of the total number of fully open RyR2 channels using [^{3}H]ryanodine binding under maximum activation conditions (100 µM Ca^{2+} and 10 mM caffeine, (**C)**).

When fitting the four parameter logistic model, the EC_{50} is defined as the concentration of agonist that provokes a response halfway between the baseline (Bottom) and maximum response (Top), while the Hill slope indicates measure of the curve steepness (Motulsky and Christopopulos 2003). The Hill equation is commonly used to quantify the degree of cooperativity in ligand binding, which in this case would be a measure of the RyR2 activation at various Ca^{2+} concentrations under equilibrium [^{3}H]ryanodine binding to RyR2, in the absence/presence of cMyBP-C. As demonstrated in **Figure 5.2 B** and **Table 5.2**, neither EC_{50} nor Hill slope were explicitly different between the two experimental conditions (both curves displayed comparable 95% confidence intervals for those parameters), but RyR2 + HA-FL cMyBP-C curve top was evidently lower when compared to RyR2 + HA (0.95 ±0.08 RyR2 + HA only versus 0.76±0.06 RyR2 + HA-FL cMyBP-C, (± representing 95% confidence intervals; **Table 5.2**). However, while data presented in **Figure 5.2,** where the RyR2 + HA-FL cMyBP-C Ca^{2+} activation yielded clearly visible trend in decreased activation at Ca^{2+} concentrations >500 nM (but with statistical difference being reached only for 1 µM Ca^{2+} point), the general large error bar overlaps at each of Ca^{2+} point between two conditions questioned the certainty regarding the observed cMyBP-C effect on RyR2. Such variability might be linked to use of HEK293 homogenates as testing material, which despite similar total protein content can display heterogeneous RyR2 and/or cMyBP-C protein distribution even within same sample. The rationale behind the use of cell homogenates as opposed to microsomes was based on the fact that the majority of the cMyBP-C remains in the HEK293 cytosol when co-expressed with RyR2 (Chapter 3). Thus, there was a possibility that the reduced cMyBP-C levels (compared to when cMyBP-C is co-expressed with RyR2) in the microsomal fraction might be too low to mediate any functional effects.

Since ryanodine binds to a RyR conformation associated with an open state of the channel (Sutko et al. 1997), it is possible that cMyBP-C may weakly affect the Ca^{2+} sensitivity of RyR2 opening at micromolar Ca^{2+} levels, which due to considerable variability of the assay (as indicated by the large error bars seen in the graphs) did not reflect in the change of EC_{50}. Another possible explanation is that cMyBP-C influenced the association/dissociation rate of Ca^{2+} and/or [^{3}H]ryanodine itself, however it is highly unlikely as the mapped cMyBP-C binding site does not appear to be positioned in or near the pore-forming region of the RyR2 channel, within which the residues deemed critical for ryanodine binding are situated (Chen et al. 2002). The possible influence of cMyBP-C on ryanodine dissociation could be tested using reversible ryanodine analog, ryanodol (Sigalas et al. 2009), which could help to determine if indeed cMyBP-C presence affect the RyR2 open probability or simply disrupt the ryanodine:RyR2 binding. Notably, as the contaminant free Ca^{2+} of used solutions was not measured, the total free Ca^{2+} concentrations may not reflect the desired amounts tested in our experimental conditions, and could add to the aforementioned variability of the assay. Since the results from the [^{3}H]ryanodine binding were rather inconclusive, single cell Ca^{2+} imaging was used as a second functional assay, in order to detect the effects of cMyBP-C protein presence on RyR2, while co-expressed in HEK293 cells.

Prior to single cell analysis, new cMyBP-C fusion construct was made, tagged with red fluorescent mCherry protein to allow *in vivo* real-time monitoring of spontaneously oscillating cells (indicative of RyR2 expression) and concomitant selection of cells co-expressing cMyBP-C. We made use of the fact that mCherry is a monomeric red fluorescent protein with an excitation/emission optimum of 587/610 nm (Shaner et al. 2004), which does not overlap with that of the green fluorescent Ca^{2+} indicator Fluo-3 (506/526 nm of Ca^{2+} bound form). The possible influence of the new tag on cMyBP-C interaction with RyR2 was verified using the co-IP assay, and was found to display no statistically significant difference between the binding of RyR2 + mCherry- FL cMyBP-C and RyR2 + HA-FL cMyBP-C (**Graph 5.5**). Moreover, as presented in **Figure 5.4**, mCherry-FL cMyBP-C fusion retained the previously reported cytosolic expression in HEK293 cells (see **Section 3.4.2**), implying that the mCherry tag at the N-terminal end of cMyBP-C does not cause any detectable alteration in cMyBP-C protein trafficking, further highlighted by the clearly distinguishable mCherry pattern of expression (mainly nuclear with weak cytoplasmic expression, **Figure 5.5**). Notably, similar localisation of mCherry protein in HEK293 cells has been observed previously (Kashir et al. 2011; Auslander et al. 2014).

To monitor cytosolic Ca^{2+} transients, HEK293 cells transfected with RyR2 only, or co-transfected with RyR2 + mCherry or RyR2 + mCherry-FL cMyBP-C were loaded with Fluo-3 and were maintained in 1.3 mM extracellular Ca^{2+}. As expected, cells from all three conditions readily displayed recombinant RyR2-driven spontaneous Ca^{2+} transients (Jiang et al. 2002), with a few, statistically significant differences (**Figure 5.9**). Surprisingly, both cells co-expressing RyR2 and either of mCherry constructs (the fluorescent protein only or as cMyBP-C fusion) displayed higher mean duration and therefore prolonged Ca^{2+} transients compared with RyR2 only. Thus, higher Ca^{2+} transient duration is accounted by the mCherry protein tag, and not cMyBP-C. Importantly, Ca^{2+} transients had substantially decreased frequency/number of events and thus displayed parallel increase in inter-SCR duration in RyR2 + mCherry-FL cMyBP-C co-expressing cells, compared to both controls (RyR2 only and RyR2 + mCherry). These data demonstrate that cMyBP-C decreases the propensity of RyR2 for spontaneous Ca^{2+} release when co-expressed in HEK293 cells. Interestingly, we have not observed any statistically significant differences in spontaneous Ca^{2+} transient activation (Pohlmann et al. 2007) nor decay time as reported by (Song et al. 2003; Brickson et al. 2007; Pohlmann et al. 2007) in mouse models of cMyBP-C abrogation, implying that the observed effects could be due to compensatory remodelling events and not directly linked to cMyBP-C absence, or perhaps simply demonstrate the limitations of our recombinant RyR2 HEK293 SCR model.

It is important to note that the observed effect was not influenced by changes in ER Ca^{2+} content, since it is known that increased amount of available Ca^{2+} in the stores correspondingly results in an increase the opening of RyR2 by SOICR (Jiang et al. 2005). The ER load tested with 10 mM caffeine application in all three conditions was shown to be comparable, without any detectable changes in amplitude of observed SCR **(Figure 5.9, A** and **H).** However, as caffeine application is an indirect measurement of ER load due to ER Ca^{2+}-ATPase activity and pumping Ca^{2+} back into ER after caffeine induced-RyR2-mediated release (Berridge et al. 2003), a more direct approach to study the amount of the Ca^{2+} contained within ER stores would be a simultaneous treatment of caffeine together with thapsigargin, a known inhibitor of the ER Ca^{2+}-ATPase (Thastrup et al. 1990). If possible, the future experiments should include measurement of both cytosolic Ca^{2+} and ER Ca^{2+} load to establish their influence on the obtained results.

5.5.2 Tested S166C, R176Q, R420Q and L433P N-terminal RyR2 mutations have no effect on RyR2:cMyBP-C interaction

To quantitatively evaluate the possible impact of each disease-linked RyR2 mutation on RyR2:cMyBP-C interaction, the amount of recovered co-precipitated mutant BT4L following HA-cMyBP-C immunoprecipitation, densitometry-based analysis was performed (**Figure 5.10**). Unfortunately, none of the assessed interactions scored for a statistically significant difference in the cMyBP-C C-terminal fragment (CT) binding propensities between the four mutants and the WT RyR2 N-terminal fragment (BT4L), implying that, at least in terms of the tested mutations, RyR2 binding with cMyBP-C in not affected. However, the functional impact of these mutations cannot be dismissed, and thus the contribution of cMyBP-C towards the pathological conditions needs to be assessed by functional assay, i.e. expression of RyR2 mutant channels in our HEK293 SCR model in the presence of cMyBP-C or by [^{3}H]ryanodine binding. Further studies should help to unravel whether and how cMyBP-C:RyR2 association can be involved in channel dysfunction and aberrant intracellular Ca^{2+} release, thus affecting cardiac contraction/relaxation.

5.5.3 Conclusions

The single cell Ca^{2+} imaging investigations suggest that cMyBP-C has an inhibitory effect on frequency of spontaneous calcium oscillation, indicative of potential inhibitory role of cMyBP-C on RyR2 function. Further, when assessed by co-IP, the relative binding ability of cMyBP-C and RyR2 appears unaffected by four different RyR2 single point mutation variants, known to be causative of RyR2-linked pathological conditions, namely DCM, CPVT and ARVD phenotypes.

Chapter 6

Summary of findings and conclusions

6 Summary of findings and conclusions

Human RyR2 channel present in the SR membrane of cardiac myocytes plays a critical role in ECC by mediating SR calcium release, whereas aberrant regulation of the channel is implicated in cardiac arrhythmias as well as cardiomyopathy. On the other hand, cMyBP-C is a predominantly sarcomeric modular protein anchored to the thick filament through its C-terminal region, while the N-terminal region of cMyBP-C is thought to regulate myocardial contractility by modifying actin-myosin cross-bridge cycling. In the work presented here, we provide several lines of evidence indicating cMyBP-C as a new RyR2 binding partner, which could constitute a novel aspect of SR Ca^{2+} release regulation by a sarcomere component.

Firstly, co-immunoprecipitation data presented in **Chapter 3** indicate that the detected interaction between RyR2 and cMyBP-C can be applicable to large mammalian species as well as to recombinant human proteins, with RyR2 N-terminus and cMyBP-C C-terminus being responsible for the binding. Secondly, in **Chapter 4,** by using the two complementary techniques, namely co-IP and Y2H, we showed that RyR2 residues 1-167, 175-346 (corresponding to subdomain A and B of RyR2 NTD) and 654-906 (domain SPRY1 and P1) are important determinants for the binding with cMyBP-C. Further cMyBP-C binding region co-IP mapping studies indicated that cMyBP-C residues 820-972 and 1061-1274 are involved in the interaction with RyR2, with cMyBP-C Fn domain/s proposed to be directly responsible for the binding. Additionally, we found that the corresponding N-terminus region (RyR2 1-906 amino acids) of mammalian isoforms RyR1 can also interact with MyBP-C, which could indicate that the detected association can be relevant in the regulation of ECC coupling not only in cardiac, but also in skeletal muscle. Finally, in **Chapter 5** we pursued the possible functional significance of RyR2:cMyBP-C interaction. The results from single cell Ca^{2+} imaging implied that cMyBP-C interaction with RyR2 may have an inhibitory effect on Ca^{2+} release channel function, with cMyBP-C binding diminishing RyR2 channel activity. Lastly, cMyBP-C:RyR2 binding was shown to not be affected by four different RyR2 single point mutation variants (S166C, R176Q, R420Q and L433P), associated with different channel pathological phenotypes. However, as the influence of those mutations on cMyBP-C binding to the intact RyR2 channel (as opposed to the use of mutant fragments) cannot be dismissed, more studies are needed to understand what role cMyBP-C plays in channel dysfunction. As such, expression of mutant channels in our HEK293 SCR model and assessment of spontaneous Ca^{2+} release events would provide more insights on potential role of cMyBP-C in those conditions.

Proper cardiac activation-relaxation kinetics is of a paramount importance for healthy circulation, as in between the two beats heart muscle needs to relax to allow for proper ventricular filling. Contrary to the thought that relaxation is a mere passive process that simply follows contraction, the interplay between three main events can limit the rate of relaxation, namely rate of intracellular calcium decline, the rate of thin-filament de-activation and the rate of cross-bridge cycling (Biesiadecki et al. 2014). Each of these processes is directly regulated by a plethora of molecular events, and impairment of a single event can result in incomplete filling of ventricles upon initiation of the next systole, causing a diminished volume at the beginning of the cycle. Thus, even if the contractile activation appears to be similar to the healthy heart, slowed relaxation would lead to reduced cardiac output, and if left untreated, the impaired balance of systolic/diastolic heart function would lead to development of heart failure (Bers 2008; Fearnley et al. 2011).

As discussed in **Chapter 1** an increase in systolic Ca^{2+} is achieved by Ca^{2+} influx through LTCC and following RyR2-mediated efflux from SR, the main process of CICR. The rate at which the Ca^{2+} transient declines is an important factor that contributes to the cardiomyocyte relaxation and it is mainly modulated by coordinated action of SERCA and NCX (Bers 2002). For human heart (and other large mammal species such as dog, guinea pig and rabbit), the apparent contribution is ~70% by SERCA and ~28% by NCX (in the forward mode), respectively, while mouse and rat display a ratio of ~92% and ~7%, respectively (Fearnley et al. 2011). This corresponds to a varied number of myocyte Ca^{2+} pumps in each of species (i.e. the expression of SERCA is higher in mouse/rat than in rabbit/dog), with pathological conditions known to cause the apparent shifts in the contribution of the two routes of cytosolic Ca^{2+} removal, i.e. reduction in SERCA expression and increase in NCX expression as reported in human and rabbit heart failure, with 50%:50% change in contribution to the Ca^{2+} transient decline (Piacentino et al. 2003). Since SERCA has a much greater Ca^{2+} transport efficiency that NCX, those protein changes result in a general slower Ca^{2+} transient decay. Notably, during advanced heart failure, in which SR Ca^{2+} release is low and cytoplasmic Na^{+} levels are elevated, the NCX outward mode can contribute towards Ca^{2+} influx throughout most of the AP (Weber et al. 2003). Further, the possible SR Ca^{2+} leak through the RyR2, which normally is minimal but could be substantial in pathological conditions (Marx et al. 2000; Kubalova et al. 2005), can also add to the impaired relaxation (Bers 2014).

Calcium release from SR is also mediated via inositol 1, 4, 5-trisphosphate receptors (IP3R), which despite only ~30% identity in primary sequence with RyRs, they display substantial structural homology and surprisingly high conservation of structure-function relationship (Seo et al. 2012). IP3Rs are activated by inositol 1, 4, 5 triphosphate (IP3) produced by phospholipase C in response to the stimulation of G protein-coupled receptors or tyrosine kinase receptors located at the plasma membrane (Patterson et al. 2004). The binding of IP3 increases the sensitivity of the receptor to Ca^{2+} and triggers Ca^{2+} release from the SR further stimulating the channel, that can induce additional SR Ca release via RyR2s (via local CICR)(Bers 2014). This IP3R-dependent Ca^{2+} efflux is plays an important role in the modulation of ECC in atrial tissue, where IP3Rs are more highly expressed than in ventricular myocytes (Li et al. 2005). In the latter, IP3R are relatively localized at the nuclear envelope, but nevertheless it has been shown that the IP3R-mediated SR Ca^{2+} leak (with a RyR boost) can both contribute to arrhythmogenic events in atrial myocytes as well as ventricular hypertrophic gene program activation (Wu et al. 2006; Ljubojevic et al. 2014). The release of Ca^{2+} from SR has also been suggested to be coupled to the activation of the two-pore channels (TPC) located on acidic organelles such as lysosomes (Macgregor et al. 2007). It has been proposed that TPCs respond to NAADP (nicotinic acid dinucleotide phosphate) by releasing Ca^{2+} from acidic stores, leading to the local increase in Ca^{2+} concentration (Collins et al. 2011). This is thought to contribute to the stimulation of RyR and IP3R, triggering larger Ca^{2+} release events, possibly also influencing to the SR-Ca^{2+} leak as enhanced Ca^{2+} loading of the SR has been observed following NAADP release (Collins et al. 2011; Aston et al. 2017).

Ca^{2+} binding to Tn/Tm complex is essential to the initiation of sarcomere contraction, and although Ca^{2+} itself does not directly regulate actin:myosin association, it acts as a signalling molecule through binding to the thin filament regulatory protein TnC. This interaction maintains the activated state of the thin filament, where TnI is bound to TnC-Ca^{2+} to favour a Tm conformation enhancing actin-exposing myosin binding sites. As long as the thin filament is active, the cross-bridges will freely cycle and muscle will contract. While the rate of cytosolic Ca^{2+} decline is an important and initiating event in myocardial relaxation (the Ca^{2+} transient must decay prior to start of contractile force dissipation), the removal of Ca^{2+} from TnC and subsequent deactivation of the thin filament, which inhibits the acto-myosin cross-bridge formation, are the two crucial processes that allow efficient diastolic ventricular filling (Fearnley et al. 2011; Eisner et al. 2013). This dissociation weakens TnI:TnC binding to favour TnI inhibitory binding to actin, with additional changes in TnT and Tm further contributing to steric block of cross-bridge formation, with the Ca^{2+} dissociation rate directly increased or decreased by Tn and Tm isoform switching, post-translational modifications and mutations implicated in pathological conditions (Biesiadecki et al. 2014).

Notably, (Previs et al. 2015) have recently demonstrated that cMyBP-C Ig domains C0-C3 are also involved in Tm binding in a phosphorylation-dependent manner and activation of cross-bridge cycling. The same group also proposed that cMyBP-C acts as tunable mechanism element of healthy heart within the thick filament that, synergistically with Ca^{2+}, shifts Tm from blocked to closed position at low Ca^{2+} levels, thus correcting the non-uniformity in calcium activation by directly sensitizing the contractile apparatus to Ca^{2+} and counterbalancing the RyR2-released SR calcium gradient. Further, both the follow-up study by (Previs et al. 2016) and a report by an independent group (Colson et al. 2016) have suggested that phosphorylation of cMyBP-C may result in the formation of a calcium-binding motif within the M-domain, which could provide previously overlooked, additional level of sarcomere regulation by cMyBP-C. In this way, it could be possible for cMyBP-C phosphorylation-mediated cardiomyocyte activation to be antagonistically overridden by high Ca^{2+} levels, and have similar to MI-driven effect on heart function (Sadayappan et al. 2006; Sadayappan et al. 2009) by inducing cMyBP-C dephosphorylation and following release from the sarcomere, thus ultimately contributing to diminished contractile force.

In the heart, following acute MI, the deprivation of oxygen and nutrient supply results in a series of abrupt biochemical and metabolic changes. The absence of oxygen switches cell metabolism to anaerobic respiration, resulting in a drop of intracellular pH (to <7.0) (Hausenloy and Yellon 2013). This induces NCX to extrude H^+ and results in intracellular Na^+ overload, which in turn switches the reverse NCX mode to extrude Na^+ and leads to intracellular Ca^{2+} overload and cardiomyocyte hyper contractility (Avkiran and Marber 2002). During reperfusion, the electron transport chain is reactivated, generating reactive oxygen species, and mediating dysfunction of the SR, which further contributes to the intracellular Ca^{2+} overload, oxidative damage to DNA, diminished cardiomyocyte contracture and necrosis (Hausenloy and Yellon 2013). Notably, since it has been shown that the MI-driven dephosphorylated cMyBP-C could be released from the sarcomere, with detectable levels of full-length cMyBP-C in the cytosol (Decker et al. 2012; Kuster et al. 2014; Baker et al. 2015), it is tempting to hypothesize that elevated Ca^{2+} levels (to which enhanced/prolonged RyR2 channels opening contribute), might have direct effect on cMyBP-C. Thus both cMyBP-C dephosphorylation and high cytosolic Ca^{2+} levels could directly induce cMyBP-C release, either as full-length cMyBP-C and/or its proteolytic fragments, allowing for the translocation of cMyBP-C from the thick filament to cytosol and/or SR. This would enable for cMyBP-C to bind to RyR2 N-terminus and induce its proposed by us inhibitory effect on RyR2, i.e. to diminish the frequency of RyR2 openings, as indicated by our Ca^{2+} imaging data (**Chapter 5**), and thus ultimately contribute to lowering the cytosolic Ca^{2+} concertation and conferring to the already established cardioprotective role of cMyBP-C during MI (Sadayappan et al. 2006; Sadayappan et al. 2009). Therefore, at least under pathophysiological conditions, cMyBP-C could act as a negative feedback mechanism on RyR2- SR Ca^{2+} release, comprising a novel retrograde sarcomeric control of RyR2 Ca^{2+} release. It is important to note that the proposed mechanism might not be operational in healthy hearts, where Ca^{2+} concertation is well regulated and stay within the physiological levels, but instead plays a role in aforementioned post-MI recovery and/or during prolonged β-AR stimulation, where Ca^{2+} homeostasis is perturbed (**Section 1.1.2**).

Our study raises the possibility that the perturbation of Ca^{2+} homeostasis due to disrupted cMyBP:RyR2 interactions may constitute a novel pathogenic mechanism for the development of heart failure. Future studies should help to unravel the role of RyR2 and cMyBP-C association in cardiac physiology and disease.

Chapter 7

Future work

7 Future work

The identified RyR2:cMyBP-C association provides novel insights into the putative regulation of RyR2 function by the sarcomeric component cMyBP-C, however the understanding of how this mechanism may be applicable to healthy/diseased heart is lacking. The work presented here determined the RyR2:cMyBP-C interaction biochemically from both native tissue and also a recombinant cell model, which in the case of the latter may be lacking the cardiac-specific proteins present in the intact, live cardiomyocyte. This is a clear disadvantage in respect to the extrapolation of this data to the crowded cellular milieu, where the interplay of many factors are known to affect muscle contraction (Bers 2008; Fearnley et al. 2011; Eisner et al. 2013).

The valuable information regarding the possible translocation of cMyBP-C due to MI and high-Ca^{2+} levels (Decker et al. 2012; Kuster et al. 2014) could be verified by immunocytochemistry co-localisation experiments on primary animal cardiomyocytes, preferably using next-generation fluorescence super-resolution microscopy, allowing to study biological structures with details approaching molecular structure sizes (Godin et al. 2014). For example, a model of *in vivo* simulated ischemia on adult primary rodent cardiomyocytes could be used, achieved by metabolic blockade with high potassium content performed on already isolated cells (Baker et al. 2015) to assess early stages of cMyBP-C dissociation. However, as our results point that the cMyBP-C and RyR2 appear to form protein complexes in higher mammals (**Chapter 3**), co-localisation experiments on cardiomyocytes obtained from ischemic pig hearts following coronary artery ligation should also be considered (Tarvinder et al. 2017). That would allow to compare the co-distribution of RyR2 and cMyBP-C and its proteolytic fragments in healthy and pathophysiological conditions, and evaluate if cMyBP-C dislocation from the sarcomere results in potential association with RyR2. Notably, the described experiments could also help to determine the reciprocal significance of cMyBP-C:RyR2 binding, where the calpain-cleaved RyR2 N-terminal fragment (which is slightly bigger than our recombinant BT4L construct) could dissociate from SR junctions (Fauconnier et al. 2013) and exert a possible functional impact on sarcomere contraction via C-zone located cMyBP-C.

Cell Ca^{2+} homeostasis is tightly regulated by the interplay of many factors, i.e. SR/ER Ca^{2+} re-uptake and cytoplasmic Ca^{2+} removal (Bers 2008), it is crucial to determine whether the observed diminished frequency of spontaneous Ca^{2+} release events (**Chapter 5**) is attributable specifically due to cMyBP-C:RyR2 interaction and whether it can be recapitulated in intact cardiomyocytes. As such, RyR2 Ca^{2+} release at the single cell level can be studied by fluorimetric Ca^{2+} imaging, which will allow to further assess the channel function with RyR2 in its native conformation and subcellular context. For example, the endogenous cMyBP-C levels in isolated rodent and/or porcine cardiomyocytes could be downregulated using adenovirus-mediated delivery of short hairpin RNA (Rinne et al. 2009) to generate the cMyBP-C-KO model cells. The RT-PCR and WB analysis could be used to confirm reduced transcript and protein levels, respectively, with possibility for obtained model to mimic either the cMyBP-C KO or KI heart and display reported changes in the Ca^{2+} transients (Song et al. 2003; Brickson et al. 2007; Pohlmann et al. 2007). If our hypothesis that cMyBP-C influences RyR2 SR Ca^{2+} release is true, we should be able to normalise affected Ca^{2+} transients by addition of purified recombinant full-length cMyBP-C protein and/or C6-C7 and C8-C9 protein fragments. The fluorescently tagged full-length protein and peptides can be introduced into the isolated model cMyBP-C KO living cardiomyocytes using the microinjection technique (Golebiewska and Scarlata 2011). The detailed analysis of intracellular Ca^{2+} mobilisation characteristic of resting and stimulated cells by caffeine and isoproterenol (George et al. 2003a; George et al. 2006) could be directly compared to the results obtained from our HEK293 SCR model. Further, protein expression of RyR2, NCX, SERCA, phospholamban and phospholamban phosphorylation status can also be verified, to see if their involvement in Ca^{2+} handling is affected by diminished and reconstituted cMyBP-C levels.

To assess the direct effect of cMyBP-C on RyR2 at molecular level, single channel recording could be used. The stable cMyBP-C-expressing HEK293 cell line could be generated, and further transiently transfected using Ca^{2+} phosphate precipitation to allow for co-expression of recombinant human RyR2 (Handhle et al. 2016). RyR2 only and RyR2 + cMyBP-C HEK293 enriched microsomal fractions would be prepared by differential centrifugation (Mason et al. 2012), with protein assessed by WB analysis to ensure that cMyBP-C is retained during RyR2 purification. After incorporation into the planar lipid bilayers, the channel behavior could be tested by single channel electrophysiological recordings under a range of free calcium concentrations to verify if the RyR2:cMyBP-C binding is Ca^{2+}-dependent (Sitsapesan and Williams 1994; Mason et al. 2012). The detailed analysis of open probability, gating kinetics, channel conductance and ion-handling properties of individual RyR2 channels under voltage-clamp conditions would provide detailed information on the possible mechanisms underlying altered channel function in the presence of cMyBP-C.

The aforementioned studies could help to determine the significance of the novel interaction between the sarcomeric component cMyBP-C and SR Ca^{2+} release channel RyR2, thus enhancing our understanding of the possible involvement of sarcomere retrograde regulation of Ca^{2+} signaling. In the longer term, the obtained findings also open up completely new and exciting avenues for further research and therapeutic applications.

Appendix

8 Appendix

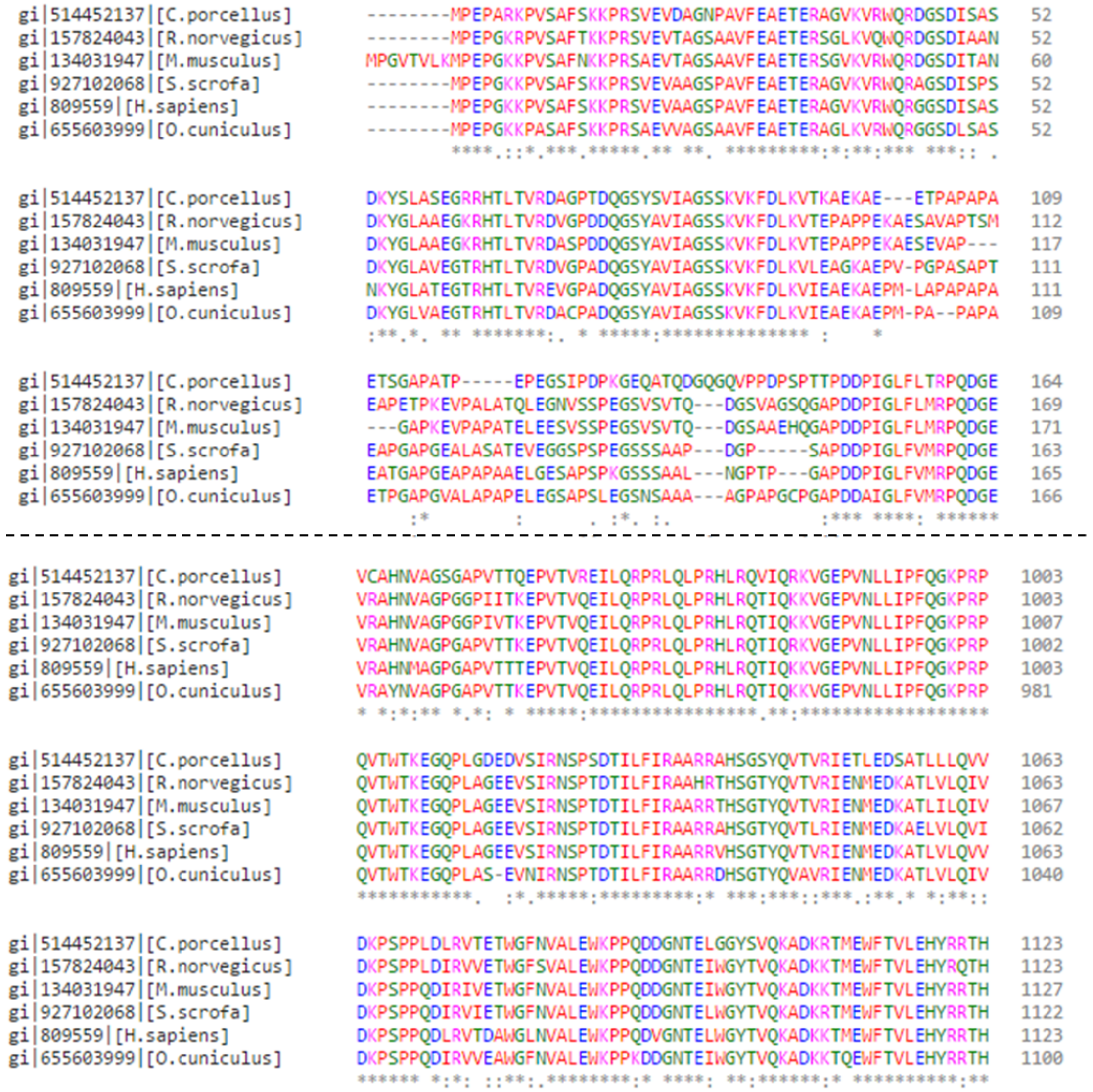

```
gi|514452137|[C.porcellus]      --------MPEPARKPVSAFSKKPRSVEVDAGNPAVFEAETERAGVKVRWQRDGSDISAS   52
gi|157824043|[R.norvegicus]     --------MPEPGKRPVSAFTKKPRSVEVTAGSAAVFEAETERSGLKVQWQRDGSDIAAN   52
gi|134031947|[M.musculus]       MPGVTVLKMPEPGKKPVSAFNKKPRSAEVTAGSAAVFEAETERSGVKVRWQRDGSDITAN   60
gi|927102068|[S.scrofa]         --------MPEPGKKPVSAFSKKPRSVEVAAGSPAVFEAETERAGVKVRWQRAGSDISPS   52
gi|809559|[H.sapiens]           --------MPEPGKKPVSAFSKKPRSVEVAAGSPAVFEAETERAGVKVRWQRGGSDISAS   52
gi|655603999|[O.cuniculus]      --------MPEPGKKPASAFSKKPRSAEVVAGSAAVFEAETERAGLKVRWQRGGSDLSAS   52
                                        ****.::*.***.*****.** **. *********:*:**:*** ***:: .

gi|514452137|[C.porcellus]      DKYSLASEGRRHTLTVRDAGPTDQGSYSVIAGSSKVKFDLKVTKAEKAE---ETPAPAPA   109
gi|157824043|[R.norvegicus]     DKYGLAAEGKRHTLTVRDVGPDDQGSYAVIAGSSKVKFDLKVTEPAPPEKAESAVAPTSM   112
gi|134031947|[M.musculus]       DKYGLAAEGKRHTLTVRDASPDDQGSYAVIAGSSKVKFDLKVTEPAPPEKAESEVAP---   117
gi|927102068|[S.scrofa]         DKYGLAVEGTRHTLTVRDVGPADQGSYAVIAGSSKVKFDLKVLEAGKAEPV-PGPASAPT   111
gi|809559|[H.sapiens]           NKYGLATEGTRHTLTVREVGPADQGSYAVIAGSSKVKFDLKVIEAEKAEPM-LAPAPAPA   111
gi|655603999|[O.cuniculus]      DKYGLVAEGTRHTLTVRDACPADQGSYAVIAGSSKVKFDLKVIEAEKAEPM-PA--PAPA   109
                                :**.*. ** *******:. * *****:************** :    *

gi|514452137|[C.porcellus]      ETSGAPATP-----EPEGSIPDPKGEQATQDGQGQVPPDPSPTTPDDPIGLFLTRPQDGE   164
gi|157824043|[R.norvegicus]     EAPETPKEVPALATQLEGNVSSPEGSVSVTQ---DGSVAGSQGAPDDPIGLFLMRPQDGE   169
gi|134031947|[M.musculus]       ---GAPKEVPAPATELEESVSSPEGSVSVTQ---DGSAAEHQGAPDDPIGLFLMRPQDGE   171
gi|927102068|[S.scrofa]         EAPGAPGEALASATEVEGGSPSPEGSSSAAP---DGP-----SAPDDPIGLFVMRPQDGE   163
gi|809559|[H.sapiens]           EATGAPGEAPAPAAELGESAPSPKGSSSAAL---NGPTP---GAPDDPIGLFVMRPQDGE   165
gi|655603999|[O.cuniculus]      ETPGAPGVALAPAPELEGSAPSLEGSNSAAA---AGPAPGCPGAPDDAIGLFVMRPQDGE   166
                                    :*        :      . :*. :.              :*** ****: ******
------------------------------------------------------------------------------------------
gi|514452137|[C.porcellus]      VCAHNVAGSGAPVTTQEPVTVREILQRPRLQLPRHLRQVIQRKVGEPVNLLIPFQGKPRP   1003
gi|157824043|[R.norvegicus]     VRAHNVAGPGGPIITKEPVTVQEILQRPRLQLPRHLRQTIQKKVGEPVNLLIPFQGKPRP   1003
gi|134031947|[M.musculus]       VRAHNVAGPGGPIVTKEPVTVQEILQRPRLQLPRHLRQTIQKKVGEPVNLLIPFQGKPRP   1007
gi|927102068|[S.scrofa]         VRAHNVAGPGAPVTTKEPVTVQEILQRPRLQLPRHLRQTIQRKVGEPVNLLIPFQGKPRP   1002
gi|809559|[H.sapiens]           VRAHNMAGPGAPVTTTEPVTVQEILQRPRLQLPRHLRQTIQKKVGEPVNLLIPFQGKPRP   1003
gi|655603999|[O.cuniculus]      VRAYNVAGPGAPVTTKEPVTVQEILQRPRLQLPRHLRQTIQKKVGEPVNLLIPFQGKPRP   981
                                * *:*:** *.*: * *****:****************.**:******************

gi|514452137|[C.porcellus]      QVTWTKEGQPLGDEDVSIRNSPSDTILFIRAARRAHSGSYQVTVRIETLEDSATLLLQVV   1063
gi|157824043|[R.norvegicus]     QVTWTKEGQPLAGEEVSIRNSPTDTILFIRAAHRTHSGTYQVTVRIENMEDKATLVLQIV   1063
gi|134031947|[M.musculus]       QVTWTKEGQPLAGEEVSIRNSPTDTILFIRAARRTHSGTYQVTVRIENMEDKATLILQIV   1067
gi|927102068|[S.scrofa]         QVTWTKEGQPLAGEEVSIRNSPTDTILFIRAARRAHSGTYQVTLRIENMEDKAELVLQVI   1062
gi|809559|[H.sapiens]           QVTWTKEGQPLAGEEVSIRNSPTDTILFIRAARRVHSGTYQVTVRIENMEDKATLVLQVV   1063
gi|655603999|[O.cuniculus]      QVTWTKEGQPLAS-EVNIRNSPTDTILFIRAARRDHSGTYQVAVRIENMEDKATLVLQIV   1040
                                ***********.  :*.*****:*********:* ***:***::***.:**.* *:**::

gi|514452137|[C.porcellus]      DKPSPPLDLRVTETWGFNVALEWKPPQDDGNTELGGYSVQKADKRTMEWFTVLEHYRRTH   1123
gi|157824043|[R.norvegicus]     DKPSPPLDIRVVETWGFSVALEWKPPQDDGNTEIWGYTVQKADKKTMEWFTVLEHYRQTH   1123
gi|134031947|[M.musculus]       DKPSPPQDIRIVETWGFNVALEWKPPQDDGNTEIWGYTVQKADKKTMEWFTVLEHYRRTH   1127
gi|927102068|[S.scrofa]         DKPSPPQDIRVIETWGFNVALEWKPPQDDGNTELWGYTVQKADKRTMEWFTVLEHYRRTH   1122
gi|809559|[H.sapiens]           DKPSPPQDLRVTDAWGLNVALEWKPPQDVGNTELWGYTVQKADKKTMEWFTVLEHYRRTH   1123
gi|655603999|[O.cuniculus]      DKPSPPQDIRVVEAWGFNVALEWKPPKDDGNTEIWGYTVQKADKKTQEWFTVLEHYRRTH   1100
                                ****** *:*: ::**:.********:* ****: **:******:* **********:**
```

Figure 8.1 N-terminal and C-terminal cMyBP-C coding sequence are well conserved between different isoform of cMyBP-C. Shown are multiple protein alignment with coordinates corresponding to human cMyBP-C (upper panel) amino acids 1-165 and (lower panel) residues 944-1123). Human cMyBP-C coding sequence [Homo sapiens] (GenBank: CAA58882.1) was compared to coding sequences of cMyBP-C from 5 animal species : pig [Sus scrofa] (NCBI Reference Sequence: XP_013849807.1); rat [Rattus norvegicus](NCBI Reference Sequence: NP_001099960.1); mouse [Mus musculus](NCBI Reference Sequence: NP_032679.2); guinea pig [Cavia porcellus](NCBI Reference Sequence: XP_003465195.2); and rabbt [Oryctolagus cuniculus] NCBI Reference Sequence: XP_008270674.1t). Multiple protein alignment was produced using Clustal Omega software accessed via the European Bioinformatics Institute (http://www.ebi.ac.uk/). Legend: an asterisk (*) indicates positions which have a single, fully conserved residue; a colon (:) indicates conservation between groups of strongly similar properties, whereas a period (.) shows weak conservation.

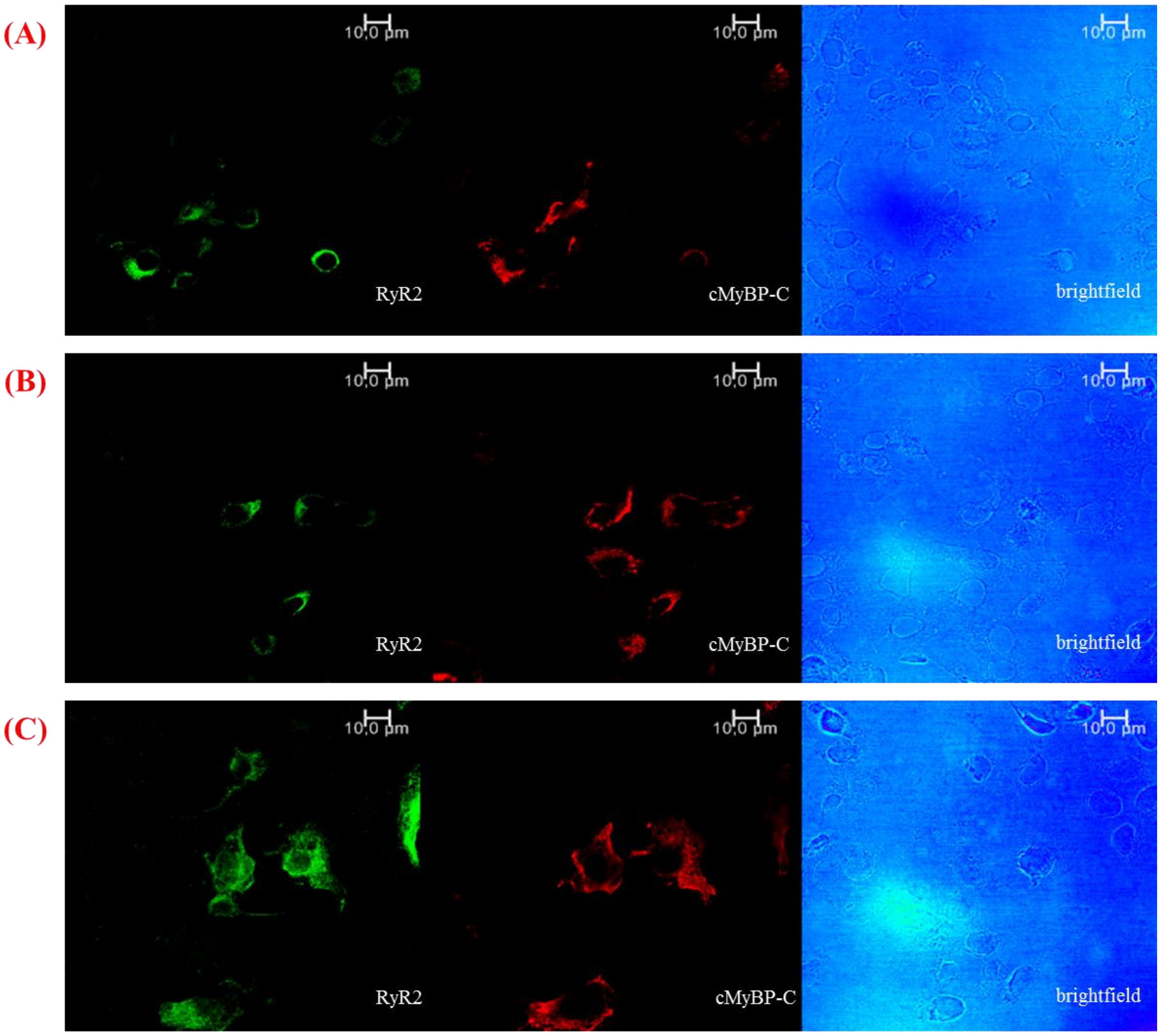

Figure 8.2 Imaging of RyR2 co-expression with cMyBP-C HA-FL in co-transfected HEK293 cell populations (A-C) three fields of form three independent experiments are shown; panels depict green (RyR2) signal detection, red (cMyBP-C) signal detection and (brightfield) corresponding brightfield image.

Table 8.1 GraphPad results for Kruskal Wallis test with Dunn's multiple comparisons for BT4L + NT/CT/FL co-IP results

Kruskal-Wallis test	
P value	<0.0001
Exact or approximate *p* value?	Approximate
P value summary	****
Do the medians vary signif. (*P* < 0.05)?	Yes
Number of groups	6
Kruskal-Wallis statistic	32.62

Dunn's multiple comparisons test	Mean rank diff.	Significant?	Summary
CT + BT4L VS. CT + BT7	23.81	Yes	**
CT + BT4L VS. NT + BT4L	13.97	No	ns
CT + BT4L VS. NT + BT7	27.21	Yes	***
CT + BT4L VS. FL + BT4L	1.397	No	ns
CT + BT4L VS. FL + BT7	15.71	No	ns
CT + BT7 VS. NT + BT4L	-9.843	No	ns
CT + BT7 VS. NT + BT7	3.4	No	ns
CT + BT7 VS. FL + BT4L	-22.41	Yes	**
CT + BT7 VS. FL + BT7	-8.1	No	ns
NT + BT4L VS. NT + BT7	13.24	No	ns
NT + BT4L VS. FL + BT4L	-12.57	No	ns
NT + BT4L VS. FL + BT7	1.743	No	ns
NT + BT7 VS. FL + BT4L	-25.81	Yes	**
NT + BT7 VS. FL + BT7	-11.5	No	ns
FL + BT4L VS. FL + BT7	14.31	No	ns

Table 8.2 GraphPad results for Kruskal Wallis test with Dunn's multiple comparisons for BT mapping

Kruskal-Wallis test	
P value	<0.0001
Exact or approximate P value?	Approximate
P value summary	****
Do the medians vary signif. (P < 0.05)?	Yes
Number of groups	11
Kruskal-Wallis statistic	44.03

Dunn's multiple comparisons test	Mean rank diff.	Significant?	Summary
BT4L VS. BT7	45.98	Yes	**
BT4L VS. BT4	23.28	No	ns
BT4L VS. BT4A	36.78	Yes	**
BT4L VS. BT4B	38.49	Yes	**
BT4L VS. BT4C	47.98	Yes	***
BT4L VS. BT4D	23.49	No	ns
BT4L VS. BT4BL	38.49	Yes	**
BT4L VS. BT4DL	12.28	No	ns
BT4L VS. BT4EL	28.63	No	ns
BT4L VS. BT4L DELTA89	4.178	No	ns
BT7 VS. BT4	-22.7	No	ns
BT7 VS. BT4A	-9.2	No	ns
BT7 VS. BT4B	-7.486	No	ns
BT7 VS. BT4C	2	No	ns
BT7 VS. BT4D	-22.49	No	ns
BT7 VS. BT4BL	-7.486	No	ns
BT7 VS. BT4DL	-33.7	No	ns
BT7 VS. BT4EL	-17.34	No	ns
BT7 VS. BT4L DELTA89	-41.8	Yes	*
BT4 VS. BT4A	13.5	No	ns
BT4 VS. BT4B	15.21	No	ns
BT4 VS. BT4C	24.7	No	ns
BT4 VS. BT4D	0.2143	No	ns
BT4 VS. BT4BL	15.21	No	ns
BT4 VS. BT4DL	-11	No	ns
BT4 VS. BT4EL	5.357	No	ns
BT4 VS. BT4L DELTA89	-19.1	No	ns
BT4A VS. BT4B	1.714	No	ns
BT4A VS. BT4C	11.2	No	ns
BT4A VS. BT4D	-13.29	No	ns
BT4A VS. BT4BL	1.714	No	ns
BT4A VS. BT4DL	-24.5	No	ns
BT4A VS. BT4EL	-8.143	No	ns
BT4A VS. BT4L DELTA89	-32.6	No	ns
BT4B VS. BT4C	9.486	No	ns

BT4B VS. BT4D	-15	No	ns
BT4B VS. BT4BL	0	No	ns
BT4B VS. BT4DL	-26.21	No	ns
BT4B VS. BT4EL	-9.857	No	ns
BT4B VS. BT4L DELTA89	-34.31	No	ns
BT4C VS. BT4D	-24.49	No	ns
BT4C VS. BT4BL	-9.486	No	ns
BT4C VS. BT4DL	-35.7	No	ns
BT4C VS. BT4EL	-19.34	No	ns
BT4C VS. BT4L DELTA89	-43.8	Yes	*
BT4D VS. BT4BL	15	No	ns
BT4D VS. BT4DL	-11.21	No	ns
BT4D VS. BT4EL	5.143	No	ns
BT4D VS. BT4L DELTA89	-19.31	No	ns
BT4BL VS. BT4DL	-26.21	No	ns
BT4BL VS. BT4EL	-9.857	No	ns
BT4BL VS. BT4L DELTA89	-34.31	No	ns
BT4DL VS. BT4EL	16.36	No	ns
BT4DL VS. BT4L DELTA89	-8.1	No	ns
BT4EL VS. BT4L DELTA89	-24.46	No	ns

Table 8.3 GraphPad results for one-way ANOVA with Bonferroni's multiple comparisons test for BT4L RyR1 and RyR3 co-IP.

ANOVA summary	
F	1.464
P value	**0.2626**
P value summary	**ns**
Significant diff. among means (P < 0.05)?	No
R square	0.1633

Bonferroni's multiple comparisons test	Mean Diff.	95.00% CI of diff.	Significant?	Summary
BT4L + CT VS. BT4L RYR1 + CT	-9.189	-77.66 to 59.28	No	ns
BT4L + CT VS. BT4L RYR3 + CT	-49.68	-130 to 30.61	No	ns
BT4L RYR1 + CT VS. BT4L RYR3 + CT	-40.49	-120.8 to 39.8	No	ns

Table 8.4 GraphPad results for Kruskal Wallis test with Dunn's multiple comparisons test for cMyBP-C mapping and GraphPad results for one-way ANOVA with Bonferroni's multiple comparisons test for BT4L binding with CT, C8-C9 and C9-C10.

Kruskal-Wallis test	
P value	<0.0001
Exact or approximate P value?	Approximate
P value summary	****
Do the medians vary signif. (P < 0.05)?	Yes
Number of groups	11
Kruskal-Wallis statistic	53

Dunn's multiple comparisons test	Mean rank diff.	Significant?	Summary
CT VS. C6-C8	-14,11	No	ns
CT VS. C8-C10	6,472	No	ns
CT VS. FC6-C7	-2,444	No	ns
CT VS. C6-C7	-11,53	No	ns
CT VS. FC6	32,91	Yes	*
CT VS. C7	33,78	Yes	*
CT VS. C8	34,35	Yes	*
CT VS. C9	33,72	Yes	*
CT VS. C8-C9	22,47	No	ns
CT VS. C9-C10	0,4722	No	ns
C6-C8 VS. C8-C10	20,58	No	ns
C6-C8 VS. FC6-C7	11,67	No	ns
C6-C8 VS. C6-C7	2,583	No	ns
C6-C8 VS. FC6	47,02	Yes	*
C6-C8 VS. C7	47,9	Yes	*
C6-C8 VS. C8	48,46	Yes	*
C6-C8 VS. C9	47,83	Yes	*
C6-C8 VS. C8-C9	36,58	No	ns
C6-C8 VS. C9-C10	14,58	No	ns
C8-C10 VS. FC6-C7	-8,917	No	ns
C8-C10 VS. C6-C7	-18	No	ns
C8-C10 VS. FC6	26,44	No	ns
C8-C10 VS. C7	27,31	No	ns
C8-C10 VS. C8	27,88	No	ns
C8-C10 VS. C9	27,25	No	ns

C8-C10 VS. C8-C9	16	No	ns
C8-C10 VS. C9-C10	-6	No	ns
FC6-C7 VS. C6-C7	-9,083	No	ns
FC6-C7 VS. FC6	35,35	No	ns
FC6-C7 VS. C7	36,23	No	ns
FC6-C7 VS. C8	36,79	No	ns
FC6-C7 VS. C9	36,17	No	ns
FC6-C7 VS. C8-C9	24,92	No	ns
FC6-C7 VS. C9-C10	2,917	No	ns
C6-C7 VS. FC6	44,44	Yes	*
C6-C7 VS. C7	45,31	Yes	**
C6-C7 VS. C8	45,88	Yes	**
C6-C7 VS. C9	45,25	Yes	*
C6-C7 VS. C8-C9	34	No	ns
C6-C7 VS. C9-C10	12	No	ns
FC6 VS. C7	0,875	No	ns
FC6 VS. C8	1,438	No	ns
FC6 VS. C9	0,8125	No	ns
FC6 VS. C8-C9	-10,44	No	ns
FC6 VS. C9-C10	-32,44	No	ns
C7 VS. C8	0,5625	No	ns
C7 VS. C9	-0,0625	No	ns
C7 VS. C8-C9	-11,31	No	ns
C7 VS. C9-C10	-33,31	No	ns
C8 VS. C9	-0,625	No	ns
C8 VS. C8-C9	-11,88	No	ns
C8 VS. C9-C10	-33,88	No	ns
C9 VS. C8-C9	-11,25	No	ns
C9 VS. C9-C10	-33,25	No	ns
C8-C9 VS. C9-C10	-22	No	ns

ANOVA summary	
F	13.05
P value	0.0004
P value summary	***
Significant diff. among means (P < 0.05)?	Yes

R square	0.62

Bonferroni's multiple comparisons test	Mean Diff.	95.00% CI of diff.	Significant?	Summary
CT VS. C8-C9	99.72	43.13 to 156.3	Yes	***
CT VS. C9-C10	-4.886	-69.42 to 59.65	No	ns
C8-C9 VS. C9-C10	-104.6	-173.9 to -35.29	Yes	**

Table 8.5 GraphPad results for one-way ANOVA with Bonferroni's multiple comparisons test for RyR2 mutant BT4L binding (S166C, R176Q, R420Q or L433P) with cMyBP-C CT or FL.

ANOVA summary	
F	1.235
P value	**0.3054**
P value summary	**ns**
Significant diff. among means (P < 0.05)?	No
R square	0.2359

Bonferroni's multiple comparisons test	Mean Diff.	95.00% CI of diff.	Significant?	Summary
BT4L + CT vs. BT4L S166C + CT	-0.7062	-114 to 112.6	No	ns
BT4L + CT vs. BT4L R176Q + CT	-34.07	-147.4 to 79.27	No	ns
BT4L + CT vs. BT4L R420Q + CT	-3.937	-117.3 to 109.4	No	ns
BT4L + CT vs. BT4L L433P + CT	-9.825	-123.2 to 103.5	No	ns
BT4L S166C + CT vs. BT4L R176Q + CT	-33.36	-161.2 to 94.5	No	ns
BT4L S166C + CT vs. BT4L R420Q + CT	-3.231	-131.1 to 124.6	No	ns
BT4L S166C + CT vs. BT4L L433P + CT	-9.119	-137 to 118.7	No	ns
BT4L R176Q + CT vs. BT4L R420Q + CT	30.13	-97.73 to 158	No	ns
BT4L R176Q + CT vs. BT4L L433P + CT	24.24	-103.6 to 152.1	No	ns
BT4L R420Q + CT vs. BT4L L433P + CT	-5.888	-133.7 to 122	No	ns

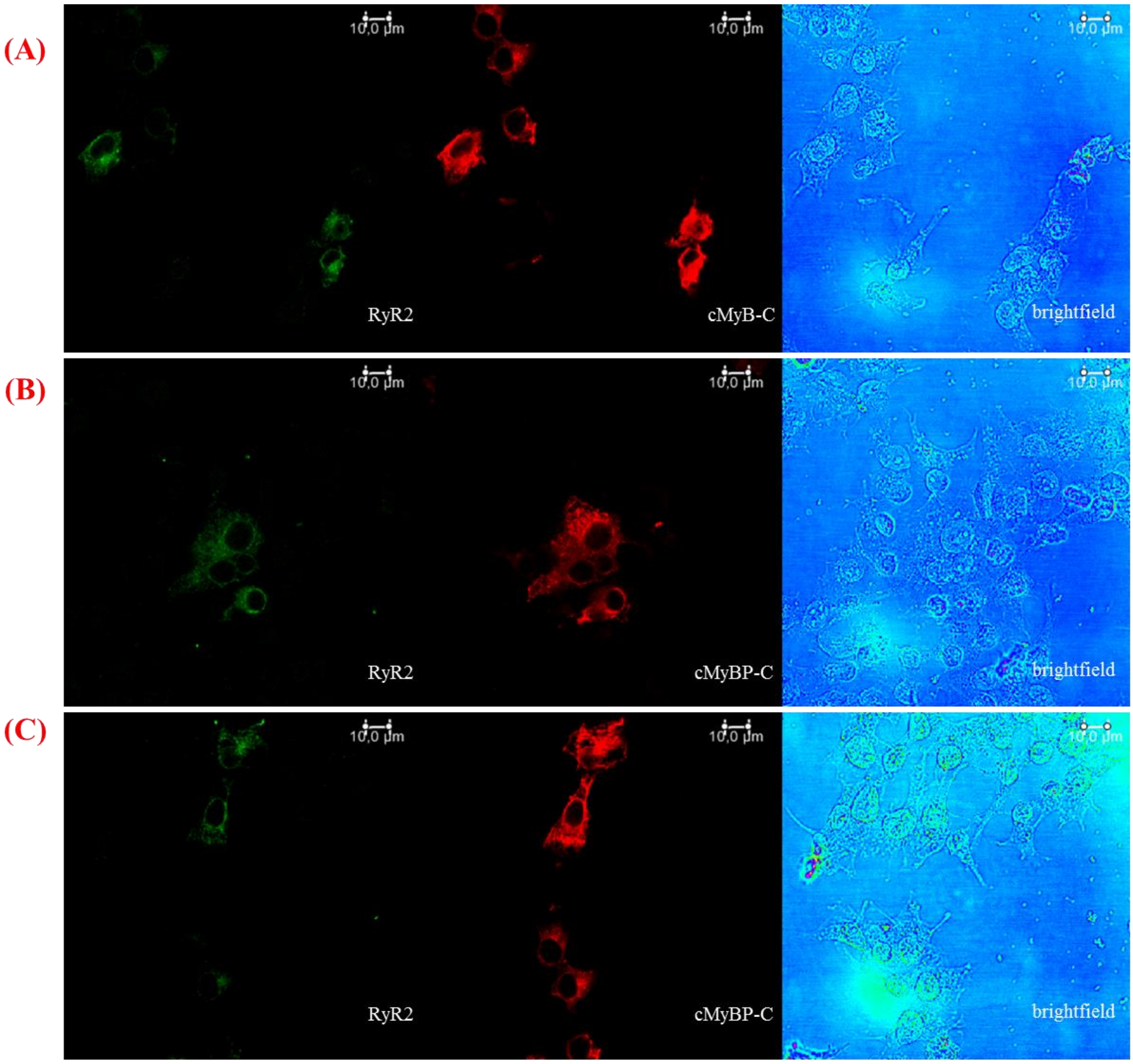

Figure 8.3 Imaging of RyR2 co-expression with cMyBP-C mCherry-FL in co-transfected HEK293 cell populations (A-C) three representative fields of form three independent experiments are shown; panels show green (RyR2) signal detection, (2) red (cMyBP-C) signal detection and (brightfield) corresponding brightfield image.

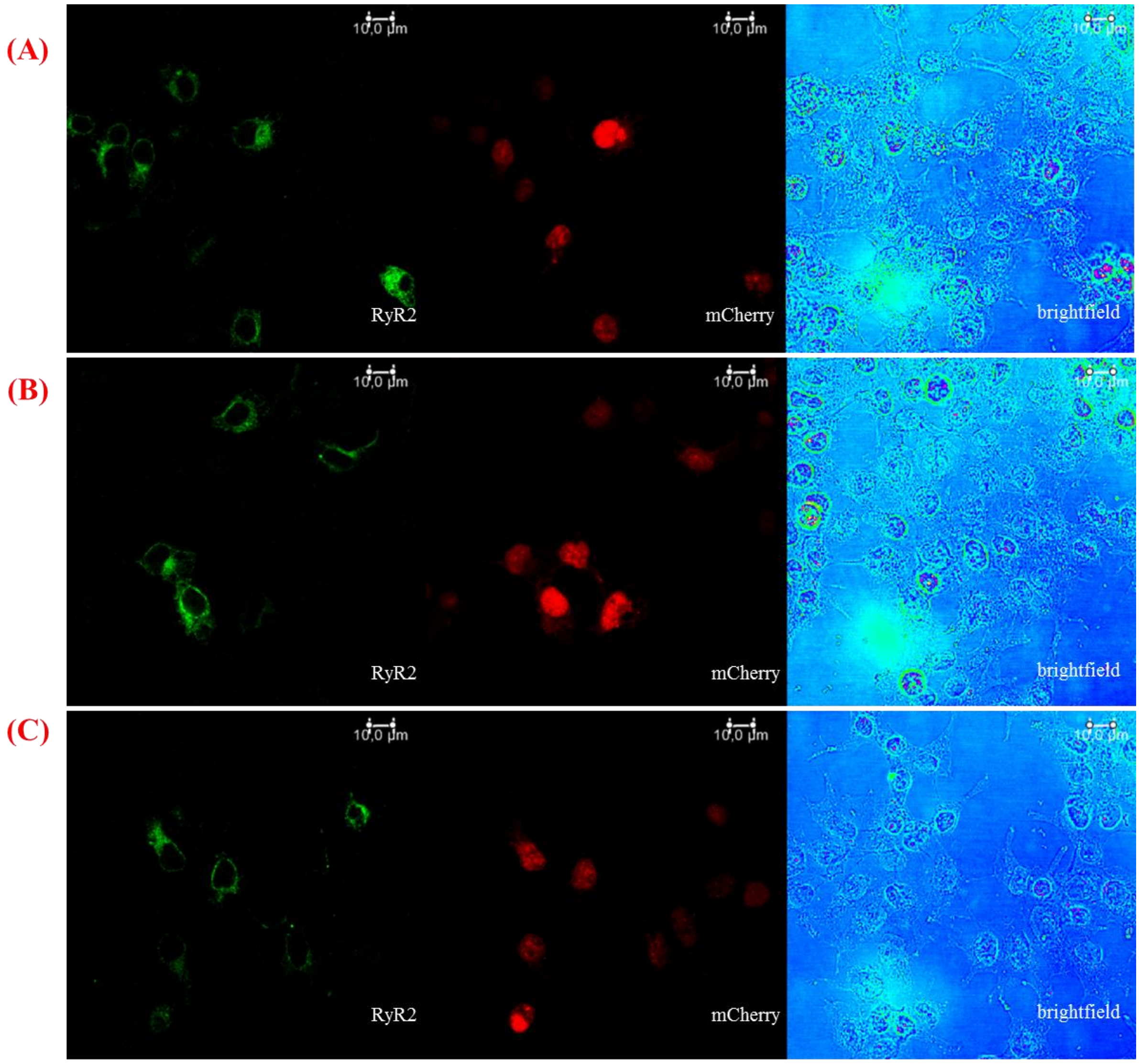

Figure 8.4 Imaging of RyR2 co-expression with mCherry in co-transfected HEK293 cell populations (A-C) three representative fields of form three independent experiments are shown; panels show green (RyR2) signal detection, red (mCherry) signal detection and (brightfield) corresponding brightfield image.

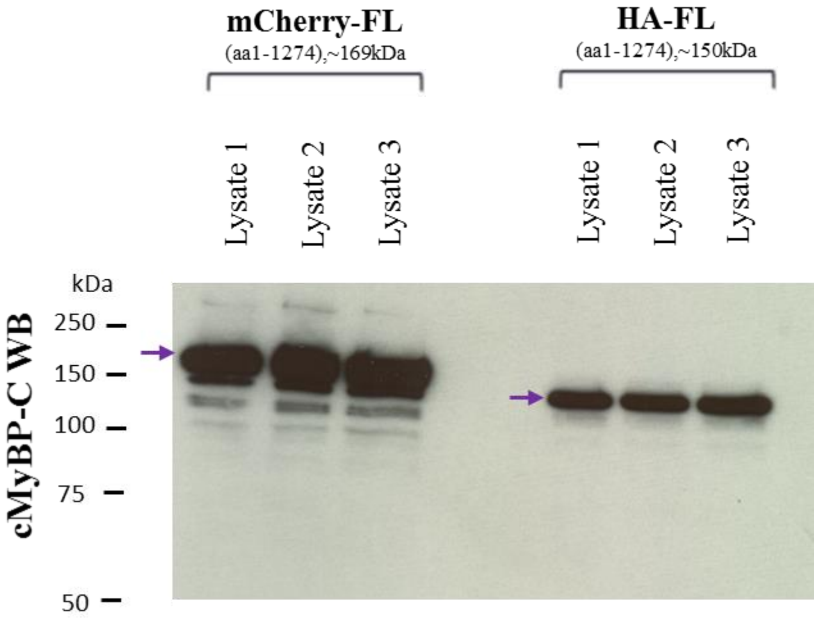

Figure 8.5 Blot displaying mCherry-FL and HA-FL expression in CHAP-solubilised HEK293 lysates, detected using cMyBP-C C-t Ab. Loaded 1/200 of amount processes in co-IP samples per lane, each being separate biological replicate used in co-IP analysis (Section 5.4.6).

Table 8.6 GraphPad results for single cell Ca^{2+} imaging with either one-way ANOVA with Bonferroni's multiple comparisons or Kruskal Wallis test with Dunn's multiple comparisons test for RyR2 versus RyR2 + mCherry-FL cMyBP-C versus RyR2 + mCherry parameters: (A) amplitude, (B) mean duration, (C) rate of Ca^{2+} release, (D) rate of Ca^{2+} decay, (E) inter-SCR duration, (F) frequency, (G) number of events, (H) ER Ca^{2+} store load

ANOVA summary	**(A) Amplitude**
F	0,4066
P value	**0,6666**
P value summary	**ns**
Significant diff. among means (P < 0.05)?	No
R square	0,004678

Bonferroni's multiple comparisons test	Mean Diff.	95.00% CI of diff.	Significant?	Summary
RyR2 + mCherry-FL amplitude vs. RyR2 amplitude	-0,09436	-0.4773 to 0.2886	No	ns
RyR2 + mCherry-FL amplitude vs. RyR2 + mCherry amplitude	0,07565	-0.4078 to 0.5591	No	ns

RyR2 amplitude vs. RyR2 + mCherry-FL amplitude	0,17	-0.3102 to 0.6502	No	ns

Kruskal-Wallis test	**(B) Mean duration**
P value	<0.0001
Exact or approximate P value?	Approximate
P value summary	****
Do the medians vary signif. (P < 0.05)?	Yes
Number of groups	3
Kruskal-Wallis statistic	23,12

Dunn's multiple comparisons test	Mean rank diff.	Significant?	Summary
RyR2 + mCherry-FL mean duration vs. RyR2 mean duration	38,88	Yes	****
RyR2 + mCherry-FL mean duration vs. RyR2 + mCherry mean duration	6,128	No	ns
RyR2 mean duration vs. RyR2 + mCherry mean duration	-32,75	Yes	**

ANOVA summary	**(C) Rate of Ca^{2+} release**
F	0,3184
P value	**0,7277**
P value summary	**ns**
Significant diff. among means (P < 0.05)?	No
R square	0,003667

Bonferroni's multiple comparisons test	Mean Diff.	95.00% CI of diff.	Significant ?	Summary

RyR2 + mCherry-FL mean rate up vs. RyR2 mean rate up	-0,04055	-0.1909 to 0.1098	No	ns
RyR2 + mCherry-FL mean rate up vs. RyR2 + mCherry mean rate up	0,01232	-0.1774 to 0.2021	No	ns
RyR2 mean rate up vs. RyR2 + mCherry mean rate up	0,05287	-0.1356 to 0.2414	No	ns

ANOVA summary	**(D) Rate of Ca^{2+} decay**
F	6,661
P value	0,0016
P value summary	**
Significant diff. among means (P < 0.05)?	Yes
R square	0,0715

Bonferroni's multiple comparisons test	Mean Diff.	95.00% CI of diff.	Significant ?	Summary
RyR2 + mCherry-FL mean rate down vs. Ryr2 mean rate down	-0,0655	-0.1119 to -0.01915	Yes	**
RyR2 + mCherry-FL mean rate down vs. RyR2 + mCherry mean rate down	-0,00499	-0.0635 to 0.05351	No	ns
RyR2 mean rate down vs. RyR2 + mCherry mean rate down	0,06051	0.002388 to 0.1186	Yes	*

ANOVA summary	**(E) Inter-SCR duration**
F	5,177
P value	0,0067
P value summary	**
Significant diff. among means (P < 0.05)?	Yes
R square	0,06498

Bonferroni's multiple comparisons test	Mean Diff.	95.00% CI of diff.	Significant?	Summary
RyR2 + mCherry-FL mean intr scr dur vs. RyR2 mean intr scr dur	7,742	0.02083 to 15.46	Yes	*
RyR2 + mCherry-FL mean intr scr dur vs. RyR2 + mCherry mean intr soc dur	11,84	2.198 to 21.49	Yes	*
RyR2 mean intr scr dur vs. RyR2 + mCherry mean intr scr dur	4,102	-5.182 to 13.39	No	ns

Kruskal-Wallis test	**(F) Frequency**
P value	0,0031
Exact or approximate P value?	Approximate
P value summary	**
Do the medians vary signif. (P < 0.05)?	Yes
Number of groups	3
Kruskal-Wallis statistic	11,52

Dunn's multiple comparisons test	Mean rank diff.	Significant?	Summary
RyR2 + mCherry-FL frequency vs. RyR2 frequency	-27,1	Yes	**
RyR2 + mCherry-FL frequency vs. RyR2 + mCherry frequency	-25,54	No	ns
RyR2 frequency vs. RyR2 + mCherry frequency	1,553	No	ns

Kruskal-Wallis test	**(G) Number of events**
P value	0,0124
Exact or approximate P value?	Approximate
P value summary	*
Do the medians vary signif. (P < 0.05)?	Yes
Number of groups	3

Kruskal-Wallis statistic	8,773

Dunn's multiple comparisons test	Mean rank diff.	Significant?	Summary
RyR2 + mCherry-FL no of events vs. RyR2 no of events	-21,3	Yes	*
RyR2 + mCherry-FL no of events vs. RyR2 + mCherry no of events	-26,14	Yes	*
RyR2 no of events vs. RyR2 + mCherry no of events	-4,847	No	ns

Kruskal-Wallis test	**(H)** **ER store content**
P value	0,2923
Exact or approximate P value?	Approximate
P value summary	**ns**
Do the medians vary signif. (P < 0.05)?	No
Number of groups	3
Kruskal-Wallis statistic	2,46

Dunn's multiple comparisons test	Mean rank diff.	Significant?	Summary
PC caffeine response vs. caffeine response	-8,187	No	ns
PC caffeine response vs. mc caffeine response	8,363	No	ns
caffeine response vs. mc caffeine response	16,55	No	ns

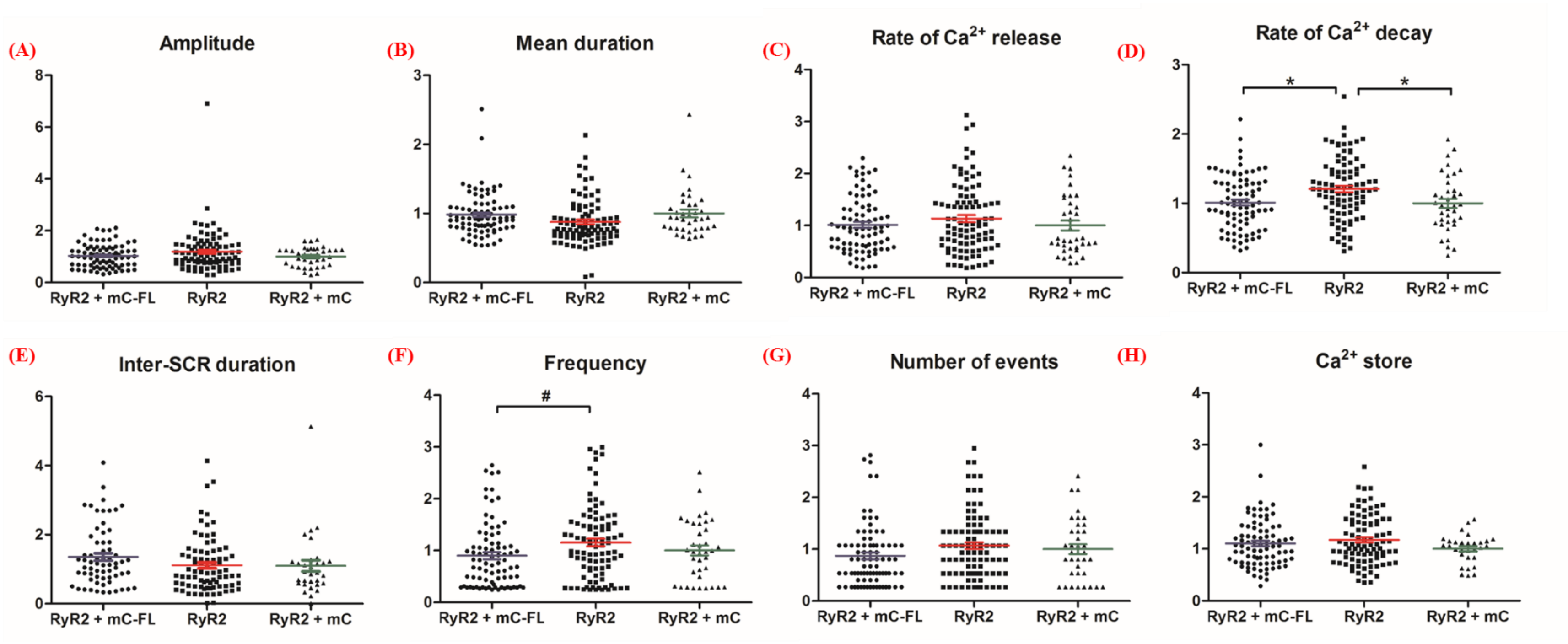

*Figure 8.6 Summary of raw data (all outliers included) of spontaneous Ca^{2+} release events examination using single cell Ca^{2+} imaging. Data are normalized for RyR2 + mCherry and shown as mean ±SD.. Samples: RyR2 + mCherry-FL (cMyBP-C) n=83, RyR2 only n=94, and RyR2 + mCherry n=37, from ≥8 independent experiments; * statistical significance at $p<0.05$ calculated using one-way ANOVA with Bonferroni's multiple comparisons test, # statistical significance at $p<0.05$ calculated using Kruskal-Wallis test with Dunn's multiple comparisons test.*

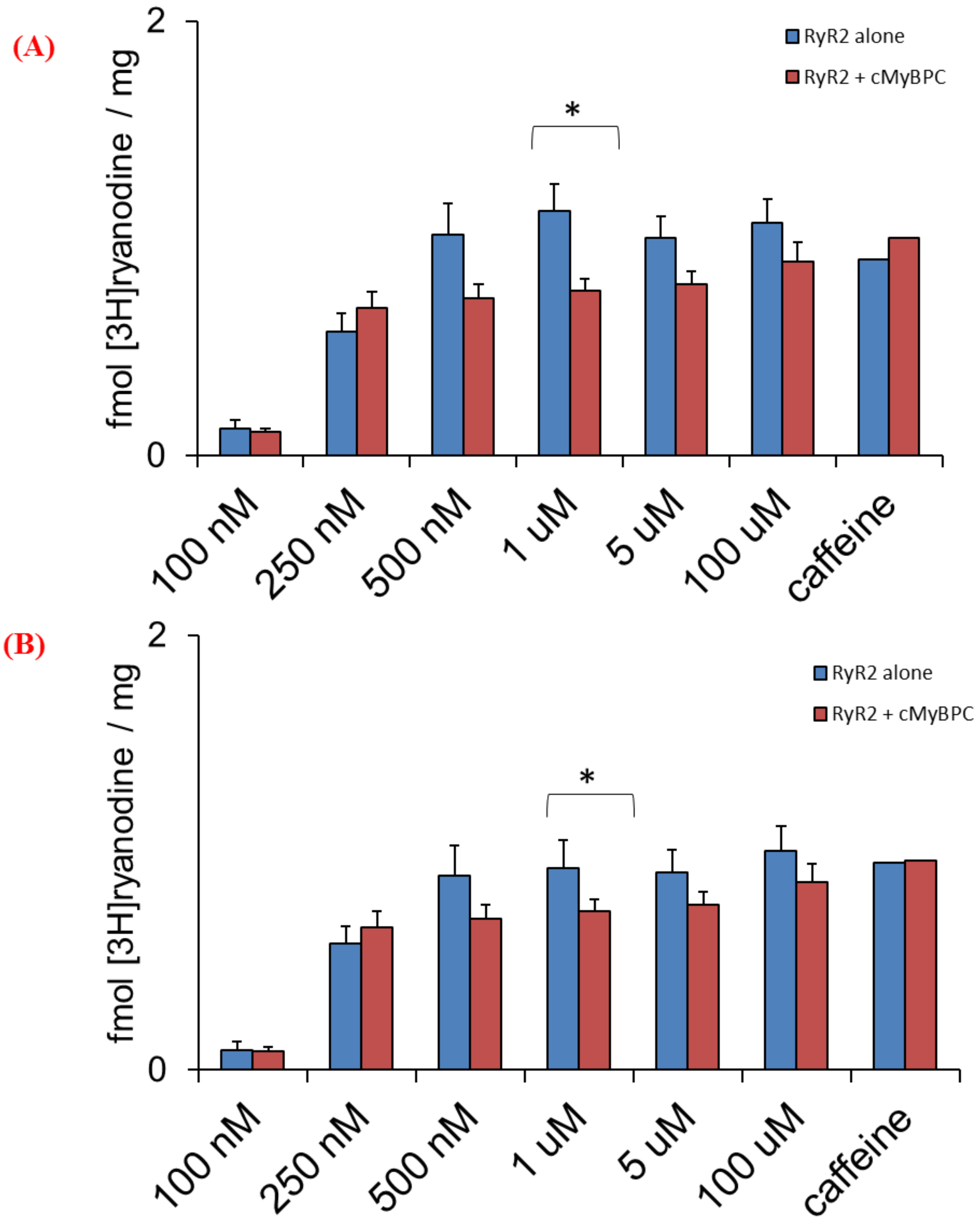

*Figure 8.7 Summary of raw data (all outliers included) and post-outlier removed data (as in Figure 5.2,A) as assessed in [^{3}H]ryanodine binding assay over a range of free Ca^{2+} concentrations. (A) raw data, (B) post-outlier removed data, both presented relative to maximum binding obtained for the RyR2 (+HA) at 100µmol Ca^{2+} and shown as mean ±SEM, * statistical significance at $p<0.05$ calculated using unpaired, 2-tailed Student's t-test, n≥15 for each Ca^{2+} concertation point.*

References

9 References

Ababou, A. et al. 2007. Dissecting the N-terminal myosin binding site of human cardiac myosin-binding protein C. Structure and myosin binding of domain C2. *J Biol Chem* 282(12), pp. 9204-9215. doi: 10.1074/jbc.M610899200

Ababou, A. et al. 2008. Myosin binding protein C positioned to play a key role in regulation of muscle contraction: structure and interactions of domain C1. *J Mol Biol* 384(3), pp. 615-630. doi: 10.1016/j.jmb.2008.09.065

Ackermann, M. A. et al. 2009. Obscurin interacts with a novel isoform of MyBP-C slow at the periphery of the sarcomeric M-band and regulates thick filament assembly. *Mol Biol Cell* 20(12), pp. 2963-2978. doi: 10.1091/mbc.E08-12-1251

Ackermann, M. A. et al. 2015. Myosin Binding Protein-C Slow Phosphorylation is Altered in Duchenne Dystrophy and Arthrogryposis Myopathy in Fast-Twitch Skeletal Muscles. *Sci Rep* 5, p. 13235. doi: 10.1038/srep13235

Adler, J. and Parmryd, I. 2010. Quantifying colocalization by correlation: the Pearson correlation coefficient is superior to the Mander's overlap coefficient. *Cytometry A* 77(8), pp. 733-742. doi: 10.1002/cyto.a.20896

Alyonycheva, T. N. et al. 1997. Isoform-specific interaction of the myosin-binding proteins (MyBPs) with skeletal and cardiac myosin is a property of the C-terminal immunoglobulin domain. *J Biol Chem* 272(33), pp. 20866-20872.

Amador, F. J. et al. 2013. Type 2 ryanodine receptor domain A contains a unique and dynamic alpha-helix that transitions to a beta-strand in a mutant linked with a heritable cardiomyopathy. *J Mol Biol* 425(21), pp. 4034-4046. doi: 10.1016/j.jmb.2013.08.015

Amador, F. J. et al. 2009. Crystal structure of type I ryanodine receptor amino-terminal beta-trefoil domain reveals a disease-associated mutation "hot spot" loop. *Proc Natl Acad Sci U S A* 106(27), pp. 11040-11044. doi: 10.1073/pnas.0905186106

Aryal, B. et al. 2014. Doxorubicin-induced carbonylation and degradation of cardiac myosin binding protein C promote cardiotoxicity. *Proc Natl Acad Sci U S A* 111(5), pp. 2011-2016. doi: 10.1073/pnas.1321783111

Asghari, P. et al. 2009. Axial tubules of rat ventricular myocytes form multiple junctions with the sarcoplasmic reticulum.*Biophys J*. Vol. 96. United States, pp. 4651-4660.

Asghari, P. et al. 2014. Nonuniform and variable arrangements of ryanodine receptors within mammalian ventricular couplons.*Circ Res*. Vol. 115. United States: 2014 American Heart Association, Inc., pp. 252-262.

Aston, D. et al. 2017. High resolution structural evidence suggests the Sarcoplasmic Reticulum forms microdomains with Acidic Stores (lysosomes) in the heart. *Sci Rep* 7, p. 40620. doi: 10.1038/srep40620

Auslander, S. et al. 2014. A general design strategy for protein-responsive riboswitches in mammalian cells. *Nat Methods* 11(11), pp. 1154-1160. doi: 10.1038/nmeth.3136

Avkiran, M. and Marber, M. S. 2002. Na(+)/H(+) exchange inhibitors for cardioprotective therapy: progress, problems and prospects. *J Am Coll Cardiol* 39(5), pp. 747-753.

Baddeley, D. et al. 2009. Optical single-channel resolution imaging of the ryanodine receptor distribution in rat cardiac myocytes. *Proc Natl Acad Sci U S A* 106(52), pp. 22275-22280. doi: 10.1073/pnas.0908971106

Bahrudin, U. et al. 2011. Impairment of ubiquitin-proteasome system by E334K cMyBPC modifies channel proteins, leading to electrophysiological dysfunction. *J Mol Biol* 413(4), pp. 857-878. doi: 10.1016/j.jmb.2011.09.006

Bahrudin, U. et al. 2008. Ubiquitin-proteasome system impairment caused by a missense cardiac myosin-binding protein C mutation and associated with cardiac dysfunction in hypertrophic cardiomyopathy. *J Mol Biol* 384(4), pp. 896-907. doi: 10.1016/j.jmb.2008.09.070

Baker, J. O. et al. 2015. Cardiac myosin-binding protein C: a potential early biomarker of myocardial injury. *Basic Res Cardiol* 110(3), p. 478. doi: 10.1007/s00395-015-0478-5

Bardswell, S. C. et al. 2010. Distinct sarcomeric substrates are responsible for protein kinase D-mediated regulation of cardiac myofilament Ca2+ sensitivity and cross-bridge cycling. *J Biol Chem* 285(8), pp. 5674-5682. doi: 10.1074/jbc.M109.066456

Barefield, D. et al. 2014. Contractile dysfunction in a mouse model expressing a heterozygous MYBPC3 mutation associated with hypertrophic cardiomyopathy. *Am J Physiol Heart Circ Physiol* 306(6), pp. H807-815. doi: 10.1152/ajpheart.00913.2013

Beam, K. G. et al. 1992. Function of a truncated dihydropyridine receptor as both voltage sensor and calcium channel. *Nature* 360(6400), pp. 169-171. doi: 10.1038/360169a0

Benian, G. M. and Mayans, O. 2015. Titin and obscurin: giants holding hands and discovery of a new Ig domain subset. *J Mol Biol* 427(4), pp. 707-714. doi: 10.1016/j.jmb.2014.12.017

Berridge, M. J. 2006. Calcium microdomains: organization and function. *Cell Calcium* 40(5-6), pp. 405-412. doi: 10.1016/j.ceca.2006.09.002

Berridge, M. J. et al. 2003. Calcium signalling: dynamics, homeostasis and remodelling. *Nat Rev Mol Cell Biol* 4(7), pp. 517-529. doi: 10.1038/nrm1155

Bers, D. M. 2002. Cardiac excitation-contraction coupling. *Nature* 415(6868), pp. 198-205. doi: 10.1038/415198a

Bers, D. M. 2004. Macromolecular complexes regulating cardiac ryanodine receptor function. *J Mol Cell Cardiol* 37(2), pp. 417-429. doi: 10.1016/j.yjmcc.2004.05.026

Bers, D. M. 2008. Calcium cycling and signaling in cardiac myocytes. *Annu Rev Physiol* 70, pp. 23-49. doi: 10.1146/annurev.physiol.70.113006.100455

Bers, D. M. 2014. Cardiac sarcoplasmic reticulum calcium leak: basis and roles in cardiac dysfunction. *Annu Rev Physiol* 76, pp. 107-127. doi: 10.1146/annurev-physiol-020911-153308

Bers, D. M. and Shannon, T. R. 2013. Calcium movements inside the sarcoplasmic reticulum of cardiac myocytes. *J Mol Cell Cardiol* 58, pp. 59-66. doi: 10.1016/j.yjmcc.2013.01.002

Berul, C. I. et al. 2001. Ventricular arrhythmia vulnerability in cardiomyopathic mice with homozygous mutant Myosin-binding protein C gene. *Circulation* 104(22), pp. 2734-2739.

Bezprozvanny, I. et al. 1991. Bell-shaped calcium-response curves of Ins(1,4,5)P3- and calcium-gated channels from endoplasmic reticulum of cerebellum. *Nature* 351(6329), pp. 751-754. doi: 10.1038/351751a0

Biesiadecki, B. J. et al. 2014. Tri-modal regulation of cardiac muscle relaxation; intracellular calcium decline, thin filament deactivation, and cross-bridge cycling kinetics. *Biophys Rev* 6(3-), pp. 273-289. doi: 10.1007/s12551-014-0143-5

Biesmans, L. et al. 2011. Subcellular heterogeneity of ryanodine receptor properties in ventricular myocytes with low T-tubule density. *PLoS One* 6(10), p. e25100. doi: 10.1371/journal.pone.0025100

Bootman, M. D. et al. 2006. Calcium signalling during excitation-contraction coupling in mammalian atrial myocytes. *J Cell Sci* 119(Pt 19), pp. 3915-3925. doi: 10.1242/jcs.03223

Borko, L. et al. 2014. Structural insights into the human RyR2 N-terminal region involved in cardiac arrhythmias. *Acta Crystallogr D Biol Crystallogr* 70(Pt 11), pp. 2897-2912. doi: 10.1107/s1399004714020343

Brickson, S. et al. 2007. In vivo left ventricular functional capacity is compromised in cMyBP-C null mice. *Am J Physiol Heart Circ Physiol* 292(4), pp. H1747-1754. doi: 10.1152/ajpheart.01037.2006

Bround, M. J. et al. 2016. Cardiac Ryanodine Receptor (Ryr2)-mediated Calcium Signals Specifically Promote Glucose Oxidation via Pyruvate Dehydrogenase. *J Biol Chem* 291(45), pp. 23490-23505. doi: 10.1074/jbc.M116.756973

Bround, M. J. et al. 2013. Cardiomyocyte ATP production, metabolic flexibility, and survival require calcium flux through cardiac ryanodine receptors in vivo. *J Biol Chem* 288(26), pp. 18975-18986. doi: 10.1074/jbc.M112.427062

Cannell, M. B. and Cody, S. H. 2006. Fluorescent ion measurement. *Handbook Of Biological Confocal Microscopy*. Springer US.

Carrier, L. et al. 2004. Asymmetric septal hypertrophy in heterozygous cMyBP-C null mice. *Cardiovasc Res* 63(2), pp. 293-304. doi: 10.1016/j.cardiores.2004.04.009

Carrier, L. et al. 2015. Cardiac myosin-binding protein C (MYBPC3) in cardiac pathophysiology. *Gene* 573(2), pp. 188-197. doi: 10.1016/j.gene.2015.09.008

Cecchi, F. et al. 2012. Clinical and molecular classification of cardiomyopathies. *Glob Cardiol Sci Pract* 2012(1), p. 4. doi: 10.5339/gcsp.2012.4

Chelu, M. G. et al. 2004. Regulation of ryanodine receptors by FK506 binding proteins. *Trends Cardiovasc Med* 14(6), pp. 227-234. doi: 10.1016/j.tcm.2004.06.003

Chen, S. R. et al. 2002. Role of the proposed pore-forming segment of the Ca^{2+} release channel (ryanodine receptor) in ryanodine interaction. *Biophys J* 82(5), pp. 2436-2447.

Chen, S. R. et al. 1997. Functional characterization of the recombinant type 3 Ca^{2+} release channel (ryanodine receptor) expressed in HEK293 cells. *J Biol Chem* 272(39), pp. 24234-24246.

Chen-Izu, Y. et al. 2006. Three-dimensional distribution of ryanodine receptor clusters in cardiac myocytes.*Biophys J*. Vol. 91. United States, pp. 1-13.

Cheng, Y. et al. 2013. Impaired contractile function due to decreased cardiac myosin binding protein C content in the sarcomere. *Am J Physiol Heart Circ Physiol* 305(1), pp. H52-65. doi: 10.1152/ajpheart.00929.2012

Chi, E. Y. et al. 2003. Physical stability of proteins in aqueous solution: mechanism and driving forces in nonnative protein aggregation. *Pharm Res* 20(9), pp. 1325-1336.

Ching, L. L. et al. 2000. Evidence for Ca(2+) activation and inactivation sites on the luminal side of the cardiac ryanodine receptor complex. *Circ Res* 87(3), pp. 201-206.

Chiu, C. et al. 2010. Mutations in alpha-actinin-2 cause hypertrophic cardiomyopathy: a genome-wide analysis.*J Am Coll Cardiol*. Vol. 55. United States: 2010 American College of Cardiology Foundation. Published by Elsevier Inc, pp. 1127-1135.

Clapham, D. E. 2007. Calcium signaling. *Cell* 131(6), pp. 1047-1058. doi: 10.1016/j.cell.2007.11.028

Clark, K. A. et al. 2002. Striated muscle cytoarchitecture: an intricate web of form and function. *Annu Rev Cell Dev Biol* 18, pp. 637-706. doi: 10.1146/annurev.cellbio.18.012502.105840

Collins, T. P. et al. 2011. NAADP influences excitation-contraction coupling by releasing calcium from lysosomes in atrial myocytes. *Cell Calcium* 50(5), pp. 449-458. doi: 10.1016/j.ceca.2011.07.007

Colson, B. A. et al. 2016. Site-directed spectroscopy of cardiac myosin-binding protein C reveals effects of phosphorylation on protein structural dynamics. *Proc Natl Acad Sci U S A* 113(12), pp. 3233-3238. doi: 10.1073/pnas.1521281113

Cuello, F. et al. 2011. Novel role for p90 ribosomal S6 kinase in the regulation of cardiac myofilament phosphorylation. *J Biol Chem* 286(7), pp. 5300-5310. doi: 10.1074/jbc.M110.202713

d'Amati, G. et al. 2005. Juvenile sudden death in a family with polymorphic ventricular arrhythmias caused by a novel RyR2 gene mutation: evidence of specific morphological substrates. *Hum Pathol* 36(7), pp. 761-767. doi: 10.1016/j.humpath.2005.04.019

Decker, R. S. et al. 2012. The dynamic role of cardiac myosin binding protein-C during ischemia.*J Mol Cell Cardiol*. Vol. 52. England: 2012 Elsevier Ltd, pp. 1145-1154.

Del Prete, D. et al. 2014. Ryanodine receptors: physiological function and deregulation in Alzheimer disease. *Mol Neurodegener* 9, p. 21. doi: 10.1186/1750-1326-9-21

Dhandapany, P. S. et al. 2009. A common MYBPC3 (cardiac myosin binding protein C) variant associated with cardiomyopathies in South Asia. *Nat Genet* 41(2), pp. 187-191. doi: 10.1038/ng.309

Dhoot, G. K. et al. 1985. The isoforms of C protein and their distribution in mammalian skeletal muscle. *J Muscle Res Cell Motil* 6(4), pp. 487-505.

Dobrev, D. and Wehrens, X. H. 2014. Role of RyR2 phosphorylation in heart failure and arrhythmias: Controversies around ryanodine receptor phosphorylation in cardiac disease. *Circ Res* 114(8), pp. 1311-1319; discussion 1319. doi: 10.1161/circresaha.114.300568

Dokuparti, M. V. et al. 2005. Etiopathogenesis of arrhythmogenic right ventricular cardiomyopathy. *J Hum Genet* 50(8), pp. 375-381. doi: 10.1007/s10038-005-0273-5

Domingo, D. et al. 2014. Non-ventricular, Clinical, and Functional Features of the RyR2 Mutation Causing Catecholaminergic Polymorphic Ventricular Tachycardia. *Rev Esp Cardiol (Engl Ed)*, doi: 10.1016/j.rec.2014.04.023

Du, G. G. et al. 1998. Characterization of recombinant rabbit cardiac and skeletal muscle Ca^{2+} release channels (ryanodine receptors) with a novel [3H]ryanodine binding assay. *J Biol Chem* 273(50), pp. 33259-33266.

Du, G. G. et al. 2000. Mutation of divergent region 1 alters caffeine and Ca(2+) sensitivity of the skeletal muscle Ca(2+) release channel (ryanodine receptor). *J Biol Chem* 275(16), pp. 11778-11783.

Dunn, K. W. et al. 2011. A practical guide to evaluating colocalization in biological microscopy. *Am J Physiol Cell Physiol* 300(4), pp. C723-742. doi: 10.1152/ajpcell.00462.2010

Eager, K. R. and Dulhunty, A. F. 1998. Activation of the cardiac ryanodine receptor by sulfhydryl oxidation is modified by Mg^{2+} and ATP. *J Membr Biol* 163(1), pp. 9-18.

Efremov, R. G. et al. 2015. Architecture and conformational switch mechanism of the ryanodine receptor. *Nature* 517(7532), pp. 39-43. doi: 10.1038/nature13916

Eisner, D. et al. 2013. Calcium flux balance in the heart. *J Mol Cell Cardiol* 58, pp. 110-117. doi: 10.1016/j.yjmcc.2012.11.017

El-Armouche, A. et al. 2007. Decreased phosphorylation levels of cardiac myosin-binding protein-C in human and experimental heart failure.*J Mol Cell Cardiol*. Vol. 43. England, pp. 223-229.

Elion, E. A. 2007. Detection of protein-protein interactions by coprecipitation. *Curr Protoc Immunol* Chapter 8, p. Unit 8.7. doi: 10.1002/0471142727.im0807s76

Escobar, M. et al. 2011. Structural evidence for perinuclear calcium microdomains in cardiac myocytes. *J Mol Cell Cardiol* 50(3), pp. 451-459. doi: 10.1016/j.yjmcc.2010.11.021

Farrell, E. F. et al. 2003. Sorcin inhibits calcium release and modulates excitation-contraction coupling in the heart. *J Biol Chem* 278(36), pp. 34660-34666. doi: 10.1074/jbc.M305931200

Fashena, S. J. et al. 2000. The continued evolution of two-hybrid screening approaches in yeast: how to outwit different preys with different baits. *Gene* 250(1-2), pp. 1-14.

Fauconnier, J. et al. 2013. Type 2 ryanodine receptor: a novel therapeutic target in myocardial ischemia/reperfusion. *Pharmacol Ther* 138(3), pp. 323-332. doi: 10.1016/j.pharmthera.2013.01.015

Fearnley, C. J. et al. 2011. Calcium signaling in cardiac myocytes. *Cold Spring Harb Perspect Biol* 3(11), p. a004242. doi: 10.1101/cshperspect.a004242

Ferrantini, C. et al. 2013. The transverse-axial tubular system of cardiomyocytes. *Cell Mol Life Sci* 70(24), pp. 4695-4710. doi: 10.1007/s00018-013-1410-5

Ferreiro, A. et al. 2002. Mutations of the selenoprotein N gene, which is implicated in rigid spine muscular dystrophy, cause the classical phenotype of multiminicore disease: reassessing the nosology of early-onset myopathies. *Am J Hum Genet* 71(4), pp. 739-749. doi: 10.1086/342719

Fert-Bober, J. and Sokolove, J. 2014. Proteomics of citrullination in cardiovascular disease. *Proteomics Clin Appl* 8(7-8), pp. 522-533. doi: 10.1002/prca.201400013

Fessenden, J. D. et al. 2004. Mutational analysis of putative calcium binding motifs within the skeletal ryanodine receptor isoform, RyR1. *J Biol Chem* 279(51), pp. 53028-53035. doi: 10.1074/jbc.M411136200

Flashman, E. et al. 2008. Support for a trimeric collar of myosin binding protein C in cardiac and fast skeletal muscle, but not in slow skeletal muscle. *FEBS Lett* 582(3), pp. 434-438. doi: 10.1016/j.febslet.2008.01.004

Franzini-Armstrong, C. et al. 1999. Shape, size, and distribution of Ca(2+) release units and couplons in skeletal and cardiac muscles. *Biophys J* 77(3), pp. 1528-1539. doi: 10.1016/s0006-3495(99)77000-1

Fraysse, B. et al. 2012. Increased myofilament Ca^{2+} sensitivity and diastolic dysfunction as early consequences of Mybpc3 mutation in heterozygous knock-in mice.*J Mol Cell Cardiol*. Vol. 52. England: 2012 Elsevier Ltd, pp. 1299-1307.

Freiburg, A. and Gautel, M. 1996. A Molecular Map of the Interactions between Titin and Myosin-Binding Protein C. *European Journal of Biochemistry* 235(1-2), pp. 317-323. doi: 10.1111/j.1432-1033.1996.00317.x

Fruen, B. R. et al. 2003. Regulation of the RYR1 and RYR2 Ca^{2+} release channel isoforms by Ca^{2+}-insensitive mutants of calmodulin. *Biochemistry* 42(9), pp. 2740-2747. doi: 10.1021/bi0267689

Furst, D. O. et al. 1992. Mammalian skeletal muscle C-protein: purification from bovine muscle, binding to titin and the characterization of a full-length human cDNA. *J Cell Sci* 102 (Pt 4), pp. 769-778.

Futatsugi, A. et al. 1995. Tissue-specific and developmentally regulated alternative splicing in mouse skeletal muscle ryanodine receptor mRNA. *Biochem J* 305 (Pt 2), pp. 373-378.

Galfre, E. et al. 2012. FKBP12 activates the cardiac ryanodine receptor Ca^{2+}-release channel and is antagonised by FKBP12.6. *PLoS One* 7(2), p. e31956. doi: 10.1371/journal.pone.0031956

Gao, L. et al. 1997. Evidence for a role of C-terminal amino acid residues in skeletal muscle Ca^{2+} release channel (ryanodine receptor) function. *FEBS Lett* 412(1), pp. 223-226.

Gautel, M. and Djinovic-Carugo, K. 2016. The sarcomeric cytoskeleton: from molecules to motion. *J Exp Biol* 219(Pt 2), pp. 135-145. doi: 10.1242/jeb.124941

Gautel, M. et al. 1995. Phosphorylation switches specific for the cardiac isoform of myosin binding protein-C: a modulator of cardiac contraction? *Embo j* 14(9), pp. 1952-1960.

Gedicke, C. 2011. Hypertrophic cardiomyopathy: Development of new molecular strategies for mutation analysis and therapy. Doctoral dissertation, University of Hamburg.

George, C. H. et al. 2003a. Ryanodine receptor mutations associated with stress-induced ventricular tachycardia mediate increased calcium release in stimulated cardiomyocytes.*Circ Res*. Vol. 93. United States, pp. 531-540.

George, C. H. et al. 2003b. Dysregulated ryanodine receptors mediate cellular toxicity: restoration of normal phenotype by FKBP12.6. *J Biol Chem* 278(31), pp. 28856-28864. doi: 10.1074/jbc.M212440200

George, C. H. et al. 2006. Arrhythmogenic mutation-linked defects in ryanodine receptor autoregulation reveal a novel mechanism of Ca^{2+} release channel dysfunction.*Circ Res*. Vol. 98. United States, pp. 88-97.

George, C. H. et al. 2007. Alternative splicing of ryanodine receptors modulates cardiomyocyte Ca^{2+} signaling and susceptibility to apoptosis.*Circ Res*. Vol. 100. United States, pp. 874-883.

Giannini, G. et al. 1995. The ryanodine receptor/calcium channel genes are widely and differentially expressed in murine brain and peripheral tissues. *J Cell Biol* 128(5), pp. 893-904.

Giannini, G. and Sorrentino, V. 1995. Molecular structure and tissue distribution of ryanodine receptors calcium channels. *Med Res Rev* 15(4), pp. 313-323.

Gilbert, R. et al. 1999. Identification of the A-band localization domain of myosin binding proteins C and H (MyBP-C, MyBP-H) in skeletal muscle. *J Cell Sci* 112 (Pt 1), pp. 69-79.

Gilbert, R. et al. 1996. The carboxyl terminus of myosin binding protein C (MyBP-C, C-protein) specifies incorporation into the A-band of striated muscle. *J Cell Sci* 109 (Pt 1), pp. 101-111.

Gillard, E. F. et al. 1991. A substitution of cysteine for arginine 614 in the ryanodine receptor is potentially causative of human malignant hyperthermia. *Genomics* 11(3), pp. 751-755.

Godin, A. G. et al. 2014. Super-resolution microscopy approaches for live cell imaging. *Biophys J* 107(8), pp. 1777-1784. doi: 10.1016/j.bpj.2014.08.028

Golebiewska, U. and Scarlata, S. 2011. Measuring fast calcium fluxes in cardiomyocytes. *J Vis Exp* (57), p. e3505. doi: 10.3791/3505

Gorza, L. et al. 1997. Regional and age-related differences in mRNA composition of intracellular Ca(2+)-release channels of rat cardiac myocytes. *J Mol Cell Cardiol* 29(3), pp. 1023-1036. doi: 10.1006/jmcc.1996.0346

Govada, L. et al. 2008. Crystal structure of the C1 domain of cardiac myosin binding protein-C: implications for hypertrophic cardiomyopathy. *J Mol Biol* 378(2), pp. 387-397. doi: 10.1016/j.jmb.2008.02.044

Govindan, S. et al. 2012. Cardiac myosin binding protein-C is a potential diagnostic biomarker for myocardial infarction. *J Mol Cell Cardiol* 52(1), pp. 154-164. doi: 10.1016/j.yjmcc.2011.09.011

Graham, F. L. et al. 1977. Characteristics of a human cell line transformed by DNA from human adenovirus type 5. *J Gen Virol* 36(1), pp. 59-74. doi: 10.1099/0022-1317-36-1-59

Gruen, M. and Gautel, M. 1999. Mutations in β-myosin S2 that cause familial hypertrophic cardiomyopathy (FHC) abolish the interaction with the regulatory domain of myosin-binding protein-C. *Journal of Molecular Biology* 286(3), pp. 933-949. doi: http://dx.doi.org/10.1006/jmbi.1998.2522

Guo, A. et al. 2013. Emerging mechanisms of T-tubule remodelling in heart failure. *Cardiovasc Res* 98(2), pp. 204-215. doi: 10.1093/cvr/cvt020

Guo, T. et al. 2010. Kinetics of FKBP12.6 binding to ryanodine receptors in permeabilized cardiac myocytes and effects on Ca sparks. *Circ Res* 106(11), pp. 1743-1752. doi: 10.1161/circresaha.110.219816

Guo, W. et al. 2016. The EF-hand Ca^{2+} Binding Domain Is Not Required for Cytosolic Ca^{2+} Activation of the Cardiac Ryanodine Receptor. *J Biol Chem* 291(5), pp. 2150-2160. doi: 10.1074/jbc.M115.693325

Gurnett, C. A. et al. 2010. Myosin binding protein C1: a novel gene for autosomal dominant distal arthrogryposis type 1. *Hum Mol Genet* 19(7), pp. 1165-1173. doi: 10.1093/hmg/ddp587

Gyorke, I. et al. 2004. The role of calsequestrin, triadin, and junctin in conferring cardiac ryanodine receptor responsiveness to luminal calcium. *Biophys J* 86(4), pp. 2121-2128. doi: 10.1016/s0006-3495(04)74271-x

Gyorke, S. and Terentyev, D. 2008. Modulation of ryanodine receptor by luminal calcium and accessory proteins in health and cardiac disease. *Cardiovasc Res* 77(2), pp. 245-255. doi: 10.1093/cvr/cvm038

Haas, J. et al. 2014. Atlas of the clinical genetics of human dilated cardiomyopathy. *Eur Heart J*, doi: 10.1093/eurheartj/ehu301

Hakamata, Y. et al. 1992. Primary structure and distribution of a novel ryanodine receptor/calcium release channel from rabbit brain. *FEBS Lett* 312(2-3), pp. 229-235.

Handhle, A. et al. 2016. Calsequestrin interacts directly with the cardiac ryanodine receptor luminal domain. *J Cell Sci* 129(21), pp. 3983-3988. doi: 10.1242/jcs.191643

Harpaz, Y. and Chothia, C. 1994. Many of the immunoglobulin superfamily domains in cell adhesion molecules and surface receptors belong to a new structural set which is close to that containing variable domains. *J Mol Biol* 238(4), pp. 528-539. doi: 10.1006/jmbi.1994.1312

Harris, S. P. et al. 2002. Hypertrophic cardiomyopathy in cardiac myosin binding protein-C knockout mice. *Circ Res* 90(5), pp. 594-601.

Harris, S. P. et al. 2011. In the thick of it: HCM-causing mutations in myosin binding proteins of the thick filament. *Circ Res* 108(6), pp. 751-764. doi: 10.1161/circresaha.110.231670

Hausenloy, D. J. and Yellon, D. M. 2013. Myocardial ischemia-reperfusion injury: a neglected therapeutic target. *J Clin Invest* 123(1), pp. 92-100. doi: 10.1172/jci62874

Hayashi, T. et al. 2009. Three-dimensional electron microscopy reveals new details of membrane systems for Ca^{2+} signaling in the heart. *J Cell Sci* 122(Pt 7), pp. 1005-1013. doi: 10.1242/jcs.028175

Hayek, S. M. et al. 1999. A negatively charged region of the skeletal muscle ryanodine receptor is involved in Ca(2+)-dependent regulation of the Ca(2+) release channel. *FEBS Lett* 461(3), pp. 157-164.

Hiess, F. et al. 2015. Distribution and Function of Cardiac Ryanodine Receptor Clusters in Live Ventricular Myocytes. *J Biol Chem* 290(33), pp. 20477-20487. doi: 10.1074/jbc.M115.650531

Hitomi, N. et al. 2010. A frameshift deletion mutation in the cardiac myosin-binding protein C gene associated with dilated phase of hypertrophic cardiomyopathy and dilated cardiomyopathy. *J Cardiol* 56(2), pp. 189-196. doi: 10.1016/j.jjcc.2010.04.003

Hofmann, P. A. et al. 1991. C-protein limits shortening velocity of rabbit skeletal muscle fibres at low levels of Ca^{2+} activation. *J Physiol* 439, pp. 701-715.

Hohenegger, M. and Suko, J. 1993. Phosphorylation of the purified cardiac ryanodine receptor by exogenous and endogenous protein kinases. *Biochem J* 296 (Pt 2), pp. 303-308.

Hou, Y. et al. 2015. Nanoscale analysis of ryanodine receptor clusters in dyadic couplings of rat cardiac myocytes. *J Mol Cell Cardiol* 80, pp. 45-55. doi: 10.1016/j.yjmcc.2014.12.013

Howarth, J. W. et al. 2012. Structural insight into unique cardiac myosin-binding protein-C motif: a partially folded domain. *J Biol Chem* 287(11), pp. 8254-8262. doi: 10.1074/jbc.M111.309591

Hwang, H. S. et al. 2014. Divergent regulation of ryanodine receptor 2 calcium release channels by arrhythmogenic human calmodulin missense mutants. *Circ Res* 114(7), pp. 1114-1124. doi: 10.1161/circresaha.114.303391

Idowu, S. M. et al. 2003. Structure, stability and dynamics of the central domain of cardiac myosin binding protein C (MyBP-C): implications for multidomain assembly and causes for cardiomyopathy. *J Mol Biol* 329(4), pp. 745-761.

Ikemoto, T. et al. 1995. Enhancing effect of calmodulin on Ca($^{2+}$)-induced Ca^{2+} release in the sarcoplasmic reticulum of rabbit skeletal muscle fibres. *J Physiol* 487 (Pt 3), pp. 573-582.

Ingles, J. et al. 2005. Compound and double mutations in patients with hypertrophic cardiomyopathy: implications for genetic testing and counselling.*J Med Genet*. Vol. 42. England, p. e59.

Inui, M. et al. 1987. Isolation of the ryanodine receptor from cardiac sarcoplasmic reticulum and identity with the feet structures. *J Biol Chem* 262(32), pp. 15637-15642.

Jayaraman, T. et al. 1992. FK506 binding protein associated with the calcium release channel (ryanodine receptor). *J Biol Chem* 267(14), pp. 9474-9477.

Jayasinghe, I. D. et al. 2012. Nanoscale organization of junctophilin-2 and ryanodine receptors within peripheral couplings of rat ventricular cardiomyocytes.*Biophys J*. Vol. 102. United States: Copyright (c) 2012 Biophysical Society. Published by Elsevier Inc. All rights reserved., pp. L19-21.

Jayasinghe, I. D. et al. 2009. Organization of ryanodine receptors, transverse tubules, and sodium-calcium exchanger in rat myocytes.*Biophys J*. Vol. 97. United States, pp. 2664-2673.

Jeffries, C. M. et al. 2011. Human cardiac myosin binding protein C: structural flexibility within an extended modular architecture. *J Mol Biol* 414(5), pp. 735-748. doi: 10.1016/j.jmb.2011.10.029

Jeffries, C. M. et al. 2008. Small-angle X-ray scattering reveals the N-terminal domain organization of cardiac myosin binding protein C. *J Mol Biol* 377(4), pp. 1186-1199. doi: 10.1016/j.jmb.2008.01.080

Jiang, D. et al. 2010. Characterization of a novel mutation in the cardiac ryanodine receptor that results in catecholaminergic polymorphic ventricular tachycardia.*Channels (Austin)*. Vol. 4. United States, pp. 302-310.

Jiang, D. et al. 2005. Enhanced store overload-induced Ca^{2+} release and channel sensitivity to luminal Ca^{2+} activation are common defects of RyR2 mutations linked to ventricular tachycardia and sudden death.*Circ Res*. Vol. 97. United States, pp. 1173-1181.

Jiang, D. et al. 2002. Enhanced basal activity of a cardiac Ca^{2+} release channel (ryanodine receptor) mutant associated with ventricular tachycardia and sudden death. *Circ Res* 91(3), pp. 218-225.

Jordan, M. and Wurm, F. 2004. Transfection of adherent and suspended cells by calcium phosphate. *Methods* 33(2), pp. 136-143. doi: 10.1016/j.ymeth.2003.11.011

Jungbluth, H. 2007. Central core disease. *Orphanet J Rare Dis* 2, p. 25. doi: 10.1186/1750-1172-2-25

Kaboord, B. and Perr, M. 2008. Isolation of proteins and protein complexes by immunoprecipitation. *Methods Mol Biol* 424, pp. 349-364. doi: 10.1007/978-1-60327-064-9_27

Kaindl, A. M. et al. 2004. Missense mutations of ACTA1 cause dominant congenital myopathy with cores.*J Med Genet*. Vol. 41. England, pp. 842-848.

Karsai, A. et al. 2011. Mechanical unfolding of cardiac myosin binding protein-C by atomic force microscopy. *Biophys J* 101(8), pp. 1968-1977. doi: 10.1016/j.bpj.2011.08.030

Kashir, J. et al. 2011. Loss of activity mutations in phospholipase C zeta (PLCzeta) abolishes calcium oscillatory ability of human recombinant protein in mouse oocytes. *Hum Reprod* 26(12), pp. 3372-3387. doi: 10.1093/humrep/der336

Kimlicka, L. et al. 2013. The cardiac ryanodine receptor N-terminal region contains an anion binding site that is targeted by disease mutations. *Structure* 21(8), pp. 1440-1449. doi: 10.1016/j.str.2013.06.012

Kimura, T. et al. 2007. A variably spliced region in the type 1 ryanodine receptor may participate in an inter-domain interaction. *Biochem J* 401(1), pp. 317-324. doi: 10.1042/bj20060686

Kohr, M. J. et al. 2011. Characterization of potential S-nitrosylation sites in the myocardium. *Am J Physiol Heart Circ Physiol* 300(4), pp. H1327-1335. doi: 10.1152/ajpheart.00997.2010

Koide, A. et al. 1998. The fibronectin type III domain as a scaffold for novel binding proteins. *J Mol Biol* 284(4), pp. 1141-1151. doi: 10.1006/jmbi.1998.2238

Konno, T. et al. 2003. A novel missense mutation in the myosin binding protein-C gene is responsible for hypertrophic cardiomyopathy with left ventricular dysfunction and dilation in elderly patients. *J Am Coll Cardiol* 41(5), pp. 781-786.

Kooij, V. et al. 2013. Characterization of the cardiac myosin binding protein-C phosphoproteome in healthy and failing human hearts. *J Mol Cell Cardiol* 60, pp. 116-120. doi: 10.1016/j.yjmcc.2013.04.012

Korte, F. S. et al. 2003. Loaded shortening, power output, and rate of force redevelopment are increased with knockout of cardiac myosin binding protein-C. *Circ Res* 93(8), pp. 752-758. doi: 10.1161/01.res.0000096363.85588.9a

Kubalova, Z. et al. 2005. Abnormal intrastore calcium signaling in chronic heart failure.*Proc Natl Acad Sci U S A*. Vol. 102. United States, pp. 14104-14109.

Kulikovskaya, I. et al. 2007. Multiple forms of cardiac myosin-binding protein C exist and can regulate thick filament stability. *J Gen Physiol* 129(5), pp. 419-428. doi: 10.1085/jgp.200609714

Kuster, D. W. et al. 2014. Release kinetics of circulating cardiac myosin binding protein-C following cardiac injury. *Am J Physiol Heart Circ Physiol* 306(4), pp. H547-556. doi: 10.1152/ajpheart.00846.2013

Kuster, D. W. et al. 2015. A Hypertrophic Cardiomyopathy-associated MYBPC3 Mutation Common in Populations of South Asian Descent Causes Contractile Dysfunction.*J Biol Chem*. Vol. 290. United States: 2015 by The American Society for Biochemistry and Molecular Biology, Inc., pp. 5855-5867.

Kuster, D. W. et al. 2013. GSK3beta phosphorylates newly identified site in the proline-alanine-rich region of cardiac myosin-binding protein C and alters cross-bridge cycling kinetics in human: short communication. *Circ Res* 112(4), pp. 633-639. doi: 10.1161/circresaha.112.275602

Lahat, H. et al. 2001. A missense mutation in a highly conserved region of CASQ2 is associated with autosomal recessive catecholamine-induced polymorphic ventricular tachycardia in Bedouin families from Israel. *Am J Hum Genet* 69(6), pp. 1378-1384. doi: 10.1086/324565

Lai, F. A. et al. 1992. Expression of a cardiac Ca(2+)-release channel isoform in mammalian brain. *Biochem J* 288 (Pt 2), pp. 553-564.

Lai, F. A. et al. 1988. Purification and reconstitution of the calcium release channel from skeletal muscle. *Nature* 331(6154), pp. 315-319. doi: 10.1038/331315a0

Landmann, L. and Marbet, P. 2004. Colocalization analysis yields superior results after image restoration. *Microsc Res Tech* 64(2), pp. 103-112. doi: 10.1002/jemt.20066

Lanner, J. T. et al. 2010. Ryanodine receptors: structure, expression, molecular details, and function in calcium release. *Cold Spring Harb Perspect Biol* 2(11), p. a003996. doi: 10.1101/cshperspect.a003996

Laver, D. R. 2010. Regulation of RyR Channel Gating by Ca(2+), Mg(2+) and ATP. *Curr Top Membr* 66, pp. 69-89. doi: 10.1016/s1063-5823(10)66004-8

Laver, D. R. et al. 2008. A domain peptide of the cardiac ryanodine receptor regulates channel sensitivity to luminal Ca^{2+} via cytoplasmic Ca^{2+} sites. *Eur Biophys J* 37(4), pp. 455-467. doi: 10.1007/s00249-007-0238-z

Laver, D. R. et al. 1997. Reduced inhibitory effect of Mg^{2+} on ryanodine receptor-Ca^{2+} release channels in malignant hyperthermia. *Biophys J* 73(4), pp. 1913-1924. doi: 10.1016/s0006-3495(97)78222-5

Leahy, D. J. et al. 1992. Structure of a fibronectin type III domain from tenascin phased by MAD analysis of the selenomethionyl protein. *Science* 258(5084), pp. 987-991.

Lee, K. et al. 2015. Orientation of myosin binding protein C in the cardiac muscle sarcomere determined by domain-specific immuno-EM. *J Mol Biol* 427(2), pp. 274-286. doi: 10.1016/j.jmb.2014.10.023

Li, J. et al. 2013. ss-Adrenergic stimulation increases RyR2 activity via intracellular Ca^{2+} and Mg^{2+} regulation. *PLoS One* 8(3), p. e58334. doi: 10.1371/journal.pone.0058334

Li, L. et al. 1998. Cardiac myocyte calcium transport in phospholamban knockout mouse: relaxation and endogenous CaMKII effects. *Am J Physiol* 274(4 Pt 2), pp. H1335-1347.

Li, P. and Chen, S. R. 2001. Molecular basis of Ca(2)+ activation of the mouse cardiac Ca(2)+ release channel (ryanodine receptor). *J Gen Physiol* 118(1), pp. 33-44.

Li, X. et al. 2005. Endothelin-1-induced arrhythmogenic Ca^{2+} signaling is abolished in atrial myocytes of inositol-1,4,5-trisphosphate(IP3)-receptor type 2-deficient mice. *Circ Res* 96(12), pp. 1274-1281. doi: 10.1161/01.RES.0000172556.05576.4c

Lin, F. et al. 2011. Fibronectin growth factor-binding domains are required for fibroblast survival. *J Invest Dermatol* 131(1), pp. 84-98. doi: 10.1038/jid.2010.253

Linke, W. A. 2008. Sense and stretchability: the role of titin and titin-associated proteins in myocardial stress-sensing and mechanical dysfunction. *Cardiovasc Res* 77(4), pp. 637-648. doi: 10.1016/j.cardiores.2007.03.029

Liu, N. et al. 2006. Arrhythmogenesis in catecholaminergic polymorphic ventricular tachycardia: insights from a RyR2 R4496C knock-in mouse model. *Circ Res* 99(3), pp. 292-298. doi: 10.1161/01.RES.0000235869.50747.e1

Liu, Y. et al. 2013. The CPVT-associated RyR2 mutation G230C enhances store overload-induced Ca^{2+} release and destabilizes the N-terminal domains.*Biochem J*. Vol. 454. England, pp. 123-131.

Liu, Y. et al. 2015. Roles of the NH2-terminal Domains of Cardiac Ryanodine Receptor in Ca^{2+} Release Activation and Termination.*J Biol Chem*. Vol. 290. United States: 2015 by The American Society for Biochemistry and Molecular Biology, Inc., pp. 7736-7746.

Ljubojevic, S. et al. 2014. Early remodeling of perinuclear Ca^{2+} stores and nucleoplasmic Ca^{2+} signaling during the development of hypertrophy and heart failure. *Circulation* 130(3), pp. 244-255. doi: 10.1161/circulationaha.114.008927

Lobo, P. A. et al. 2011. The deletion of exon 3 in the cardiac ryanodine receptor is rescued by beta strand switching. *Structure* 19(6), pp. 790-798. doi: 10.1016/j.str.2011.03.016

Lobo, P. A. and Van Petegem, F. 2009. Crystal structures of the N-terminal domains of cardiac and skeletal muscle ryanodine receptors: insights into disease mutations. *Structure* 17(11), pp. 1505-1514. doi: 10.1016/j.str.2009.08.016

Lokuta, A. J. et al. 1997. Modulation of cardiac ryanodine receptors by sorcin. *J Biol Chem* 272(40), pp. 25333-25338.

Lopes, L. R. and Elliott, P. M. 2014. A straightforward guide to the sarcomeric basis of cardiomyopathies. *Heart* 100(24), pp. 1916-1923. doi: 10.1136/heartjnl-2014-305645

Lu, Y. et al. 2012. The motif of human cardiac myosin-binding protein C is required for its Ca^{2+}-dependent interaction with calmodulin. *J Biol Chem* 287(37), pp. 31596-31607. doi: 10.1074/jbc.M112.383299

Lukyanenko, V. et al. 2007. Functional groups of ryanodine receptors in rat ventricular cells.*J Physiol*. Vol. 583. England, pp. 251-269.

Lynch, T. L. t. et al. 2015. Oxidative Stress in Dilated Cardiomyopathy Caused by MYBPC3 Mutation. *Oxid Med Cell Longev* 2015, p. 424751. doi: 10.1155/2015/424751

MacDonnell, S. M. et al. 2008. Adrenergic regulation of cardiac contractility does not involve phosphorylation of the cardiac ryanodine receptor at serine 2808. *Circ Res* 102(8), pp. e65-72. doi: 10.1161/circresaha.108.174722

Macgregor, A. et al. 2007. NAADP controls cross-talk between distinct Ca^{2+} stores in the heart. *J Biol Chem* 282(20), pp. 15302-15311. doi: 10.1074/jbc.M611167200

MacLennan, D. H. et al. 1990. Ryanodine receptor gene is a candidate for predisposition to malignant hyperthermia. *Nature* 343(6258), pp. 559-561. doi: 10.1038/343559a0

Manders, E. M. M. et al. 1993. Measurement of co-localization of objects in dual-colour confocal images. Journal of Microscopy.

Marks, A. R. 1996. Cellular functions of immunophilins. *Physiol Rev* 76(3), pp. 631-649.

Marston, S. et al. 2009. Evidence from human myectomy samples that MYBPC3 mutations cause hypertrophic cardiomyopathy through haploinsufficiency. *Circ Res* 105(3), pp. 219-222. doi: 10.1161/circresaha.109.202440

Martino, M. M. and Hubbell, J. A. 2010. The 12th-14th type III repeats of fibronectin function as a highly promiscuous growth factor-binding domain. *Faseb j* 24(12), pp. 4711-4721. doi: 10.1096/fj.09-151282

Marx, S. O. et al. 2001. Coupled gating between cardiac calcium release channels (ryanodine receptors). *Circ Res* 88(11), pp. 1151-1158.

Marx, S. O. et al. 2000. PKA phosphorylation dissociates FKBP12.6 from the calcium release channel (ryanodine receptor): defective regulation in failing hearts. *Cell* 101(4), pp. 365-376.

Marziali, G. et al. 1996. cDNA cloning reveals a tissue specific expression of alternatively spliced transcripts of the ryanodine receptor type 3 (RyR3) calcium release channel. *FEBS Lett* 394(1), pp. 76-82.

Mason, S. A. et al. 2012. The contribution of hydrophobic residues in the pore-forming region of the ryanodine receptor channel to block by large tetraalkylammonium cations and Shaker B inactivation peptides. *J Gen Physiol* 140(3), pp. 325-339. doi: 10.1085/jgp.201210851

Mattei, M. G. et al. 1994. Chromosomal localization of murine ryanodine receptor genes RYR1, RYR2, and RYR3 by in situ hybridization. *Genomics* 22(1), pp. 202-204. doi: 10.1006/geno.1994.1362

McConnell, B. K. et al. 1999. Dilated cardiomyopathy in homozygous myosin-binding protein-C mutant mice. *J Clin Invest* 104(9), pp. 1235-1244. doi: 10.1172/jci7377

McNally, E. M. et al. 2015. The genetic landscape of cardiomyopathy and its role in heart failure. *Cell Metab* 21(2), pp. 174-182. doi: 10.1016/j.cmet.2015.01.013

Mead-Savery, F. C. et al. 2009. Changes in negative charge at the luminal mouth of the pore alter ion handling and gating in the cardiac ryanodine-receptor.*Biophys J*. Vol. 96. United States, pp. 1374-1387.

Medeiros-Domingo, A. et al. 2009. The RYR2-encoded ryanodine receptor/calcium release channel in patients diagnosed previously with either catecholaminergic polymorphic ventricular tachycardia or genotype negative, exercise-induced long QT syndrome: a comprehensive open reading frame mutational analysis. *J Am Coll Cardiol* 54(22), pp. 2065-2074. doi: 10.1016/j.jacc.2009.08.022

Meissner, G. 1984. Adenine nucleotide stimulation of Ca^{2+}-induced Ca^{2+} release in sarcoplasmic reticulum. *J Biol Chem* 259(4), pp. 2365-2374.

Meissner, G. and el-Hashem, A. 1992. Ryanodine as a functional probe of the skeletal muscle sarcoplasmic reticulum Ca^{2+} release channel. *Mol Cell Biochem* 114(1-2), pp. 119-123.

Meissner, G. and Henderson, J. S. 1987. Rapid calcium release from cardiac sarcoplasmic reticulum vesicles is dependent on Ca^{2+} and is modulated by Mg^{2+}, adenine nucleotide, and calmodulin. *J Biol Chem* 262(7), pp. 3065-3073.

Milting, H. et al. 2006. Composite polymorphisms in the ryanodine receptor 2 gene associated with arrhythmogenic right ventricular cardiomyopathy. *Cardiovasc Res* 71(3), pp. 496-505. doi: 10.1016/j.cardiores.2006.04.004

Mohamed, A. S. et al. 1998. Cardiac myosin-binding protein C (MyBP-C): identification of protein kinase A and protein kinase C phosphorylation sites. *Arch Biochem Biophys* 358(2), pp. 313-319. doi: 10.1006/abbi.1998.0857

Monnier, N. et al. 1997. Malignant-hyperthermia susceptibility is associated with a mutation of the alpha 1-subunit of the human dihydropyridine-sensitive L-type voltage-dependent calcium-channel receptor in skeletal muscle. *Am J Hum Genet* 60(6), pp. 1316-1325.

Monnier, N. et al. 2001. Familial and sporadic forms of central core disease are associated with mutations in the C-terminal domain of the skeletal muscle ryanodine receptor. *Hum Mol Genet* 10(22), pp. 2581-2592.

Moolman-Smook, J. et al. 2002. Identification of novel interactions between domains of Myosin binding protein-C that are modulated by hypertrophic cardiomyopathy missense mutations. *Circ Res* 91(8), pp. 704-711.

Moore, C. P. et al. 1999. Apocalmodulin and Ca^{2+} calmodulin bind to the same region on the skeletal muscle Ca^{2+} release channel. *Biochemistry* 38(26), pp. 8532-8537. doi: 10.1021/bi9907431

Moore, J. R. et al. 2012. Understanding cardiomyopathy phenotypes based on the functional impact of mutations in the myosin motor. *Circ Res* 111(3), pp. 375-385. doi: 10.1161/circresaha.110.223842

Moss, R. L. et al. 2015. Cardiac MyBP-C Regulates the Rate and Force of Contraction in Mammalian Myocardium.*Circ Res*. Vol. 116. (c) 2015 American Heart Association, Inc., pp. 183-192.

Most, P. et al. 2003. Transgenic overexpression of the Ca^{2+}-binding protein S100A1 in the heart leads to increased in vivo myocardial contractile performance. *J Biol Chem* 278(36), pp. 33809-33817. doi: 10.1074/jbc.M301788200

Motulsky, M. and Christopopulos, A. 2003. Fitting the models to biological data using linear and nonlinear regression. A practical guide to curve fitting. San Diego: GraphPad Software Inc.

Mrosek, M. et al. 2007. Molecular determinants for the recruitment of the ubiquitin-ligase MuRF-1 onto M-line titin. *Faseb j* 21(7), pp. 1383-1392. doi: 10.1096/fj.06-7644com

Nadvi, N. A. et al. 2016. Clinically Linked Mutations in the Central Domains of Cardiac Myosin-Binding Protein C with Distinct Phenotypes Show Differential Structural Effects. *Structure* 24(1), pp. 105-115. doi: 10.1016/j.str.2015.11.001

NCBI. 2016a. Online Database: Conserved Protein Domain Family, FN3. *Accessed on 6.06.2016*.

NCBI. 2016b. Online Database: Conserved Protein Domain Family, Ig_Titin_like. *Accessed on 06.06.2016*.

Neylon, C. B. et al. 1995. Multiple types of ryanodine receptor/Ca^{2+} release channels are expressed in vascular smooth muscle. *Biochem Biophys Res Commun* 215(3), pp. 814-821. doi: 10.1006/bbrc.1995.2536

Noboru F et al. 2006. A novel missense mutation in cardiac ryanodine receptor gene as a possible cause of hypertrophic cardiomyopathy: evidence from familial analysis. Circulation, Am Heart Assoc.

Nyegaard, M. et al. 2012. Mutations in calmodulin cause ventricular tachycardia and sudden cardiac death. *Am J Hum Genet* 91(4), pp. 703-712. doi: 10.1016/j.ajhg.2012.08.015

Oakley, C. E. et al. 2004. Myosin binding protein C: structural abnormalities in familial hypertrophic cardiomyopathy. *Cell Res* 14(2), pp. 95-110. doi: 10.1038/sj.cr.7290208

Offer, G. et al. 1973. A new protein of the thick filaments of vertebrate skeletal myofibrils. Extractions, purification and characterization. *J Mol Biol* 74(4), pp. 653-676.

Opie, L. H. 2004. *Heart physiology: from cell to circulation*. Lippincott Williams & Wilkins.

Otey, C. A. et al. 2009. Cytoplasmic Ig-domain proteins: cytoskeletal regulators with a role in human disease. *Cell Motil Cytoskeleton* 66(8), pp. 618-634. doi: 10.1002/cm.20385

Otsu, K. et al. 1990. Molecular cloning of cDNA encoding the Ca^{2+} release channel (ryanodine receptor) of rabbit cardiac muscle sarcoplasmic reticulum. *J Biol Chem* 265(23), pp. 13472-13483.

Palmer, B. M. et al. 2004. Role of cardiac myosin binding protein C in sustaining left ventricular systolic stiffening. *Circ Res* 94(9), pp. 1249-1255. doi: 10.1161/01.res.0000126898.95550.31

Park, H. et al. 2004. Comparing skeletal and cardiac calsequestrin structures and their calcium binding: a proposed mechanism for coupled calcium binding and protein polymerization. *J Biol Chem* 279(17), pp. 18026-18033. doi: 10.1074/jbc.M311553200

Patterson, R. L. et al. 2004. Inositol 1,4,5-trisphosphate receptors as signal integrators. *Annu Rev Biochem* 73, pp. 437-465. doi: 10.1146/annurev.biochem.73.071403.161303

Pereira, L. et al. 2014. Calcium signaling in diabetic cardiomyocytes. *Cell Calcium* 56(5), pp. 372-380. doi: 10.1016/j.ceca.2014.08.004

Perez, C. F. et al. 2003. Amino acids 1-1,680 of ryanodine receptor type 1 hold critical determinants of skeletal type for excitation-contraction coupling. Role of divergence domain D2. *J Biol Chem* 278(41), pp. 39644-39652. doi: 10.1074/jbc.M305160200

Perfetto, L. et al. 2013. Exploring the diversity of SPRY/B30.2-mediated interactions. *Trends Biochem Sci* 38(1), pp. 38-46. doi: 10.1016/j.tibs.2012.10.001

Pessah, I. N. et al. 1985. The calcium-ryanodine receptor complex of skeletal and cardiac muscle. *Biochem Biophys Res Commun* 128(1), pp. 449-456.

Piacentino, V., 3rd et al. 2003. Cellular basis of abnormal calcium transients of failing human ventricular myocytes. *Circ Res* 92(6), pp. 651-658. doi: 10.1161/01.res.0000062469.83985.9b

Pierschbacher, M. D. and Ruoslahti, E. 1984. Cell attachment activity of fibronectin can be duplicated by small synthetic fragments of the molecule. *Nature* 309(5963), pp. 30-33.

Pohlmann, L. et al. 2007. Cardiac myosin-binding protein C is required for complete relaxation in intact myocytes. *Circ Res* 101(9), pp. 928-938. doi: 10.1161/circresaha.107.158774

Pompey, S. N. et al. 2013. Quantitative fluorescence co-localization to study protein-receptor complexes. *Methods Mol Biol* 1008, pp. 439-453. doi: 10.1007/978-1-62703-398-5_16

Popova, O. B. et al. 2012. Identification of ATP-binding regions in the RyR1 Ca(2)(+) release channel. *PLoS One* 7(11), p. e48725. doi: 10.1371/journal.pone.0048725

Previs, M. J. et al. 2016. Phosphorylation and calcium antagonistically tune myosin-binding protein C's structure and function. *Proc Natl Acad Sci U S A* 113(12), pp. 3239-3244. doi: 10.1073/pnas.1522236113

Previs, M. J. et al. 2015. Myosin-binding protein C corrects an intrinsic inhomogeneity in cardiac excitation-contraction coupling. *Sci Adv* 1(1), doi: 10.1126/sciadv.1400205

Priori, S. G. and Chen, S. R. 2011. Inherited dysfunction of sarcoplasmic reticulum Ca^{2+} handling and arrhythmogenesis. *Circ Res* 108(7), pp. 871-883. doi: 10.1161/circresaha.110.226845

Priori, S. G. et al. 2002. Clinical and molecular characterization of patients with catecholaminergic polymorphic ventricular tachycardia. *Circulation* 106(1), pp. 69-74.

Priori, S. G. et al. 2001. Mutations in the cardiac ryanodine receptor gene (hRyR2) underlie catecholaminergic polymorphic ventricular tachycardia. *Circulation* 103(2), pp. 196-200.

Probst, S. et al. 2011. Sarcomere gene mutations in isolated left ventricular noncompaction cardiomyopathy do not predict clinical phenotype. *Circ Cardiovasc Genet* 4(4), pp. 367-374. doi: 10.1161/circgenetics.110.959270

Rajagopal, V. et al. 2015. Examination of the Effects of Heterogeneous Organization of RyR Clusters, Myofibrils and Mitochondria on Ca^{2+} Release Patterns in Cardiomyocytes. *PLoS Comput Biol* 11(9), p. e1004417. doi: 10.1371/journal.pcbi.1004417

Rinne, A. et al. 2009. Adenovirus-mediated delivery of short hairpin RNA (shRNA) mediates efficient gene silencing in terminally differentiated cardiac myocytes. *Methods Mol Biol* 515, pp. 107-123. doi: 10.1007/978-1-59745-559-6_7

Robinson, R. L. et al. 2002. RYR1 mutations causing central core disease are associated with more severe malignant hyperthermia in vitro contracture test phenotypes. *Hum Mutat* 20(2), pp. 88-97. doi: 10.1002/humu.10098

Rosenberg, H. et al. 2015. Malignant hyperthermia: a review. *Orphanet J Rare Dis* 10, p. 93. doi: 10.1186/s13023-015-0310-1

Rottbauer, W. et al. 1997. Novel splice donor site mutation in the cardiac myosin-binding protein-C gene in familial hypertrophic cardiomyopathy. Characterization Of cardiac transcript and protein. *J Clin Invest* 100(2), pp. 475-482. doi: 10.1172/jci119555

Roux-Buisson, N. et al. 2012. Absence of triadin, a protein of the calcium release complex, is responsible for cardiac arrhythmia with sudden death in human. *Hum Mol Genet* 21(12), pp. 2759-2767. doi: 10.1093/hmg/dds104

Sadayappan, S. and de Tombe, P. P. 2012. Cardiac myosin binding protein-C: redefining its structure and function. *Biophys Rev* 4(2), pp. 93-106. doi: 10.1007/s12551-012-0067-x

Sadayappan, S. et al. 2009. Cardiac myosin binding protein-C phosphorylation in a {beta}-myosin heavy chain background. *Circulation* 119(9), pp. 1253-1262. doi: 10.1161/circulationaha.108.798983

Sadayappan, S. et al. 2005. Cardiac myosin-binding protein-C phosphorylation and cardiac function. *Circ Res* 97(11), pp. 1156-1163. doi: 10.1161/01.RES.0000190605.79013.4d

Sadayappan, S. et al. 2006. Cardiac myosin binding protein C phosphorylation is cardioprotective. *Proc Natl Acad Sci U S A* 103(45), pp. 16918-16923. doi: 10.1073/pnas.0607069103

Salnikov, V. et al. 2009. Distribution of ryanodine receptors in rat ventricular myocytes. *J Muscle Res Cell Motil* 30(3-4), pp. 161-170. doi: 10.1007/s10974-009-9186-9

Sambrook, J. et al. 1989. *Molecular cloning*. Cold spring harbor laboratory press New York.

Samso, M. et al. 2009. Coordinated movement of cytoplasmic and transmembrane domains of RyR1 upon gating.*PLoS Biol*. Vol. 7. United States, p. e85.

Samso, M. et al. 2005. Internal structure and visualization of transmembrane domains of the RyR1 calcium release channel by cryo-EM. *Nat Struct Mol Biol* 12(6), pp. 539-544. doi: 10.1038/nsmb938

Sato, N. et al. 2003. A novel variant of cardiac myosin-binding protein-C that is unable to assemble into sarcomeres is expressed in the aged mouse atrium. *Mol Biol Cell* 14(8), pp. 3180-3191. doi: 10.1091/mbc.E02-10-0685

Scoote, M. and Williams, A. J. 2004. Myocardial calcium signalling and arrhythmia pathogenesis. *Biochem Biophys Res Commun* 322(4), pp. 1286-1309. doi: 10.1016/j.bbrc.2004.08.034

Scriven, D. R. et al. 2013. Microarchitecture of the dyad. *Cardiovasc Res* 98(2), pp. 169-176. doi: 10.1093/cvr/cvt025

Sebillon, P. et al. 2001. COOH-terminal truncated human cardiac MyBP-C alters myosin filament organization. *C R Acad Sci III* 324(3), pp. 251-260.

Seidel, M. 2014. Characterisation of inter-subunit interactions within cardiac ryanodine receptor. . Dissertation, Cardiff University.

Seidel, M. et al. 2015. Dantrolene rescues aberrant N-terminus intersubunit interactions in mutant pro-arrhythmic cardiac ryanodine receptors. *Cardiovasc Res* 105(1), pp. 118-128. doi: 10.1093/cvr/cvu240

Seiler, S. H. et al. 1996. Modulation of myosin filament organization by C-protein family members. *Mol Biol Cell* 7(1), pp. 113-127.

Seo, M. D. et al. 2012. Structural and functional conservation of key domains in InsP3 and ryanodine receptors. *Nature* 483(7387), pp. 108-112. doi: 10.1038/nature10751

Serysheva, II et al. 2008. Subnanometer-resolution electron cryomicroscopy-based domain models for the cytoplasmic region of skeletal muscle RyR channel. *Proc Natl Acad Sci U S A* 105(28), pp. 9610-9615. doi: 10.1073/pnas.0803189105

Shacklock, P. S. et al. 1995. Local Ca^{2+} transients (Ca^{2+} sparks) originate at transverse tubules in rat heart cells. *J Physiol* 487 (Pt 3), pp. 601-608.

Shaner, N. C. et al. 2004. Improved monomeric red, orange and yellow fluorescent proteins derived from Discosoma sp. red fluorescent protein.*Nat Biotechnol*. Vol. 22. United States, pp. 1567-1572.

Shannon, T. R. et al. 2003. Elevated sarcoplasmic reticulum Ca^{2+} leak in intact ventricular myocytes from rabbits in heart failure.*Circ Res*. Vol. 93. United States, pp. 592-594.

Sharma, P. et al. 2012. Structural determination of the phosphorylation domain of the ryanodine receptor. *Febs j* 279(20), pp. 3952-3964. doi: 10.1111/j.1742-4658.2012.08755.x

Sigalas, C. et al. 2009. Ca^{2+}-calmodulin increases RyR2 open probability yet reduces ryanoid association with RyR2. *Biophys J* 97(7), pp. 1907-1916. doi: 10.1016/j.bpj.2009.07.027

Sitsapesan, R. and Williams, A. J. 1994. Gating of the native and purified cardiac SR Ca(2+)-release channel with monovalent cations as permeant species. *Biophys J* 67(4), pp. 1484-1494. doi: 10.1016/s0006-3495(94)80622-8

Sondergaard, M. T. et al. 2015. Arrhythmogenic Calmodulin Mutations Affect the Activation and Termination of Cardiac Ryanodine Receptor-mediated Ca^{2+} Release. *J Biol Chem* 290(43), pp. 26151-26162. doi: 10.1074/jbc.M115.676627

Song, L. et al. 2007. Calsequestrin 2 (CASQ2) mutations increase expression of calreticulin and ryanodine receptors, causing catecholaminergic polymorphic ventricular tachycardia. *J Clin Invest* 117(7), pp. 1814-1823. doi: 10.1172/jci31080

Song, L. S. et al. 2006. Orphaned ryanodine receptors in the failing heart. *Proc Natl Acad Sci U S A* 103(11), pp. 4305-4310. doi: 10.1073/pnas.0509324103

Song, Q. et al. 2003. Rescue of cardiomyocyte dysfunction by phospholamban ablation does not prevent ventricular failure in genetic hypertrophy. *J Clin Invest* 111(6), pp. 859-867. doi: 10.1172/jci16738

Spezzacatene, A. et al. 2015. Arrhythmogenic Phenotype in Dilated Cardiomyopathy: Natural History and Predictors of Life-Threatening Arrhythmias. *J Am Heart Assoc* 4(10), p. e002149. doi: 10.1161/jaha.115.002149

Spirito, P. and Bellone, P. 1994. Natural history of hypertrophic cardiomyopathy. *Br Heart J* 72(6 Suppl), pp. S10-12.

Spooner, P. M. et al. 2012. Large isoforms of UNC-89 (obscurin) are required for muscle cell architecture and optimal calcium release in Caenorhabditis elegans. *PLoS One* 7(7), p. e40182. doi: 10.1371/journal.pone.0040182

Stange, M. et al. 2003. Characterization of recombinant skeletal muscle (Ser-2843) and cardiac muscle (Ser-2809) ryanodine receptor phosphorylation mutants. *J Biol Chem* 278(51), pp. 51693-51702. doi: 10.1074/jbc.M310406200

Stathopoulou, K. et al. 2016. S-glutathiolation impairs phosphoregulation and function of cardiac myosin-binding protein C in human heart failure. *Faseb j* 30(5), pp. 1849-1864. doi: 10.1096/fj.201500048

Stelzer, J. E. et al. 2006a. Ablation of cardiac myosin-binding protein-C accelerates stretch activation in murine skinned myocardium. *Circ Res* 98(9), pp. 1212-1218. doi: 10.1161/01.RES.0000219863.94390.ce

Stelzer, J. E. et al. 2006b. Ablation of myosin-binding protein-C accelerates force development in mouse myocardium. *Biophys J* 90(11), pp. 4119-4127. doi: 10.1529/biophysj.105.078147

Stewart, R. et al. 2003. Oligomerization of the cardiac ryanodine receptor C-terminal tail. *Biochem J* 376(Pt 3), pp. 795-799. doi: 10.1042/bj20030597

Stoyanovsky, D. et al. 1997. Nitric oxide activates skeletal and cardiac ryanodine receptors. *Cell Calcium* 21(1), pp. 19-29.

Stynen, B. et al. 2012. Diversity in genetic in vivo methods for protein-protein interaction studies: from the yeast two-hybrid system to the mammalian split-luciferase system. *Microbiol Mol Biol Rev* 76(2), pp. 331-382. doi: 10.1128/mmbr.05021-11

Subramanian, S. et al. 2001. Underlying mechanisms of symmetric calcium wave propagation in rat ventricular myocytes.*Biophys J*. Vol. 80. United States, pp. 1-11.

Sutko, J. L. et al. 1997. The Pharmacology of Ryanodine and Related Compounds. *Pharmacological Reviews*.

Swan, R. C. and Fischman, D. A. 1986. Electron microscopy of C-protein molecules from chicken skeletal muscle. *J Muscle Res Cell Motil* 7(2), pp. 160-166.

Takasago, T. et al. 1989. Phosphorylation of the cardiac ryanodine receptor by cAMP-dependent protein kinase. *J Biochem* 106(5), pp. 872-877.

Takeshima, H. et al. 1998. Embryonic lethality and abnormal cardiac myocytes in mice lacking ryanodine receptor type 2. *EMBO J* 17(12), pp. 3309-3316. doi: 10.1093/emboj/17.12.3309

Takeshima, H. et al. 1989. Primary structure and expression from complementary DNA of skeletal muscle ryanodine receptor. *Nature* 339(6224), pp. 439-445. doi: 10.1038/339439a0

Tang, Y. et al. 2012. Abnormal termination of Ca^{2+} release is a common defect of RyR2 mutations associated with cardiomyopathies.*Circ Res*. Vol. 110. United States, pp. 968-977.

Tarvinder, S. D. et al. 2017. Massive Accumulation of Myofibroblasts in the Critical Isthmus Is Associated With Ventricular Tachycardia Inducibility in Post-Infarct Swine Heart. JACC: Clinical Electrophysiology

Taylor, S. C. et al. 2013. A defined methodology for reliable quantification of Western blot data. *Mol Biotechnol* 55(3), pp. 217-226. doi: 10.1007/s12033-013-9672-6

Terentyev, D. et al. 2008. Modulation of SR Ca release by luminal Ca and calsequestrin in cardiac myocytes: effects of CASQ2 mutations linked to sudden cardiac death. *Biophys J* 95(4), pp. 2037-2048. doi: 10.1529/biophysj.107.128249

Terentyev, D. et al. 2003. Protein phosphatases decrease sarcoplasmic reticulum calcium content by stimulating calcium release in cardiac myocytes. *J Physiol* 552(Pt 1), pp. 109-118. doi: 10.1113/jphysiol.2003.046367

Thastrup, O. et al. 1990. Thapsigargin, a tumor promoter, discharges intracellular Ca^{2+} stores by specific inhibition of the endoplasmic reticulum Ca2(+)-ATPase. *Proc Natl Acad Sci U S A* 87(7), pp. 2466-2470.

Thomas, D. et al. 2000. A comparison of fluorescent Ca^{2+} indicator properties and their use in measuring elementary and global Ca^{2+} signals. *Cell Calcium* 28(4), pp. 213-223. doi: 10.1054/ceca.2000.0152

Thomas, N. L. et al. 2004. Functional heterogeneity of ryanodine receptor mutations associated with sudden cardiac death. *Cardiovasc Res* 64(1), pp. 52-60. doi: 10.1016/j.cardiores.2004.06.009

Thomas, N. L. et al. 2005. Differential Ca^{2+} sensitivity of RyR2 mutations reveals distinct mechanisms of channel dysfunction in sudden cardiac death. *Biochem Biophys Res Commun* 331(1), pp. 231-238. doi: 10.1016/j.bbrc.2005.02.194

Thomas, P. and Smart, T. G. 2005. HEK293 cell line: a vehicle for the expression of recombinant proteins. *J Pharmacol Toxicol Methods* 51(3), pp. 187-200. doi: 10.1016/j.vascn.2004.08.014

Tilgen, N. et al. 2001. Identification of four novel mutations in the C-terminal membrane spanning domain of the ryanodine receptor 1: association with central core disease and alteration of calcium homeostasis. *Hum Mol Genet* 10(25), pp. 2879-2887.

Timerman, A. P. et al. 1996. Selective binding of FKBP12.6 by the cardiac ryanodine receptor. *J Biol Chem* 271(34), pp. 20385-20391.

Tiso, N. et al. 2001. Identification of mutations in the cardiac ryanodine receptor gene in families affected with arrhythmogenic right ventricular cardiomyopathy type 2 (ARVD2). *Hum Mol Genet* 10(3), pp. 189-194.

Treves, S. et al. 1997. Interaction of S100A1 with the Ca^{2+} release channel (ryanodine receptor) of skeletal muscle. *Biochemistry* 36(38), pp. 11496-11503. doi: 10.1021/bi970160w

Tung, C. C. et al. 2010. The amino-terminal disease hotspot of ryanodine receptors forms a cytoplasmic vestibule. *Nature* 468(7323), pp. 585-588. doi: 10.1038/nature09471

Tunwell, R. E. et al. 1996. The human cardiac muscle ryanodine receptor-calcium release channel: identification, primary structure and topological analysis. *Biochem J* 318 (Pt 2), pp. 477-487.

van der Werf, C. and Wilde, A. A. 2013. Catecholaminergic polymorphic ventricular tachycardia: from bench to bedside. *Heart* 99(7), pp. 497-504. doi: 10.1136/heartjnl-2012-302033

van Dijk, S. J. et al. 2009. Cardiac myosin-binding protein C mutations and hypertrophic cardiomyopathy: haploinsufficiency, deranged phosphorylation, and cardiomyocyte dysfunction.*Circulation*. Vol. 119. United States, pp. 1473-1483.

van Dijk, S. J. et al. 2012. Contractile dysfunction irrespective of the mutant protein in human hypertrophic cardiomyopathy with normal systolic function.*Circ Heart Fail*. Vol. 5. United States, pp. 36-46.

Van Petegem, F. 2015. Ryanodine receptors: allosteric ion channel giants. *J Mol Biol* 427(1), pp. 31-53. doi: 10.1016/j.jmb.2014.08.004

Vassilakopoulou, V. et al. 2015. Distinctive malfunctions of calmodulin mutations associated with heart RyR2-mediated arrhythmic disease. *Biochim Biophys Acta*, doi: 10.1016/j.bbagen.2015.07.001

Vignier, N. et al. 2009. Nonsense-mediated mRNA decay and ubiquitin-proteasome system regulate cardiac myosin-binding protein C mutant levels in cardiomyopathic mice. *Circ Res* 105(3), pp. 239-248. doi: 10.1161/circresaha.109.201251

Waldmuller, S. et al. 2003. Novel deletions in MYH7 and MYBPC3 identified in Indian families with familial hypertrophic cardiomyopathy. *J Mol Cell Cardiol* 35(6), pp. 623-636.

Walweel, K. et al. 2014. Differences in the regulation of RyR2 from human, sheep, and rat by Ca(2)(+) and Mg(2)(+) in the cytoplasm and in the lumen of the sarcoplasmic reticulum. *J Gen Physiol* 144(3), pp. 263-271. doi: 10.1085/jgp.201311157

Weber, C. R. et al. 2003. Dynamic regulation of sodium/calcium exchange function in human heart failure. *Circulation* 108(18), pp. 2224-2229. doi: 10.1161/01.cir.0000095274.72486.94

Weber, F. E. et al. 1993. Complete sequence of human fast-type and slow-type muscle myosin-binding-protein C (MyBP-C). Differential expression, conserved domain structure and chromosome assignment. *Eur J Biochem* 216(2), pp. 661-669.

Wehrens, X. H. et al. 2003. FKBP12.6 deficiency and defective calcium release channel (ryanodine receptor) function linked to exercise-induced sudden cardiac death. *Cell* 113(7), pp. 829-840.

Wehrens, X. H. et al. 2004. Ca^{2+}/calmodulin-dependent protein kinase II phosphorylation regulates the cardiac ryanodine receptor. *Circ Res* 94(6), pp. e61-70. doi: 10.1161/01.res.0000125626.33738.e2

Welikson, R. E. and Fischman, D. A. 2002. The C-terminal IgI domains of myosin-binding proteins C and H (MyBP-C and MyBP-H) are both necessary and sufficient for the intracellular crosslinking of sarcomeric myosin in transfected non-muscle cells. *J Cell Sci* 115(Pt 17), pp. 3517-3526.

Wilson, K. J. et al. 2012. UNC-89 (obscurin) binds to MEL-26, a BTB-domain protein, and affects the function of MEI-1 (katanin) in striated muscle of Caenorhabditis elegans. *Mol Biol Cell* 23(14), pp. 2623-2634. doi: 10.1091/mbc.E12-01-0055

Witcher, D. R. et al. 1991. Unique phosphorylation site on the cardiac ryanodine receptor regulates calcium channel activity. *J Biol Chem* 266(17), pp. 11144-11152.

Wright, N. T. et al. 2008. S100A1 and calmodulin compete for the same binding site on ryanodine receptor. *J Biol Chem* 283(39), pp. 26676-26683. doi: 10.1074/jbc.M804432200

Wu, X. et al. 2006. Local InsP3-dependent perinuclear Ca^{2+} signaling in cardiac myocyte excitation-transcription coupling. *J Clin Invest* 116(3), pp. 675-682. doi: 10.1172/jci27374

Xiao, B. et al. 2005. Characterization of a novel PKA phosphorylation site, serine-2030, reveals no PKA hyperphosphorylation of the cardiac ryanodine receptor in canine heart failure. *Circ Res* 96(8), pp. 847-855. doi: 10.1161/01.RES.0000163276.26083.e8

Xiao, B. et al. 2006. Ser-2030, but not Ser-2808, is the major phosphorylation site in cardiac ryanodine receptors responding to protein kinase A activation upon beta-adrenergic stimulation in normal and failing hearts. *Biochem J* 396(1), pp. 7-16. doi: 10.1042/bj20060116

Xiao, J. et al. 2007. Removal of FKBP12.6 does not alter the conductance and activation of the cardiac ryanodine receptor or the susceptibility to stress-induced ventricular arrhythmias. *J Biol Chem* 282(48), pp. 34828-34838. doi: 10.1074/jbc.M707423200

Xiong, L. et al. 2006. A Ca^{2+}-binding domain in RyR1 that interacts with the calmodulin binding site and modulates channel activity. *Biophys J* 90(1), pp. 173-182. doi: 10.1529/biophysj.105.066092

Xu, J. et al. 2015. Investigation of Pathogenic Genes in Chinese sporadic Hypertrophic Cardiomyopathy Patients by Whole Exome Sequencing. *Sci Rep* 5, p. 16609. doi: 10.1038/srep16609

Xu, L. et al. 1998. Activation of the cardiac calcium release channel (ryanodine receptor) by poly-S-nitrosylation. *Science* 279(5348), pp. 234-237.

Yamaguchi, N. et al. 2011. Modulation of sarcoplasmic reticulum Ca^{2+} release in skeletal muscle expressing ryanodine receptor impaired in regulation by calmodulin and S100A1. *Am J Physiol Cell Physiol* 300(5), pp. C998-c1012. doi: 10.1152/ajpcell.00370.2010

Yamaguchi, N. et al. 2003. Molecular basis of calmodulin binding to cardiac muscle Ca(2+) release channel (ryanodine receptor). *J Biol Chem* 278(26), pp. 23480-23486. doi: 10.1074/jbc.M301125200

Yan, Z. et al. 2015. Structure of the rabbit ryanodine receptor RyR1 at near-atomic resolution. *Nature* 517(7532), pp. 50-55. doi: 10.1038/nature14063

Yang, H. T. et al. 2002. The ryanodine receptor modulates the spontaneous beating rate of cardiomyocytes during development. *Proc Natl Acad Sci U S A* 99(14), pp. 9225-9230. doi: 10.1073/pnas.142651999

Yang, Q. et al. 1999. In vivo modeling of myosin binding protein C familial hypertrophic cardiomyopathy. *Circ Res* 85(9), pp. 841-847.

Yang, W. et al. 2008. Proteomic approaches to the analysis of multiprotein signaling complexes. *Proteomics* 8(4), pp. 832-851. doi: 10.1002/pmic.200700650

Yano, M. et al. 2005. Correction of defective interdomain interaction within ryanodine receptor by antioxidant is a new therapeutic strategy against heart failure. *Circulation* 112(23), pp. 3633-3643. doi: 10.1161/circulationaha.105.555623

Yao, A. et al. 1998. Effects of overexpression of the Na+-Ca^{2+} exchanger on $[Ca^{2+}]$i transients in murine ventricular myocytes. *Circ Res* 82(6), pp. 657-665.

Yasuda, M. et al. 1995. Complete primary structure of chicken cardiac C-protein (MyBP-C) and its expression in developing striated muscles. *J Mol Cell Cardiol* 27(10), pp. 2275-2286.

Yuchi, Z. et al. 2012. Disease mutations in the ryanodine receptor central region: crystal structures of a phosphorylation hot spot domain. *Structure* 20(7), pp. 1201-1211. doi: 10.1016/j.str.2012.04.015

Yuchi, Z. et al. 2015. Crystal structures of ryanodine receptor SPRY1 and tandem-repeat domains reveal a critical FKBP12 binding determinant. *Nat Commun* 6, p. 7947. doi: 10.1038/ncomms8947

Zahradnikova, A. et al. 2003. Regulation of dynamic behavior of cardiac ryanodine receptor by Mg^{2+} under simulated physiological conditions. *Am J Physiol Cell Physiol* 285(5), pp. C1059-1070. doi: 10.1152/ajpcell.00118.2003

Zalk, R. et al. 2015. Structure of a mammalian ryanodine receptor. *Nature* 517(7532), pp. 44-49. doi: 10.1038/nature13950

Zhang, H. et al. 2003. A noncontiguous, intersubunit binding site for calmodulin on the skeletal muscle Ca^{2+} release channel. *J Biol Chem* 278(10), pp. 8348-8355. doi: 10.1074/jbc.M209565200

Zhang, H. B. et al. 2013. Ultrastructural uncoupling between T-tubules and sarcoplasmic reticulum in human heart failure. *Cardiovasc Res* 98(2), pp. 269-276. doi: 10.1093/cvr/cvt030

Zhang, L. et al. 1997. Complex formation between junctin, triadin, calsequestrin, and the ryanodine receptor. Proteins of the cardiac junctional sarcoplasmic reticulum membrane. *J Biol Chem* 272(37), pp. 23389-23397.

Zhang, Y. et al. 1993. A mutation in the human ryanodine receptor gene associated with central core disease. *Nat Genet* 5(1), pp. 46-50. doi: 10.1038/ng0993-46

Zheng, W. 2015. Toward decrypting the allosteric mechanism of the ryanodine receptor based on coarse-grained structural and dynamic modeling. *Proteins* 83(12), pp. 2307-2318. doi: 10.1002/prot.24951

Zissimopoulos, S. et al. 2007. Redox sensitivity of the ryanodine receptor interaction with FK506-binding protein.*J Biol Chem*. Vol. 282. United States, pp. 6976-6983.

Zissimopoulos, S. and Lai, F. A. 2005. Central domain of the human cardiac muscle ryanodine receptor does not mediate interaction with FKBP12.6.*Cell Biochem Biophys*. Vol. 43. United States, pp. 203-219.

Zissimopoulos, S. et al. 2014. N-terminus oligomerization is conserved in intracellular calcium release channels. *Biochem J* 459(2), pp. 265-273. doi: 10.1042/bj20131061

Zissimopoulos, S. et al. 2012. Disparities in the association of the ryanodine receptor and the FK506-binding proteins in mammalian heart.*J Cell Sci*. Vol. 125. England, pp. 1759-1769.

Zissimopoulos, S. et al. 2009. FKBP12.6 binding of ryanodine receptors carrying mutations associated with arrhythmogenic cardiac disease.*Biochem J*. Vol. 419. England, pp. 273-278.

Zissimopoulos, S. et al. 2013. N-terminus oligomerization regulates the function of cardiac ryanodine receptors.*J Cell Sci*. Vol. 126. England, pp. 5042-5051.

Zissimopoulos, S. et al. 2006. Ryanodine receptor interaction with the SNARE-associated protein snapin.*J Cell Sci*. Vol. 119. England, pp. 2386-2397.

Zorzato, F. et al. 2007. Functional effects of mutations identified in patients with multiminicore disease. *IUBMB Life* 59(1), pp. 14-20. doi: 10.1080/15216540601187803